LIPOSOMES ENCAPSULATING DNA-INTERCALATING MOLECULES: AN APPROACH FOR PHOTODYNAMIC THERAPY APPLICATION

THAIS PRISCILLA PIVETTA

BSc in Pharmacy-Biochemistry

LIPOSOMES ENCAPSULATING DNA-INTERCALATING MOLECULES: AN APPROACH FOR PHOTODYNAMIC THERAPY APPLICATION

THAIS PRISCILLA PIVETTA

BSc in Pharmacy-Biochemistry

Adviser:	Maria de Fátima Guerreiro da Silva Campos Raposo Associate Professor with Habilitation, NOVA University Lisbon
Co-advisers:	Paulo António Martins Ferreira Ribeiro Associate Professor, NOVA University Lisbon

Examination Committee:

Chair:	José Paulo Moreira dos Santos, Full Professor, NOVA University Lisbon
Rapporteurs:	Ana Margarida Madeira Viegas de Barros Timmons, Assistant Professor, Universidade de Aveiro
	Cecília Ribeiro da Cruz Calado, Adjunct Professor, Instituto Superior de Engenharia de Lisboa
Adviser:	Maria de Fátima Guerreiro da Silva Campos Raposo, Associate Professor with Habilitation, NOVA University Lisbon
Members:	João Miguel Pinto Coelho, Researcher Assistant, Faculdade de Ciências da Universidade de Lisboa

DOCTORATE IN RADIATION BIOLOGY AND BIOPHYSICS

NOVA University Lisbon
March, 2022

Liposomes encapsulating DNA-intercalating molecules: an approach for Photodynamic Therapy application

This document was created with Microsoft Word text processor and the NOVAthesis Word template.

In memory of my grandparents.

ACKNOWLEDGMENTS

First of all, I would like to acknowledge my supervisor Prof. Dr. Maria Raposo, who gave me a great support during these four years, being always available for discussion and open-minded for new ideas regarding this project. Thank you for all the encouragement and for all the strength given to me for the development of this thesis. I also appreciate all the opportunities for the participation in conferences and training schools. Thank you for the sympathy, the kindness and the care given to me in these last years.

To my co-supervisor Prof. Dr. Paulo Ribeiro who was always supportive and helpful, mainly with the irradiation system. For sure, was always in a good mood and brought many smiles to my face. Thank you for the good energy, it was extremely necessary for this journey.

I would like to acknowledge Prof. Dr. Pedro Tavares that is the coordinator of the Radiation Biology and Biophysics Doctoral Training Programme and Prof. Dr. Paulo Limão-Vieira and Prof. Dr. Alice Pereira from the Executive Committee of the Doctoral Training Programme for giving me the opportunity to pursue this PhD.

I would like to thank Prof. Dr. Jorge Silva, who was kind and supportive and received me into his laboratory to perform the cell studies.

I would like to acknowledge Prof. Dr. Sandra Simões from the Faculty of Pharmacy, University of Lisbon, for allowing the Dynamic Light Scattering measurements.

Thanks to Prof. Dr. Susana Sério that provided the facility to carry out the UV-vis measurements and to Dr. Quirina Ferreira, for helping me with the beginning of some AFM measurements.

To my colleagues from the Functional Molecular Systems group, in particularly Paulo Zagalo and Carlota Conceição that were always helpful, supportive, and comprehensive with me, thank you for the friendship.

To Dr. Simone Barbosa and Dr. Acelino De Sá who came for a short time and brought so much joy to the Functional Molecular Systems group. In special, thanks to Dr. Simone who was really helpful and gave me suggestions regarding the liposomes preparation, to overcome some obstacles that I was facing with this part of the thesis.

I would like to acknowledge Dr. Tânia Vieira for all the support, the lessons about the cell culture and for all the help, understanding and the kind talks that came along this way.

I want to thank Dr. Filipe Almeida for giving me helpful knowledge on cell culture and for all the help dispensed in the laboratory. Also, thanks for allowing the studies with the melanoma cell line.

To all the people from the GreatLab, people who are still there and those who already left, thank you for all the help and for the great companionship.

I would like to acknowledge Prof. Dr. Osvaldo Novais Oliveira Jr. that made possible the visit to the São Carlos Institute of Physics for the development of the Langmuir studies.

To Dr. Ellen Wrobel and Karen Jochelavicius, I appreciate all the time dispensed to help me initiate my experiments with Langmuir monolayers.

My acknowledgements to Dr. Bruno Bassi who dedicated some time to show me the laboratories and helped me locate in the Group of Polymers "Prof. Bernhard Gross" at the Sao Carlos Institute of Physics, University of Sao Paulo. Also, thanks to Dr. Débora Balogh for all the assistance in the laboratory and to all the people from the Group of Polymers, thank you for receiving me so well.

Thanks to the secretariat of the Physics Department for helping me with the orders of materials and other bureaucracies. In special Mrs. Ana Cruz, that always tried her best to help me, thank you so much for all the assistance and for your friendship.

I would like to acknowledge my friend Caroline Botteon who gave me so much strength during this time and was such a good writing partner in the review article. Thanks to my friends Letícia Bueno and Ivana Carvalho that, despite the time spent apart, were always there for me when I needed the most.

To João Carmo, thank you for all the love, support, and the strength you gave to me. I am grateful for your good vibes, your positivity and for always making me smile when I had a hard time.

Lastly, I would like to thank my parents and my sister that, despite the long time I spent apart from the family, gave me an incredible support during these years. Thank you for believing in me, caring about me and helping me pursue my dreams.

"Not all of us can do great things,

but we can do small things with great love."

- Mother Teresa

ABSTRACT

Photodynamic Therapy (PDT) has been widely explored for the treatment of some types of cancer as a selective and minimally invasive therapy, making use of photosensitizers (PS) that in presence of oxygen and light produce reactive oxygen species and consequent cell death. Many molecules have been investigated regarding the photosensitizing potential, however, most of the PS present some drawbacks such as aggregation and low solubility in physiological environments influencing the efficacy. The use of nanostructures for the PS molecules encapsulation has been addressed by means of lipid nanostructures that are biocompatible and biodegradable. Liposomes are lipid-based vesicles able to encapsulate both hydrophilic and hydrophobic drugs and are promising alternatives to enhance the therapy efficacy. The main goal of this work was to select non-conventional photosensitizers among some DNA-intercalating molecules, followed by the encapsulation of these molecules aiming the PDT application in skin cancer cells. For this purpose, the phototoxic potential of a set of DNA-intercalating molecules was investigated. Results revealed that Methylene Blue (MB) and Acridine Orange (AO) molecules present the most significant phototoxic effects in a skin cancer cell line. Liposome's stability has also been evaluated, and the most promising formulations were able to provide higher stability for the encapsulation of the MB and AO photosensitizers which also revealed, in general, higher encapsulation efficiency. Phototoxicity was shown not to be significantly affected by PS encapsulation however, different effects on the size and encapsulation efficiency were observed for MB and AO. Langmuir monolayer studies unveiled the effect of the selected molecules on the lipid's interaction with results suggesting that MB and AO cause a decrease in the monolayer order and consequently increasing the membrane elasticity. In summary, MB-liposomes has cytotoxic potential for cancer cells while AO-liposomes presents phototoxic potential at very low concentrations. These results are important to comprehend the possible application of these systems for skin cancer photodynamic therapy.

Keywords: Photodynamic Therapy, Photosensitizers, DNA-intercalating molecules, Nanoparticles, Liposomes, Methylene Blue, Acridine Orange, Lipids.

RESUMO

Fototerapia dinâmica (PDT) tem sido extensivamente explorada para o tratamento de alguns tipos de cancro como uma terapia seletiva e minimamente invasiva, fazendo uso de fotossensibilizadores (PS) que, na presença de oxigénio e luz, produz espécies reativas de oxigénio e consequente morte celular. Muitas moléculas tem sido investigadas em relação ao potencial fotossensibilizador no entanto, a maioria dos PS apresentam desvantagens como agregação e pouca solubilidade em ambientes fisiológicos, influenciando a eficácia. O uso de nanoestruturas para o encapsulamento de PS tem sido direcionado pelo uso de nanoestruturas lipídicas que são biocompatíveis e biodegradáveis. Lipossomas são vesículas lipídicas, capazes de encapsular compostos hidrofílicos e hidrofóbicos e são promissoras alternativas para melhorar a eficácia da terapia. O objetivo principal deste trabalho foi selecionar fotossensibilizadores não-convencionais entre algumas moléculas intercalantes do DNA, seguido pelo encapsulamento destas moléculas para applicação da PDT em células de cancro da pele. Para isto, o potencial fototóxico de um conjunto de moléculas intercalantes de DNA foi investigado. Os resultados revelaram que as moléculas de Azul de Metileno (MB) e Laranja de Acridina (AO) apresentam os efeitos fototóxicos mais significativos na linhagem de cancro da pele. A estabilidade dos lipossomas também foi avaliada e as formulações mais promissoras foram capazes de providenciar maior estabilidade para o encapsulamento dos fotossensibilizadores MB e AO o que também revelou, no geral, uma maior eficiência de encapsulamento. A fototoxicidade mostrou não ser significativamente afetada pelo encapsulamento dos PS entretanto, diferentes efeitos no tamanho e na eficiência de encapsulamento foram observados para o MB e AO. Estudos em monocamadas de Langmuir revelaram o efeito das moléculas selecionadas nas interações com os lípidos, sugerindo que MB e AO causam uma diminuição da ordem da camada e consequentemente aumentam a elasticidade da membrana. Em suma, lipossomas com MB tem potencial citotóxico para as células de cancro enquanto que lipossomas com AO apresentam um potencial fototóxico em concentrações muito baixas. Estes resultados são importantes para compreender a possível aplicação destes sistemas para a fototerapia dinâmica do cancro da pele.

Palavras-chave: Terapia fotodinâmica, Fossensibilizadores, Moléculas intercalantes do DNA, Nanopartículas, Lipossomas, Azul de Metileno, Laranja de Acridina, Lípidos.

CONTENTS

LIST OF FIGURES

LIST OF TABLES

ACRONYMS

(16:0)LysoPC   1-palmitoyl-2-hydroxy-sn-glycero-3-phosphocholine

2-OH-E$^+$ 2-hydroxyethidium

AIE   Aggregation-induced emission

AFM   Atomic force microscopy

AO   Acridine orange

AVOs   Acidic vesicular organelles

BAM   Brewster angle microscopy

BIPY   2,2'-bipyridyl

BODIPY   Boron dipyrromethene

BPD   Benzoporphyrin derivative

CDs   Cyclodextrin

Ce6   Chlorin e6

CHOL   Cholesterol

CMC   Critical micelle concentration

CR   Cumulant release

CUR   Curcumin

DHE   Dihydroethidium

DLS   Dynamic Light Scattering

DMEM   Dulbecco's Modified Eagle Medium

DMPC   1,2-dimyristoyl-sn-glycero-3-phosphocholine

DMPG   1,2-dimyristoyl-sn-glycero-3-phospho-(1′-rac-glycerol)

DMSO   Dimethyl sulfoxide

DNA	Deoxyribonucleic acid
DOPC	1,2-dioleoyl-sn-glycero-3-phosphocholine
DOPE	1,2-dioleoyl-sn-glycero-3-phosphoethanolamine
DOPG	1,2-Dioleoyl-sn-glycero-3-phospho-rac-(1-glycerol)
DOTAP	1,2-dioleoyl-3-trimethylammonium-propane
DPPC	1,2-dipalmitoyl-sn-glycero-3-phosphocholine
DPPG	1,2-dipalmitoyl-sn-glycero-3-phospho-(1'-rac-glycerol)
DSPC	1,2-distearoyl-sn-glycero-3-phosphocholine
DSPE-PEG(2000)	1,2-distearoyl-sn-glycero-3-phosphoethanolamine-N-[amino(polyethylene glycol)-2000]
DSPG	1,2-distearoyl-sn-glycero-3-phospho-(1′-rac-glycerol)
E$^+$	Ethidium
EE	Encapsulation efficiency
EGCG	Epigallocatechin-gallate
FA	Folic acid
FADH$_2$	Reduced form of flavin adenine dinucleotide
FBS	Fetal bovine serum
FMNH$_2$	Reduced form of flavin mononucleotide
FTIR	Fourier transform infrared spectroscopy
GUVs	Giant unilamellar vesicles
GV	Gentian violet
HA	Hyaluronic acid
IR	Infrared
IRR	Irradiation
L1	Lipid composition containing DPPC and DPPG
L1sc	Lipid composition containing DPPC, DPPG and sodium cholate
L1sp	Lipid composition containing DPPC, DPPG and Span® 80
L2	Composition containing DPPC, DPPG and cholesterol
L2sc	Composition containing DPPC, DPPG, cholesterol and sodium cholate
L2sp	Composition containing DPPC, DPPG and cholesterol plus Span® 80

L3	Composition containing DPPC, DPPG and DOPG
L3sc	Composition containing DPPC, DPPG, DOPG and sodium cholate
L3sp	Composition containing DPPC, DPPG, DOPG and Span® 80
LC	Liquid condensed phase
LE	Liquid expanded phase
LED	Light emitting diode
LM	Lipid mixture containing DPPC, DPPG and cholesterol
LM-SC	Lipid mixture containing DPPC, DPPG and cholesterol plus sodium cholate
LM-SP	Lipid mixture containing DPPC, DPPG and cholesterol plus Span® 80
LUVs	Large unilamellar vesicles
MB	Methylene blue
MLVs	Multilamellar vesicles
MVVs	Multivesicular vesicles
MWCO	Molecular weight cut-off
NADH	Reduced nicotinamide adenine dinucleotide
NADPH	Reduced nicotinamide adenine dinucleotide phosphate
NC	Negative control of cell death
NEO	Neocuproine
NIR	Near-infrared
NLCs	Nanostructured lipid carriers
NPs	Nanoparticles
PBS	Phosphate-buffered saline
PC	Positive control of cell death
PdI	Polydispersity Index
PDT	Photodynamic therapy
PEG	Poly(ethylene glycol)
PLGA	Poly(lactic-co-glycolide)
PHE	Phenanthroline
PLLA	Poly(L-lactide)
PM-IRRAS	Polarization modulation-infrared reflection-adsorption spectroscopy

PNPs	Polymeric nanoparticles
PS	Photosensitizer
PTT	Photothermal therapy
QT	Quercetin
ROS	Reactive Oxygen Species
SC	Control of the solvent influence on cell viability
SLNs	Solid lipid nanoparticles
SNPs	Silica nanoparticles
SUVs	Small unilamellar vesicles
TEL	Tetraether lipids
UV	Ultraviolet
UVA	Ultraviolet A
UVC	Ultraviolet C
UV-vis	Ultraviolet Visible

SYMBOLS

a	Cross-section area of the head group
A	Absorbance
A_m	Mean molecular area
A_0	Extrapolated value of the area to zero pressure
A^0_{123}	Predicted average area per molecule of a mixed monolayer
b	Path length of the cuvette
c	Concentration of the sample
C_f	Concentration of free drug not encapsulated
C_n	Concentration at the selected time
CO_2	Carbon dioxide
Cs^{-1}	Compressional modulus
C_t	Total concentration of drug encapsulated in liposomes
D	Diffusion coefficient
E_0	Redox potential
F	Force of the surface taking the plate down
H_2O_2	Hydrogen peroxide
I	Transmitted light intensity
I_0	Incident light intensity
IC_{50}	Half-maximal inhibitory concentration
k_b	Boltzmann constant (1.380×10^{-23} kg.m².s^{-2}.K^{-1})
l	Molecular length
L	Perimeter of contact

$^1O_2$	Singlet oxygen
$O_2^{\cdot -}$	Superoxide radical
$^{\cdot}OH$	Hydroxyl radical
P	Packing parameter
Q	Amount of drug released
Q_t	Total amount of drug
R_h	Hydrodynamic radius
R_p	Reflectivity of the polarization "p"
R_s	Reflectivity of the polarization "s"
T	Temperature
T_c	Phase-transition temperature
v	Molecular volume
V_a	Volume of aliquot withdrawn from the release studies
V_t	Total volume of phosphate buffered saline in the release studies
x	Proportion of the lipids
γ	Surface tension
γ_0	Surface tension of the pure liquid
$\Delta R/R$	Differential reflectivity
ε	Molar absorption coefficient
η	Viscosity of the medium
θ	Contact angle between subphase and the plate
λ_{em}	Emission wavelength
λ_{ex}	Excitation wavelength
π	Surface pressure
π_c	Surface pressure at the collapse
τ	Time constant

$\Big|$ **1**

INTRODUCTION

1.1 General introduction

According to the World Health Organization cancer was reported as the second leading cause of death in 2019 under 70 years old age. GLOBOCAN, an online database that provides global statistics of cancer, estimated the occurrence of 19.3 million new cases of cancer in 2020 and nearly 10 million deaths due to this disease [1]. Melanoma and non-melanoma skin cancer counts with a high incidence [2] and non-melanoma skin cancer is the fourth most common, behind the breast cancer, lung cancer and prostate cancer [1]. There are several factors involved in the increase of the cases of skin cancer with special highlight to UV radiation exposure [3].

As most non-melanoma skin cancers are a localized disease, there are several strategies that can be adopted for the treatment such as the surgical excision and radiation therapy [4]. As photodynamic therapy (PDT) is a minimally invasive type of treatment, its use has increased for the treatment of non-melanoma skin cancers and can be an alternative to the surgical excisions [5,6]. PDT demands for three components: presence of oxygen, a photosensitizer drug, and a light source. The combination of these elements can generate reactive oxygen species (ROS) that will lead to the cell death. Therefore, the selection of the photosensitizer is important in order to obtain an efficient photodynamic therapy [7].

There are many molecules that have sensitizing potential induced by light. Among these molecules there are dyes, natural products and many others chemical substances [8]. The PDT-induced damage can affect biomolecules as a result of the oxidizing power of the reactive species. The DNA is one of the biomolecules that can be subjected to damage and is the main target for anticancer drugs [9]. In this context, there is still a lot to explore and study about DNA-intercalating agents aiming phototherapy applications.

Nanotechnology can be also used to ameliorate the PDT efficacy, overcoming some problems of the photosensitizers such as poor solubility and aggregation tendency in physiological conditions [10]. Due to the biodegradability, biocompatibility and non-toxicity, lipid nanoparticles are widely used for topical application including for PDT. Liposomes are among the lipid-based nanoparticles that can

be used for the encapsulation of hydrophobic and hydrophilic drugs and can be used for the delivery of photosensitizers in the skin [11].

Under this context, the aim of this work was the study of DNA-intercalating agents combined to nanotechnology for the potential application in PDT. A selection of photosensitizers was performed among a set of DNA-intercalating molecules (the dyes methylene blue, acridine orange and gentian violet; the natural products curcumin, quercetin, and epigallocatechin gallate; and the chelating compounds neocuproine, 1,10-phenanthroline and 2,2'-bipyridyl) followed by the development and optimization of liposomes to obtain small and stable vesicles, able to encapsulate the selected photosensitizers methylene blue and acridine orange. The work is concluded with studies of the interactions occurring between the selected molecules and the DNA when submitted to different sources of irradiation as well as the interactions between the photosensitizers and the lipids from the liposomes.

1.2 Dissertation layout

The document is divided in nine sections. This first chapter is a general introduction about the theme and the structure of the document. The second and third chapter present an introduction about the work. The fourth chapter is an experimental section, with concepts of the techniques used. The fifth to the eighth chapter are those containing the results obtained and finally the nineth chapter contains the main conclusions of this work.

Chapter 1: General Information

Here, a broad view of the aspects regarding the aim of the work and the structure of the document is presented with a brief description of each chapter and the related subject.

Chapter 2: Nanoparticles Systems for Cancer Phototherapy: an Overview

This chapter in divided in three main sections with an introduction about the phototherapy application in cancer therapy with the combination to nanoparticles followed by a section that focus on the concepts of photodynamic therapy, and the combination of nanoparticles with photodynamic therapy for organic carriers (solid lipid nanoparticles, liposomes, micelles, nanoemulsions, polymeric nanoparticles, cyclodextrins and protein nanoparticles), carbon-based nanomaterials, silica nanoparticles, magnetics nanoparticles and hybrid nanoparticles.

Chapter 3: Liposomes as a drug delivery system for Phototherapy application

In this chapter it is addressed a more detailed discussion about the topic liposomes as a drug delivery system and their application in photodynamic therapy. The concepts of liposomes are described as well as the types of liposomes regarding their size and lamellarity. The lipids that can be used for the

preparation are cited and the possibility of functionalization of these nanoparticles is also discussed. The concepts behind the novel classes of liposomes are approached as well as a topic about molecules for possible photodynamic therapy application.

Chapter 4: Experimental concepts

In this chapter the main concepts regarding the techniques and methodology employed during the development of this work are described. It is divided in sections and the first section is about the experiments in cell culture, encompassing the cell viability assays and the detection of reactive oxygen species. The second section focus on the method of liposomes preparation. The third section describe the technique used for the characterization of the liposomes size, namely dynamic light scattering. Ultraviolet visible is the fourth section, with the concepts of the technique that was used for several studies such as for the quantification of the compounds in the encapsulation efficiency and release studies, and for the interaction studies with the DNA. The fifth section is about the lipid interaction experiments on Langmuir monolayers and polarization modulation-infrared reflection-adsorption spectroscopy (PM-IRRAS). The sixth section shows the characteristics of the irradiation systems employed in this work.

Chapter 5: DNA-intercalating Agents: a study of the Photosensitizing effect

Here there is a brief introduction about the photosensitizers' role in photodynamic therapy with the presentation of some types of compounds that can be used for photosensitizing purpose. The compounds studied in this chapter were divided in three main groups: dyes, natural products and chelating agents. The results of the cytotoxicity assays in non-cancer keratinocytes and cancer keratinocytes cell line are exhibited, followed by the phototoxicity assays in the cancer keratinocytes cell line. With the results of the screening, two molecules proceeded in the studies: methylene blue and acridine orange. These molecules were tested in a method for the detection of reactive oxygen species and finally were tested in a melanoma cell line regarding their potential cytotoxicity and phototoxicity.

Chapter 6: Optimization of Nanoliposomes for the topical delivery of Photosensitizers

After the chapter five where several compounds were submitted to a screening regarding their phototoxicity, here in this chapter the dyes methylene blue and acridine orange are incorporated in nanoparticles. The first section is an introduction to liposomes and the incorporation of photosensitizers in nanoparticles. For the preparation of the nanoparticles an optimization process was performed, testing four types of lipids and three surfactants, in different combinations in order to achieve formulations with homogeneous population of nanoparticles, with small size and good stability. The results section presents the optimization of the liposomes, the formulations selected that were used for the encapsulation of the dyes and characterized regarding their size and encapsulation efficiency. The pattern of release was also studied and, finally, the assays in cell culture were performed for the evaluation of the cytotoxicity in non-cancer and cancer keratinocytes and the phototoxicity in cancer keratinocytes cell line.

Chapter 7: Exploiting the use of Acridine Orange and Methylene Blue in biological systems I: an Analysis of the Dyes effects on the DNA

Following the sequency of experiments (screening of compounds and encapsulation in liposomes) there are the studies of the interactions. In this chapter is presented the investigation of the effect of irradiation on the systems: DNA in presence of methylene blue or in presence of acridine orange. The first section is an introduction about these DNA-intercalating agents and in the results and discussion, the samples characteristics are presented and the kinetics of the compounds individually and with the DNA is analyzed.

Chapter 8: Exploiting the use of Acridine Orange and Methylene Blue in biological systems II: an Investigation of the Dyes effects on Lipids

In this chapter the interaction of the most promising lipid mixtures was studied with the dyes methylene blue and acridine orange. The interaction studies on lipids is divided in two parts: evaluation of the surface pressure – area isotherms and the PM-IRRAS. From the isotherms several parameters were obtained for the comparison between systems of mixed monolayers such as the extrapolated area, the compressional modulus and the collapse pressure. PM-IRRAS spectra were analyzed regarding the main groups found in the lipids studied. Finally, some perspectives related to the interaction of the dyes and the lipid mixtures are summed up in the conclusions.

Chapter 9: Conclusions

This final chapter show the main results obtained in the studies with the final remarks of the thesis as well as the perspectives of future.

References

1.   Sung, H.; Ferlay, J.; Siegel, R.L.; Laversanne, M.; Soerjomataram, I.; Jemal, A.; Bray, F. Global Cancer Statistics 2020: GLOBOCAN Estimates of Incidence and Mortality Worldwide for 36 Cancers in 185 Countries. *CA. Cancer J. Clin.* **2021**, *71*, 209–249, doi:10.3322/caac.21660.

2.   Linos, E.; Katz, K.A.; Colditz, G.A. Skin Cancer—The Importance of Prevention. *JAMA Intern. Med.* **2016**, *176*, 1435–1436, doi:10.1001/jamainternmed.2016.5008.

3.   Apalla, Z.; Nashan, D.; Weller, R.B.; Castellsagué, X. Skin Cancer: Epidemiology, Disease Burden, Pathophysiology, Diagnosis, and Therapeutic Approaches. *Dermatol. Ther. (Heidelb).* **2017**, *7*, 5–19, doi:10.1007/s13555-016-0165-y.

4.   Orthaber, K.; Pristovnik, M.; Skok, K.; Perić, B.; Maver, U. Skin Cancer and Its Treatment: Novel Treatment Approaches with Emphasis on Nanotechnology. *J. Nanomater.* **2017**, *2017*,

2606271, doi:10.1155/2017/2606271.

5. Zhao, B.; He, Y.-Y. Recent advances in the prevention and treatment of skin cancer using photodynamic therapy. *Expert Rev. Anticancer Ther.* **2010**, *10*, 1797–1809, doi:10.1586/era.10.154.

6. Khan, N.H.; Mir, M.; Qian, L.; Baloch, M.; Ali Khan, M.F.; Rehman, A.-; Ngowi, E.E.; Wu, D.-D.; Ji, X.-Y. Skin cancer biology and barriers to treatment: Recent applications of polymeric micro/nanostructures. *J. Adv. Res.* **2022**, *36*, 223–247, doi:10.1016/j.jare.2021.06.014.

7. Champeau, M.; Vignoud, S.; Mortier, L.; Mordon, S. Photodynamic therapy for skin cancer: How to enhance drug penetration? *J. Photochem. Photobiol. B Biol.* **2019**, *197*, 111544, doi:10.1016/j.jphotobiol.2019.111544.

8. Oniszczuk, A.; Wojtunik-Kulesza, K.A.; Oniszczuk, T.; Kasprzak, K. The potential of photodynamic therapy (PDT)—Experimental investigations and clinical use. *Biomed. Pharmacother.* **2016**, *83*, 912–929, doi:10.1016/j.biopha.2016.07.058.

9. Crous, A.; Chizenga, E.; Hodgkinson, N.; Abrahamse, H. Targeted Photodynamic Therapy: A Novel Approach to Abolition of Human Cancer Stem Cells. *Int. J. Opt.* **2018**, *2018*, 1–9, doi:10.1155/2018/7317063.

10. Hamblin, M.R.; Chiang, L.Y.; Lakshmanan, S.; Huang, Y.-Y.; Garcia-Diaz, M.; Karimi, M.; de Souza Rastelli, A.N.; Chandran, R. Nanotechnology for photodynamic therapy: a perspective from the Laboratory of Dr. Michael R. Hamblin in the Wellman Center for Photomedicine at Massachusetts General Hospital and Harvard Medical School. *Nanotechnol. Rev.* **2015**, *4*, 359–372, doi:10.1515/ntrev-2015-0027.

11. Pivetta, T.P.; Botteon, C.E.A.; Ribeiro, P.A.; Marcato, P.D.; Raposo, M. Nanoparticle Systems for Cancer Phototherapy: An Overview. *Nanomaterials* **2021**, *11*, 3132, doi:10.3390/nano11113132.

<div style="text-align: right">

2
</div>

NANOPARTICLE SYSTEMS FOR CANCER PHOTO-THERAPY: AN OVERVIEW [1]

Abstract: Photodynamic therapy (PDT) consists of photo-mediated treatments with different mechanisms of action that can be addressed for cancer treatment. Phototherapy is a highly successful and barely or non-invasive type of treatment that have gained attention in the past few years. The death of cancer cells as a result of the application of PDT is caused by the formation of reactive oxygen species, which leads to oxidative stress. Advancement in nanotechnology allowed significant benefit to these therapies through the use of nanoparticles, allowing both tuning of the process and increase of effectiveness. The encapsulation of drugs, development of the most different organic and inorganic nanoparticles as well as the possibility of surfaces' functionalization are some strategies used to combine phototherapy and nanotechnology, with the aim of an effective treatment with minimal side effects. This chapter presents an overview on the use of nanostructures in association with phototherapy, in the view of cancer treatment.

2.1 Introduction

Cancer is a leading cause of death worldwide, with an estimated 19.3 million new cases and nearly 10 million deaths caused by cancer in 2020 [1]. During the 20th century, there was an undeniable technological development aiming to enhance the treatment of cancer, mainly regarding to the discovery of chemotherapy. Nowadays, chemotherapy is one of the pillars for cancer treatment, along with surgery and radiotherapy [2,3]. However, it is known that chemotherapy and radiotherapy have severe side effects to the patient, mainly due to the non-specificity of the treatment [4]. Within this context, phototherapy has gained attention as an alternative treatment with reduced side effects [4].

Photodynamic therapy (PDT) and photothermal therapy (PTT) are photo-mediated therapies with different damage mechanisms that consist in the generation of reactive oxygen species (ROS) and heat, respectively [4,5]. These effects result in the cells' death, thereby, with a potential application for treatment of several types of cancer [6]. PDT requires the application of photosensitizer drugs (PS) that will be triggered by radiation. These drugs generally present poor solubility in physiological conditions, which can impair therapy's success [7]. For this purpose, it is necessary to find appropriate nanoparticulate systems that can deliver these drugs to the cancer cells. Although, there is not an unique definition that is internationally accepted, nanomaterials are often described in the scale of 1–1000 nm [8]. Nanotechnology emerged in order to overcome problems related to drugs' solubility and provide a targeted treatment, enabling to reduce drugs' dosage and also minimize several side effects in patients [9]. Additionally, through nanotechnology research, there are several types of nanoparticles, particularly metallic nanoparticles such as gold nanoparticles, that can generate heat upon exposition to light, which can be useful for PTT [10] as it induces hyperthermia in the tumour environment, consequently leading to cancer cells' death [11]. PTT is a non-invasive and selective technique which can potentially suppress many kinds of tumours [12]. Cancer treatment with the PTT approach offers many advantages, such as sensitization of hypoxic regions, reinforcement of the immune system, releasing of thermo-sensitive substances and increasing susceptibility of cancer cells to chemotherapeutic agents [13]. The combination of PDT and PTT is also possible through the use of a sensitizing agent able to produce ROS and hyperthermia [5].

Nanoparticles (NPs) for phototherapy have been extensively investigated and reported in the literature [14,15], and in this work, new issues concerning NP systems' design, in view of cancer treatment under photodynamic and photothermal therapies, will be addressed. The referred new issues are intended to exemplify recent approaches related to nanoparticle conditions, such as the targeting of drugs in the tumour site and issues and/or new achievements related to the phototherapy. The overall research situation and trend in both therapies using nanoparticles is clearly demonstrated in Figure 2.1, which shows, in the last ten years, both number of publications and number of citations listed in the Web of Science platform using "Photodynamic Therapy AND Nanoparticles" and "Photothermal Therapy AND Nanoparticles" as search topics, where both number of publications and of citations are strongly increasing in the recent years.
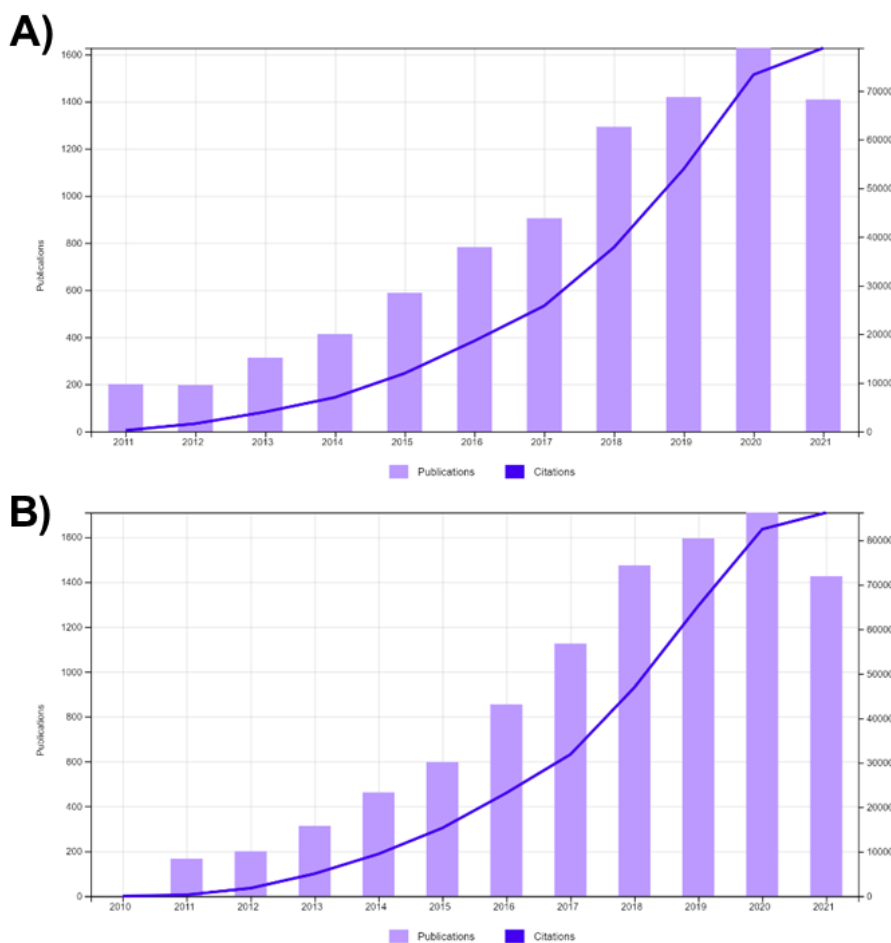
Figure 2.1: Updated number of publications and number of citations in the last ten years listed in the Web of Science platform using as search topics: (**A**) "Photodynamic Therapy AND Nanoparticles" and (**B**) "Photothermal Therapy AND Nanoparticles" (November 2021). Reproduced from the article that based this chapter [1].

2.2 Photodynamic Therapy

2.2.1 A Brief Introduction

PDT has been used for centuries, mainly to treat skin disorders, with most treatments involving the intake of extracts of some types of plants followed by sun exposition [16]. The main discovery took place in Germany in 1900, where Oscar Raab and Hermann von Tappeiner were investigating the behavior of protozoan *Paramecium* spp. in the presence of the dye acridine orange. They verified that the protozoan died after the exposure to the sunlight coming from an adjacent window. This discovery was

---

important later for the successful achievements on the human skin carcinoma treatment, and by 1904, it was found that the presence of oxygen was important for the treatment, originating the name photodynamic [17]. Currently, PDT is a highly successful and barely or non-invasive type of treatment for several skin disorders, such as psoriasis and cancers [18]. There are three important elements to perform PDT, which are a photosensitizer drug, the light source, and the presence of oxygen. The interaction of these elements results in reactive oxygen species (ROS), which play a key role in the treatment [19]. Upon a specific light wavelength, the photosensitizers (PS) can absorb a photon, which will lead to a conversion from the singlet ground state to the singlet excited state, as shown in Figure 2.2. From there, it can make an intersystem crossing to a metastable triplet state, which in its turn can take two possible paths known as PDT type I and type II. In type I, the activated photosensitizer can trigger a series of reactions with biomolecules generating radicals that interact with oxygen molecules, creating ROS. On the other hand, in PDT type II, the PS by itself can transfer energy directly to oxygen, resulting in ROS molecules [20,21]. Due to their high oxidizing power, ROS molecules have cytotoxic effects, however, due to the short lifetime, the effect of ROS on cell damage will occur around the created species [22].

However, PDT has a limited application that can depend on several factors to achieve a successful treatment. A special mention should be given to the light source which is an important variable to take into consideration because different light wavelengths have different penetration depths in tissues. For example, ultraviolet (UV) light is known to cause several damages in biomolecules such as the DNA, but presents low penetration compared to longer light wavelengths [23–27]. Near-infrared (NIR) light, on the other hand, is capable of higher penetration depths, with the capability of generation of local heat even with low energy input. NIR is also safer than UV, which can cause sunburns, inflammation, and even skin cancer [23,28].
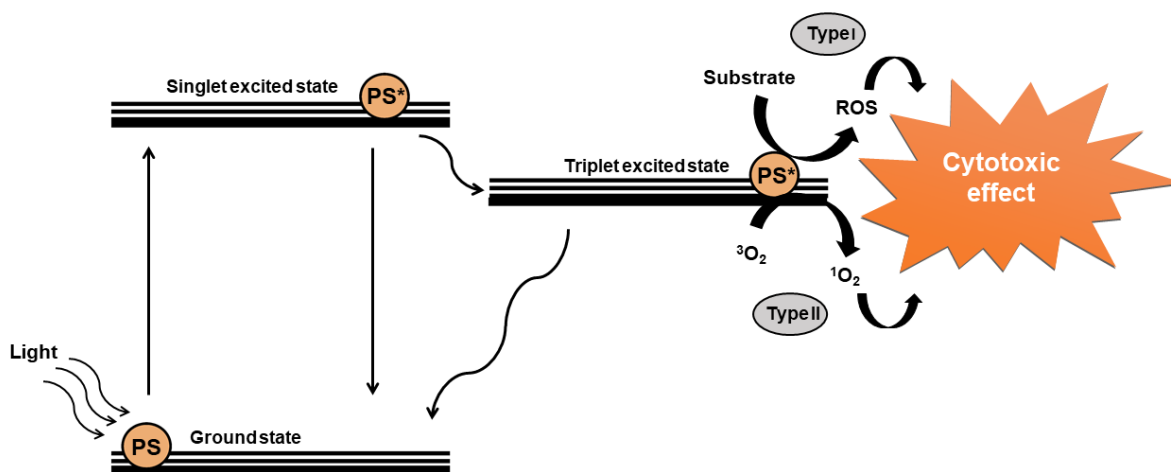
Figure 2.2: Jablonski diagram representation and the photodynamic therapy mechanism of action. Adapted from the article that based this chapter [1].

Another factor that can impair the PDT efficacy is the hypoxic tumour microenvironment. To overcome this challenge, some strategies involved the elaboration of nanoparticles with molecules such as catalase, that can react and generate oxygen, or hemoglobin and perfluorocarbon, which serve as an oxygen carrier. Therefore, the inclusion of these molecules in nanoparticles is able to improve the PDT efficacy [29].

The photosensitizer drugs themselves are another element that can interfere with the PDT. For example, some PS can present poor solubility under physiologic conditions and impair the correct distribution of the drug to the target tissue, which of course will interfere with the therapy's success. To circumvent such a drawback, the use of nanoparticulate systems is addressed, enhancing the drug's solubility and the cellular uptake, and consequently the PDT efficacy [7,30]. Many types of nanoparticles for PDT have been attempted for different types of cancers, and some aspects of nanoparticle systems for PDT will be discussed in this section.

2.2.2 Nanoparticles for PDT Application

As mentioned before, in phototherapy, the delivery of PS molecules to the target tissue is a relevant issue, as it is in all cases of drug delivery systems. The NPs systems to be used should be suitable to release the active components over a defined period of time with control over the nanoparticle size. The raw materials employed and their biodegradability are also important to consider for nanoparticles' preparation. The most common NPs used in PDT are not only organic-based but also inorganic,

---

[1] This chapter is based on the published review article:

such as silica and magnetic NPs. In the next sections, some of the best achievements with the use of nanocarriers will be presented.

2.2.2.1   Organic Nanoparticles

Organic nanoparticles are the most used systems to encapsulate molecules which can be used in PDT. There are several categories based on different materials and respective organization. Figure 2.3 is a representation that summarizes the most common categories of organic nanoparticles, and in Table 2.1, there is a brief description with examples of nanoparticulate systems that are cited in this chapter.
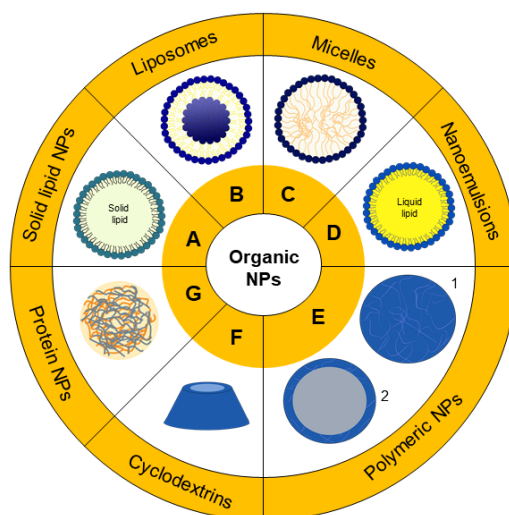
Figure 2.3: Illustration of different organic nanoparticles that can be used for photodynamic therapy: (A) solid lipid nanoparticles, (B) liposomes, (C) micelles, (D) nanoemulsions, (E) polymeric nanoparticles, (F) cyclodextrins and (G) protein nanoparticles. Reproduced from the article that based this chapter [1].

2.2.2.1.1   Solid Lipid Nanoparticles

Solid lipid nanoparticles (SLNs) were developed in the 1990s and, ever since, these particles have become the perfect model of safe nanoparticles with an occlusive effect that can also increase the drug permeation in the skin [31]. Generally, these NPs are composed of a surfactant layer, with a lipidic nucleus (Figure 2.3 – A), and can be prepared by the Müller and Lucks method based on high-pressure homogenization (1996) or by the microemulsion technique developed by Gasco (1993) [32,33].

Either way, SLNs production requires lipids that are solid at body temperature, such as some triglycerides or glycerides mixtures. Due to their composition, SLNs are well-tolerated, are biodegradable and can easily be produced on a large scale and at low cost [31,34,35]. However, SLNs present some disadvantages, such as the limited encapsulation efficiency and the possibility of drug release during the storage time. In order to overcome these problems, a second generation of SLNs was developed [34], the so-called nanostructured lipid carriers (NLCs). They consist of SLNs with a less ordered solid matrix based on a mixture of lipids. There are three types of NLCs: imperfect, amorphous and multiple [34]. The imperfect NLCs are composed by a blend of solid lipids with different chain lengths as well as the lipid saturation degree, characteristics that lead to the creation of an imperfect solid matrix. The amorphous type is produced from special solid and liquid lipids, creating a solid particle that does not crystalize. The combination of solid lipids with higher amounts of liquid lipids results in the multiple type, in which there is the creation of oil nano-compartments inside the solid matrix [34,36].

Nanostructured lipid carriers with a photosensitizer precursor (5-aminolevulinic acid) were developed by Qidwai and collaborators [37], aiming for use in basal-cell carcinoma treatment. In their study, the nanoparticles exhibited a sustained release profile, higher retention of the drug in the skin layers and enhanced toxicity. Similarly, solid lipid nanoparticles were used to encapsulate curcumin, a natural product with potential in phototherapy application. Curcumin nanoparticles were revealed to enhance drug uptake into the lung cancerous cells and were able to produce ROS under light exposition, thus presenting potential for phototherapy [38].

Most of the studies employing SLNs and NLCs are intended for skin delivery. For example, Goto et al. [39] developed solid lipid nanoparticles containing aluminium chloride phthalocyanine for melanoma treatment. The developed system showed great stability and the measurements of forced stability indicated that the system would be stable for 12 months. *In vitro* studies showed no toxicity under dark conditions but, when submitted to a light source, the toxicity was seen dependent on the radiation dose. Almeida et al. [40] also encapsulated phthalocyanine in lipid nanoparticle formulations and demonstrated an enhancement of the drug penetration in the skin, when compared to the control group. Interestingly, NLC formulation with higher amounts of the liquid lipid oleic acid showed greater retainment (89.5%) in the deeper skin layers when compared to the NLC with less oleic acid and the solid lipid nanoparticle. *In vitro* studies carried out on melanoma cells revealed that the free drug did not lead to cell toxicity under light conditions, probably due to poor accumulation in the cells but, on the other hand, drugs encapsulated in NLC showed a significant reduction in cell viability starting from 0.1 µg/mL. Therefore, the composition of solid lipid nanoparticles is a relevant parameter that can directly result in a higher effect in therapeutics.

2.2.2.1.2 Liposomes

Liposomes are formed by auto-organization of phospholipids in bilayers that, in an aqueous medium, tend to fold on themselves creating vesicles (Figure 2.3 – B) [41]. Due to the lipid's amphiphilic nature, hydrophilic and hydrophobic drugs can be stored in different compartments of liposomes [42]. These vesicles are usually employed as a model in the study of cell membranes, considering the similarity between them, however, liposomes can also be applied to drug delivery [43,44]. The lipid composition provides great biocompatibility, biodegradability and additionally, does not present toxicity [42,45]. The functionalization of these particles with polyethylene glycol (PEG) can lead to the creation of stealth liposomes, that are able to evade from the immune system and increase their blood circulation [46,47]. Other types of ligands can be used in the functionalization, such as antibodies, which in turn manage a robust targeted drug delivery [48]. Due to the system's versatility, liposomes are great candidates for photodynamic therapy application.

Foscan® is a commercial photosensitizer formulation already approved in Europe for neck and head cancers application. The active drug of Foscan®, known as temoporfin, also originated Foslip® and Fospeg®, which are liposomes formulations [49]. The temoporfin encapsulation in the lipid carriers presents a similar phototoxicity as Foscan® with significantly lower toxicity. Fospeg®, a derivative from Foslip® and distinguished by a PEGylation, is able to provide enhanced pharmacokinetics with longer circulation in the blood [50,51]. Studies in HeLa spheroids showed that the drug delivery via liposomes is a way to decrease the drug's toxicity in the absence of light, increase the cellular internalization and, consequently, PDT effectiveness [49]. Foslip® and Fospeg® are just examples of formulations developed with an approved photosensitizer and that are under evaluation, however many other liposomal systems containing photosensitizers can be explored targeted to different tumor types.

To overcome issues related with low encapsulation efficiency, drug expulsion and quenching caused by molecules' aggregation, Cai et al. [52] incorporated fluorogens with singular aggregation-induced emission characteristics (AIEgens) in the lipid, creating a conjugate. Liposomes produced from these conjugates (AIEsomes) were able to show a superior ROS production compared to conventional liposomal systems containing photosensitizer molecules. *In vitro* studies carried out under dark conditions proved that both AIEsomes and conventional liposomes were toxic for a breast cancer cell line, however when irradiated with white light, AIEsomes exhibited more toxicity compared to conventional liposomes. Afterwards, *in vivo* studies revealed AIEsomes' ability to target and image in the tumor site, factors intrinsically related to their accumulation mainly in tumors. Furthermore, irradiation of animals after injection of AIEsomes was able to suppress tumor growth and induce necrosis in the tissue, which did not happen to other experimental groups, revealing the potential of liposomes prepared with AIEgen-lipid conjugates for targeted PDT.

A similar technique was employed by Kim et al. [53] with liposomes prepared from lipid conjugated with pheophorbide A, which were used as photosensitizers aiming for photo-induced immunotherapy in cholangiocarcinoma. Regardless of whether the technique used to exploit photosensitizer

incorporation in liposomes consists in a PS-lipid conjugation or encapsulation, these systems have been studied for PDT in several types of cancer, such as gastric, breast, ovarian, liver, skin and others [45,54–57]. Liposomes' features provide an extensive range of new possibilities to create therapeutic carriers that can improve PDT.

2.2.2.1.3 Micelles

Similar to the previous description of liposomes formation, micelles (Figure 2.3 – C) are also formed by the self-organization of amphiphilic molecules, and the resultant particle is different from the vesicles because of the different packing parameters [58,59]. The concentration of amphiphilic molecules must reach values above the designated critical micellar concentration (CMC) to form stable micelles, with a confined hydrophobic interior isolated from the aqueous medium. Polymers can also be materials used for micelles preparation if the polymers present hydrophobic and hydrophilic segments. Therefore, the choice of the amphiphilic molecule that will be used is important due to different CMC values [60].

Aiming a dual action of chemo- and photo-therapy in melanoma, Zhang et al. [61] investigated the preparation of micelles from block copolymer for the co-delivery of the classical anticancer agents doxorubicin and pheophorbide A. These compounds were incorporated in the polymer chain, and the prepared micelles were successfully internalized into melanoma cells with ROS formation induced by light observed *in vitro* and *in vivo*. Micelles showed high inhibition of tumor growth, almost twice that of micelles without irradiation treatment, and significantly higher than treatment with doxorubicin only.

To obtain a target system for ovarian cancer and metastatic melanoma cells, Lamch et al. [62] developed micelles with a di-block copolymer mPEG45-PLLA70 conjugated with folic acid for the encapsulation of the photosensitizer zinc (II) phthalocyanine. Wang et al. [63], in turn, used hyaluronic acid functionalization in micelles containing protoporphyrin IX to target cells with overexpression of CD44 receptors. The *in vitro* application of these micelles in monolayers and spheroids of human lung adenocarcinoma cells suggested that the enhanced cytotoxicity was due to higher internalization, and the effect of the interaction between the ligand hyaluronic acid and the receptor. Therefore, these studies suggest that micelles' functionalization can be an approach to enhance photodynamic therapy using this kind of nanostructure.

2.2.2.1.4 Nanoemulsions

A nanoemulsion is a mixture of oil and surfactant in aqueous phase, which demands energy to form small droplets of 20–200 nm (Figure 2.3 – D) [64]. Nanoemulsions can be employed as a strategy to enhance the bioavailability of several lipophilic drugs. For example, studies by Machado et al. [65] on formulations of nanoemulsions containing curcumin, a natural product, as a photosensitizer drug revealed that curcumin-nanoemulsion was highly phototoxic to breast cancer cells and produced high

levels of ROS. Mongue-Fuentes et al. [66] also used natural raw materials for the development of nano-emulsions for PDT. In their work, acai oil was used for the nanoemulsion preparation, which, combined with light irradiation, resulted in 85% death of melanoma cells, results which were also confirmed by animal studies in mice, with a decrease of the tumor volume.

2.2.2.1.5   Polymeric NPs

On the nanotechnology timeline, polymer-based nanoparticles were firstly reported in 1976 [67]. Since then, the great interest in these NPs resulted in the development of several methods to produce polymeric nanoparticles or PNPs (representation of 1-nanospheres and 2-nanocapsules in Figure 2.3 – E), such as by nanoprecipitation and solvent evaporation. The solvent evaporation method is an example of a two-step procedure where an emulsion is created, homogenized or sonicated, and then an evaporation step is required to remove the organic solvent in which the polymer was dissolved. On the other hand, nanoprecipitation is a one-step procedure where the polymer and drug are dissolved in a solvent miscible in water and dripped in an aqueous solution containing stabilizer. In both methods, organic solvents are employed, and although toxic solvents such as chloroform are no longer used, ether and acetone are currently used for the preparation of nanoparticles. In these cases, evaporation and purification methods are required to remove solvent residues from the dispersion [68–70].

Eltahan and collaborators developed polymeric nanoparticles co-loaded with NVP-BEZ235 and Chlorin-e6 (Ce6), named NVP/Ce6@NPs [71]. Ce6 was the selected photosensitizer and NVP-BEZ235 was used due to its ability to inhibit the PI3K/AKT/mTOR pathway that is related to tumor progression and proliferation and inhibit the repair of DNA damage in tumor cells. This sophisticated system plus irradiation was able to generate ROS by the Singlet Oxygen Sensor Green method, followed by tests in the triple-negative breast cancer cell line, and by flow cytometry, the authors discovered that treatment with NVP/Ce6@NPs and irradiation presented a fluorescence approximately 5 times greater compared to the control and nanoparticles without Ce6. These achievements showed the effect of a biochemical and PDT combination to treat a severe type of cancer.

Polymeric nanoparticles can be used to enhance the solubility of drugs as well as to provide drugs' stability and sustained release [72]. PNPs were used to encapsulate the photosensitizer zinc phthalocyanine, and as result, the phototoxicity showed a 500 times increase compared to the free drug in a lung cancer cell line [73]. Polymers' functionalization is another strategy able to achieve multifunctional nanoparticles [74]. The addition of some type of ligand such as an antibody to the nanoparticle surface allows it to bind specifically to sites where there is an overexpression of the receptor (Figure 2.4). Transferrin receptors, for example, are overexpressed in breast cancer. Regarding this, Jadia and collaborators [75] functionalized polymers with a peptide (hTf) that is able to bind to transferrin receptor and prepared nanoparticles containing the drug benzoporphyrin monoacid. As expected, functionalized nanoparticles exhibited specificity to the cell line in their study and enhanced the phototoxicity

compared to non-functionalized nanoparticles. This successful strategy led to the synthesis of polymers containing different ligands, resulting in nanoparticles with different biological activities such as bioimaging and photodynamic therapy [74].
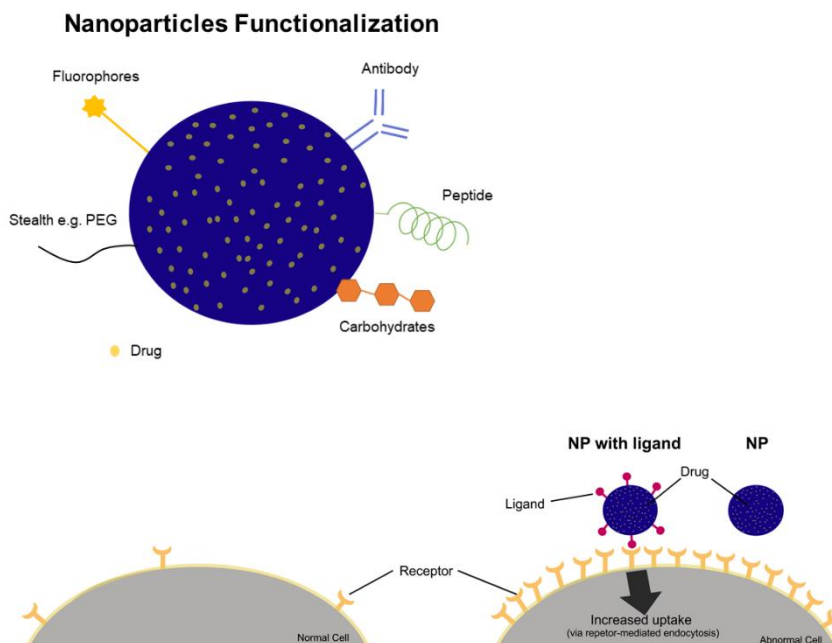
Figure 2.4: Representation of examples of functionalization to NPs with PEG for stealth NP, with fluorophores for imaging. Functionalization with ligands (e.g., antibody, peptide, carbohydrate and others) can show an advantage in abnormal cells with receptor's overexpression to enhance uptake by the cells mediated by a receptor endocytosis. Reproduced from the article that based this chapter [1].

Polyethylene glycol has gained attention due to its stealth behaviour [72]. PEG has shown promising application due to several properties, namely, inertness in biological systems combined with the non-activation of immune components and low adsorption of biomolecules, such as proteins providing a prolonged circulation in the blood [30,76]. The importance of PEG in PDT was investigated by Yang and collaborators [77] using Ce6 as a photosensitizer, a PDT light source based on a 660 nm laser and synthetized polymers with different proportions of PEG. It was demonstrated that the drug was detected in the circulation for a prolonged time and a higher amount of Ce6 was detected in nanoparticles with high degree of PEG in the polymer synthesis. On the other hand, the PDT effectiveness was dependent on the cellular internalization, which is maximized when applied nanoparticles based on low degree of PEG in the synthetic polymer [77]. Therefore, these achievements debate the need of a parameter balance in the design of the nanoparticles to achieve an effective therapy.

---

[1] This chapter is based on the published review article:

Pivetta, T.P., Botteon, C.E.A., Marcato, P.D., Ribeiro, P.A., Raposo, M. Nanoparticle Systems for Cancer Phototherapy: An Overview. Nanomaterials, **2021**, 11, 3132. https://doi.org/10.3390/nano11113132.

Studies developed by Luo et al. [78] focused on the development of polymeric nanoparticles with co-encapsulation of doxorubicin and a photosensitizer. To avoid the known toxicity of doxorubicin, the strategy used was to link doxorubicin to the polymer, a link that can be cleaved by ROS, and thereby the activation of the nanoparticle is ROS-dependent. They encapsulated the catalase enzyme to act on the intracellular H_2O_2 to produce more O_2 and functionalized particles with a peptide IF7 to target the tumor. This versatile and complex system IF7-ROSPCNP was shown to be an effective nanoparticle with accurate tumor targeting, that was able to inhibit tumor growth and prolong survival time when submitted to laser irradiation. Mice treated with ROSPCNP and IF7-ROSPCNP, but not irradiated, were also submitted to histopathological studies, which showed that other tissues were no different from the control group, which suggests that the nanoparticles were safe.

Deng and collaborators [79] developed systems with tetrakis(4-carboxyphenyl)porphyrin as a photosensitizer, where the drug doxorubicin was encapsulated forming π-π interactions with PNP to enhance the drug loading. These researchers obtained high drug loading (17.9%) and encapsulation efficiency (89.3%) associated with π-π interactions, as proven by the fluorescence method. Furthermore, *in vivo* studies showed that the PNPs developed were able to inhibit the growth of breast tumor in Balb/c mice when exposed to laser irradiation. The studies discussed in this topic were a few examples among many reports of photodynamic therapy exploiting PNPs in several types of cancer, such as in cervical adenocarcinoma, glioblastoma, highly aggressive breast cancer and hepatocellular carcinoma, showing the versatility of combining PNPs and PDT for cancer treatment [72,79–81].

2.2.2.1.6   Cyclodextrins

Cyclodextrins (CDs) are biodegradable and biocompatible structures composed by oligosaccharides of D(+)-glucose that are able to form nanosized particles by self-organization in aqueous medium [82,83]. As shown in Figure 2.3 – F, CDs present a conic shape where the hydrophobic cavity provides a way for the solubilization and delivery of hydrophobic drugs [84,85]. The conjugation of the photosensitizer phthalocyanine and cyclodextrin was a strategy employed to increase the PS solubility. In the work from Lourenço et al. [86] assays performed in human bladder cancer cells demonstrated that those conjugates, with higher solubility in water, were more phototoxic to the cells. A similar strategy was adopted by Semeraro and collaborators with a cyclodextrin-chlorophyll *a* conjugate, with a potential photo-induced toxicity in human colorectal adenocarcinoma cells reiterating the versatility of CDs-PS complexation for PDT applications [87].

Table 2.1: Brief description of some organic nanostructures cited in this review as well as their materials, methods of preparation and type of cancer used to test the potential photodynamic therapy of the formulation.

Nanostructures	Materials Employed		Drug	Method of Preparation	Investigated for	Ref.
NLC	Lipid Surfactant	Compritol® ATO 888 Oleic acid Tween® 20	5-aminolevulinic acid	Microemulsion technique	Basal-cell carcinoma	[37]
SLN	Lipid Surfactant	Lecithin Stearic acid Myrj52	Curcumin	Emulsification and low-tempera-ture solidification method	Lung cancer	[38]
SLN	Lipid Surfactant	Compritol 888 CG ATO Stearic acid Sorbitan Isostearate Polyoxyethylene-40 hydro-genated	Aluminum chloride Phthalocya-nine	Direct emulsification method	Melanoma	[39]
SLN NLC	Lipid Surfactant	Stearic acid Oleic acid Sodium lauryl sulfate	Chloroaluminum Phthalocyanine	Solvent diffusion technique	Lung cancer Melanoma	[40]
Liposome	Lipid	DSPC DSPG TEL	Curcumin	Thin-film hydration and sonication	Ovarian adenocarcinoma	[45]
Liposome	Lipid Modified Lipid	DPPC Cholesterol DOPE DSPE-PEG-Pheophorbide A	Gemcitabine	Thin-film hydration	Biliary tract cancer	[53]
Liposome	Lipid	DMPC DMPG Cholesterol	Photofrin	Thin-film hydration plus sonication and extrusion	Gastric cancer	[54]

Table 2.1: Continued.

Liposome	Lipid Modified lipid	DPPC Cholesterol DSPE-PEG DOTAP (16:0)LysoPC-BPD	Benzoporphyrin derivative	Thin-film hydration with freeze–thaw cycles and extrusion	Breast cancer	[55]
Liposome	Lipid Edge activator	SPC Sodium deoxycholate	Tetra (4-Tiophenyl) sulfonated phthalocyaninatozinc(II)	Thin film hydration and sonication	Liver cancer	[56]
Liposome	Lipid Surfactant	DOPC DMPC Tween® 20	Zinc phthalocyanine Ruthenium complex [Ru(NH.NHq)(tpy)NO]3+	Ethanol injection method	Skin melanoma	[57]
Micelle	Modified block copolymer	Pluronic® F127 - Pheophorbide A	Doxorubicin Pheophorbide A	Thin-film hydration	Melanoma	[61]
Micelle	Modified block copolymer	FA-PEG-PLLA	Zinc(II) Phthalocyanine	Modified dialysis method	Melanoma Ovarian carcinoma	[62]
Micelle	Modified block copolymer	HA-PLGA	Protoporphyrin IX	Solvent dialysis method	Lung cancer	[63]
Nanoemulsion	Lipid Surfactant	Lipoid S100 Poloxamer 188	Curcumin	Interfacial pre-polymer deposition and spontaneous nano-emulsification	Breast cancer	[65]
PNP	Polymer	PEG-b-PLGA	Synthetic zinc phthalocyanine	-	Lung cancer	[73]
PNP	Polymer	PLGA-PEG PLGA-PEG-methoxy PLGA-PEG-maleimide	Benzoporphyrin monoacid	Nanoprecipitation	Breast cancer	[75]
PNP	Polymer	PLGA PEMA PVA	Curcumin	Nanoprecipitation	Glioblastoma	[80]
PNP	Modified polymer	PEGylated Bodipy	Doxorubicin	-	Breast cancer	[81]

2.2.2.1.1 Protein Nanoparticles

Proteins are polymeric-type macromolecules formed by repeated amino acid monomers. Due to their biodegradability and low toxicity, proteins gained attention as drug delivery systems, as represented in Figure 2.3 – G [88,89]. Recently, Ye and Chi [90] published a review about the recent progress in drug and protein encapsulation. This includes a revision on the different encapsulation techniques, namely, emulsion evaporation, self-emulsifying drug delivery system as well as supercritical fluid, and proposed a novel method using foam that can be quite interesting in the encapsulation. Many types of proteins have been explored for the formation of protein-based nanoparticles, such as albumin.

Nanoparticle albumin-bound (Nab™) technology was developed to produce albumin nanoparticles. The success of these NPs has already generated a commercial formulation containing paclitaxel, Abraxane®, which presented advantages mainly with respect to tumor targeting and drugs' toxicity decrease [91,92]. In order to be applied to PDT, the association of protein nanoparticles with photosensitizers such as chlorin e6 was investigated by Phuong and collaborators using Nab™ technology [92]. The treatment with the nanoparticles and submission to 660 nm light radiation resulted in a significantly higher toxicity in breast cancer cells and *in vivo* tumor suppression of 7 times less than the control group, revealing a promising application of protein nanoparticles in PDT.

2.2.2.2 Carbon-Based Nanomaterials

Nanotubes, fullerenes and graphenes are among the several carbon-based nanomaterials that became widely explored for medical purposes, mainly due to the π-π interactions in their chemical structure and the ability to produce ROS, as a result of acting as a photosensitizer in PDT [93–95].

The potential of graphitic carbon nitride nanoparticles in PDT using visible light was analyzed by Heo et al. [95] using cervical cancer cells. Their study showed that the PDT allied with nanoparticles selectively killed more cancer cells than the normal cell lines. Other light sources in the NIR region are also found in the literature to carry out PDT with carbon nanoparticles derived from glucose, which resulted in an efficient ROS production [93]. The surface modification technique can also be employed to bind specifically to receptors that are overexpressed in some cancer cells types, as investigated by Xie and collaborators [96]. In their studies, hollow carbon nanospheres with doxorubicin presented peptide and hyaluronic acid moieties in the surface to enhance the uptake and damage by dual targeting in a lung cancer cell line.

Carbon dots are carbon-based nanomaterials that can be applied for bioimaging, drug delivery and can also be used for PDT [97]. He et al. [98] designed diketopyrrole-based fluorescent carbon dots and the *in vitro* and *in vivo* studies showed that they were able to inhibit the tumor growth when irradiated.

2.2.2.3 Silica Nanoparticles

Silica nanoparticles (SNPs) present several advantages that can be useful for the design of nanoparticles for PDT, such as the easy production, possibility of functionalization and to obtain particles with a controlled size [99]. An efficient anti-tumor effect was achieved by Liu et al. [100] when exploring the complex combination of a photosensitizer (rose Bengal), carbon dots and the drug doxorubicin in mesoporous silica nanoparticles. In their studies, the developed nanoparticle had high drug loading capacity and the problems related to carbon dots and PS aggregation were prevented. This system was also able to produce a higher amount of singlet oxygen compared to PS rose Bengal, and the combination with doxorubicin provided a synergy between chemotherapy and phototherapy that resulted in a 90% decrease of cell viability.

The high surface area of silica nanoparticles is another advantage as it allows its modification and functionalization, as demonstrated by the work of Lin and collaborators [101], who developed silica nanoparticles with the PS chlorin e6 encapsulated and a gene plasmid at the surface. Through a photo-induced cleavage of coumarin and detachment of the polycation PDMAEMA, with which the cytocidal gene presented an interaction, the nanoparticles could provide the release of the gene, activation of the PS and therefore a synergistic effect of the gene and phototherapy.

Bretin et al. [102] studied the anticancer potential of the photosensitizer 5-(4-hydroxyphenyl)-10,15,20-triphenylporphyrin (TPPOH) and developed silica nanoparticles coated with the conjugate xylan-TPPOH for photodynamic therapy of cancer. In the xenograft tumor model of colorectal cancer, they studied the biodistribution using Cy5.5-labeled free TPPOH and TPPOH-X SNPs. The fluorescence signal was observed at 24 h post-injection it was a strong signal for TPPOH-X SNPs, while it showed a minimal accumulation for free TPPOH administration. An *ex vivo* fluorescence imaging of tumors and organs showed that liver and kidney presented higher intensity compared to the others, but the fluorescence of tumors treated with TPPOH-X SNPs had a superior intensity compared to the other organs when compared to the free TPPOH. It was also confirmed by a quantitative analysis of fluorescence.

2.2.2.4 Magnetic Nanoparticles

Due to their magnetics properties, magnetic nanoparticles can be used in therapy based on the application of an external magnetic field to a targeted tissue. Besides this, it is also possible to attach molecules to it, thus working as a carrier [103].

For example, a delivery system prepared with iron oxide magnetic nanoparticles was employed for the targeted delivery of the anticancer doxorubicin and PDT therapy using a hematoporphyrin. The synergistic effect of PDT with the anticancer drug was shown to provide an effective inhibition of breast cancer *in vivo* [104]. Recently, Zhang et al. [105] used nanomotors with iron oxide nanoparticles for the delivery of zinc phthalocyanine, and due to the magnetic properties of the iron nanoparticles, the NPs

can be targeted to the desired tumor tissue These nanomotors generate O_2 by catalyzing endogenous H_2O_2 for the creation of O_2 as power to create the nanomotor's displacement. The system allowed an extended distribution of the photosensitizer as well as ROS generation. Additionally, the generation of O_2 also supplied an efficient PDT process.

2.2.2.5 Hybrid Nanoparticles

The hybrid NPs consist in a combination of two or more types of NPs to achieve a unique multifunctional structure [106]. Hybrid NPs composed by the combination of polymers and lipids is a quite common topic found in the literature over the past few years that can also be applied to PDT, as investigated by Pramual and collaborators [107]. In their study, the polymer-lipid-PEG nanoparticles were used for the encapsulation of a PS molecule that exhibited enhanced ROS production and phototoxicity in thyroid cancer cells. Another type of combination was explored by Shumatbaeva et al. [108] that demonstrated an effective PDT in Hela cells with the irradiation in combination to the treatment with silver nanoparticles stabilized by a PEG conjugate.

2.3 Final Remarks

This review shows that nanoparticles are being extensively investigated for phototherapy nowadays. Regardless of the type of nanoparticle, there a few characteristics that can summarize the current state of this technology for medical application. The main advantages include the minimally invasive method of therapy, the minimization of side effects and the possibility to target and enhance accumulation of drugs in the tumor. Therefore, it is possible to achieve a targeted therapy with a reduction of drug dosage and greater drug stability. In conclusion, nanoparticle systems are multifaceted structures that are under extensive investigation to create alternatives for conventional therapies of cancer in combination with phototherapy. There are still parameters such as the hypoxic tumor microenvironment that can be an obstacle for PDT, and for phototherapy in general, the limited penetration depth of the light can hinder the use of these systems in cancer therapy. Finally, scale-up and clinical studies are indeed the main challenges in the next few years, however, the incredible diversity of nanoparticles as well as their multiple qualities allied to phototherapy are a promising combination that can result in a more effective and safer treatment for the patients.

Acknowledgments

References

1. Sung, H.; Ferlay, J.; Siegel, R.L.; Laversanne, M.; Soerjomataram, I.; Jemal, A.; Bray, F. Global Cancer Statistics 2020: GLOBOCAN Estimates of Incidence and Mortality Worldwide for 36 Cancers in 185 Countries. *CA Cancer J. Clin.* **2021**, *71*, 209–249. https://doi.org/10.3322/caac.21660.

2. Falzone, L.; Salomone, S.; Libra, M. Evolution of cancer pharmacological treatments at the turn of the third millennium. *Front. Pharmacol.* **2018**, *9*, 1300. https://doi.org/10.3389/fphar.2018.01300.

3. Sivarajakumar, R.; Mallukaraj, D.; Kadavakollu, M.; Neelakandan, N.; Chandran, S.; Bhojaraj, S.; Karri, V.V.S.R. Nanoparticles for the treatment of lung cancers. *J. Young Pharm.* **2018**, *10*, 276–281. https://doi.org/10.5530/jyp.2018.10.62.

4. Zhen, X.; Cheng, P.; Pu, K. Recent Advances in Cell Membrane-Camouflaged Nanoparticles for Cancer Phototherapy. *Small* **2019**, *15*, 1804105. https://doi.org/10.1002/smll.201804105.

5. He, Z.; Zhao, L.; Zhang, Q.; Chang, M.; Li, C.; Zhang, H.; Lu, Y.; Chen, Y. An Acceptor–Donor–Acceptor Structured Small Molecule for Effective NIR Triggered Dual Phototherapy of Cancer. *Adv. Funct. Mater.* **2020**, *30*, 1910301. https://doi.org/10.1002/adfm.201910301.

6. Liu, P.; Yang, W.; Shi, L.; Zhang, H.; Xu, Y.; Wang, P.; Zhang, G.; Chen, W.R.; Zhang, B.; Wang, X. Concurrent photothermal therapy and photodynamic therapy for cutaneous squamous cell carcinoma by gold nanoclusters under a single NIR laser irradiation. *J. Mater. Chem. B* **2019**, *7*, 6924–6933. https://doi.org/10.1039/c9tb01573f.

7. Hong, E.J.; Choi, D.G.; Shim, M.S. Targeted and effective photodynamic therapy for cancer using functionalized nanomaterials. *Acta Pharm. Sin. B* **2016**, *6*, 297–307. https://doi.org/10.1016/j.apsb.2016.01.007.

8. Jeevanandam, J.; Barhoum, A.; Chan, Y.S.; Dufresne, A.; Danquah, M.K. Review on nanoparticles and nanostructured materials: History, sources, toxicity and regulations. *Beilstein J. Nanotechnol.* **2018**, *9*, 1050–1074. https://doi.org/10.3762/bjnano.9.98.

9.   Wolfram, J.; Zhu, M.; Yang, Y.; Shen, J.; Gentile, E.; Paolino, D.; Fresta, M.; Nie, G.; Chen, C.; Shen, H.; et al. Safety of Nanoparticles in Medicine. *Curr. Drug Targets* **2015**, *16*, 1671–1681. https://doi.org/10.2174/1389450115666140804124808.

10.   Rodrigues, A.R.O.; Matos, J.O.G.; Nova Dias, A.M.; Almeida, B.G.; Pires, A.; Pereira, A.M.; Araújo, J.P.; Queiroz, M.J.R.P.; Castanheira, E.M.S.; Coutinho, P.J.G. Development of multifunctional liposomes containing magnetic/plasmonic MnFe$_2$O$_4$/Au core/shell nanoparticles. *Pharmaceutics* **2019**, *11*, 10. https://doi.org/10.3390/pharmaceutics11010010.

11.   Bunney, P.E.; Zink, A.N.; Holm, A.A.; Billington, C.J.; Kotz, C.M. Orexin activation counteracts decreases in nonexercise activity thermogenesis (NEAT) caused by high-fat diet. *Physiol. Behav.* **2017**, *176*, 139–148. https://doi.org/10.1016/j.physbeh.2017.03.040.

12.   Nam, J.; Son, S.; Ochyl, L.J.; Kuai, R.; Schwendeman, A.; Moon, J.J. Chemo-photothermal therapy combination elicits anti-tumor immunity against advanced metastatic cancer. *Nat. Commun.* **2018**, *9*, 1074. https://doi.org/10.1038/s41467-018-03473-9.

13.   Liu, Y.; Crawford, B.M.; Vo-Dinh, T. Gold nanoparticles-mediated photothermal therapy and immunotherapy. *Immunotherapy* **2018**, *10*, 1175–1188. https://doi.org/10.2217/imt-2018-0029.

14.   Hak, A.; Ravasaheb Shinde, V.; Rengan, A.K. A review of advanced nanoformulations in phototherapy for cancer therapeutics. *Photodiagn. Photodyn. Ther.* **2021**, *33*, 102205. https://doi.org/10.1016/j.pdpdt.2021.102205.

15.   Montaseri, H.; Kruger, C.A.; Abrahamse, H. Review: Organic nanoparticle based active targeting for photodynamic therapy treatment of breast cancer cells. *Oncotarget* **2020**, *11*, 2120–2136. https://doi.org/10.18632/oncotarget.27596.

16.   Hönigsmann, H. History of phototherapy in dermatology. *Photochem. Photobiol. Sci.* **2013**, *12*, 16–21. https://doi.org/10.1039/c2pp25120e.

17.   Sharma, S.K.; Mroz, P.; Dai, T.; Huang, Y.; Denis, T.G., St.; Hamblin, M.R. Photodynamic Therapy for Cancer and for Infections: What Is the Difference? *Isr. J. Chem.* **2012**, *52*, 691–705. https://doi.org/10.1002/ijch.201100062.

18.   Agostinis, P.; Berg, K.; Cengel, K.A.; Foster, T.H.; Girotti, A.W.; Gollnick, S.O.; Hahn, S.M.; Hamblin, M.R.; Juzeniene, A.; Kessel, D.; et al. Photodynamic therapy of cancer: An update. *CA Cancer J. Clin.* **2011**, *61*, 250–281. https://doi.org/10.3322/caac.20114.

19.   Oniszczuk, A.; Wojtunik-Kulesza, K.A.; Oniszczuk, T.; Kasprzak, K. The potential of photodynamic therapy (PDT)—Experimental investigations and clinical use. *Biomed. Pharmacother.* **2016**, *83*, 912–929. https://doi.org/10.1016/j.biopha.2016.07.058.

20.   Kim, M.; Jung, H.Y.; Park, H.J. Topical PDT in the treatment of benign skin diseases: Principles and new applications. *Int. J. Mol. Sci.* **2015**, *16*, 23259–23278. https://doi.org/10.3390/ijms161023259.

21. Wen, X.; Li, Y.; Hamblin, M.R. Photodynamic therapy in dermatology beyond non-melanoma cancer: An update. *Photodiagn. Photodyn. Ther.* **2017**, *19*, 140–152. https://doi.org/10.1016/j.pdpdt.2017.06.010.

22. Zhao, B.; He, Y.-Y. Recent advances in the prevention and treatment of skin cancer using photodynamic therapy. *Expert Rev. Anticancer Ther.* **2010**, *10*, 1797–1809. https://doi.org/10.1586/era.10.154.

23. Costa, D.F.; Mendes, L.P.; Torchilin, V.P. The effect of low-and high-penetration light on localized cancer therapy. *Adv. Drug Deliv. Rev.* **2019**, *138*, 105–116. https://doi.org/10.1016/j.addr.2018.09.004.

24. Schuch, A.P.; Moreno, N.C.; Schuch, N.J.; Menck, C.F.M.; Garcia, C.C.M. Sunlight damage to cellular DNA: Focus on oxidatively generated lesions. *Free Radic. Biol. Med.* **2017**, *107*, 110–124. https://doi.org/10.1016/j.freeradbiomed.2017.01.029.

25. Gomes, P.J.; Ribeiro, P.A.; Shaw, D.; Mason, N.J.; Raposo, M. UV degradation of deoxyribonucleic acid. *Polym. Degrad. Stab.* **2009**, *94*, 2134–2141. https://doi.org/10.1016/j.polymdegradstab.2009.09.013.

26. Gomes, P.J.; Coelho, M.; Dionísio, M.; António Ribeiro, P.; Raposo, M. Probing radiation damage by alternated current conductivity as a method to characterize electron hopping conduction in DNA molecules. *Appl. Phys. Lett.* **2012**, *101*, 123702. https://doi.org/10.1063/1.4754287.

27. Gomes, P.J.; Ferraria, A.M.; Botelho Do Rego, A.M.; Hoffmann, S.V.; Ribeiro, P.A.; Raposo, M. Energy thresholds of DNA damage induced by UV radiation: An XPS study. *J. Phys. Chem. B* **2015**, *119*, 5404–5411. https://doi.org/10.1021/acs.jpcb.5b01439.

28. Vangipuram, R.; Feldman, S.R. Ultraviolet phototherapy for cutaneous diseases: A concise review. *Oral Dis.* **2016**, *22*, 253–259. https://doi.org/10.1111/odi.12366.

29. Shen, Z.; Ma, Q.; Zhou, X.; Zhang, G.; Hao, G.; Sun, Y.; Cao, J. Strategies to improve photodynamic therapy efficacy by relieving the tumor hypoxia environment. *NPG Asia Mater.* **2021**, *13*, 39, doi:10.1038/s41427-021-00303-1.

30. El Mohtadi, F.; D'Arcy, R.; Yang, X.; Turhan, Z.Y.; Alshamsan, A.; Tirelli, N. Main Chain Polysulfoxides as Active 'Stealth' Polymers with Additional Antioxidant and Anti-Inflammatory Behaviour. *Int. J. Mol. Sci.* **2019**, *20*, 4583. https://doi.org/10.3390/ijms20184583.

31. Müller, R.H.; Radtke, M.; Wissing, S.A. Solid lipid nanoparticles (SLN) and nanostructured lipid carriers (NLC) in cosmetic and dermatological preparations. *Adv. Drug Deliv. Rev.* **2002**, *54*, 131–155. https://doi.org/10.1016/S0169-409X(02)00118-7.

32. Müller, R.; Lucks, S. Arzneistoffträger Aus Festen Lipidteilchen, Feste Lipidnanosphären (SLN). European Patent Application No. EP0605497B2, 20 March 1996.

33. Gasco, M.R. Method for Producing Solid Lipid Microspheres Having a Narrow Size Distribution. U.S. Patent Application No. US5250236A, 5 October 1993.

34. Müller, R.H.; Radtke, M.; Wissing, S.A. Nanostructured lipid matrices for improved microencapsulation of drugs. *Int. J. Pharm.* **2002**, *242*, 121–128. https://doi.org/10.1016/S0378-5173(02)00180-1.

35. Naseri, N.; Valizadeh, H.; Zakeri-Milani, P. Solid lipid nanoparticles and nanostructured lipid carriers: Structure preparation and application. *Adv. Pharm. Bull.* **2015**, *5*, 305–313. https://doi.org/10.15171/apb.2015.043.

36. Üner, M.; Yener, G. Importance of solid lipid nanoparticles (SLN) in various administration routes and future perspective. *Int. J. Nanomed.* **2007**, *2*, 289–300.

37. Qidwai, A.; Khan, S.; Md, S.; Fazil, M.; Baboota, S.; Narang, J.K.; Ali, J. Nanostructured lipid carrier in photodynamic therapy for the treatment of basal-cell carcinoma. *Drug Deliv.* **2016**, *23*, 1476–1485. https://doi.org/10.3109/10717544.2016.1165310.

38. Jiang, S.; Zhu, R.; He, X.; Wang, J.; Wang, M.; Qian, Y.; Wang, S. Enhanced photocytotoxicity of curcumin delivered by solid lipid nanoparticles. *Int. J. Nanomed.* **2017**, *12*, 167–178. https://doi.org/10.2147/IJN.S123107.

39. Goto, P.L.; Siqueira-Moura, M.P.; Tedesco, A.C. Application of aluminum chloride phthalocyanine-loaded solid lipid nanoparticles for photodynamic inactivation of melanoma cells. *Int. J. Pharm.* **2017**, *518*, 228–241. https://doi.org/10.1016/j.ijpharm.2017.01.004.

40. Almeida, E.D.P.; Dipieri, L.V.; Rossetti, F.C.; Marchetti, J.M.; Bentley, M.V.L.B.; Nunes, R.D.S.; Sarmento, V.H.V.; Valerio, M.E.G.; Rodrigues Júnior, J.J.; Montalvão, M.M.; et al. Skin permeation, biocompatibility and antitumor effect of chloroaluminum phthalocyanine associated to oleic acid in lipid nanoparticles. *Photodiagn. Photodyn. Ther.* **2018**, *24*, 262–273. https://doi.org/10.1016/j.pdpdt.2018.10.002.

41. Antonietti, M.; Förster, S. Vesicles and Liposomes: A Self-Assembly Principle Beyond Lipids. *Adv. Mater.* **2003**, *15*, 1323–1333. https://doi.org/10.1002/adma.200300010.

42. Yang, Y.; Yang, X.; Li, H.; Li, C.; Ding, H.; Zhang, M.; Guo, Y.; Sun, M. Near-infrared light triggered liposomes combining photodynamic and chemotherapy for synergistic breast tumor therapy. *Coll. Surf. B Biointerfaces* **2019**, *173*, 564–570. https://doi.org/10.1016/j.colsurfb.2018.10.019.

43. Matos, C.; Moutinho, C.; Lobão, P. Liposomes as a model for the biological membrane: Studies on Daunorubicin bilayer interaction. *J. Membr. Biol.* **2012**, *245*, 69–75. https://doi.org/10.1007/s00232-011-9414-2.

44. Peetla, C.; Stine, A.; Labhasetwar, V. Biophysical Interactions with Model Lipid Membranes: Applications in Drug Discovery and Drug Delivery. *Mol. Pharm.* **2009**, *6*, 1264–1276. https://doi.org/10.1021/mp9000662.

45. Duse, L.; Pinnapireddy, S.R.; Strehlow, B.; Jedelská, J.; Bakowsky, U. Low level LED photodynamic therapy using curcumin loaded tetraether liposomes. *Eur. J. Pharm. Biopharm.* **2018**, *126*, 233–241. https://doi.org/10.1016/j.ejpb.2017.10.005.

46. Immordino, M.L.; Franco, D.; Cattel, L. Stealth liposomes: Review of the basic science, rationale, and clinical applications, existing and potential. *Int. J. Nanomed.* **2006**, *1*, 297–315.

47. Yang, Q.; Jones, S.W.; Parker, C.L.; Zamboni, W.C.; Bear, J.E.; Lai, S.K. Evading immune cell uptake and clearance requires PEG grafting at densities substantially exceeding the minimum for brush conformation. *Mol. Pharm.* **2014**, *11*, 1250–1258. https://doi.org/10.1021/mp400703d.

48. Ohradanova-Repic, A.; Nogueira, E.; Hartl, I.; Gomes, A.C.; Preto, A.; Steinhuber, E.; Mühlgrabner, V.; Repic, M.; Kuttke, M.; Zwirzitz, A.; et al. Fab antibody fragment-functionalized liposomes for specific targeting of antigen-positive cells. *Nanomed. Nanotechnol. Biol. Med.* **2018**, *14*, 123–130. https://doi.org/10.1016/j.nano.2017.09.003.

49. Gaio, E.; Scheglmann, D.; Reddi, E.; Moret, F. Uptake and photo-toxicity of Foscan®, Foslip® and Fospeg® in multicellular tumor spheroids. *J. Photochem. Photobiol. B Biol.* **2016**, *161*, 244–252. https://doi.org/10.1016/j.jphotobiol.2016.05.011.

50. Reshetov, V.; Kachatkou, D.; Shmigol, T.; Zorin, V.; D'Hallewin, M.-A.; Guillemin, F.; Bezdetnaya, L. Redistribution of meta-tetra(hydroxyphenyl)chlorin (m-THPC) from conventional and PEGylated liposomes to biological substrates. *Photochem. Photobiol. Sci.* **2011**, *10*, 911–919. https://doi.org/10.1039/c0pp00303d.

51. Reshetov, V.; Lassalle, H.-P.; François, A.; Dumas, D.; Hupont, S.; Gräfe, S.; Filipe, V.; Jiskoot, W.; Guillemin, F.; Zorin, V.; et al. Photodynamic therapy with conventional and pegylated liposomal formulations of mTHPC(temoporfin): Comparison of treatment efficacy and distribution characteristics *in vivo*. *Int. J. Nanomed.* **2013**, *8*, 3817–3831. https://doi.org/10.2147/IJN.S51002.

52. Cai, X.; Mao, D.; Wang, C.; Kong, D.; Cheng, X.; Liu, B. Multifunctional Liposome: A Bright AIEgen–Lipid Conjugate with Strong Photosensitization. *Angew. Chem.* **2018**, *57*, 16396–16400. https://doi.org/10.1002/anie.201809641.

53. Kim, D.H.; Im, B.N.; Hwang, H.S.; Na, K. Gemcitabine-loaded DSPE-PEG-PheoA liposome as a photomediated immune modulator for cholangiocarcinoma treatment. *Biomaterials* **2018**, *183*, 139–150. https://doi.org/10.1016/j.biomaterials.2018.08.052.

54. Igarashi, A.; Konno, H.; Tanaka, T.; Nakamura, S.; Sadzuka, Y.; Hirano, T.; Fujise, Y. Liposomal photofrin enhances therapeutic efficacy of photodynamic therapy against the human gastric cancer. *Toxicol. Lett.* **2003**, *145*, 133–141. https://doi.org/10.1016/S0378-4274(03)00241-8.

55. Baglo, Y.; Liang, B.J.; Robey, R.W.; Ambudkar, S. V.; Gottesman, M.M.; Huang, H.-C. Porphyrin-lipid assemblies and nanovesicles overcome ABC transporter-mediated photodynamic therapy resistance in cancer cells. *Cancer Lett.* **2019**, *457*, 110–118. https://doi.org/10.1016/j.canlet.2019.04.037.

56. Abdel Fadeel, D.; Al-Toukhy, G.M.; Elsharif, A.M.; Al-Jameel, S.S.; Mohamed, H.H.; Youssef, T.E. Improved photodynamic efficacy of thiophenyl sulfonated zinc phthalocyanine loaded in

lipid nano-carriers for hepatocellular carcinoma cancer cells. *Photodiagn. Photodyn. Ther.* **2018**, *23*, 25–31. https://doi.org/10.1016/j.pdpdt.2018.06.003.

57. de Lima, R.G.; Tedesco, A.C.; da Silva, R.S.; Lawrence, M.J. Ultradeformable liposome loaded with zinc phthalocyanine and [Ru(NH.NHq)(tpy)NO]$^{3+}$ for photodynamic therapy by topical application. *Photodiagn. Photodyn. Ther.* **2017**, *19*, 184–193. https://doi.org/10.1016/j.pdpdt.2017.05.013.

58. Salim, M.; Minamikawa, H.; Sugimura, A.; Hashim, R. Amphiphilic designer nano-carriers for controlled release: From drug delivery to diagnostics. *MedChemComm* **2014**, *5*, 1602–1618. https://doi.org/10.1039/c4md00085d.

59. Dutt, S.; Siril, P.F.; Remita, S. Swollen liquid crystals (SLCs): A versatile template for the synthesis of nano structured materials. *RSC Adv.* **2017**, *7*, 5733–5750. https://doi.org/10.1039/c6ra26390a.

60. Gaucher, G.; Marchessault, R.H.; Leroux, J.C. Polyester-based micelles and nanoparticles for the parenteral delivery of taxanes. *J. Control. Release* **2010**, *143*, 2–12. https://doi.org/10.1016/j.jconrel.2009.11.012.

61. Zhang, C.; Zhang, J.; Qin, Y.; Song, H.; Huang, P.; Wang, W.; Wang, C.; Li, C.; Wang, Y.; Kong, D. Co-delivery of doxorubicin and pheophorbide A by pluronic F127 micelles for chemo-photodynamic combination therapy of melanoma. *J. Mater. Chem. B* **2018**, *6*, 3305–3314. https://doi.org/10.1039/c7tb03179c.

62. Lamch, Ł.; Kulbacka, J.; Dubińska-Magiera, M.; Saczko, J.; Wilk, K.A. Folate-directed zinc (II) phthalocyanine loaded polymeric micelles engineered to generate reactive oxygen species for efficacious photodynamic therapy of cancer. *Photodiagn. Photodyn. Ther.* **2019**, *25*, 480–491. https://doi.org/10.1016/j.pdpdt.2019.02.014.

63. Wang, X.; Wang, J.; Li, J.; Huang, H.; Sun, X.; Lv, Y. Development and evaluation of hyaluronic acid-based polymeric micelles for targeted delivery of photosensitizer for photodynamic therapy *in vitro*. *J. Drug Deliv. Sci. Technol.* **2018**, *48*, 414–421. https://doi.org/10.1016/j.jddst.2018.10.018.

64. Marzuki, N.H.C.; Wahab, R.A.; Hamid, M.A. An overview of nanoemulsion: Concepts of development and cosmeceutical applications. *Biotechnol. Biotechnol. Equip.* **2019**, *33*, 779–797. https://doi.org/10.1080/13102818.2019.1620124.

65. Machado, F.C.; Adum de Matos, R.P.; Primo, F.L.; Tedesco, A.C.; Rahal, P.; Calmon, M.F. Effect of curcumin-nanoemulsion associated with photodynamic therapy in breast adenocarcinoma cell line. *Bioorgan. Med. Chem.* **2019**, *27*, 1882–1890. https://doi.org/10.1016/j.bmc.2019.03.044.

66. Monge-Fuentes, V.; Muehlmann, L.A.; Longo, J.P.F.; Silva, J.R.; Fascineli, M.L.; de Souza, P.; Faria, F.; Degterev, I.A.; Rodriguez, A.; Carneiro, F.P.; et al. Photodynamic therapy mediated by acai oil (*Euterpe oleracea* Martius) in nanoemulsion: A potential treatment for melanoma. *J.*

Photochem. Photobiol. B Biol. **2017**, *166*, 301–310. https://doi.org/10.1016/j.jphoto-biol.2016.12.002.

67. Langer, R.; Folkman, J. Polymers for the sustained release of proteins and other macromolecules. *Nature* **1976**, *263*, 797–800. https://doi.org/10.1038/263797a0.

68. Amoabediny, G.; Haghiralsadat, F.; Naderinezhad, S.; Helder, M.N.; Kharanaghi, E.A.; Arough, J.M.; Zandieh-Doulabi, B. Overview of preparation methods of polymeric and lipid-based (niosome, solid lipid, liposome) nanoparticles: A comprehensive review. *Int. J. Polym. Mater. Polym. Biomater.* **2018**, *67*, 383–400. https://doi.org/10.1080/00914037.2017.1332623.

69. Crucho, C.I.C.; Barros, M.T. Polymeric nanoparticles: A study on the preparation variables and characterization methods. *Mater. Sci. Eng. C* **2017**, *80*, 771–784. https://doi.org/10.1016/j.msec.2017.06.004.

70. Grabnar, P.A.; Kristl, J. The manufacturing techniques of drug-loaded polymeric nanoparticles from preformed polymers. *J. Microencapsul.* **2011**, *28*, 323–335. https://doi.org/10.3109/02652048.2011.569763.

71. Eltahan, A.S.; Liu, L.; Okeke, C.I.; Huang, M.; Han, L.; Chen, J.; Xue, X.; Bottini, M.; Guo, W.; Liang, X.J. NVP-BEZ235/Chlorin-e6 co-loaded nanoparticles ablate breast cancer by biochemical and photodynamic synergistic effects. *Nano Res.* **2018**, *11*, 4846–4858. https://doi.org/10.1007/s12274-018-2074-0.

72. Gangopadhyay, M.; Singh, T.; Behara, K.K.; Karwa, S.; Ghosh, S.K.; Singh, N.D.P. Coumarin-containing-star-shaped 4-arm-polyethylene glycol: Targeted fluorescent organic nanoparticles for dual treatment of photodynamic therapy and chemotherapy. *Photochem. Photobiol. Sci.* **2015**, *14*, 1329–1336. https://doi.org/10.1039/c5pp00057b.

73. Mehraban, N.; Musich, P.R.; Freeman, H.S. Synthesis and encapsulation of a new zinc phthalocyanine photosensitizer into polymeric nanoparticles to enhance cell uptake and phototoxicity. *Appl. Sci.* **2019**, *9*, 401. https://doi.org/10.3390/app9030401.

74. Lin, W.; Zhang, W.; Sun, T.; Liu, S.; Zhu, Y.; Xie, Z. Rational Design of Polymeric Nanoparticles with Tailorable Biomedical Functions for Cancer Therapy. *ACS Appl. Mater. Interfaces* **2017**, *9*, 29612–29622. https://doi.org/10.1021/acsami.7b10763.

75. Jadia, R.; Kydd, J.; Rai, P. Remotely Phototriggered, Transferrin-Targeted Polymeric Nanoparticles for the Treatment of Breast Cancer. *Photochem. Photobiol.* **2018**, *94*, 765–774. https://doi.org/10.1111/php.12903.

76. D'souza, A.A.; Shegokar, R. Polyethylene glycol (PEG): A versatile polymer for pharmaceutical applications. *Expert Opin. Drug Deliv.* **2016**, *13*, 1257–1275. https://doi.org/10.1080/17425247.2016.1182485.

77. Yang, X.; Li, J.; Yu, Y.; Wang, J.; Li, D.; Cao, Z.; Yang, X. Engineering of a universal polymeric nanoparticle platform to optimize the PEG density for photodynamic therapy. *Sci. China Chem.* **2019**, *62*, 1379–1386. https://doi.org/10.1007/s11426-019-9505-y.

78. Luo, Z.; Li, M.; Zhou, M.; Li, H.; Chen, Y.; Ren, X.; Dai, Y. O2-evolving and ROS-activable nanoparticles for treatment of multi-drug resistant Cancer by combination of photodynamic therapy and chemotherapy. *Nanomed. Nanotechnol. Biol. Med.* **2019**, *19*, 49–57. https://doi.org/10.1016/j.nano.2019.03.007.

79. Deng, X.; Liang, Y.; Peng, X.; Su, T.; Luo, S.; Cao, J.; Gu, Z.; He, B. A facile strategy to generate polymeric nanoparticles for synergistic chemo-photodynamic therapy. *Chem. Commun.* **2015**, *51*, 4271–4274. https://doi.org/10.1039/c4cc10226f.

80. Jamali, Z.; Khoobi, M.; Hejazi, S.M.; Eivazi, N.; Abdolahpour, S.; Imanparast, F.; Moradi-Sardareh, H.; Paknejad, M. Evaluation of targeted curcumin (CUR) loaded PLGA nanoparticles for *in vitro* photodynamic therapy on human glioblastoma cell line. *Photodiagn. Photodyn. Ther.* **2018**, *23*, 190–201. https://doi.org/10.1016/j.pdpdt.2018.06.026.

81. Wang, S.; Li, J.; Ye, Z.; Li, J.; Wang, A.; Hu, J.; Bai, S.; Yin, J. Self-assembly of photosensitive and chemotherapeutic drugs for combined photodynamic-chemo cancer therapy with real-time tracing property. *Coll. Surf. A Physicochem. Eng. Asp.* **2019**, *574*, 44–51. https://doi.org/10.1016/j.colsurfa.2019.04.060.

82. Datz, S.; Illes, B.; Gößl, D.; Schirnding, C.V.; Engelke, H.; Bein, T. Biocompatible crosslinked β-cyclodextrin nanoparticles as multifunctional carriers for cellular delivery. *Nanoscale* **2018**, *10*, 16284–16292. https://doi.org/10.1039/c8nr02462f.

83. Loftsson, T. Self-assembled cyclodextrin nanoparticles and drug delivery. *J. Incl. Phenom. Macrocycl. Chem.* **2014**, *80*, 1–7. https://doi.org/10.1007/s10847-013-0375-1.

84. Gidwani, B.; Vyas, A. A Comprehensive Review on Cyclodextrin-Based Carriers for Delivery of Chemotherapeutic Cytotoxic Anticancer Drugs. *BioMed Res. Int.* **2015**, *2015*, 198268. https://doi.org/10.1155/2015/198268.

85. Lakkakula, J.R.; Krause, R.W.M. A vision for cyclodextrin nanoparticles in drug delivery systems and pharmaceutical applications. *Nanomedicine* **2014**, *9*, 877–894. https://doi.org/10.2217/nnm.14.41.

86. Lourenço, L.M.O.; Pereira, P.M.R.; Maciel, E.; Válega, M.; Domingues, F.M.J.; Domingues, M.R.M.; Neves, M.G.P.M.S.; Cavaleiro, J.A.S.; Fernandes, R.; Tomé, J.P.C. Amphiphilic phthalocyanine-cyclodextrin conjugates for cancer photodynamic therapy. *Chem. Commun.* **2014**, *50*, 8363–8366. https://doi.org/10.1039/c4cc02226b.

87. Semeraro, P.; Chimienti, G.; Altamura, E.; Fini, P.; Rizzi, V.; Cosma, P. Chlorophyll a in cyclodextrin supramolecular complexes as a natural photosensitizer for photodynamic therapy (PDT) applications. *Mater. Sci. Eng. C* **2018**, *85*, 47–56. https://doi.org/10.1016/j.msec.2017.12.012.

88. De Frates, K.; Markiewicz, T.; Gallo, P.; Rack, A.; Weyhmiller, A.; Jarmusik, B.; Hu, X. Protein polymer-based nanoparticles: Fabrication and medical applications. *Int. J. Mol. Sci.* **2018**, *19*, 1717. https://doi.org/10.3390/ijms19061717.

89.   Lohcharoenkal, W.; Wang, L.; Chen, Y.C.; Rojanasakul, Y. Protein Nanoparticles as Drug Delivery Carriers for Cancer Therapy. *BioMed Res. Int.* **2014**, *2014*, 180549. https://doi.org/10.1155/2014/180549.

90.   Ye, C.; Chi, H. A review of recent progress in drug and protein encapsulation: Approaches, applications and challenges. *Mater. Sci. Eng. C* **2018**, *83*, 233–246. https://doi.org/10.1016/j.msec.2017.10.003.

91.   Lu, C.; Li, X.; Liang, X.; Zhang, X.; Yin, T.; Gou, J.; He, H.; Zhang, Y.; Tang, X. Liver Targeting Albumin-Coated Silybin-Phospholipid Particles Prepared by Nab^{TM} Technology for Improving Treatment Effect of Acute Liver Damage in Intravenous Administration. *AAPS PharmSciTech* **2019**, *20*, 293. https://doi.org/10.1208/s12249-019-1504-y.

92.   Phuong, P.T.T.; Lee, S.; Lee, C.; Seo, B.; Park, S.; Oh, K.T.; Lee, E.S.; Choi, H.G.; Shin, B.S.; Youn, Y.S. Beta-carotene-bound albumin nanoparticles modified with chlorin e6 for breast tumor ablation based on photodynamic therapy. *Coll. Surf. B Biointerfaces* **2018**, *171*, 123–133. https://doi.org/10.1016/j.colsurfb.2018.07.016.

93.   Kokalari, I.; Gassino, R.; Giovannozzi, A.M.; Croin, L.; Gazzano, E.; Bergamaschi, E.; Rossi, A.M.; Perrone, G.; Riganti, C.; Ponti, J.; et al. Pro-and anti-oxidant properties of near-infrared (NIR) light responsive carbon nanoparticles. *Free Radic. Biol. Med.* **2019**, *134*, 165–176. https://doi.org/10.1016/j.freeradbiomed.2019.01.013.

94.   Pérez, E.M.; Martín, N. π–π interactions in carbon nanostructures. *Chem. Soc. Rev.* **2015**, *44*, 6425–6433. https://doi.org/10.1039/c5cs00578g.

95.   Heo, N.S.; Lee, S.U.; Rethinasabapathy, M.; Lee, E.Z.; Cho, H.J.; Oh, S.Y.; Choe, S.R.; Kim, Y.; Hong, W.G.; Krishnan, G.; et al. Visible-light-driven dynamic cancer therapy and imaging using graphitic carbon nitride nanoparticles. *Mater. Sci. Eng. C* **2018**, *90*, 531–538. https://doi.org/10.1016/j.msec.2018.04.035.

96.   Xie, R.; Lian, S.; Peng, H.; Ouyang, C.; Li, S.; Lu, Y.; Cao, X.; Zhang, C.; Xu, J.; Jia, L. Mitochondria and Nuclei Dual-Targeted Hollow Carbon Nanospheres for Cancer Chemophotodynamic Synergistic Therapy. *Mol. Pharm.* **2019**, *16*, 2235–2248. https://doi.org/10.1021/acs.molpharmaceut.9b00259.

97.   Nocito, G.; Calabrese, G.; Forte, S.; Petralia, S.; Puglisi, C.; Campolo, M.; Esposito, E.; Conoci, S. Carbon Dots as Promising Tools for Cancer Diagnosis and Therapy. *Cancers* **2021**, *13*, 1991. https://doi.org/10.3390/cancers13091991.

98.   He, H.; Zheng, X.; Liu, S.; Zheng, M.; Xie, Z.; Wang, Y.; Yu, M.; Shuai, X. Diketopyrrolopyrrole-based carbon dots for photodynamic therapy. *Nanoscale* **2018**, *10*, 10991–10998. https://doi.org/10.1039/C8NR02643B.

99.   Jeelani, P.G.; Mulay, P.; Venkat, R.; Ramalingam, C. Multifaceted Application of Silica Nanoparticles. A Review. *Silicon* **2020**, *12*, 1337–1354. https://doi.org/10.1007/s12633-019-00229-y.

100. Liu, Y.; Liu, X.; Xiao, Y.; Chen, F.; Xiao, F. A multifunctional nanoplatform based on mesoporous silica nanoparticles for imaging-guided chemo/photodynamic synergetic therapy. *RSC Adv.* **2017**, *7*, 31133–31141. https://doi.org/10.1039/c7ra04549b.

101. Lin, X.; Wu, M.; Li, M.; Cai, Z.; Sun, H.; Tan, X.; Li, J.; Zeng, Y.; Liu, X.; Liu, J. Photoresponsive hollow silica nanoparticles for light-triggered genetic and photodynamic synergistic therapy. *Acta Biomater.* **2018**, *76*, 178–192. https://doi.org/10.1016/j.actbio.2018.07.007.

102. Bretin, L.; Pinon, A.; Bouramtane, S.; Ouk, C.; Richard, L.; Perrin, M.; Chaunavel, A.; Carrion, C.; Bregier, F.; Sol, V.; et al. Photodynamic Therapy Activity of New Porphyrin-Xylan-Coated Silica Nanoparticles in Human Colorectal Cancer. *Cancers* **2019**, *11*, 1474. https://doi.org/10.3390/cancers11101474.

103. Matlou, G.G.; Oluwole, D.O.; Prinsloo, E.; Nyokong, T. Photodynamic therapy activity of zinc phthalocyanine linked to folic acid and magnetic nanoparticles. *J. Photochem. Photobiol. B Biol.* **2018**, *186*, 216–224. https://doi.org/10.1016/j.jphotobiol.2018.07.025.

104. Zhang, L.K.; Du, S.; Wang, X.; Jiao, Y.; Yin, L.; Zhang, Y.; Guan, Y.Q. Bacterial cellulose based composites enhanced transdermal drug targeting for breast cancer treatment. *Chem. Eng. J.* **2019**, *370*, 749–759. https://doi.org/10.1016/j.cej.2019.03.216.

105. Zhang, P.; Wu, G.; Zhao, C.; Zhou, L.; Wang, X.; Wei, S. Magnetic stomatocyte-like nanomotor as photosensitizer carrier for photodynamic therapy based cancer treatment. *Coll. Surf. B Biointerfaces* **2020**, *194*, 111204. https://doi.org/10.1016/j.colsurfb.2020.111204.

106. Sailor, M.J.; Park, J.-H. Hybrid Nanoparticles for Detection and Treatment of Cancer. *Adv. Mater.* **2012**, *24*, 3779–3802. https://doi.org/10.1002/adma.201200653.

107. Pramual, S.; Lirdprapamongkol, K.; Svasti, J.; Bergkvist, M.; Jouan-Hureaux, V.; Arnoux, P.; Frochot, C.; Barberi-Heyob, M.; Niamsiri, N. Polymer-lipid-PEG hybrid nanoparticles as photosensitizer carrier for photodynamic therapy. *J. Photochem. Photobiol. B Biol.* **2017**, *173*, 12–22. https://doi.org/10.1016/j.jphotobiol.2017.05.028.

108. Shumatbaeva, A.M.; Morozova, J.E.; Sapunova, A.S.; Voloshina, A.D.; Saifina, A.F.; Gubaidullin, A.T.; Nizameev, I.R.; Kadirov, M.K.; Antipin, I.S. The construction of supramolecular and hybrid Ag-AgCl nanoparticles with photodynamic therapy action on the base of tetraundecylcalix[4]resorcinarene-mPEG conjugate. *Colloids Surfaces A Physicochem. Eng. Asp.* **2021**, 619, 126524, doi:10.1016/j.colsurfa.2021.126524.

<div align="right">

3

</div>

LIPOSOMES AS A DRUG DELIVERY SYSTEM FOR PHOTOTHERAPY APPLICATION

Abstract: The encapsulation of drug molecules for topical applications has increased specially with the use of lipid-based nanoparticles that are biocompatible, biodegradable and are non-toxic. Liposomes are lipid-based vesicles able to encapsulate hydrophilic and hydrophobic drugs and can be prepared from a wide range of lipids. Novel classes of liposomes such as the transfersomes, ethosomes and transethosomes have been developed to obtain flexible vesicles able to penetrate the skin and achieve the epidermis and/or the dermis. Therefore, the selection of the liposomes composition is dependent on the desired effect and the target tissue. The combination of liposomes in photodynamic therapy can be a useful tool for the encapsulation of photosensitizer drugs, as well as to enable a photo-triggered release of the drug. This chapter presents an overview about liposomes, topical delivery from liposomes and encapsulation of photosensitizer molecules to be used in photodynamic therapy.

3.1 Introduction

Currently, there is an increasing number of nanotechnology-based research in the health field. The research of nanoparticles in medicine has increased in order to solve problems related to systemic side effects, with intention of a possible dosage reduction as well as create a targeting particle and improve the bioavailability with a sustained release of the drug from the nanoparticles [1,2].

There are some types of nanoparticles that are more appropriate for the skin delivery such as the solid lipid nanoparticles, their successors the nanostructured lipid carriers as well as liposomes [3]. These are lipid-based nanoparticles that present great biodegradability, biocompatibility and due to the lipid nature are non-toxic [4,5]. Solid lipid nanoparticles are prepared with solid lipid at room and at body temperature, forming particles with lipidic nucleus and, therefore, are able to encapsulate hydrophobic compounds [6,7]. Liposomes, on the other hand, are composed by phospholipids that present a polar "head" group and a hydrophobic "tail", which enable the organization in bilayers resulting in

vesicles with the ability to retain hydrophobic compounds in the lipid bilayer and encapsulate hydrophilic compounds in its hydrophilic core or on its surface [8,9].

These characteristics turn liposomes in nanocarriers with great potential for the delivery of photosensitizers. Therefore, the liposomes concepts, their structure as well as the novel classes of liposomes are addressed in this work as well as the application of liposomes for the topical delivery of photosensitizers.

3.2 Liposomes

Amphiphilic molecules are those that present hydrophilic and hydrophobic portions, leading to a characteristic ordered structure that depends on the molecular shape [10]. Amphiphilic molecules such as lipids can present different packing parameters can be calculated according to Equation 3.1 where v is the molecular volume, a is the cross-section area of the head group and l is the molecule length. The packing parameter (P) value is very useful to predict the structural organization [11–13].

$$\text{Equation 3.1} \quad P = \frac{v}{a.l}$$

Liposomes, for example, are formed by lipids with a characteristic molecular shape ($\frac{1}{2} < P < 1$) [12] such as some phospholipids (Figure 3.1), which enable the organization as a bilayer and its self-assembly into a vesicle with the bilayer isolating the aqueous cavity from the aqueous exterior (Figure 3.2) [14,15]. Liposomes have the ability to entrap both hydrophilic and hydrophobic compounds showing several advantages such as allowing high encapsulation and protection from degradation and/or inactivation [16,17]. Liposomes also enable coating or even the functionalization of the surface, giving opportunity to attach a wide range of ligands [18]. For example, polyethylene glycol (PEG) can be used in the surface of the liposomes turning into the so-called stealth liposomes, making these particles able to evade the immune system and, consequently, prolonging the circulation time [18–20]. Functionalization with antibody is an interesting strategy that can turn the liposomes into a target system, selective for a specific tissue-site [21]. Therefore, liposomes are versatile particles, allowing modifications with ligands for specific interactions and, consequently, for different purposes.
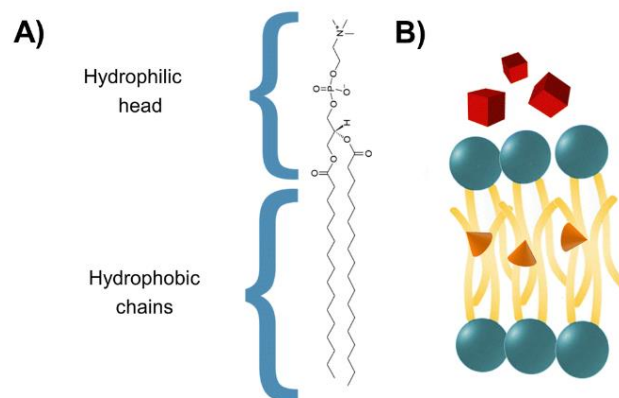
Figure 3.1: Representation of phospholipids. A) Structure of hydrogenated soybean phosphatidylcholine. B) Scheme of phospholipid and hydrophobic (cone shape) and hydrophilic drugs (cube shape). Adapted from reference [8]. Copyright 2019, Cancer Nanotechnology.
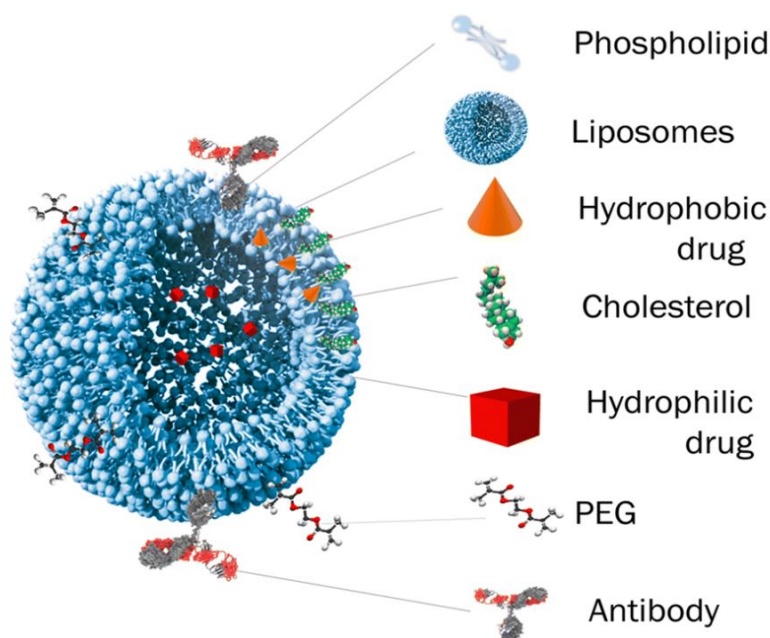
Figure 3.2: Representation of liposome and the encapsulation of hydrophobic and hydrophilic drug as well as the possible ligands (PEG and antibody). Reproduced from reference [8]. Copyright 2019, Cancer Nanotechnology.

There are several lipids with cylindrical shape that can be employed for the preparation of liposomes such as the phosphatidylcholine, phosphatidylinositol, phosphatidylglycerol, cardiolipin and others. These phospholipids are classified by their "head" group and can present different characteristics such as the length and saturation of the acyl chains. Due to the "head" group, phospholipids can present different electrical charge, and can be classified as zwitterionic, anionic and cationic phospholipids [14]. Table 3.1 shows some examples of these characteristics, where DPPC present a phosphocholine group giving its zwitterionic characteristic, along with a saturated acyl chain with sixteen carbons. Differently from DPPC, DPPG present a glycerophosphate group, giving this lipid an anionic characteristic.

DOTAP, on the other side, is not a phospholipid since it does not present phosphate group, however it presents a cylindrical shape with longer acyl chain (eighteen carbons), unsaturation and a cationic polar "head" group, which is useful for the preparation of cationic liposomes [22–25].

Cholesterol can be used in liposomes composition and plays an important role on the fluidity of the vesicle, the packing of the phospholipids and in the improvement of the vesicle's stability [26–28].

Table 3.1: Description of some characteristics of different lipids, namely, 1,2-dipalmitoyl-sn-glycero-3-phospho-choline (DPPC), 1,2-dioleoyl-sn-glycero-3-phosphocholine (DOPC), 1,2-dipalmitoyl-sn-glycero-3-phospho-(1'-rac-glycerol) (sodium salt) (DPPG), 1,2-dioleoyl-sn-glycero-3-phospho-(1'-rac-glycerol), sodium salt (DOPG), and 1,2-dioleoyl-3-trimethylammonium-propane (chloride salt) (DOTAP).

Name	Charge	T_c (ºC) [14]	Length of acyl chain and saturation	Chemical structure
DPPC	Zwitterionic	41	16:0	
DOPC	Zwitterionic	-22	18:1 (Δ9-Cis)	
DPPG	Anionic	41	16:0	
DOPG	Anionic	-18	18:1 (Δ9-Cis)	
DOTAP	Cationic	-	18:1	

Another characteristic of the phospholipids is the phase transition temperature (T_c) that is defined as the temperature of its transition from the gel (ordered) to the liquid crystalline state (disordered form) [29]. The T_c is impacted by the polar "head" group, the length of the acyl chain, the presence of unsaturation and even by the purification of the lipid. Phospholipids from natural origin have a lower T_c

compared to synthetic phospholipids [14]. Therefore, the phospholipids can have many different characteristics that can affect the liposomes size, charge, elasticity and, consequently, the purpose of application.

The liposomes can be classified regarding the lamellarity and the size of the vesicles. Small unilamellar vesicles (SUVs) usually are vesicles with less than 100 nm of diameter, the large unilamellar vesicles (LUVs) are those with diameter size between 100 – 500 nm whereas the giant unilamellar vesicles (GUVs) are those above 500 nm with a single bilayer. There are other cases such as the multilamellar vesicle (MLVs) and multivesicular vesicles (MVVs) with size above 500 nm [30].

3.3 Topical delivery of liposomes

The stratum corneum is the main barrier for the delivery of drugs in the skin layers and consists of corneocytes with lipid regions on the surroundings as shown in Figure 3.3. There are four mechanisms proposed to explain the drug delivery to the skin layer: liposomes acting as penetration enhancer, liposome adsorption to the stratum corneum with or not fusion of the vesicles, penetration of the intact liposomes and penetration via follicular path [31,32].

To improve the topical delivery other classes of vesicles derived from liposomes were developed aiming to accomplish more flexible vesicles able to penetrate the skin leading to an adequate drug delivery in the epidermis and dermis (Figure 3.3). Among these vesicles there are transfersomes composed by phospholipids and an edge activator such as surfactants. Different surfactants can be used as edge activators such as the non-ionic surfactants Span® 60, Span® 65, Span® 80, Tween® 20, Tween® 60 and Tween® 80. Also, bile salts such as sodium cholate and sodium deoxycholate can be used [33,34]. The ethosomes are another type of deformable vesicles and use high content of ethanol which gives vesicle elasticity [35,36]. Lastly, the transethosomes, a combination of transfersomes and ethosomes, were developed by Song et al. [37]. These vesicles contain not only an edge activator but also ethanol in its composition.
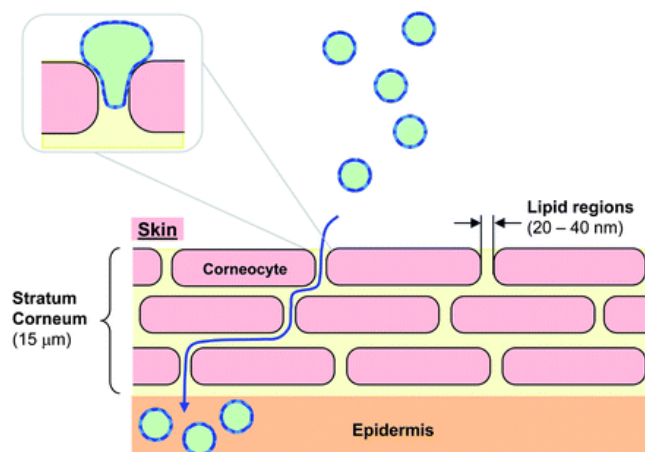
Figure 3.3: Scheme of the penetration path of deformable vesicles. Adapted from reference [38]. Copyright 2012, Soft Matter.

3.4 Application of liposomes in photodynamic therapy

The photodynamic therapy (PDT) has been widely investigated for the cancer treatment mainly because of the minimally or non-invasive procedure. PDT has also been used as an alternative therapy for some chronic inflammatory diseases in advanced stages as in the case of psoriasis, diseases related to depigmentation disorders such as vitiligo, cutaneous T-cell lymphoma and other types of skin disorders [39–41].

The photosensitizers (PS) molecules play an important role in PDT and the therapy success is dependent of its selection. More than 400 molecules have sensitizing potential induced by light. Among these molecules there are dyes, natural products and many others chemical substances [42]. The first generation of photosensitizers were the porphyrin type [43]. They have been used since the middle of the 20th century with derivative molecules from hematoporphyrin. PDT using porphyrins as photosensitizers showed to be efficient in cancer therapy and a promising sensitizer in microbial infections [42,44]. However, the wavelength able to activate the photosensitizer is usually too short for porphyrins which hinders the light penetration, besides, after activated the half-life is too long which could cause a severe phototoxicity [43,45].

A second generation of photosensitizers has been developed through alterations in the porphyrin core or in peripheral sites in order to improve the photosensitivity. Phthalocyanines are examples of this second generation derived from porphyrins. However, some authors also consider other classes of chemicals non-related to porphyrin structure as second generation photosensitizers such as anthraquinones (e.g., hypericin), phenothiazines (e.g., methylene blue), cyanines (e.g., merocyanine 540) and others [43].

The damage induced by photosensitizers is mainly due to the generation of reactive oxygen species (ROS) that can damage biomolecules as a result of the oxidizing power of the reactive species. The DNA is one of the biomolecules that can be subjected to damage and is the main target for anticancer drugs [46]. Currently, a photosensitizer widely used in phototherapy is psoralen that is used mainly to treat psoriasis, an autoimmune inflammatory disorder. Psoralen is able to intercalate the DNA and when activated by UVA it creates crosslinks, preventing cell proliferation, stimulating the immunological response and the apoptosis [40]. In this context, there is still a lot to explore and study about intercalating agents aiming phototherapy applications.

Table 3.2 displays examples of DNA-intercalating agents, some of them with many studies about the possible application to photodynamic therapy. In PDT, methylene blue shows the most different types of biological activities such as antimicrobial, anticancer and even tested for psoriatic lesions [47–53]. Acridine orange is usually employed for nucleic acid staining [54], therefore acridine orange has not been extensively investigated for PDT as methylene blue, having been explored mainly in studies with cancer cells [55–57]. Gentian violet or crystal violet also has been referenced on phototoxic action for different types of pathologies [58–60].

Natural products such as the catechins, flavonoids and curcuminoids have recently gained interest towards photodynamic therapy mainly for the cancer treatment. Many biological properties such as antioxidant, anti-inflammatory, antimicrobial and anticarcinogenic effects have been related to quercetin [61–63] and also for epigallocatechin gallate, present in green tea, that presents antioxidant and anti-inflammatory properties [64]. Researchers have been exploring the use of these flavonoids for PDT such as by the co-administration of the flavonoid plus a photosensitizer molecule [65,66]. Curcumin is a natural product found in *Curcuma longa* and has been related to properties such as antioxidant and anti-inflammatory [67] but also has been studied for PDT application showing possible application as antimicrobial, anticancer and for psoriasis treatment [68–74]. On the other hand, there are the chelating agents such as neocuproine, 1,10-phenanthroline and 2,2'-bipyridyl that can be used for complexations and have demonstrated numerous functions such as antiviral and antifungal properties [75]. Chelating agents have been investigated regarding their use for PDT [76–78].

Table 3.2: Chemical structure and therapeutic applications reported in the literature about the use of intercalating agents for photodynamic therapy.
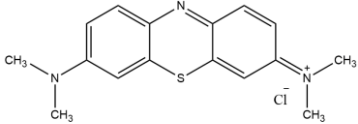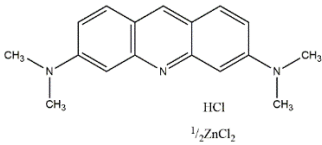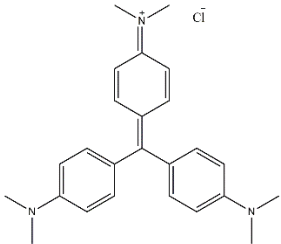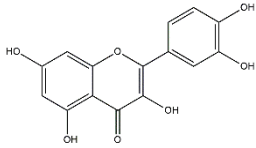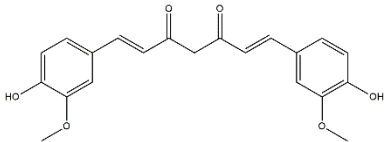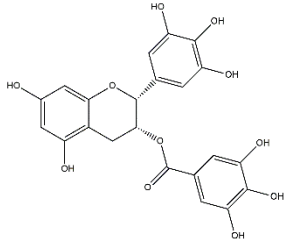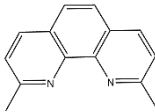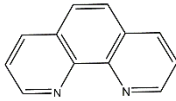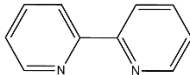
Substances	Chemical structure	Therapeutic application
Methylene blue		Bacteria [47,48] Fungus [48] Parasite [49] Cancer [50–52] Psoriasis [53]
Acridine orange		Cancer [55–57] Fungus [79]
Gentian violet		Bacteria [58,80] Fungus [80] Virus [59] Parasite [60]
Quercetin		Cancer [65,81]
Curcumin		Bacteria [68] Fungus [69] Parasite [70] Cancer [71–73] Psoriasis [74]
Epigallocatechin gallate		Cancer [66, 82–84]

Table 3.2: Continued.

Neocuproine		Cancer [85]
1,10-Phenanthroline		Cancer [76]
2,2'-Bipyridyl		Cancer [77]

PDT has been widely applied for topical diseases such as skin tumors, infectious and inflammatory skin disorders. After topical application it is required some time for the drug penetrate the skin and be retained in the target tissue before the activation with a light source [44]. Although some substances are not good candidates for skin delivery, nanotechnology approaches can be used to enhance its penetration in the tissue and provide a more effective PDT therapy.

Under physiologic conditions aggregation or poor solubility can take place with photosensitizers and interfere in PDT action. Additionally, the accumulation of the photosensitizer in the target tissue is important to provide a more effective response with less side effects. Therefore, the use of nanoparticles as drug delivery could be useful to enhance the photosensitizer solubility, its cellular uptake and reduce side effects [86]. In fact, nowadays there is a strong increase in the research allying nanotechnology to PDT giving rise to a third generation of photosensitizers.
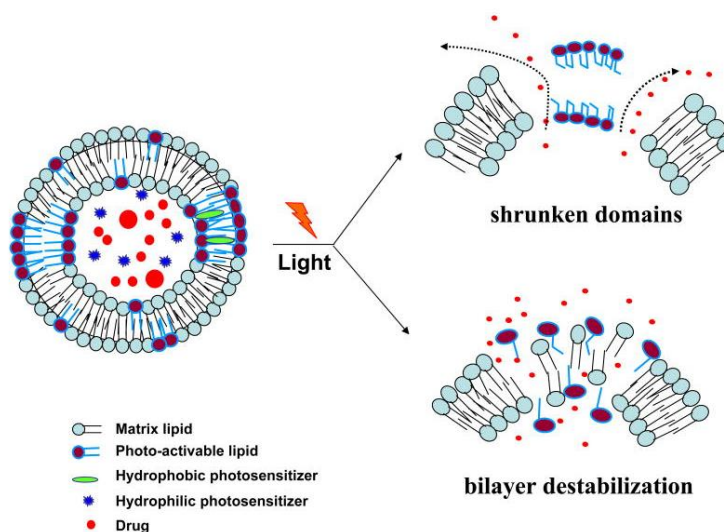
Figure 3.4: Representation of the photo-induced release. Adapted from reference [87]. Copyright 2010, Molecular Membrane Biology.

In addition to the advantages of the photosensitizers' encapsulation in liposomes and the drug delivery of these molecules, there are liposomes that can be activated by a stimulus that lead to the destabilization of the liposomes and, consequently, the release of the drugs. Figure 3.4 represent light as a stimulus that can trigger the liposomes destabilization whereas the photosensitizer, in its turn, can lead to the photo-oxidation of the lipid [87,88]. In this context, PDT can be a useful tool for the photo-activation of liposomes, allowing the release of the drugs.

3.5 Conclusions

Lipid-based nanoparticles are suitable carriers to use aiming the topical delivery of drugs such as the photosensitizers for application in PDT. Liposomes are versatile vesicles, that can be composed by several types of lipids, with different charges, saturation, and chain length. The addition of surfactants and/or ethanol can turn vesicles into more deformable particles, able to cross the skin and achieve the epidermis and dermis. Furthermore, depending on the composition, liposomes can be stimuli-triggerable such as by photo-activation liposomes, which enables the release of the drug for PDT application.

References

1. Hua, S.; de Matos, M.B.C.; Metselaar, J.M.; Storm, G. Current Trends and Challenges in the Clinical Translation of Nanoparticulate Nanomedicines: Pathways for Translational

Development and Commercialization. *Front. Pharmacol.* **2018**, *9*, 790, doi:10.3389/fphar.2018.00790.

2. Abdel-Mageed, H.M.; AbuelEzz, N.Z.; Radwan, R.A.; Mohamed, S.A. Nanoparticles in nanomedicine: a comprehensive updated review on current status, challenges and emerging opportunities. *J. Microencapsul.* **2021**, *38*, 414–436, doi:10.1080/02652048.2021.1942275.

3. Krishnan, V.; Mitragotri, S. Nanoparticles for topical drug delivery: Potential for skin cancer treatment. *Adv. Drug Deliv. Rev.* **2020**, *153*, 87–108, doi:10.1016/j.addr.2020.05.011.

4. García-Pinel, B.; Porras-Alcalá, C.; Ortega-Rodríguez, A.; Sarabia, F.; Prados, J.; Melguizo, C.; López-Romero, J.M. Lipid-Based Nanoparticles: Application and Recent Advances in Cancer Treatment. *Nanomaterials* **2019**, *9*, 638, doi:10.3390/nano9040638.

5. Li, C.; Zhang, J.; Zu, Y.-J.; Nie, S.-F.; Cao, J.; Wang, Q.; Nie, S.-P.; Deng, Z.-Y.; Xie, M.-Y.; Wang, S. Biocompatible and biodegradable nanoparticles for enhancement of anti-cancer activities of phytochemicals. *Chin. J. Nat. Med.* **2015**, *13*, 641–652, doi:10.1016/S1875-5364(15)30061-3.

6. Musielak, E.; Feliczak-Guzik, A.; Nowak, I. Synthesis and Potential Applications of Lipid Nanoparticles in Medicine. *Materials (Basel).* **2022**, *15*, 682, doi:10.3390/ma15020682.

7. Scioli Montoto, S.; Muraca, G.; Ruiz, M.E. Solid Lipid Nanoparticles for Drug Delivery: Pharmacological and Biopharmaceutical Aspects. *Front. Mol. Biosci.* **2020**, *7*, 587997, doi:10.3389/fmolb.2020.587997.

8. Beltrán-Gracia, E.; López-Camacho, A.; Higuera-Ciapara, I.; Velázquez-Fernández, J.B.; Vallejo-Cardona, A.A. Nanomedicine review: clinical developments in liposomal applications. *Cancer Nanotechnol.* **2019**, *10*, 11, doi:10.1186/s12645-019-0055-y.

9. Gonzalez Gomez, A.; Syed, S.; Marshall, K.; Hosseinidoust, Z. Liposomal Nanovesicles for Efficient Encapsulation of Staphylococcal Antibiotics. *ACS Omega* **2019**, *4*, 10866–10876, doi:10.1021/acsomega.9b00825.

10. Lombardo, D.; Kiselev, M.A.; Magazù, S.; Calandra, P. Amphiphiles Self-Assembly: Basic Concepts and Future Perspectives of Supramolecular Approaches. *Adv. Condens. Matter Phys.* **2015**, *2015*, 151683, doi:10.1155/2015/151683.

11. Doncom, K.E.B.; Blackman, L.D.; Wright, D.B.; Gibson, M.I.; O'Reilly, R.K. Dispersity effects in polymer self-assemblies: a matter of hierarchical control. *Chem. Soc. Rev.* **2017**, *46*, 4119–4134, doi:10.1039/C6CS00818F.

12. Stuart, M.C.A.; Boekema, E.J. Two distinct mechanisms of vesicle-to-micelle and micelle-to-vesicle transition are mediated by the packing parameter of phospholipid–detergent systems. *Biochim. Biophys. Acta - Biomembr.* **2007**, *1768*, 2681–2689, doi:10.1016/j.bbamem.2007.06.024.

13. Nagarajan, R. Molecular Packing Parameter and Surfactant Self-Assembly: The Neglected Role of the Surfactant Tail. *Langmuir* **2002**, *18*, 31–38, doi:10.1021/la010831y.

14.   Li, J.; Wang, X.; Zhang, T.; Wang, C.; Huang, Z.; Luo, X.; Deng, Y. A review on phospholipids and their main applications in drug delivery systems. *Asian J. Pharm. Sci.* **2015**, *10*, 81–98, doi:10.1016/j.ajps.2014.09.004.

15.   Sadasivam, M.; Avci, P.; Gupta, G.K.; Lakshmanan, S.; Chandran, R.; Huang, Y.-Y.; Kumar, R.; Hamblin, M.R. Self-assembled liposomal nanoparticles in photodynamic therapy. *Eur. J. Nanomedicine* **2013**, *5*, 1–7, doi:10.1515/ejnm-2013-0010.

16.   Daraee, H.; Etemadi, A.; Kouhi, M.; Alimirzalu, S.; Akbarzadeh, A. Application of liposomes in medicine and drug delivery. *Artif. Cells, Nanomedicine, Biotechnol.* **2016**, *44*, 381–391, doi:10.3109/21691401.2014.953633.

17.   Sercombe, L.; Veerati, T.; Moheimani, F.; Wu, S.Y.; Sood, A.K.; Hua, S. Advances and Challenges of Liposome Assisted Drug Delivery. *Front. Pharmacol.* **2015**, *6*, 286, doi:10.3389/fphar.2015.00286.

18.   Riaz, M.; Riaz, M.; Zhang, X.; Lin, C.; Wong, K.; Chen, X.; Zhang, G.; Lu, A.; Yang, Z. Surface Functionalization and Targeting Strategies of Liposomes in Solid Tumor Therapy: A Review. *Int. J. Mol. Sci.* **2018**, *19*, 195, doi:10.3390/ijms19010195.

19.   La-Beck, N.M.; Gabizon, A.A. Nanoparticle Interactions with the Immune System: Clinical Implications for Liposome-Based Cancer Chemotherapy. *Front. Immunol.* **2017**, *8*, 416, doi:10.3389/fimmu.2017.00416.

20.   Mohamed, M.; Abu Lila, A.S.; Shimizu, T.; Alaaeldin, E.; Hussein, A.; Sarhan, H.A.; Szebeni, J.; Ishida, T. PEGylated liposomes: immunological responses. *Sci. Technol. Adv. Mater.* **2019**, *20*, 710–724, doi:10.1080/14686996.2019.1627174.

21.   Ohradanova-Repic, A.; Nogueira, E.; Hartl, I.; Gomes, A.C.; Preto, A.; Steinhuber, E.; Mühlgrabner, V.; Repic, M.; Kuttke, M.; Zwirzitz, A.; et al. Fab antibody fragment-functionalized liposomes for specific targeting of antigen-positive cells. *Nanomedicine Nanotechnology, Biol. Med.* **2018**, *14*, 123–130, doi:10.1016/j.nano.2017.09.003.

22.   Gomes, P.J.; Gonçalves da Silva, A.M.P.S.; Ribeiro, P.A.; Oliveira, O.N.; Raposo, M. Radiation damage on Langmuir monolayers of the anionic 1.2-dipalmitoyl-sn-glycero-3-[phospho-rac-(1-glycerol)] (sodium salt)(DPPG) phospholipid at the air–DNA solution interface. *Mater. Sci. Eng. C* **2016**, *58*, 576–579, doi:10.1016/j.msec.2015.09.017.

23.   Chibowski, E.; Szcześ, A. Zeta potential and surface charge of DPPC and DOPC liposomes in the presence of PLC enzyme. *Adsorption* **2016**, *22*, 755–765, doi:10.1007/s10450-016-9767-z.

24.   Barrán-Berdón, A.L.; Martínez-Negro, M.; García-Río, L.; Domènech, Ò.; Tros de Ilarduya, C.; Aicart, E.; Junquera, E. A biophysical study of gene nanocarriers formed by anionic/zwitterionic mixed lipids and pillar[5]arene polycationic macrocycles. *J. Mater. Chem. B* **2017**, *5*, 3122–3131, doi:10.1039/C6TB02939F.

25.   Simberg, D.; Weisman, S.; Talmon, Y.; Barenholz, Y. DOTAP (and other cationic lipids): chemistry, biophysics, and transfection. *Crit. Rev. Ther. Drug Carrier Syst.* **2004**, *21*, 257–317,

doi:10.1615/critrevtherdrugcarriersyst.v21.i4.10.

26. Briuglia, M.-L.; Rotella, C.; McFarlane, A.; Lamprou, D.A. Influence of cholesterol on liposome stability and on *in vitro* drug release. *Drug Deliv. Transl. Res.* **2015**, *5*, 231–242, doi:10.1007/s13346-015-0220-8.

27. Khan, I.; Needham, R.; Yousaf, S.; Houacine, C.; Islam, Y.; Bnyan, R.; Sadozai, S.K.; Elrayess, M.A.; Elhissi, A. Impact of phospholipids, surfactants and cholesterol selection on the performance of transfersomes vesicles using medical nebulizers for pulmonary drug delivery. *J. Drug Deliv. Sci. Technol.* **2021**, *66*, 102822, doi:10.1016/j.jddst.2021.102822.

28. Kaddah, S.; Khreich, N.; Kaddah, F.; Charcosset, C.; Greige-Gerges, H. Cholesterol modulates the liposome membrane fluidity and permeability for a hydrophilic molecule. *Food Chem. Toxicol.* **2018**, *113*, 40–48, doi:10.1016/j.fct.2018.01.017.

29. Chen, W.; Duša, F.; Witos, J.; Ruokonen, S.-K.; Wiedmer, S.K. Determination of the Main Phase Transition Temperature of Phospholipids by Nanoplasmonic Sensing. *Sci. Rep.* **2018**, *8*, 14815, doi:10.1038/s41598-018-33107-5.

30. Šturm, L.; Poklar Ulrih, N. Basic Methods for Preparation of Liposomes and Studying Their Interactions with Different Compounds, with the Emphasis on Polyphenols. *Int. J. Mol. Sci.* **2021**, *22*, 6547, doi:10.3390/ijms22126547.

31. Hua, S. Lipid-based nano-delivery systems for skin delivery of drugs and bioactives. *Front. Pharmacol.* **2015**, *6*, 219, doi:10.3389/fphar.2015.00219.

32. Carneiro, G.; Aguiar, M.G.; Fernandes, A.P.; Ferreira, L.A.M. Drug delivery systems for the topical treatment of cutaneous leishmaniasis. *Expert Opin. Drug Deliv.* **2012**, *9*, 1083–1097, doi:10.1517/17425247.2012.701204.

33. Ascenso, A.; Batista, C.; Cardoso, P.; Mendes, T.; Praça, F.; Bentley, V.; Raposo, S.; Simões, S. Development, characterization, and skin delivery studies of related ultradeformable vesicles: transfersomes, ethosomes, and transethosomes. *Int. J. Nanomedicine* **2015**, *10*, 5837–5851, doi:10.2147/IJN.S86186.

34. Opatha, S.A.T.; Titapiwatanakun, V.; Chutoprapat, R. Transfersomes: A Promising Nanoencapsulation Technique for Transdermal Drug Delivery. *Pharmaceutics* **2020**, *12*, 855, doi:10.3390/pharmaceutics12090855.

35. Limsuwan, T.; Boonme, P.; Khongkow, P.; Amnuaikit, T. Ethosomes of Phenylethyl Resorcinol as Vesicular Delivery System for Skin Lightening Applications. *Biomed Res. Int.* **2017**, *2017*, 8310979, doi:10.1155/2017/8310979.

36. Garg, V.; Singh, H.; Bimbrawh, S.; Singh, S.K.; Gulati, M.; Vaidya, Y.; Kaur, P. Ethosomes and Transfersomes: Principles, Perspectives and Practices. *Curr. Drug Deliv.* **2017**, *14*, 613–633, doi:10.2174/1567201813666160520114436.

37. Song, C.K.; Balakrishnan, P.; Shim, C.-K.; Chung, S.-J.; Chong, S.; Kim, D.-D. A novel vesicular carrier, transethosome, for enhanced skin delivery of voriconazole: Characterization

and *in vitro*/*in vivo* evaluation. *Colloids Surfaces B Biointerfaces* **2012**, *92*, 299–304, doi:10.1016/j.colsurfb.2011.12.004.

38. Ogunsola, O.A.; Kraeling, M.E.; Zhong, S.; Pochan, D.J.; Bronaugh, R.L.; Raghavan, S.R. Structural analysis of "flexible" liposome formulations: new insights into the skin-penetrating ability of soft nanostructures. *Soft Matter* **2012**, *8*, 10226, doi:10.1039/c2sm26614h.

39. Keyal, U.; Bhatta, A.K.; Zhang, G.; Wang, X. Present and future perspective of photodynamic therapy for cutaneous squamous cell carcinoma. *J. Am. Acad. Dermatol.* **2018**, doi:10.1016/j.jaad.2018.10.042.

40. Vangipuram, R.; Feldman, S.R. Ultraviolet phototherapy for cutaneous diseases: A concise review. *Oral Dis.* **2016**, *22*, 253–259, doi:10.1111/odi.12366.

41. Ibbotson, S.H. A Perspective on the Use of NB-UVB Phototherapy vs . PUVA Photochemotherapy. *Front. Med.* **2018**, *5*, 1–8, doi:10.3389/fmed.2018.00184.

42. Oniszczuk, A.; Wojtunik-Kulesza, K.A.; Oniszczuk, T.; Kasprzak, K. The potential of photodynamic therapy (PDT)—Experimental investigations and clinical use. *Biomed. Pharmacother.* **2016**, *83*, 912–929, doi:10.1016/j.biopha.2016.07.058.

43. Zhang, J.; Jiang, C.; Figueiró Longo, J.P.; Azevedo, R.B.; Zhang, H.; Muehlmann, L.A. An updated overview on the development of new photosensitizers for anticancer photodynamic therapy. *Acta Pharm. Sin. B* **2018**, *8*, 137–146, doi:10.1016/j.apsb.2017.09.003.

44. Kim, M.; Jung, H.; Park, H. Topical PDT in the Treatment of Benign Skin Diseases: Principles and New Applications. *Int. J. Mol. Sci.* **2015**, *16*, 23259–23278, doi:10.3390/ijms161023259.

45. Kou, J.; Dou, D.; Yang, L. Porphyrin photosensitizers in photodynamic therapy and its applications. *Oncotarget* **2017**, *8*, 81591–81603, doi:10.18632/oncotarget.20189.

46. Crous, A.; Chizenga, E.; Hodgkinson, N.; Abrahamse, H. Targeted Photodynamic Therapy: A Novel Approach to Abolition of Human Cancer Stem Cells. *Int. J. Opt.* **2018**, *2018*, 7317063, doi:10.1155/2018/7317063.

47. Huang, Y.-Y.; Wintner, A.; Seed, P.C.; Brauns, T.; Gelfand, J.A.; Hamblin, M.R. Antimicrobial photodynamic therapy mediated by methylene blue and potassium iodide to treat urinary tract infection in a female rat model. *Sci. Rep.* **2018**, *8*, 7257, doi:10.1038/s41598-018-25365-0.

48. Tardivo, J.P.; Del Giglio, A.; de Oliveira, C.S.; Gabrielli, D.S.; Junqueira, H.C.; Tada, D.B.; Severino, D.; de Fátima Turchiello, R.; Baptista, M.S. Methylene blue in photodynamic therapy: From basic mechanisms to clinical applications. *Photodiagnosis Photodyn. Ther.* **2005**, *2*, 175–191, doi:10.1016/S1572-1000(05)00097-9.

49. Cabral, F. V.; Sabino, C.P.; Dimmer, J.A.; Sauter, I.P.; Cortez, M.J.; Ribeiro, M.S. Preclinical Investigation of Methylene Blue-mediated Antimicrobial Photodynamic Therapy on Leishmania Parasites Using Real-Time Bioluminescence. *Photochem. Photobiol.* **2020**, *96*, 604–610, doi:10.1111/php.13188.

50. dos Santos, A.F.; Terra, L.F.; Wailemann, R.A.M.; Oliveira, T.C.; Gomes, V. de M.; Mineiro,

M.F.; Meotti, F.C.; Bruni-Cardoso, A.; Baptista, M.S.; Labriola, L. Methylene blue photodynamic therapy induces selective and massive cell death in human breast cancer cells. *BMC Cancer* **2017**, *17*, 194, doi:10.1186/s12885-017-3179-7.

51. Wu, P.-T.; Lin, C.-L.; Lin, C.-W.; Chang, N.-C.; Tsai, W.-B.; Yu, J. Methylene-Blue-Encapsulated Liposomes as Photodynamic Therapy Nano Agents for Breast Cancer Cells. *Nanomaterials* **2018**, *9*, 14, doi:10.3390/nano9010014.

52. Kofler, B.; Romani, A.; Pritz, C.; Steinbichler, T.; Schartinger, V.; Riechelmann, H.; Dudas, J. Photodynamic Effect of Methylene Blue and Low Level Laser Radiation in Head and Neck Squamous Cell Carcinoma Cell Lines. *Int. J. Mol. Sci.* **2018**, *19*, 1107, doi:10.3390/ijms19041107.

53. Schick, E.; Riick, A.; Boehncke, W.-H.; Kaufmann, R. Topical photodynamic therapy using methylene blue and 5-aminolaevulinic acid in psoriasis. *J. Dermatolog. Treat.* **1997**, *8*, 17–19, doi:10.3109/09546639709160503.

54. Damas-Souza, D.M.; Nunes, R.; Carvalho, H.F. An improved acridine orange staining of DNA/RNA. *Acta Histochem.* **2019**, *121*, 450–454, doi:10.1016/j.acthis.2019.03.010.

55. Osman, H.; Elsahy, D.; Saadatzadeh, M.R.; Pollok, K.E.; Yocom, S.; Hattab, E.M.; Georges, J.; Cohen-Gadol, A.A. Acridine Orange as a Novel Photosensitizer for Photodynamic Therapy in Glioblastoma. *World Neurosurg.* **2018**, *114*, e1310–e1315, doi:10.1016/j.wneu.2018.03.207.

56. Kusuzaki, K.; Murata, H.; Matsubara, T.; Satonaka, H.; Wakabayashi, T.; Matsumine, A.; Uchida, A. Acridine orange could be an innovative anticancer agent under photon energy. *In Vivo (Brooklyn).* **2007**, *21*, 205–214.

57. Lin, Y.-C.; Lin, J.-F.; Tsai, T.-F.; Chen, H.-E.; Chou, K.-Y.; Yang, S.-C.; Tang, Y.-M.; Hwang, T.I.S. Acridine orange exhibits photodamage in human bladder cancer cells under blue light exposure. *Sci. Rep.* **2017**, *7*, 14103, doi:10.1038/s41598-017-13904-0.

58. Owusu, E.G.A.; MacRobert, A.J.; Naasani, I.; Parkin, I.P.; Allan, E.; Yaghini, E. Photoactivable Polymers Embedded with Cadmium-Free Quantum Dots and Crystal Violet: Efficient Bactericidal Activity against Clinical Strains of Antibiotic-Resistant Bacteria. *ACS Appl. Mater. Interfaces* **2019**, *11*, 12367–12378, doi:10.1021/acsami.9b02109.

59. Walker, T.; Canales, M.; Noimark, S.; Page, K.; Parkin, I.; Faull, J.; Bhatti, M.; Ciric, L. A Light-Activated Antimicrobial Surface Is Active Against Bacterial, Viral and Fungal Organisms. *Sci. Rep.* **2017**, *7*, 1–10, doi:10.1038/s41598-017-15565-5.

60. Docampo, R.; Muniz, R.P.A.; Mason, R.P. Light-Enhanced Free Radical Formation and Trypanocidal Action of Gentian Violet (Crystal Violet). *Science (80-.).* **1983**, *220*, 1292–1294.

61. Pivetta, T.P.; Silva, L.B.; Kawakami, C.M.; Araújo, M.M.; Del Lama, M.P.F.M.; Naal, R.M.Z.G.; Maria-Engler, S.S.; Gaspar, L.R.; Marcato, P.D. Topical formulation of quercetin encapsulated in natural lipid nanocarriers: Evaluation of biological properties and phototoxic effect. *J. Drug Deliv. Sci. Technol.* **2019**, *53*, 101148, doi:10.1016/j.jddst.2019.101148.

62. Li, Y.; Yao, J.; Han, C.; Yang, J.; Chaudhry, M.; Wang, S.; Liu, H.; Yin, Y. Quercetin, Inflammation and Immunity. *Nutrients* **2016**, *8*, 167, doi:10.3390/nu8030167.

63. Nguyen, T.L.A.; Bhattacharya, D. Antimicrobial Activity of Quercetin: An Approach to Its Mechanistic Principle. *Molecules* **2022**, *27*, 2494, doi:10.3390/molecules27082494.

64. Wu, Y.R.; Choi, H.J.; Kang, Y.G.; Kim, J.K.; Shin, J.-W. *In vitro* study on anti-inflammatory effects of epigallocatechin-3-gallate-loaded nano- and microscale particles. *Int. J. Nanomedicine* **2017**, *12*, 7007–7013, doi:10.2147/IJN.S146296.

65. Thakur, N.S.; Mandal, N.; Patel, G.; Kirar, S.; Reddy, Y.N.; Kushwah, V.; Jain, S.; Kalia, Y.N.; Bhaumik, J.; Banerjee, U.C. Co-administration of zinc phthalocyanine and quercetin via hybrid nanoparticles for augmented photodynamic therapy. *Nanomedicine Nanotechnology, Biol. Med.* **2021**, *33*, 102368, doi:10.1016/j.nano.2021.102368.

66. León, D.; Buchegger, K.; Silva, R.; Riquelme, I.; Viscarra, T.; Mora-Lagos, B.; Zanella, L.; Schafer, F.; Kurachi, C.; Roa, J.C.; et al. Epigallocatechin Gallate Enhances MAL-PDT Cytotoxic Effect on PDT-Resistant Skin Cancer Squamous Cells. *Int. J. Mol. Sci.* **2020**, *21*, 3327, doi:10.3390/ijms21093327.

67. Hewlings, S.; Kalman, D. Curcumin: A Review of Its Effects on Human Health. *Foods* **2017**, *6*, 92, doi:10.3390/foods6100092.

68. Dou, F.; Huang, K.; Nitin, N. Targeted Photodynamic Treatment of Bacterial Biofilms Using Curcumin Encapsulated in Cells and Cell Wall Particles. *ACS Appl. Bio Mater.* **2021**, *4*, 514–522, doi:10.1021/acsabm.0c01051.

69. Sakima, V.; Barbugli, P.; Cerri, P.; Chorilli, M.; Carmello, J.; Pavarina, A.; Mima, E. Antimicrobial Photodynamic Therapy Mediated by Curcumin-Loaded Polymeric Nanoparticles in a Murine Model of Oral Candidiasis. *Molecules* **2018**, *23*, 2075, doi:10.3390/molecules23082075.

70. Pereira, A.H.C.; Marcolino, L.M.C.; Pinto, J.G.; Ferreira-Strixino, J. Evaluation of the Photodynamic Therapy with Curcumin on L. braziliensis and L. major Amastigotes. *Antibiotics* **2021**, *10*, 634, doi:10.3390/antibiotics10060634.

71. Kazantzis, K.T.; Koutsonikoli, K.; Mavroidi, B.; Zachariadis, M.; Alexiou, P.; Pelecanou, M.; Politopoulos, K.; Alexandratou, E.; Sagnou, M. Curcumin derivatives as photosensitizers in photodynamic therapy: photophysical properties and *in vitro* studies with prostate cancer cells. *Photochem. Photobiol. Sci.* **2020**, *19*, 193–206, doi:10.1039/C9PP00375D.

72. de Matos, R.P.A.; Calmon, M.F.; Amantino, C.F.; Villa, L.L.; Primo, F.L.; Tedesco, A.C.; Rahal, P. Effect of Curcumin-Nanoemulsion Associated with Photodynamic Therapy in Cervical Carcinoma Cell Lines. *Biomed Res. Int.* **2018**, *2018*, 4057959, doi:10.1155/2018/4057959.

73. Abdel Fadeel, D.A.; Kamel, R.; Fadel, M. PEGylated lipid nanocarrier for enhancing photodynamic therapy of skin carcinoma using curcumin: in-vitro/in-vivo studies and histopathological examination. *Sci. Rep.* **2020**, *10*, 10435, doi:10.1038/s41598-020-67349-z.

74.   Gomez, C.; Muangnoi, C.; Sorasitthiyanukarn, F.; Wongpiyabovorn, J.; Rojsitthisak, P.; Rojsitthisak, P. Synergistic Effects of Photo-Irradiation and Curcumin-Chitosan/Alginate Nanoparticles on Tumor Necrosis Factor-Alpha-Induced Psoriasis-Like Proliferation of Keratinocytes. *Molecules* **2019**, *24*, 1388, doi:10.3390/molecules24071388.

75.   Kucková, L.; Jomová, K.; Švorcová, A.; Valko, M.; Segľa, P.; Moncoľ, J.; Kožíšek, J. Synthesis, Crystal Structure, Spectroscopic Properties and Potential Biological Activities of Salicylate–Neocuproine Ternary Copper(II) Complexes. *Molecules* **2015**, *20*, 2115–2137, doi:10.3390/molecules20022115.

76.   Al Hageh, C.; Al Assaad, M.; El Masri, Z.; Samaan, N.; El-Sibai, M.; Khalil, C.; Khnayzer, R.S. A long-lived cuprous bis-phenanthroline complex for the photodynamic therapy of cancer. *Dalt. Trans.* **2018**, *47*, 4959–4967, doi:10.1039/C8DT00140E.

77.   Mari, C.; Pierroz, V.; Rubbiani, R.; Patra, M.; Hess, J.; Spingler, B.; Oehninger, L.; Schur, J.; Ott, I.; Salassa, L.; et al. DNA Intercalating Ru II Polypyridyl Complexes as Effective Photosensitizers in Photodynamic Therapy. *Chem. - A Eur. J.* **2014**, *20*, 14421–14436, doi:10.1002/chem.201402796.

78.   Karges, J.; Blacque, O.; Goldner, P.; Chao, H.; Gasser, G. Towards Long Wavelength Absorbing Photodynamic Therapy Photosensitizers via the Extension of a [Ru(bipy) 3] 2+ Core. *Eur. J. Inorg. Chem.* **2019**, *2019*, 3704–3712, doi:10.1002/ejic.201900569.

79.   Romio, K.B.; dos Santos, K.F.; da Silva, R.J.; Pedro, M.F.C.; Kalck, A.S.; da Silva Sousa, M.; Possamai, L.M.; Souto, P.C.S.; Silva, J.R.; de Souza, N.C. Incorporation of triclosan and acridine orange into liposomes for evaluating the susceptibility of Candida albicans. *J. Photochem. Photobiol. B Biol.* **2017**, *173*, 514–521, doi:10.1016/j.jphotobiol.2017.06.034.

80.   Walker, T.; Canales, M.; Noimark, S.; Page, K.; Parkin, I.; Faull, J.; Bhatti, M.; Ciric, L. A Light-Activated Antimicrobial Surface Is Active Against Bacterial, Viral and Fungal Organisms. *Sci. Rep.* **2017**, *7*, 15298, doi:10.1038/s41598-017-15565-5.

81.   de Paula Rodrigues, R.; Tini, I.R.P.; Soares, C.P.; da Silva, N.S. Effect of photodynamic therapy supplemented with quercetin in HEp-2 cells. *Cell Biol. Int.* **2014**, *38*, 716–722, doi:10.1002/cbin.10251.

82.   Ferrario, A.; Luna, M.; Rucker, N.; Wong, S.; Gomer, C.J. Pro-apoptotic and anti-inflammatory properties of the green tea constituent epigallocatechin gallate increase photodynamic therapy responsiveness. *Lasers Surg. Med.* **2011**, *43*, 644–650, doi:10.1002/lsm.21081.

83.   Mun, S.T.; Bae, D.H.; Ahn, W.S. Epigallocatechin gallate with photodynamic therapy enhances anti-tumor effects in vivo and *in vitro*. *Photodiagnosis Photodyn. Ther.* **2014**, *11*, 141–147, doi:10.1016/j.pdpdt.2014.03.003.

84.   Chen, X.; Yi, Z.; Chen, G.; Ma, X.; Su, W.; Deng, Z.; Ma, L.; Tong, Q.; Ran, Y.; Li, X. Carrier-Enhanced Photodynamic Cancer Therapy of Self-Assembled Green Tea Polyphenol-Based Nanoformulations. *ACS Sustain. Chem. Eng.* **2020**, *8*, 16372–16384,

doi:10.1021/acssuschemeng.0c06645.

85. Azar, D.F.; Audi, H.; Farhat, S.; El-Sibai, M.; Abi-Habib, R.J.; Khnayzer, R.S. Phototoxicity of strained Ru(ii) complexes: is it the metal complex or the dissociating ligand? *Dalt. Trans.* **2017**, *46*, 11529–11532, doi:10.1039/C7DT02255G.

86. Hong, E.J.; Choi, D.G.; Shim, M.S. Targeted and effective photodynamic therapy for cancer using functionalized nanomaterials. *Acta Pharm. Sin. B* **2016**, *6*, 297–307, doi:10.1016/j.apsb.2016.01.007.

87. Yavlovich, A.; Smith, B.; Gupta, K.; Blumenthal, R.; Puri, A. Light-sensitive lipid-based nanoparticles for drug delivery: design principles and future considerations for biological applications. *Mol. Membr. Biol.* **2010**, *27*, 364–381, doi:10.3109/09687688.2010.507788.

88. Cheng, X.; Gao, J.; Ding, Y.; Lu, Y.; Wei, Q.; Cui, D.; Fan, J.; Li, X.; Zhu, E.; Lu, Y.; et al. Multi-Functional Liposome: A Powerful Theranostic Nano-Platform Enhancing Photodynamic Therapy. *Adv. Sci.* **2021**, *8*, 2100876, doi:10.1002/advs.202100876.

<div align="right">

4

</div>

<div align="right">

EXPERIMENTAL CONCEPTS

</div>

During the development of this work several methods were employed and, in this chapter, fundamental concepts of these techniques are described such as for experiments in cell culture (the resazurin assay and the detection of reactive oxygen species), the preparation of liposomes and the characterization of the liposomes' size by dynamic light scattering. The use of ultraviolet visible spectroscopy (UV-vis) for the studies of encapsulation efficiency, release profiles and for studies of the effect of radiation on DNA and the MB and AO molecules is another topic present in this chapter as well as the fundamentals behind the study of interaction with lipids in Langmuir monolayers.

4.1 Experiments in cell culture

4.1.1 Evaluation of cell viability

The quantification of cell viability can be done by several techniques which may involve colorimetric/fluorimetric methods with dyes, each one with different principles and methodology. Among them there is resazurin method that is very commonly used in cytotoxicity assays to, indirectly, evaluate cell viability. As resazurin is not toxic to the cells and has no interference with cell disfunction or impairment on the mitochondrial metabolism, it can be used for continuous monitoring of cell viability [1].

Resazurin is a blue redox indicator that can permeate cells and is an indicator of the reducing environment in the cells [2]. As shown in Figure 4.1, resazurin is a blue dye without fluorescence that can be reduced to resorufin, that has a pink colour and is highly fluorescent. Resazurin can act as an electron acceptor in the electron transport chain and, as it presents an oxidation-reduction potential of $+380$ mV, it can be reduced by NADPH, $FADH_2$, $FMNH_2$, NADH and cytochromes with E_0 of 320 mV, 220 mV, 210 mV, 320 mV and 290 to $+80$ mV, respectively. With the acceptance of electrons, the blue non-fluorescent resazurin turns in a reduced state with pink colour and high fluorescence resorufin. As it is transformed from the oxidized form to the reduced one, it can be quantified through the measure of

the absorbance at 570 nm and 600 nm or fluorescence measure at an excitation wavelength at $530 - 560$ nm and emission wavelength at 590 nm [1].
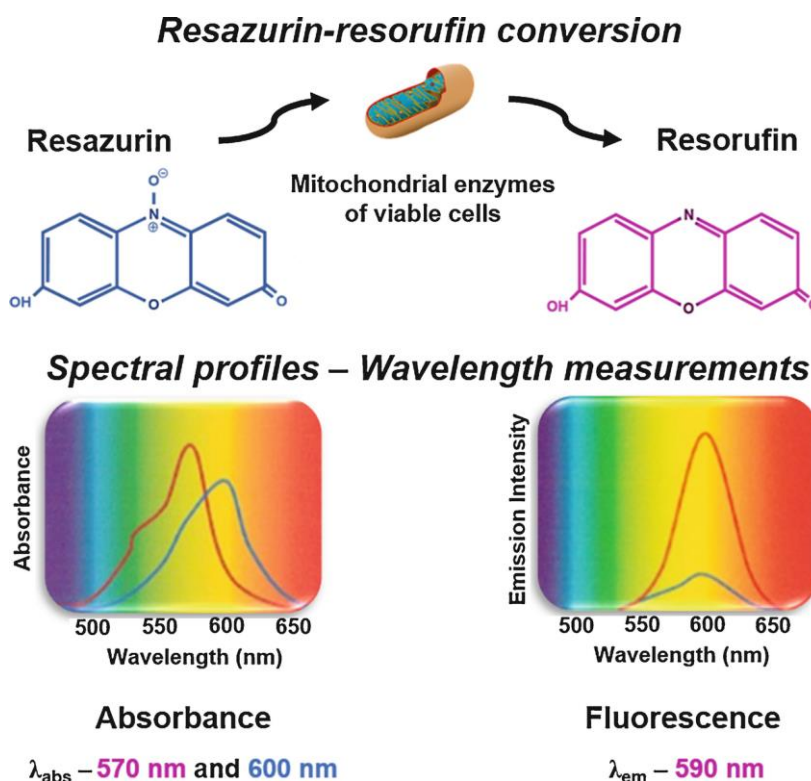
Figure 4.1: Scheme of the principle of the resazurin method, showing the reduction of resazurin (non-fluorescent, with blue colour) to resorufin (highly fluorescent, with pink colour) and the possible methods of quantification that are absorbance or fluorescence. Reproduced from reference [3]. Copyright 2020, Quantum Dots: Applications in Biology.

4.1.2 Detection of Reactive oxygen species (ROS)

Dihydroethidium is mainly known as a superoxide indicator that can permeate cells and be oxidized by $O_2^{\bullet-}$ to 2-hydroxyethidium (2-OH-E$^+$) and present red fluorescence with excitation wavelength at $500 - 530$ nm and emission wavelength at $590 - 620$ nm (Figure 4.2). However, through non-specific redox reactions such as by H_2O_2 and $^{\bullet}OH$ can be transformed to ethidium (E$^+$) with similar fluorescence spectrum ($\lambda_{ex} = 520$ nm and $\lambda_{em} = 610$ nm) [4–6].
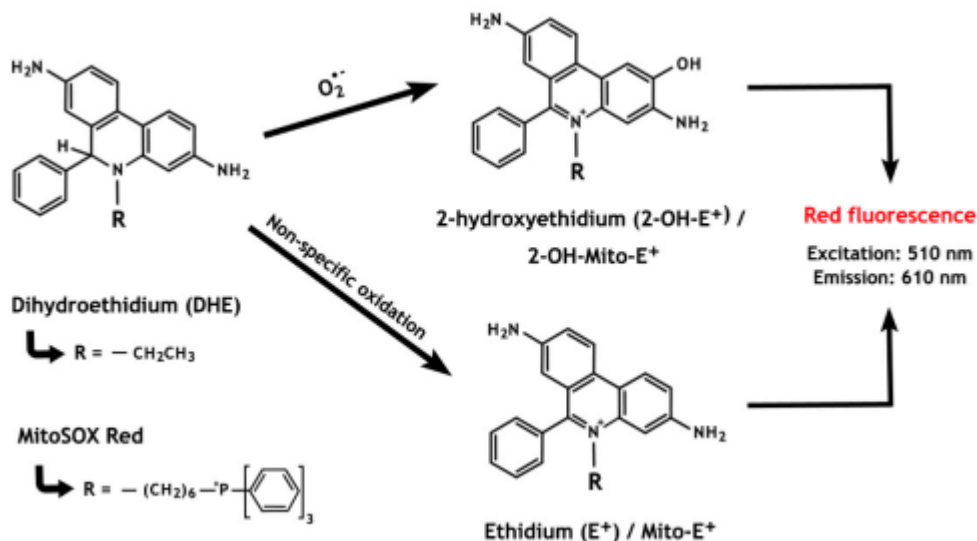
Figure 4.2: Scheme of the oxidation paths taken by dihydroethidium (DHE) and the resultant products 2-hydrox-yethidium (2-OH-E$^+$) and ethidium (E$^+$) that present red fluorescence. Reproduced from reference [4]. Copyright 2019, Antioxidants.

The assays using DHE can be done in microplates, using a microplate reader to measure the fluorescence or, in alternative, the fluorescence can be visualized in a fluorescence microscope. In our studies, the fluorescence microscopy was employed to identify if there was ROS formation induced by the photosensitizers' irradiation.
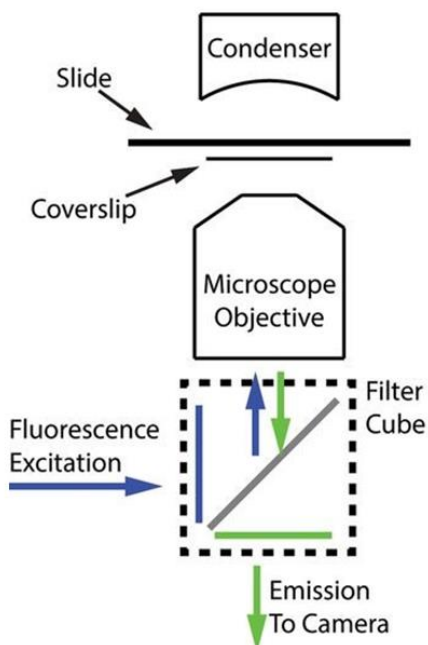
Figure 4.3: Representation of the principle of fluorescence microscopy technique showing, in particular, an inverted microscope. Adapted from reference [7]. Copyright 2016, Molecular Biology of the Cell.

Fluorescence microscopy is an important technique that allow the study of cell physiology in fixed and living cells through the detection of the fluorescence emitted by compounds with fluorescence properties usually designated as fluorescent probes. The principle of fluorescence lies on the absorption of light energy (photon) by a fluorescent probe at a specific wavelength that push a valence electron from the ground state to the excited state. This is a fast process that is followed by the return of the electron to the ground state with the emission of part of the absorbed energy as another photon with less energy. Therefore, the light emitted from the probe present longer wavelength than the one absorbed, phenomenon called Stokes shift [8,9].

The light source of fluorescence microscope is usually a mercury-vapor lamp and, as it emits light of the entire visible spectrum, optical filters are used for the separation of the light. As shown in Figure 4.3, a filter cube is used in many microscopes and placed in the excitation and emission light path, with a dichroic mirror at 45º that can separate the excitation light from the emitted light. Therefore, the excitation light provided from the source is directed to the sample and then to the detector [9].

4.2 Preparation of Liposomes

Liposomes can be prepared by several methods such as by the Bangham method, also known as thin-film hydration method, the injection method, and others [10,11]. Depending on the method the resulting vesicles can present different characteristics as shown in Figure 4.4 and can be termed as small unilamellar vesicles (SUVs), large unilamellar vesicles (LUVs), giant unilamellar vesicles (GUVs), multilamellar vesicles (MLVs) and multivesicular vesicles (MVVs) regarding their size and lamellarity [12].
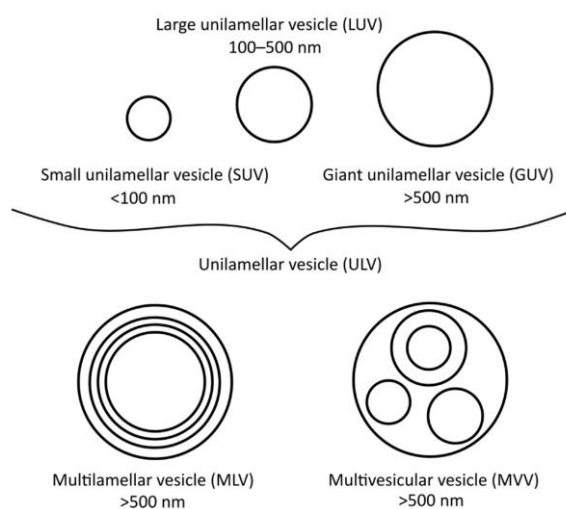
Figure 4.4: Different types of vesicles and their sizes. Reproduced from reference [12]. Copyright 2021, International Journal of Molecular Sciences.

For the thin-film hydration method the lipids are dissolved in organic solvent such as chloroform or a mixture of chloroform-methanol, depending on the solubility of the lipid, followed by the evaporation of the organic solvent to form a thin film on the walls of the flask or tube. Then the lipid film is hydrated with water or buffer solution above the phase-transition temperature (T_c), this way the lipid bilayers become fluid. With agitation the lipid bilayers detach and tend to fold on itself forming a vesicle with aqueous interior. To obtain small particles the downsizing is required which can be taken by an input of sonic energy such as sonication or by mechanical energy such as extrusion [12,13]. The methodology used in this work was the thin-film hydration method followed by extrusion as shown in Figure 4.5.
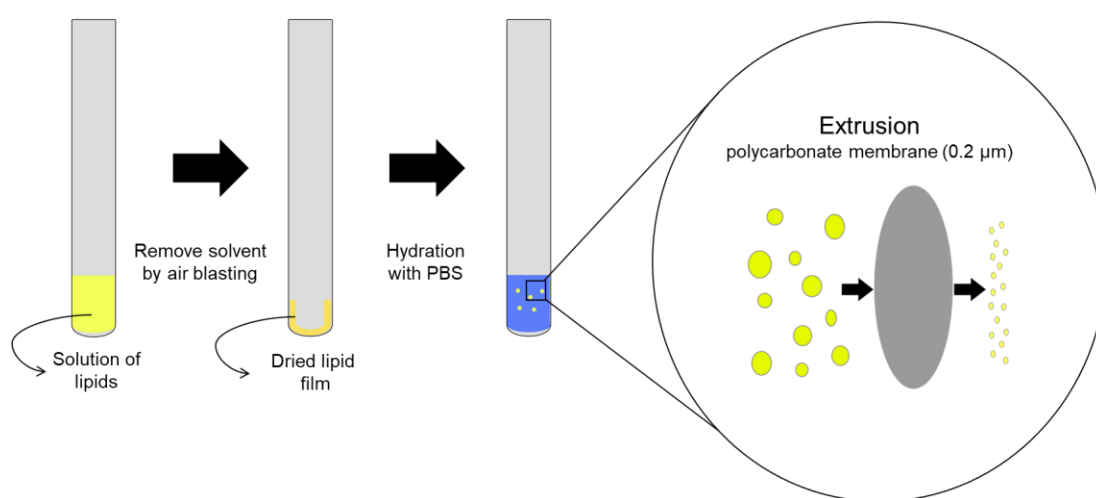
Figure 4.5: Representation of liposomes preparation by the thin-film hydration method followed by extrusion for the downsizing of the particles.

Extrusion technique is a valuable method to achieve formulations with homogeneous size distribution and it is also very reproducible. In the extrusion the pore size of the membrane is selected, and a number of cycles must be performed to form particles with homogeneous population. There are many devices that can be used for the extrusion of liposomes suspensions, devices that support larger volumes e.g., Avestin Liposo-Fast™-50 (capacity 5 – 50 mL) but also devices for small volume e.g., Avanti mini extruder that can be coupled with gas-tight syringes of 250 µL or 1000 µL [14]. For the hand-extruder (Figure 4.6) the cycles are obtained through the passage of the lipid suspension from one side to another and a minimum of 10 times is recommended [15].
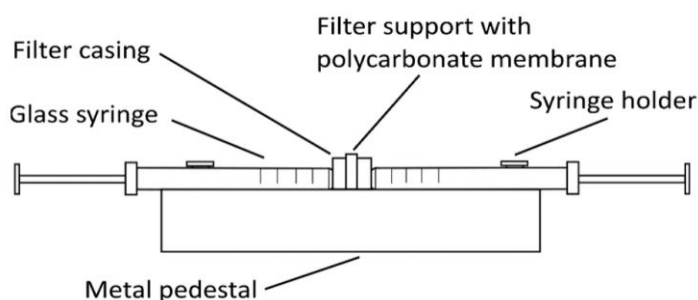
Figure 4.6: Representation of a manual glass syringe extruder. The membrane is placed in the supports, inside the extruder casing and have one syringe on each side, one filled with the lipid suspension and the other empty. The extrusion is taken by the multiple passages of the lipid suspension to the other respective empty syringe through the polycarbonate membrane. Reproduced from reference [12]. Copyright 2021, International Journal of Molecular Sciences.

4.3 Characterization of liposomes

4.3.1 Dynamic Light Scattering

The nanoparticles characterization such as by their size is important to comprehend the effect that the composition can entail on the particle since different compositions and the addition of molecules can directly affect intermolecular forces and, thereby, interfere in the permeability and fluidity of the lipid bilayers [12]. Dynamic Light Scattering (DLS) is a fast technique that allow the measurement of the particles' hydrodynamic diameter. As shown in Figure 4.7, in DLS the sample is placed in a polystyrene cuvette, is subjected to a monochromatic beam and, depending on the sample, the amount of light scattered is detected, which gives information to correlate with the size of the particles [12,16,17].
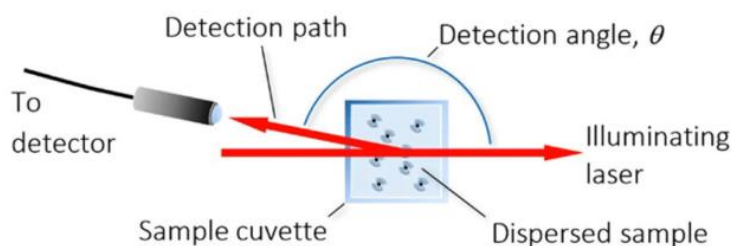
Figure 4.7: Scheme of a dynamic light scattering equipment. Adapted from reference [16]. Copyright 2018, Frontiers in Chemistry.

The incidence of a monochromatic beam on a sample containing macromolecules result in light scattering in all directions regarding to the size and shape of the macromolecules. In a dispersion, particles are not static and there are fluctuations on the intensity due to the Brownian motion of the particles,

which enable the determination of the diffusion coefficient (D). As DLS measurements are based on the detection of the intensity of light scattered during a period of time, large particles present slower diffusion while small particles present faster diffusion (Figure 4.8 – A) which reflects in the auto-correlated intensity and, therefore, on the decay of correlation (Figure 4.8 – B). A faster decay is obtained for small particles (faster diffusion) and a delayed decay for large particles (slower diffusion). Through the correlation function, the diffusion coefficient is obtained [17,18].

The diffusion coefficient can be correlated to the hydrodynamic radius (R_h) of a spherical particles through the Stokes-Einstein equation (Equation 4.1) where k_b is the Boltzmann constant (1.380 x 10^{-23} kg.m².s^{-2}.K^{-1}), T is the absolute temperature and η is the viscosity of the medium [17].

$$\text{Equation 4.1} \qquad D = \frac{k_b.T}{6\pi\eta R_h}$$
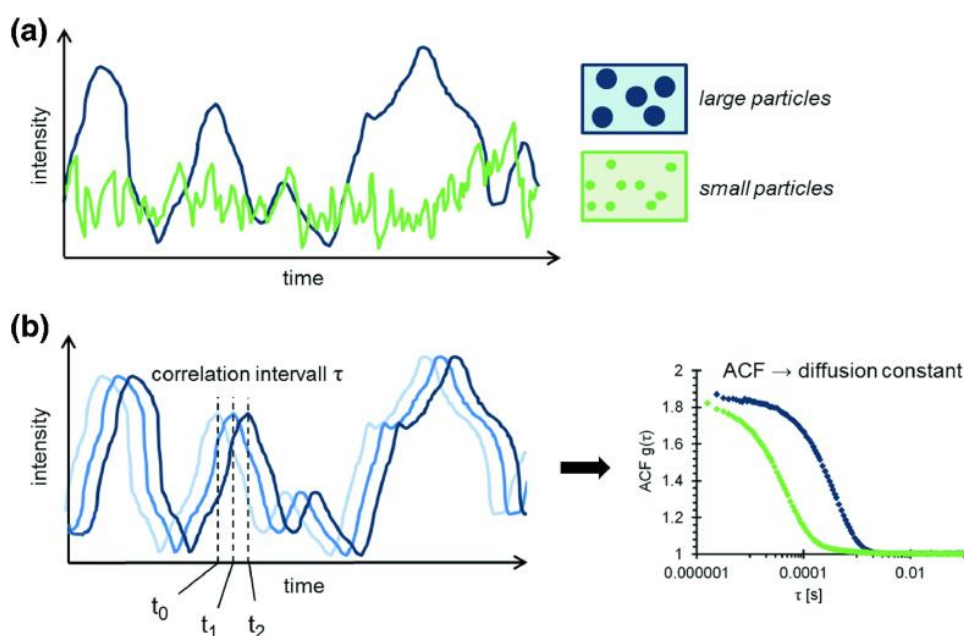
Figure 4.8: Determination of the particle size considering the Brownian motion. A) Intensity of light scattering in relation to time, B) Scheme of the autocorrelation and the autocorrelation function obtained for small particles (green) and large particles (blue). Reproduced from reference [18]. Copyright 2019, Radiation in Bioanalysis: Spectroscopic Techniques and Theoretical Methods.

4.4 Ultraviolet visible (UV-vis)

Ultraviolet visible (UV-vis) is a versatile technique that can be used for several purposes such as for quantification and characterization through measurements of the absorbance or transmittance of the light. The range of UV-vis is from 200 – 800 nm, above 800 nm start the infrared and below the 200 nm is the vacuum ultraviolet [19,20].

In a UV-vis spectrophotometer the light is directed to the sample and the sample absorb the light, which results in changes on the electrons distribution, leading the migration from the ground state to an excited state. The light that passes through the sample and the intensity of the transmitted light is acquired by the detector (Figure 4.9).

Equation 4.2 shows the relation between the incident light intensity (I_0), the transmitted light (I) and the light absorbance (A). Whereas the Beer-Lambert law (Equation 4.3) determines that the absorbance can be proportional to the path length of the cuvette (b), concentration of the sample (c) and molar absorption coefficient (ε) [19,20]. In organic compounds the absorption is mainly due to two transitions: π–π^* and n–π^* related to unsaturation bonds and heteroatom [20].
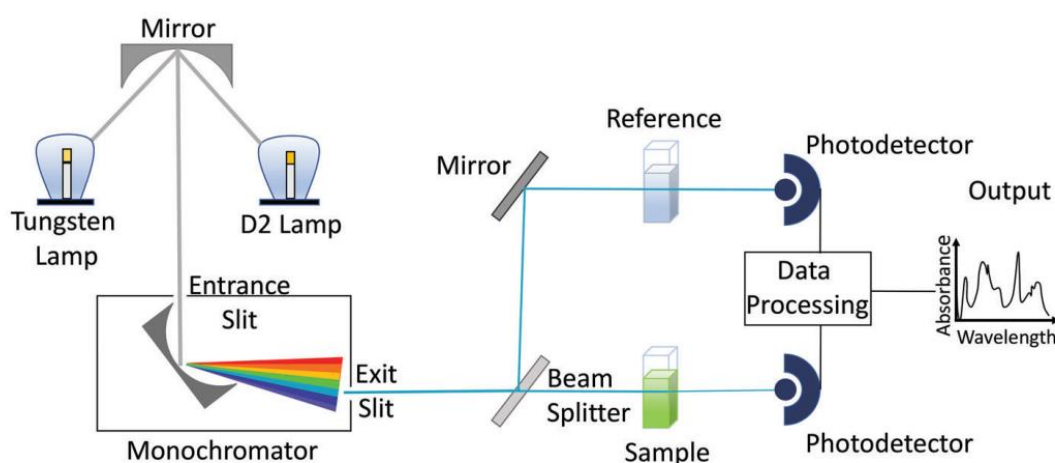
Figure 4.9: Scheme of a UV-vis spectrophotometer with double beam. Reproduced from reference [19]. Copyright 2018, The Canadian Journal of Chemical Engineering.

$$\text{Equation 4.2} \qquad A = \log_{10}\left(\frac{I_0}{I}\right)$$

$$\text{Equation 4.3} \qquad A = \varepsilon.b.c$$

Changes in the structure can lead to shifts in the absorption spectra such as in the wavelength namely bathochromic and hypsochromic for longer and shorter wavelengths, respectively. Modification in the absorption intensity can also occur, called hyperchromic and hypochromic for higher and lower absorption, respectively.

4.5 Study of lipid interactions

4.5.1 Langmuir

Langmuir monolayers are often used as a biomimetic system to simulate the cellular membrane which can be applied for the drug-lipid interaction analysis. The lipid solution is prepared in an organic solvent and is spread with a microsyringe over the surface of the subphase that can be water or a buffer. Eventually the solvent evaporates, and the lipids are oriented in a monolayer in a way to minimize the contact of the non-polar portion while enhance the contact between the subphase and their polar group (Figure 4.10) [21].
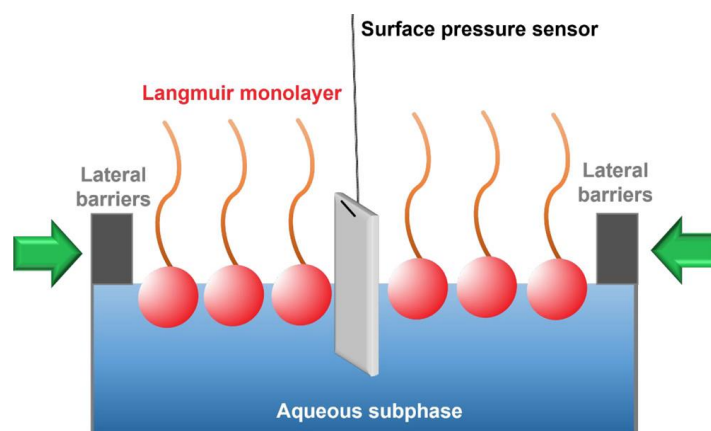
Figure 4.10: Representation of a Langmuir monolayer and the Langmuir trough with barriers to compress the monolayer and a surface pressure sensor. Reproduced from reference [22]. Copyright 2022, Chemical Reviews.

Via the surface tension measurement is possible to study the system energetics. The surface tension is measured with a Wilhelmy plate that intercept the air-water surface and is coupled to a balance. The surface tension (γ) is calculated through the use of the Wilhelmy equation (Equation 4.4), where F is the force of the surface taking the plate down, L is the perimeter of contact and θ is the contact angle between the subphase and the Wilhelmy plate. The forces generated from the intermolecular interactions at the interface tend to give a stability to the interface by reducing the surface tension and, therefore, reducing the surface Gibbs energy and then molecules from the subphase act with less intensity on the interfacial molecules resulting in a surface pressure. The surface pressure (π) can be calculated, according to Equation 4.5, by the reduction of the surface tension without the lipid, where γ_0 is the surface tension of the pure liquid or the subphase and γ is the surface tension of the subphase with the lipid [22].

Equation 4.4 $\qquad \gamma = \frac{F}{L.cos\theta}$

Equation 4.5 $\qquad \pi = \gamma_0 - \gamma$

Through the surface pressure – area is possible to study the interactions between lipid – lipid or drug – lipid. To obtain the isotherm two lateral barriers compress the monolayer at a constant rate and, as the compression increases, the surface area is reduced demanding a reorganization of the molecules. This reorganization makes the monolayer pass through different phase states as shown in Figure 4.11 [21]. The compression results in a first order transition, a liquid-like state called liquid expanded (LE) followed by the coexistence of LE with a liquid condensed state (LC) in the case of phospholipids. In the LC phase the lipids are well organized and present all-trans conformation [23].
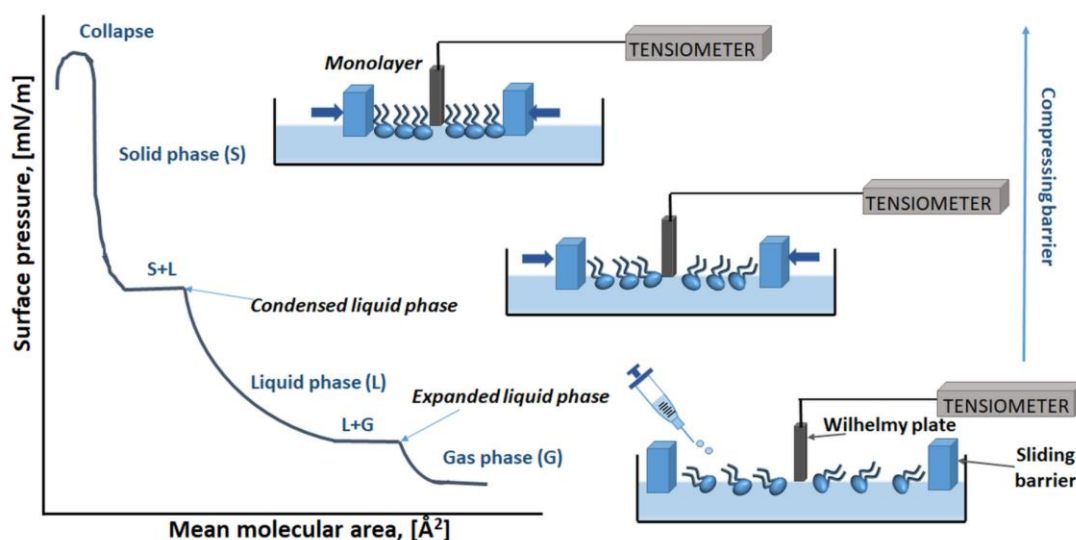
Figure 4.11: Scheme of the surface pressure – area isotherm of a Langmuir monolayer along the transition of phase states. Reproduced from reference [21]. Copyright 2021, Membranes.

4.5.2 PM-IRRAS

The polarization modulation infrared reflection (PM-IRRAS) corresponds to an infrared reflection absorption spectroscopy where the polarization from the IR beam is modulated. In PM-IRRAS there is an incident IR beam with polarization "s" and "p" for perpendicular and parallel, respectively, which results in reflection-absorption spectrum of samples on metal/air interface with practically no absorption of vapour of water or CO_2 present in the atmosphere [24]. Figure 4.12 shows the representation of PM-IRRAS in Langmuir monolayers. PM-IRRAS is a useful tool for studies at the molecular level in several

types of assemblies such as for Langmuir monolayers to comprehend the effect on lipids organization and hydration of the lipid headgroups [22,24].

The signal obtained is a portion of the reflected light and the differential reflectivity ($\Delta R/R$) is determined according to Equation 4.6, where R_p is the reflectivity of the polarization "p" and R_s is the reflectivity of the polarization "s" [22].

$$\text{Equation 4.6} \qquad \frac{\Delta R}{R} = \frac{R_p - R_s}{R_p + R_s}$$

The bands in PM-IRRAS spectra can be positive bands in relation to the baseline when the transition dipole moment is parallel to the interface while negative bands are related to transition dipole moment in the perpendicular [22].
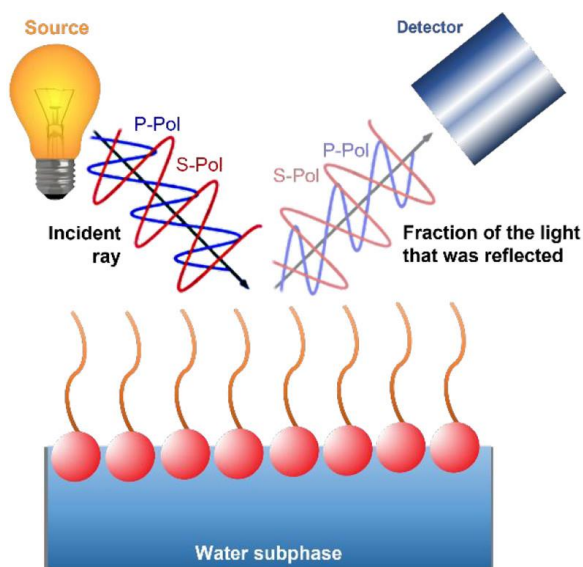
Figure 4.12: Representation of PM-IRRAS in Langmuir monolayers. Adapted from reference [22]. Copyright 2022, Chemical Reviews.

4.6 Irradiation Studies

Irradiation studies on cells were based on an UVC lamp with peak at 254 nm (PHILIPS TUV PL-S 9W/2P Hg) and a LED lamp for the other wavelengths, with emission of blue light (peak at 457 nm), yellow light (peak at 583 nm) or red light (peak at 640 nm) with irradiance values around 55 W/m², 45 W/m² and 25 W/m², respectively. The system with the lamps for the irradiation of the plates is ex-emplified in Figure 4.13 with the blue and red light irradiation and, considering the application in cells and the different irradiances emitted from the light sources, a dose of 2.5 J/cm² was standardized.

Figure 4.13: Photo of the system used for the cells irradiation exampling the blue light and the red light emissions.

For the irradiation of the molecules with the DNA an UVC lamp with peak at 254 nm (PHILIPS TUV PL-S 5W/2P Hg) was used and an equal LED lamp, as that used for the cells, was used for the emission of blue and red light showing, in these conditions, irradiance values of 9.5 W/m², 38.9 W/m² and 24.3 W/m² for UVC, blue and red light, respectively.

References

1. Rampersad, S.N. Multiple Applications of Alamar Blue as an Indicator of Metabolic Function and Cellular Health in Cell Viability Bioassays. *Sensors* **2012**, *12*, 12347–12360, doi:10.3390/s120912347.

2. Balbaied, T.; Moore, E. Resazurin-Based Assay for Quantifying Living Cells during Alkaline Phosphatase (ALP) Release. *Appl. Sci.* **2020**, *10*, 3840, doi:10.3390/app10113840.

3. Pereira, M.I.A.; Monteiro, C.A.P.; de Oliveira, W.F.; Santos, B.S.; Fontes, A.; Cabral Filho, P.E. Resazurin-Based Assay to Evaluate Cell Viability After Quantum Dot Interaction. In *Quantum Dots: Applications in Biology*; Fontes, A., Santos, B.S., Eds.; Springer US: New York, NY, 2020; pp. 213–221 ISBN 978-1-0716-0463-2.

4. Villaverde, A.I.S.B.; Netherton, J.; Baker, M.A. From Past to Present: The Link Between Reactive Oxygen Species in Sperm and Male Infertility. *Antioxidants* **2019**, *8*, 616, doi:10.3390/antiox8120616.

5. Wang, Q.; Zou, M.-H. Measurement of Reactive Oxygen Species (ROS) and Mitochondrial ROS

in AMPK Knockout Mice Blood Vessels. *Methods Mol. Biol.* **2018**, *1732*, 507–517, doi:10.1007/978-1-4939-7598-3_32.

6. Griendling, K.K.; Touyz, R.M.; Zweier, J.L.; Dikalov, S.; Chilian, W.; Chen, Y.-R.; Harrison, D.G.; Bhatnagar, A. Measurement of Reactive Oxygen Species, Reactive Nitrogen Species, and Redox-Dependent Signaling in the Cardiovascular System. *Circ. Res.* **2016**, *119*, e39–e75, doi:10.1161/RES.0000000000000110.

7. Thorn, K. A quick guide to light microscopy in cell biology. *Mol. Biol. Cell* **2016**, *27*, 219–222, doi:10.1091/mbc.e15-02-0088.

8. Ishikawa-Ankerhold, H.C.; Ankerhold, R.; Drummen, G.P.C. Advanced Fluorescence Microscopy Techniques—FRAP, FLIP, FLAP, FRET and FLIM. *Molecules* **2012**, *17*, 4047–4132, doi:10.3390/molecules17044047.

9. Sanderson, M.J.; Smith, I.; Parker, I.; Bootman, M.D. Fluorescence Microscopy. *Cold Spring Harb. Protoc.* **2014**, *2014*, pdb.top071795, doi:10.1101/pdb.top071795.

10. Akbarzadeh, A.; Rezaei-sadabady, R.; Davaran, S.; Joo, S.W.; Zarghami, N.; Hanifehpour, Y.; Samiei, M.; Kouhi, M.; Nejati-Koshki, K. Liposome: classification, preparation, and applications. *Nanoscale Res. Lett.* **2013**, *8*, 102, doi:10.1002/asia.201500957.

11. Andra, V.V.S.N.L.; Pammi, S.V.N.; Bhatraju, L.V.K.P.; Ruddaraju, L.K. A Comprehensive Review on Novel Liposomal Methodologies, Commercial Formulations, Clinical Trials and Patents. *Bionanoscience* **2022**, doi:10.1007/s12668-022-00941-x.

12. Šturm, L.; Poklar Ulrih, N. Basic Methods for Preparation of Liposomes and Studying Their Interactions with Different Compounds, with the Emphasis on Polyphenols. *Int. J. Mol. Sci.* **2021**, *22*, 6547, doi:10.3390/ijms22126547.

13. Wagner, A.; Vorauer-Uhl, K. Liposome Technology for Industrial Purposes. *J. Drug Deliv.* **2011**, *2011*, 591325, doi:10.1155/2011/591325.

14. Ong, S.; Chitneni, M.; Lee, K.; Ming, L.; Yuen, K. Evaluation of Extrusion Technique for Nanosizing Liposomes. *Pharmaceutics* **2016**, *8*, 36, doi:10.3390/pharmaceutics8040036.

15. Ahumada, M.; Calderón, C.; León, L.; Lissi, E. Rate of solute incorporation to liposomes evaluated from encapsulated enzymes activities. *Biophys. Rev.* **2014**, *6*, 161–167, doi:10.1007/s12551-013-0136-9.

16. Malm, A. V.; Corbett, J.C.W. Improved Dynamic Light Scattering using an adaptive and statistically driven time resolved treatment of correlation data. *Sci. Rep.* **2019**, *9*, 13519, doi:10.1038/s41598-019-50077-4.

17. Carvalho, P.M.; Felício, M.R.; Santos, N.C.; Gonçalves, S.; Domingues, M.M. Application of Light Scattering Techniques to Nanoparticle Characterization and Development. *Front. Chem.* **2018**, *6*, 237, doi:10.3389/fchem.2018.00237.

18. Falke, S.; Betzel, C. Dynamic Light Scattering (DLS). In *Radiation in Bioanalysis: Spectroscopic Techniques and Theoretical Methods*; Pereira, A.S., Tavares, P., Limão-Vieira,

P., Eds.; Springer International Publishing: Cham, 2019; pp. 173–193 ISBN 978-3-030-28247-9.

19. Rocha, F.S.; Gomes, A.J.; Lunardi, C.N.; Kaliaguine, S.; Patience, G.S. Experimental methods in chemical engineering: Ultraviolet visible spectroscopy-UV-Vis. *Can. J. Chem. Eng.* **2018**, *96*, 2512–2517, doi:10.1002/cjce.23344.

20. Antosiewicz, J.M.; Shugar, D. UV–Vis spectroscopy of tyrosine side-groups in studies of protein structure. Part 1: basic principles and properties of tyrosine chromophore. *Biophys. Rev.* **2016**, *8*, 151–161, doi:10.1007/s12551-016-0198-6.

21. Rojewska, M.; Smułek, W.; Kaczorek, E.; Prochaska, K. Langmuir Monolayer Techniques for the Investigation of Model Bacterial Membranes and Antibiotic Biodegradation Mechanisms. *Membranes (Basel).* **2021**, *11*, 707, doi:10.3390/membranes11090707.

22. Oliveira, O.N.; Caseli, L.; Ariga, K. The Past and the Future of Langmuir and Langmuir–Blodgett Films. *Chem. Rev.* **2022**, 122, 6459-6513, doi:10.1021/acs.chemrev.1c00754.

23. Blume, A. Lipids at the air–water interface. *ChemTexts* **2018**, *4*, 3, doi:10.1007/s40828-018-0058-z.

24. Brand, I. Application of Polarization Modulation Infrared Reflection Absorption Spectrosocpy Under Electrochemical Control for Structural Studies of Biomimetic Assemblies. *Zeitschrift für Phys. Chemie* **2016**, *230*, 133–183, doi:10.1515/zpch-2014-0657.

<div style="text-align: right">

5

</div>

DNA-INTERCALATING AGENTS: A STUDY OF THE PHOTOSENSITIZING EFFECT [1]

Abstract: Photodynamic therapy is a minimally invasive treatment of several diseases, including some types of cancer, and it is based on photosensitizer molecules which in presence of oxygen and light lead to the formation of reactive oxygen species (ROS) and consequently cell death. The selection of the photosensitizer molecule is important for the therapy efficiency, therefore, many molecules such as dyes, natural products and metallic complexes have been investigated regarding the photosensitizing potential. In this work, the phototoxic potential of some DNA-intercalating agents: the dyes methylene blue (MB), acridine orange (AO) and gentian violet (GV); the natural products curcumin (CUR), quercetin (QT) and epigallocatechin gallate (EGCG); and the chelating compounds neocuproine (NEO), 1,10-phenanthroline (PHE) and 2,2'-bipyridyl (BIPY) were analyzed. The cytotoxicity of these chemicals was tested *in vitro* in non-cancer keratinocytes (HaCaT) and cancer keratinocytes (MET1 SCC) cell lines. The phototoxicity assay and the detection of intracellular ROS were performed in MET1 SCC cell line. Results revealed that the IC_{50} values in MET1 SCC cells for the dyes and curcumin were very low (<30 µM) while the ones for the natural products QT and EGCG and the chelating agents BIPY and PHE were higher than100µM. The molecules with the most affected IC_{50} by irradiation were the MB and AO dyes when submitted to a 640 nm and 457 nm light sources, respectively. ROS detection was more evident for cells treated with AO at low concentrations. In studies with melanoma cell line (WM983b), the cells were more resistant to the MB and AO and presented slightly higher IC_{50}, the same behavior was observed in the phototoxicity assays. This study reveals that many molecules can act as photosensitizers, but effect depends on the cell line, the concentration of the chemical and the irradiation dose. Finally, has been demonstrated a significant photosensitizing activity of acridine orange at low concentrations and moderate dose of light.

5.1 Introduction

Photodynamic therapy (PDT) has been widely explored over the past decades mainly for the treatment of diseases such as skin disorders and some cancer types [1,2]. PDT is a minimally invasive therapy with local action [3] and its efficacy depends on the presence of photosensitizer (PS) molecules, of oxygen and of light. The combination of these elements has an important role for the action of PDT, which relies on the formation of reactive oxygen species (ROS) that can be taken by two types of PDT [4]. In the type I, the activated photosensitizer acts on substrates such as the biological molecules that react with oxygen generating ROS. When the photosensitizer can transfer energy to the molecular oxygen ($^3O_2$) generating the singlet oxygen ($^1O_2$), the PDT is considered type II. In both paths there is ROS generation that have a high oxidizing power and therefore can lead to the cell death through the damage in biomolecules [5]. The DNA is one of the biomolecules that can be subjected to damage and is the main target for anticancer drugs [6]. However, due to the reactive species short lifetime they act essentially at the local where were created, which gives PDT the advantage of local action [7].

The first generation of photosensitizers were the ones of the porphyrin type [8,9]. In fact, derivative molecules from hematoporphyrin have been used since the middle of the 20th century. PDT using porphyrins as photosensitizers showed to be efficient in cancer therapy and a promising sensitizer to deal with microbial infections [2,5]. However, the wavelength able to activate porphyrins photosensitizers is usually too short, which hinders the light penetration in the tissue. Moreover, after activated the half-life is too long which could cause a severe phototoxicity [9]. A second generation of photosensitizers has been developed through alterations in the porphyrin core or in peripheral sites to improve the photosensitivity. Phthalocyanines are examples of this second generation derived from porphyrins [9]. However, there are more than 400 molecules with photosensitizing potential. Among these molecules there are dyes, natural products and many others chemical substances [5,8].

Of natural or synthetic origin, the dyes are substances able to provide color and are usually water-soluble. There are several applications for these molecules such as textile, foods, cosmetics and medicine [10]. In 1900, Oscar Raab left the protozoan *Paramecium caudatum* in contact with the dye acridine orange and observed the toxic effect after sunlight exposure [11]. Nowadays, phthalocyanines are synthetic dyes extensively investigated for use in many types of cancer therapies, namely, ovarian carcinoma, melanoma, liver carcinoma and lung carcinoma [12–14]. Methylene blue is another synthetic dye that has gained the interest in studies in PDT as antimicrobial and for the cancer treatment as well [8].

Since the antiquity, natural products have been employed to treat several diseases through the use of natural herbs or extracts [15]. There are several classes of molecules with PS properties such as anthraquinones, curcuminoids, xanthenoids, etc. Hypericin for example is a natural molecule that belongs to the class of anthraquinones and is the first non-porphyrin-like molecule that has been recently introduced in clinical trials [16]. Curcumin application in photodynamic therapy of cancer has also been

widely investigated through the use of nanocarriers [17–19]. De Matos et al. [20] studied a curcumin nanoemulsion in two different cell lines derived from uterus carcinoma and observed a phototoxicity of 93.2% for Ca Ski and 83.16% for SiHa cells. There are also studies with the flavonoid quercetin that combined with PDT reduced cell viability of cervical adenocarcinoma and breast carcinoma cells [21,22]. Furthermore, some complexes have also been investigated such as the chelators 2,2'-bipyridyl and 1,10-phenanthroline that were studied in metallic complexes and presented toxicity in cervical adenocarcinoma using the HeLa cells [23].

Therefore, as many classes of molecules can act as photosensitizers, in this work we analyzed the phototoxic potential of some DNA-intercalating agents: the dyes methylene blue, acridine orange and gentian violet; the natural products curcumin, quercetin and epigallocatechin gallate; and the chelating compounds neocuproine, 1,10-phenanthroline and 2,2'-bipyridyl with respect to their use in PDT. Results revealed that MB and AO molecules present a significant phototoxic potential in MET1 SCC and WM983b cell lines, which is an unprecedent study for these cell lines.

5.2 Materials and Methods

5.2.1 Materials

Dulbecco's Modified Eagle Medium and fetal bovine serum were obtained from Biowest. Penicillin-Streptomycin and TrypLE™ Express Enzyme 1 X were purchased from Gibco. Resazurin was obtained from Alfa Aesar. Dihydroethidium and Hoechst 33342 were obtained from Biotium and Molecular Probes, respectively. Methylene blue, acridine orange, gentian violet, curcumin, quercetin, EGCG, 1,10-phenanthroline, neocuproine and 2,2'-bipyridyl were obtained from Sigma Aldrich.

5.2.2 Cells culture

MET1 SCC cell line (human squamous cell carcinoma) was obtained from Ximbio; HaCaT (immortalized human keratinocytes cell line) was obtained from Addexbio and WM983b (human metastatic melanoma cell line) was obtained from Rockland. Cells were maintained in Dulbecco's Modified Eagle Medium (DMEM) supplemented with 10% fetal bovine serum (FBS) for MET1 SCC and HaCaT and 5% for WM983b cells, and antibiotics (penicillin 100 U/mL and streptomycin 100 µg/mL). Cells were cultivated in an incubator (Sanyo MCO-19AIC-UV) at 37 °C in a 5% of CO_2 humidified atmosphere. To release the cells from the flasks, the medium was removed, and cells were washed with phosphate-buffered saline (PBS) 1X. Then the cells were harvested with TrypLE™ Express Enzyme 1X.

In this work, cytotoxicity studies were carried out in MET1 SCC cells and HaCaT cells. In the squamous carcinoma cells phototoxicity and detection of ROS studies were also performed. Lastly,

WM983b cells were used to evaluate the cytotoxicity and phototoxicity of the most promising compounds.

5.2.3 Cytotoxicity

96-well plates were seeded with a density of 20,000 cells/cm² of HaCaT or MET1 SCC cells and were incubated overnight. Then, cells were treated with different samples: MB, AO, GV, QT, CUR, EGCG, PHE, NEO and BIPY. For the cytotoxicity study of WM983b cells, plates were seeded at a cell density of 40,000 cells/cm² and cells were treated only with MB and AO. Samples' stock solutions were prepared in DMSO and were diluted in culture medium using a range of concentration starting from 1.25 µM to 320 µM of each chemical (in quadruplicate). The medium was aspirated from the wells and replaced by the samples diluted in medium. Cells treated with DMSO 0.2% were used as solvent control (SC) while for cells only with new replaced medium and cells with 10% of DMSO diluted in medium were used as negative (NC) and positive control (PC), respectively. The plates were incubated for 24 hours and 48 hours followed by the evaluation of cell viability using a colorimetric assay. To evaluate cell viability, the medium containing samples was removed, and cells were washed with PBS. Next, resazurin solution diluted in DMEM at 0.02 mg/mL was added and cells were incubated for 3 hours. Resazurin was also added to wells without cells, which were used as reference. The absorbance was measured in a microplate reader (ELX800UV, Biotek Instruments) using the wavelengths of 570 nm and 600 nm. The corrected absorbance is proportional to cell viability. The propagation of uncertainties were used to calculate the combined standard uncertainty.

5.2.4 Phototoxicity of MET1 SCC cells

For the phototoxicity studies, 96-well plates were seeded with MET1 SCC cells at a density of 20,000 cells/cm², incubated overnight and treated with different samples MB, AO, GV, QT, CUR, EGCG, PHE, NEO and BIPY. For the phototoxicity study using WM983b cells, plates were seeded at a cell density of 40,000 cells/cm² and cells were treated only with MB and AO. Samples' stock solutions were prepared in DMSO and diluted in culture medium using a range of concentration starting from 1.25 µM to 40 µM of each chemical (in sextuplicate). The medium was aspirated from the 96-well plate and replaced by the samples diluted in medium. Cells treated with DMSO 0.2% were used as SC while for cells only with new replaced medium and cells with 10% of DMSO diluted in medium were used as NC and PC, respectively. The plates were incubated for 24 hours then medium containing the chemicals was aspirated and washed with PBS 1X with calcium and magnesium. Then, DMEM without phenol red was added and the plates were submitted to a dose of 2.5 J/cm² of irradiation emitted by different wavelength light sources (254 nm lamp from Phillips and a tri-color LED lamp with intensity peaks at

457 nm [blue light], 583 nm [yellow light] and 640 nm [red light]). Plates were incubated for more 24 hours and lastly resazurin assay was performed as previously described in section 5.2.3.

5.2.5 Intracellular ROS production

24-well plates were prepared with MET1 SCC cells at a density of 20,000 cells/cm². After 24 hours, cells were treated with MB and AO that were diluted in culture medium at low concentrations 1.25 µM, 2.5 µM and 5.0 µM of each dye. The medium was aspirated from the plate and replaced by the samples diluted in medium. Plates were incubated for 24 hours and, after treatment with the dyes, cells were washed with medium, DMEM without phenol red was added and plates were submitted to 2.5 J/cm² irradiation from a red light at 640 nm for MB and 457 nm blue light for AO. Dihydroethidium (DHE) was used to evaluate ROS production. For this assay, the medium was removed after irradiation, and 20 µM of DHE diluted in medium was added. The plate was incubated for 20 minutes, then washed with medium and incubated 20 minutes with Hoechst 33342 at 5 µg/mL, that was used to stain the cells' nucleus. After removing the excess of the dyes, culture medium was added, and the cells were immediately observed by an epi-fluorescence microscope Nikon Ti-S. Experiments were performed in quadruplicate. Images were analyzed in the ImageJ software and the integrated density of red fluorescence was measured.

5.3 Results and Discussion

5.3.1 Cytotoxicity in HaCaT and MET1 SCC cells

To study the cell viability in the presence of different DNA-intercalating agents, HaCaT and MET1 SCC cells were exposed to a wide range of concentrations of those reagents (1.25 µM – 320 µM) for 24 and 48 h. Figure 5.1 and Figure 5.2 show the viability behavior of HaCaT and MET1 SCC cells, respectively, treated with dyes (methylene blue, acridine orange, gentian violet), natural compounds (quercetin, curcumin and epigallocatechin gallate) or chelating molecules (neocuproine,1,10- phenanthroline and 2,2'-bipyridyl). The values of cell viability as a function of PS concentration allowed the calculation of half maximal inhibitory concentration (IC_{50}) for the different chemicals tested. IC_{50} is usually employed to evaluate a substance efficacy and the concentration able to inhibit cells' growth [24]. The obtained IC_{50} values are displayed in Table 5.1, however some curves of cytotoxicity did not exhibit enough toxicity to calculate it.

Dyes in general show low IC_{50}, less than 20 µM, in both non-cancer and cancer cell lines (Figure 5.1 – A and Figure 5.2 – A). However, it was necessary to evaluate if the IC_{50} in non-cancer cell line was much different from the one calculated for cancer cell line. Concerning to this, results showed

slightly lower IC_{50} value for the dyes in non-cancer keratinocytes when compared to cancer keratinocytes. For the natural products, the results are generally increased showing that the natural products in the HaCaT cells (Figure 5.1 – B) are not as toxic as for MET1 SCC cells (Figure 5.2 – B). Many researchers demonstrated the selectivity of natural products that were more toxic in cancer cells than in non-cancer cell line [25–27]. Furthermore, the chelating agents showed lower IC_{50} values in the non-cancer cell line (Figure 5.1 – C) in comparison with cancer cells (Figure 5.2 – C).
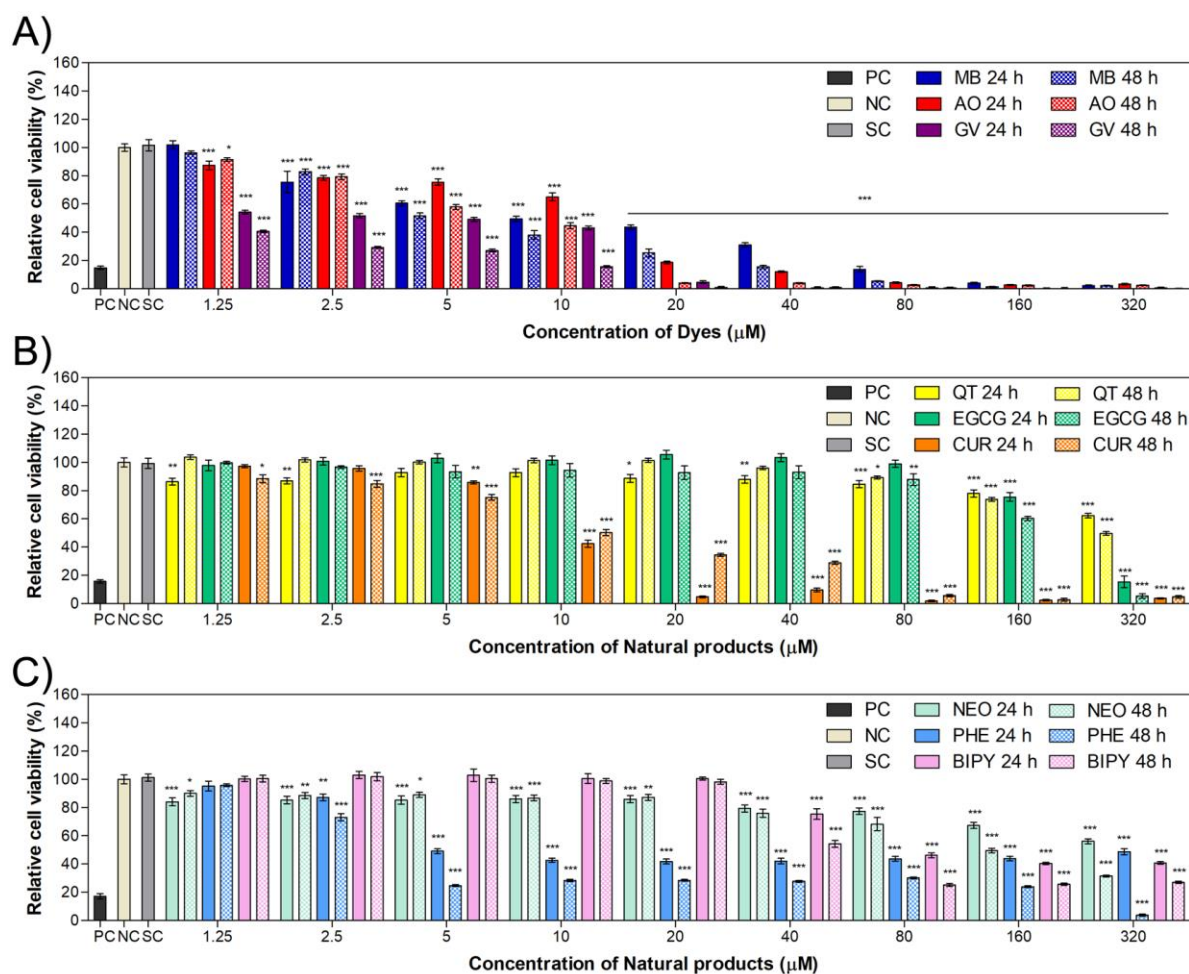
Figure 5.1: Cell viability of HaCaT cells treated for 24 or 48 hours with dyes (MB, AO, GV), natural compounds (QT, CUR, EGCG) or chelating molecules (NEO, PHE, BIPY) with a range of concentration from 1.25 μM to 320 μM. Values presented are the mean ± combined standard uncertainty (n=4) and statistical analysis comparing the results to the cell viability of the negative control was performed by a two-way ANOVA with Bonferroni post-test where * $p < 0.05$, ** $p < 0.01$ and *** $p < 0.001$. MB: methylene blue, AO: acridine orange, GV: gentian violet, QT: quercetin, EGCG: epigallocatechin gallate, CUR: curcumin, NEO: neocuproine, PHE: 1,10-phenanthroline, BIPY: 2,2'-bipyridyl, PC: positive control, NC: negative control, SC: solvent control.

Figure 5.2: Relative cell viability of MET1 cell line treated for 24 or 48 hours with the dyes (MB, AO, GV), natural compounds (QT, CUR, EGCG) or chelating molecules (NEO, PHE, BIPY) with a range of concentration from 1.25 µM to 320 µM. Values presented are the mean ± combined standard uncertainty (n=4) and statistical significances comparing the results to the cell viability of the negative control was performed by a two-way ANOVA with Bonferroni post-test where * $p < 0.05$, ** $p < 0.01$ and *** $p < 0.001$. MB: methylene blue, AO: acridine orange, GV: gentian violet, QT: quercetin, EGCG: epigallocatechin gallate, CUR: curcumin, NEO: neo-cuproine, PHE: 1,10-phenanthroline, BIPY: 2,2'-bipyridyl, PC: positive control, NC: negative control, SC: solvent control.

The high cytotoxicity of dyes is a promising result considering the use as anticancer drugs, however in the pursuit of photosensitizers, the light effect should be also considered. MB, AO and GV are very toxic for the MET1 SCC cells exhibiting IC$_{50}$ values of 14.2 µM, 15.1 µM and 3.9 µM for the 24 h experiment and 4.2 µM, 10.3 µM and 1.2 µM for the 48 hours experiment, respectively. Clearly, GV was the most toxic in comparison to the other dyes, which is a challenge considering that it would be interesting to observe a difference in viability when submitted to light irradiation in the evaluation of the phototoxic potential.

The molecule curcumin is being widely studied regarding the anticancer properties [28,29] and indeed show low IC_{50} values of 26 µM and 7.2 µM in the squamous carcinoma cells. Moreover, according to the literature [30–33] EGCG and quercetin are also some natural candidates for anticancer therapy. However, in this work the achieved IC_{50} values are not very impressive comparing to the other molecules. This same perception occurred for the chelating agents which also presented IC_{50} higher than 100 µM in the 24 hours experiment.

Table 5.1: Calculated IC_{50} of 24 and 48 hours cytotoxicity using MET1 SCC and HaCaT cells treated with the dyes (methylene blue, acridine orange, gentian violet), natural compounds (quercetin, curcumin and epigallocatechin gallate) and chelating molecules (neocuproine, 1,10-phenanthroline and 2,2'-bipyridyl) using concentrations from 1.25 µM to 320 µM.

	IC_{50} (µM)			
	MET1 SCC cells		**HaCaT cells**	
Compound	**24 h**	**48 h**	**24 h**	**48 h**
Methylene blue	14.2	4.2	11.6	7.1
Acridine orange	15.1	10.3	10.5	6.5
Gentian violet	3.9	1.2	2.8	0.9
Quercetin	429.0	109.8	-	314.8
Curcumin	26.0	7.2	9.0	11.7
Epigallocatechin gallate	173.9	136.3	211.1	173.2
Neocuproine	-	-	-	158.5
1,10-Phenanthroline	123.6	7.7	35.2	5.9
2,2'-Bipyridyl	275.0	97.2	125.2	57.8

5.3.2 Phototoxicity in MET1 SCC cells

In order to evaluate the phototoxic potential of the DNA-intercalating agents efficacy in cancer cells damage, irradiation studies were carried out in MET1 SCC cells. As seen before in the cytotoxicity experiments, the range of concentration was reduced as some molecules, mainly the dyes, presented less than 10% cell viability at concentrations higher than 40 µM. Different potential photosensitizer molecules were used in squamous carcinoma cell line and submitted to different light sources to evaluate their effect and were compared to samples kept in the dark without irradiation that were used for comparison purposes (control). The dark controls exhibited in this chapter may present difference values of IC_{50} due to an additional 24 hours incubation after removal of the treatments, to follow the procedure of the irradiated samples.

Figure 5.3 – A, B and C exhibit the cell viability results for the dyes MB, AO and GV respectively. A statistical comparison between the MB treated cells shows that all the light wavelength affected the cells viability compared to the control kept in the dark. Cells treated with MB and irradiated with the red light (640 nm) had, as exhibited in Table 5.2, the lowest IC_{50} value of 3.8 µM, almost 3 times lower than the control one. This is somehow expected, since MB has the three main characteristic bands, two at UV region with maximum absorbance at 250 nm and 300 nm and one at the visible region, with maximum of absorbance at 665 nm [34]. The irradiation with 254 nm wavelength light also shows great phototoxicity. For this reason, MB photodynamic potential on cancer cells damage has gained the researchers' interest. For example, Kofler et al. [35] studied the effect of MB in head and neck squamous cell carcinoma while Dos Santos et al. [36] in breast cancer cells and the MB mediated PDT caused significant cell death. The value of the IC_{50} of the dark control divided by the IC_{50} of the cells treated with MB and irradiated by 640 nm light was able to estimate the factor of phototoxicity, which showed in this case value of 2.9, which can be attributed to a moderate phototoxicity.

The effect of the AO dye (Figure 5.3 – B) in the cells viability is strongly dependent to the light wavelength. The effect caused by the 457 nm light on these cells is remarkable, showing cell viability less than 10% at all concentrations investigated. This is evident when analyzing the IC_{50}, which shows calculated values of 11.5 µM, 6.6 µM, 4.1 µM and 7.1 µM for dark, 640 nm, 583 nm, 254 nm wavelength of irradiation, respectively. For the 457 nm irradiation, the viability is low and the calculation of the IC_{50} value was done using concentrations in the 0.3 µM to 10 µM range (Appendix Figure A.1). The IC_{50} value obtained under this condition was 0.4 µM. The phototoxicity factor was calculated dividing cells treated with AO kept in the dark by the cells treated and exposed to blue light, which resulted in a factor of 28.8, meaning a high phototoxicity of AO with blue light irradiation. This agrees with AO spectrum, since it exhibits characteristic peaks in the UV region around 230 nm, 270 nm and 290 nm [37], in the visible region the maximum absorbance is at the 490 nm wavelength, related with the AO molecule (monomer) and a shoulder around 470 nm that can turn into a peak with the increase of concentration and which associated to possible AO dimers [38]. As a remark, there is reference to some molecules with intense peak in the blue wavelength region (Soret peak) that are very efficient as PS, attributed to a proper action of the blue region wavelength, claimed to be able to lead to the death of cancer cells at a certain depth [5]. Osman et al. [39] investigated the photosensitizing potential of AO for glioblastoma and using a low concentration of 0.001 mg/mL a very significant decrease in the cell count has been observed. The potential application of AO-PDT for bladder cancer therapy was studied by Lin et al. [40] which also revealed for this cell type a significant cell death for low AO concentrations and blue light irradiation.

Cells treated with GV and irradiated seems to be affected by light with exception of blue light (457 nm) as shown in (Figure 5.3 – C). A special decrease of cell viability can be observed for the irradiation with 583 nm resulting in an IC_{50} value of 1.0 µM. However, as previously shown in the cytotoxicity studies, this dye present high toxicity in the MET1 SCC cell line, the dark toxicity at the

lowest concentration of 1.25 µM was below 60% which indicates the sample's high cytotoxicity while for the other dyes we obtained at least 90% of viability at the same condition.

In the concentration range of 1.25 µM to 40 µM QT only shows significant results at 40 µM for irradiations with 583 nm, 457 nm and 254 nm wavelength light (Figure 5.3 – D). For EGCG no photo-toxicity was observed in the investigated range. EGCG is an example of molecule that can present a dual role of prooxidant and antioxidant depending on the concentration level [41,42]. To calculate these IC_{50} values, assays were repeated using concentrations up to 320 µM (Appendix Figure A.2). The achieved results are exhibited in Table 5.2. From these results, one can observe that IC_{50} values in general increases comparing to dark control assays. For QT, the control presented IC_{50} of 229.7 µM and was decreased when irradiating at 254 nm where an IC_{50} of 205 µM was observed. For EGCG all IC_{50} obtained from the phototoxicity studies (Figure 5.3 – E) were above of the control (190.8 µM). These compounds are often used in combination with PDT [21,22,43,44], as seen for example in the research developed by Mun et al. [43], where it has been demonstrated that PDT using radachlorin and EGCG improved anti-tumor effect *in vitro* and *in vivo*.

Cell viability studies in the presence of curcumin and irradiation with light of wavelength of 640 nm, 583 nm, 457 nm and 254 nm light showed statistically different results for the populations of the experimental conditions in comparison with the dark control, with the IC_{50} values around 10 µM (Figure 5.3 – F). As curcumin presents a characteristic absorbance band in the visible region at 430 nm [45], one expects a strong effect of 457 nm light. In fact, this is in accordance with the achieved results on the cells where an IC_{50} of 10.7 µM was observed, which is lower than the control one of 15.5 µM. Fadeel and collaborators [46] investigated the encapsulation of curcumin in PEGylated lipid carrier to be used in photodynamic therapy on human skin cancer cell line and demonstrated a cell survival decrease when using curcumin suspension, which was boosted when using encapsulated curcumin.

Studies with neocuproine using the smaller concentration range (1.25 µM – 40 µM) show a differentiate behaviour, where cell viability is seen to slightly increase as the concentration increases. Due to this behaviour, the IC_{50} value cannot be calculated (Figure 5.3 – G). However, similarly to GV, this compound shows cell viability below 70% even at dark conditions. For 1,10-phenanthroline (Figure 5.3 – H) it is possible to observe difference from the dark control at 5 µM and 10 µM. The application of agent chelators such as phenanthroline in PDT are usually associated with the incorporation into a metallic complex, as revealed in Al Hageh et al. work [47], in which a synthetized bis-phenanthroline complex was developed and was seen to be able to generate DNA damage after irradiation as a result of successful ROS production.
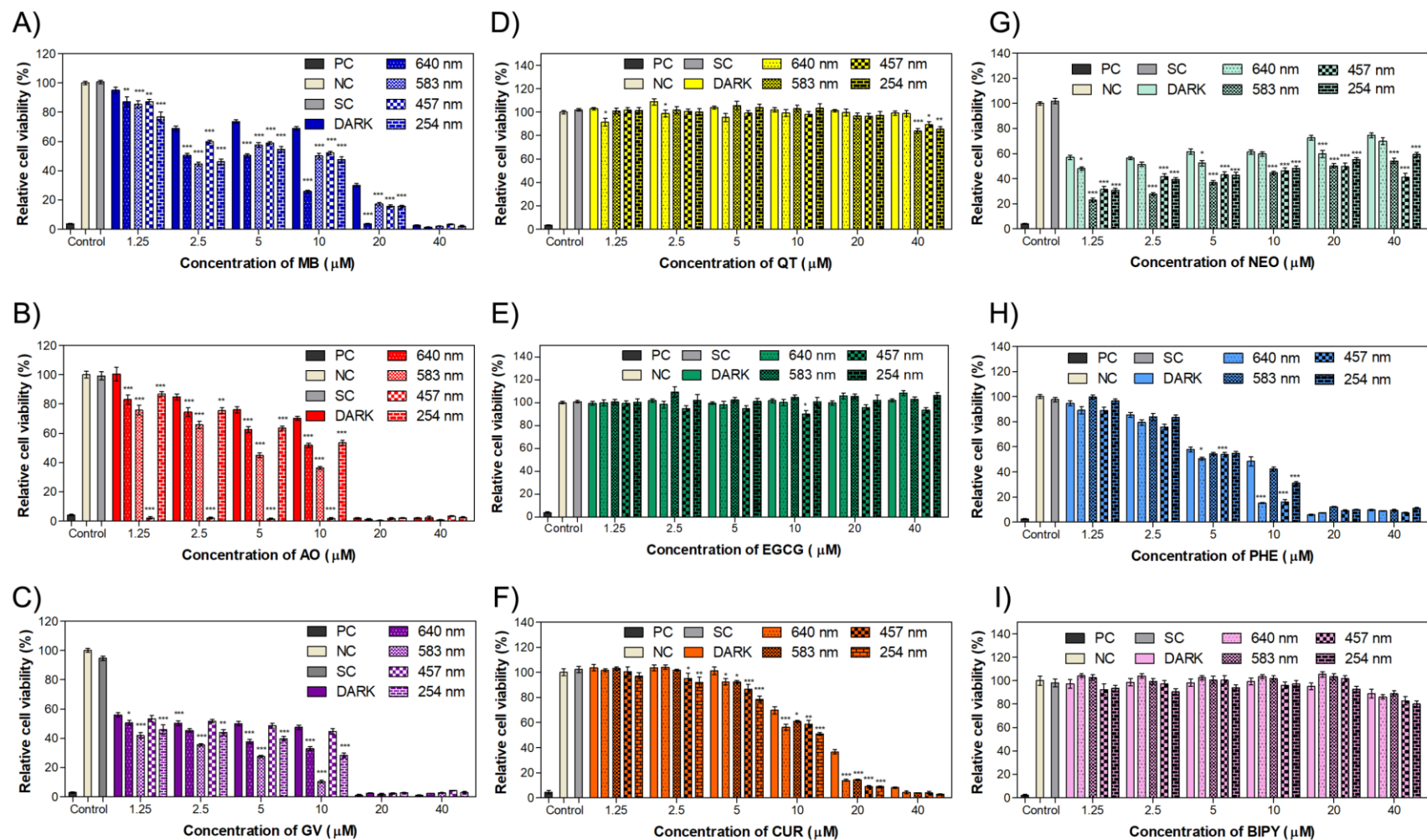
Figure 5.3: Relative cell viability of MET1 cell line treated with dyes, natural compounds, or chelating agents and submitted to irradiation. Samples kept in the dark were used as control and compared to those submitted to irradiation at different wavelengths. Values are mean ± combined standard uncertainty (n=6) and statistical analysis was done by a two-way ANOVA with Bonferroni post-test where * $p < 0.05$, ** $p < 0.01$ and *** $p < 0.001$. MB: methylene blue, AO: acridine orange, GV: gentian violet, QT: quercetin, EGCG: epigallocatechin gallate, CUR: curcumin, NEO: neocuproine, PHE: 1,10-phenanthroline, BIPY: 2,2'-bipyridyl.

The chelating agent 2,2'-bipyridyl did not show phototoxicity in the concentration range exhibited in Figure 5.3 – I and, therefore, experiments were repeated with concentrations until 320 µM (Appendix Figure A.2) for the attainment of the IC_{50}. In this case, there is a decrease in the IC_{50} values of the irradiated samples mainly for the 583 nm and 457 nm wavelength light. Alike 1,10-phenanthroline, some studies showed the efficient photosensitizing activity of 2,2'-bipyridyl in metallic complexes [48,49]. Therefore, the association of these molecules in complexes is an interesting approach to be explored.

As mentioned, some of the investigated compounds as the dyes present phototoxicity at low concentrations, while natural compounds, with the exception for curcumin, do present phototoxicity above 150 µM. Considering the results obtained with MET1 SCC cells, methylene blue and acridine orange in low concentrations range are worth to be used in further studies in melanoma cell line WM983b and in the evaluation of the intracellular ROS production in MET1 SCC cells.

Table 5.2: Comparison of IC_{50} from phototoxicity assay in MET1 SCC cells treated with the dyes (methylene blue, acridine orange, gentian violet), natural compounds (quercetin, curcumin and epigallocatechin gallate) and chelating molecules (neocuproine, phenanthroline and 2,2'-bipyridyl), submitted or not to different light sources.

Compound	IC_{50} (µM)				
	Dark	**640 nm**	**583 nm**	**457 nm**	**254 nm**
Methylene blue	10.9	3.8	5.0	6.2	4.3
Acridine orange	11.5	6.6	4.1	0.4	7.1
Gentian violet	2.9	1.8	1.0	2.7	1.5
Quercetin	229.7	340.4	269.2	287.8	205.0
Curcumin	15.5	11.0	11.5	10.7	9.3
Epigallocatechin gallate	190.8	224.4	211.1	222.2	192.9
Neocuproine	-	-	-	-	-
1,10-Phenanthroline	7.4	4.8	6.8	4.9	6.0
2,2'-Bipyridyl	228.1	202.1	190.4	171.3	224.9

5.3.3 Intracellular ROS production in MET1 SCC cells

DHE was the probe selected to evaluate ROS production by fluorescence microscopy due to DHE oxidation in the presence of superoxide radical ($O_2^{\bullet-}$), forming products with red fluorescence as the stable 2-hydroxiethidium (2-OH-E^+) and ethidium (E^+), this one as a result of non-specific oxidation such as with hydroxyl radical ($^{\bullet}OH$) or hydrogen peroxide (H_2O_2) [50].

As the results showed that both MB and AO had a significant decrease in the IC_{50} values when submitted to 640 nm and 457 nm wavelength light, fluorescence studies were directed to these molecules

using low concentrations known to have no effect on cell viability in the absence of irradiation. Fluorescence images of cells treated with MB in the presence or in the absence of light are shown in Figure 5.4. It is possible to observe a weak fluorescence in the cells of the control (0 µM, without MB) and the same pattern for the other wells containing cells treated with MB but no light. However, we can observe a slightly increase in fluorescence intensity at the concentration of 2.5 µM, in irradiated cells regarding to non-irradiated cells. This can be an indicative of a modest ROS production after irradiation. Cells fluorescence images treated with AO and submitted to the same procedure as cells treated with MB but with no irradiation showed a slight increase of fluorescence intensity with the increase of AO concentration (Figure 5.5) when compared to the cells treated with MB. However, it is notorious the difference between the fluorescence intensity of cells submitted to irradiation when compared to the ones without the irradiation, with the increase of AO concentration. Thus, we can infer the production of ROS after irradiation.
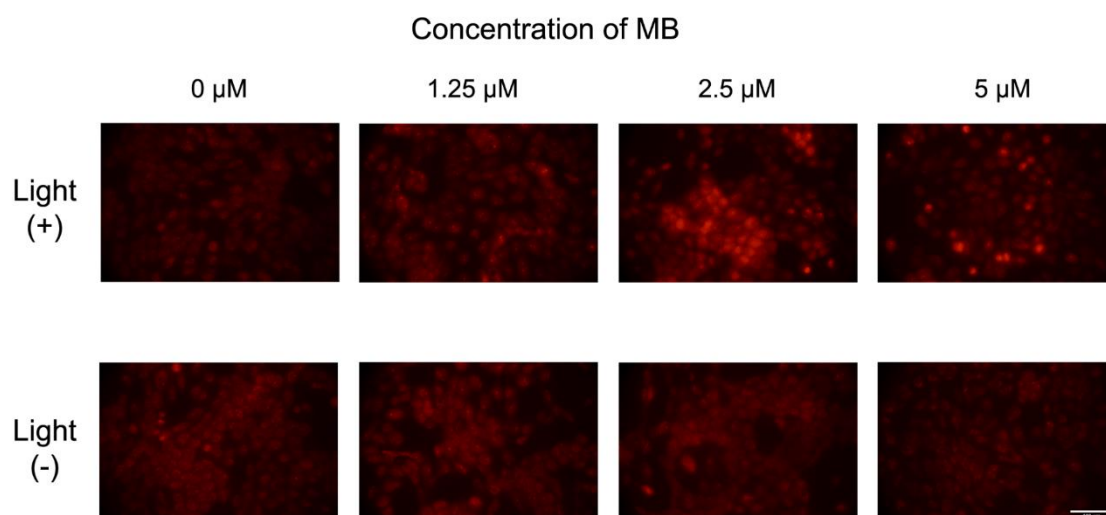
Figure 5.4: Fluorescence images of MET1 SCC cells in presence of different concentrations of methylene blue with the presence or absence of light. Scale bar = 100 µm.

Concentration of AO
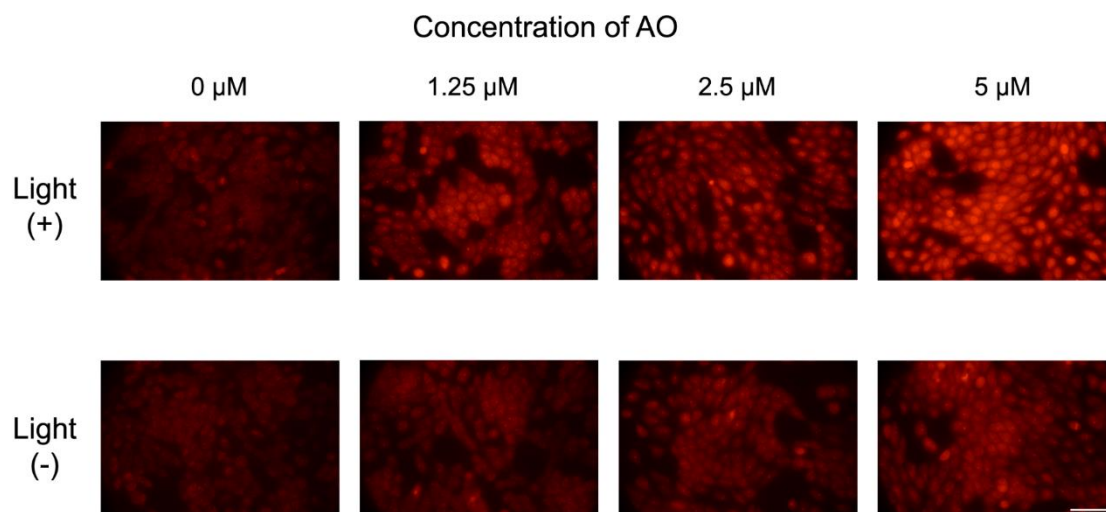
Figure 5.5: Fluorescence images of MET1 SCC cells in presence of different concentrations of acridine orange with the presence or absence of light. Scale bar = 100 µm.

Figure 5.6 exhibits the quantification of red fluorescence measured using the ImageJ software in relation to the total count of cells in the image. The study with MB (Figure 5.6 – A) shows an integrated density intensity of fluorescence around 1.1×10^6 for the non-irradiated control (0 µM, without the dye). However, a modest increase in the integrated density for samples treated with 2.5 µM of MB was observed, followed by a decrease with the highest concentration, which agrees with the fluorescence images exhibited in Figure 5.4. One can speculate that through this method it is possible to detect small amount of ROS, mainly for the lower concentrations. However, it was clear that MB presented phototoxicity in this cell line at these concentrations, in such a way that the employed probe perhaps was not the most suitable in this case and other ROS probes should be tested.

In the Figure 5.6 – B, the fluorescence intensity for cells treated with AO is displayed. From this figure one can observe an integrated density value around 1.1×10^6 for the control without AO. With the increase of AO concentration, the integrated density intensity is seen to rise for samples with and without light irradiation. However, the greater fluorescence intensity is associated, without any doubt, to the irradiation. In comparison to the non-irradiated control (0 µM, without the dye), cells treated with 5 µM AO and submitted to 457 nm irradiation presented an increase in fluorescence about 2.6-fold in the fluorescence. Comparing cells treated with 5 µM AO non-irradiated and those irradiated, there is an increase about 1.4-fold in the fluorescence intensity. AO can accumulate in acidic vesicular organelles and is often employed in fluorescence to investigate autophagy [51], therefore, as at these concentrations AO is not toxic, the mild red fluorescence of cells without light irradiation may indicate an autophagy process. Apart from the uncertain reason why AO creates a red fluorescence in the cells, it should be

reinforced that the DHE detection method was able to confirm the ability of AO to induce the production of ROS.
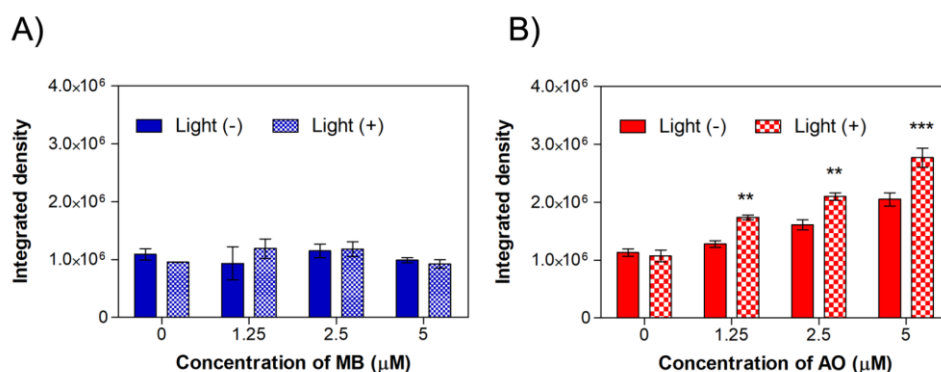
Figure 5.6: Quantification of fluorescence intensity of MET1 cells treated with (A) methylene blue and (B) acridine orange, submitted or not to irradiation at 640 nm and 457 nm, respectively. Results are displayed as mean ± standard deviation of the mean (n=4) and statistical analysis was done by a two-way ANOVA with Bonferroni post-test where ** $p < 0.01$ and *** $p < 0.001$, by the comparison of the fluorescence intensity of irradiated cells to the cells treated with the same concentration and non-irradiated.

5.3.4 Cytotoxicity and Phototoxicity in WM983b cells

To evaluate about the possible extension of using the same promising photosensitizers for other types of cancers, studies were performed in melanoma cell line. Figure 5.7 shows the WM983b cell viability study of cells treated for 24 or 48 hours with the dyes MB and AO in the concentration range of 1.25 μM to 320 μM. The IC$_{50}$ of the dyes MB and AO was low, with values of 18.0 μM and 6.1 μM for MB and 25.2 μM and 6.6 μM for AO, in the experiments of 24 and 48 hours experiments, respectively. Comparing to non-cancer and cancer keratinocytes cell lines, the melanoma cells revealed to be more resistant to these compounds mainly for the 24 hours treatment. However, they are clearly cytotoxic to this cell line at concentrations above 10 μM for MB and 20 μM for AO, concentrations which the relative cell population falls below 70%. In melanoma cancer, cells rapidly develop resistance to treatment rapidly through various molecular mechanisms [52], so it is expected that melanoma cells are more resistant than other cells.
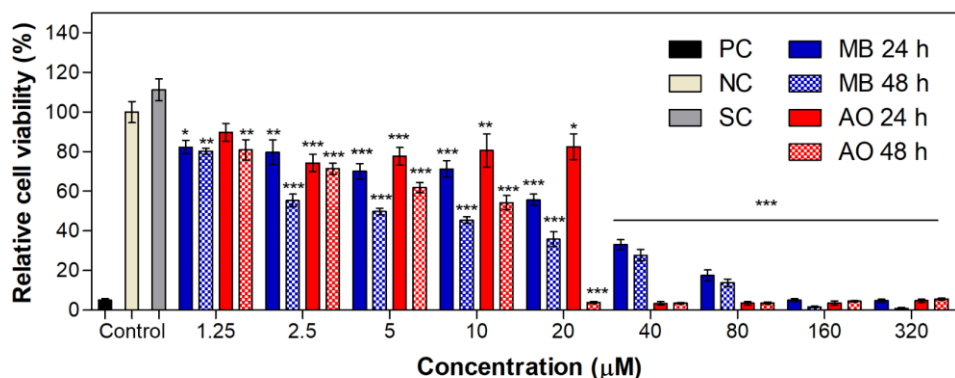
Figure 5.7: Relative cell viability of WM983b cell line treated for 24 or 48 hours with the dyes MB and AO with a range of concentration from 1.25 µM to 320 µM. Values present are the mean ± combined standard uncertainty (n=4) and statistical analysis comparing the results to the negative control was performed by a two-way ANOVA with Bonferroni post-test where * $p < 0.05$, ** $p < 0.01$ and *** $p < 0.001$. MB: methylene blue, AO: acridine orange, PC: positive control, NC: negative control, SC: solvent control.

For the cells treated with MB, phototoxicity results show IC$_{50}$ values of 2.1 µM and 7.3 µM for irradiated and for non-irradiated samples, respectively (Figure 5.8). In accordance with previous results with the squamous carcinoma cell line, the IC$_{50}$ for AO in melanoma cell line was 1.1 µM and 17.5 µM with and without irradiation, respectively. Once again AO molecules presence contributes to a more significant phototoxicity when compared with the one achieved with MB. In any case, the PDT is effective for this melanoma cell line for low dye concentrations.
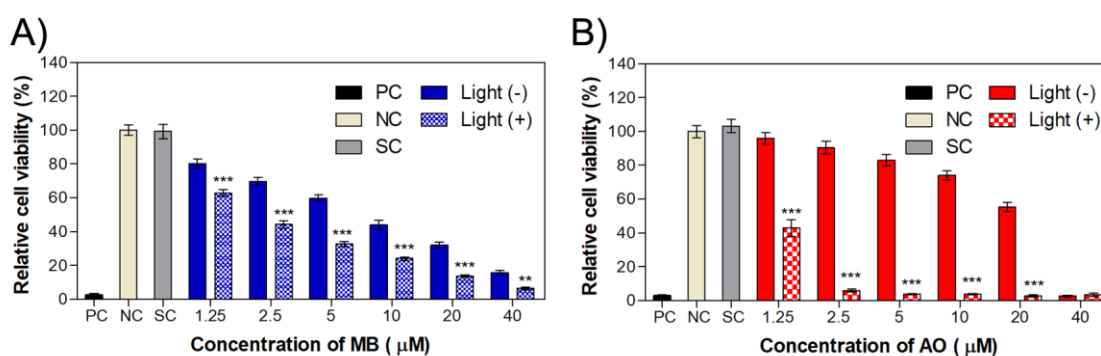
Figure 5.8: Relative cell population of WM983b cell line treated with dye molecules MB, AO and submitted to irradiation. Samples non-irradiated, light (-), was used as control compared to those submitted to different light wavelength irradiation (640 nm for MB and 457 nm for AO). Values are presented by the mean ± combined standard uncertainty (n=6) and statistical analysis was done by a two-way ANOVA with Bonferroni post-test where * $p < 0.05$, ** $p < 0.01$ and *** $p < 0.001$, in comparison with the negative control. MB: methylene blue, AO: acridine orange, PC: positive control, NC: negative control, SC: solvent control.

5.4 Conclusions

In this work, the *in vitro* cytotoxicity of several DNA-intercalating agents, namely, methylene blue, acridine orange, gentian violet, curcumin, quercetin, epigallocatechin gallate, neocuproine, 1,10-phenanthroline and 2,2'-bipyridyl, was analyzed in HaCaT cells (non-cancer keratinocytes) and MET1 SCC cells (cancer keratinocytes cell line). The achieved results allowed to conclude that non-cancer keratinocytes are more sensitive to the tested agents than the cancer cell line and, in general, dyes and curcumin revealed to be more cytotoxic (IC_{50} below 30 µM) when compared to the other compounds tested. Results of phototoxicity showed that the IC_{50} values of the dyes and curcumin are very low (below 20 µM) while for the natural products QT, EGCG and the chelating agent 2,2'-bipyridyl the values are higher than 100 µM for MET1 SCC cells. The most promising molecules that considerably reduced their IC_{50} values were MB and AO, when submitted to a 640 nm and 457 nm light irradiation, respectively. ROS detection was more evident for cells treated with AO at low concentrations. In accordance with the results obtained in MET1 SCC cells, MB and AO are also cytotoxic and phototoxic towards the melanoma cell line, with special highlight to AO, that demonstrated a significant difference between the IC_{50} values of cells with and without irradiation. This investigation also revealed that although the molecules can act as photosensitizers, the effects depend on the cell type, the concentration of the photosensitizer and the irradiation dose. Finally, this work allows to demonstrate a significant photosensitizing activity of AO using low concentrations and at moderate light dose.

Acknowledgments

References

1. Wen, X.; Li, Y.; Hamblin, M.R. Photodynamic therapy in dermatology beyond non-melanoma cancer: an update. *Photodiagnosis Photodyn. Ther.* **2017**, *19*, 140–152, doi:10.1016/j.pdpdt.2017.06.010.

2. Kim, M.; Jung, H.; Park, H. Topical PDT in the Treatment of Benign Skin Diseases: Principles

and New Applications. *Int. J. Mol. Sci.* **2015**, *16*, 23259–23278, doi:10.3390/ijms161023259.

3.   Kou, J.; Dou, D.; Yang, L. Porphyrin photosensitizers in photodynamic therapy and its applications. *Oncotarget* **2017**, *8*, 81591–81603, doi:10.18632/oncotarget.20189.

4.   Agostinis, P.; Berg, K.; Cengel, K.A.; Foster, T.H.; Girotti, A.W.; Gollnick, S.O.; Hahn, S.M.; Hamblin, M.R.; Juzeniene, A.; Kessel, D.; et al. Photodynamic therapy of cancer: An update. *CA. Cancer J. Clin.* **2011**, *61*, 250–281, doi:10.3322/caac.20114.

5.   Oniszczuk, A.; Wojtunik-Kulesza, K.A.; Oniszczuk, T.; Kasprzak, K. The potential of photodynamic therapy (PDT)—Experimental investigations and clinical use. *Biomed. Pharmacother.* **2016**, *83*, 912–929, doi:10.1016/j.biopha.2016.07.058.

6.   Crous, A.; Chizenga, E.; Hodgkinson, N.; Abrahamse, H. Targeted Photodynamic Therapy: A Novel Approach to Abolition of Human Cancer Stem Cells. *Int. J. Opt.* **2018**, *2018*, 7317063, doi:10.1155/2018/7317063.

7.   Zhao, B.; He, Y.-Y. Recent advances in the prevention and treatment of skin cancer using photodynamic therapy. *Expert Rev. Anticancer Ther.* **2010**, *10*, 1797–1809, doi:10.1586/era.10.154.

8.   Abrahamse, H.; Hamblin, M.R. New photosensitizers for photodynamic therapy. *Biochem. J.* **2016**, *473*, 347–364, doi:10.1042/BJ20150942.

9.   Zhang, J.; Jiang, C.; Figueiró Longo, J.P.; Azevedo, R.B.; Zhang, H.; Muehlmann, L.A. An updated overview on the development of new photosensitizers for anticancer photodynamic therapy. *Acta Pharm. Sin. B* **2018**, *8*, 137–146, doi:10.1016/j.apsb.2017.09.003.

10.   Tiwari, S.; Mall, C.; Solanki, P.P. Evaluation of mixed dye combination by spectral study for the application as photosensitizer in photogalvanic cells for solar energy conversion and storage. *Surfaces and Interfaces* **2022**, *29*, 101688, doi:10.1016/j.surfin.2021.101688.

11.   Raab, O. Über die wirkung fluoreszierender stoffe auf infusoren. *Z. Biol.* **1900**, *39*, 524–546.

12.   Lamch, Ł.; Kulbacka, J.; Dubińska-Magiera, M.; Saczko, J.; Wilk, K.A. Folate-directed zinc (II) phthalocyanine loaded polymeric micelles engineered to generate reactive oxygen species for efficacious photodynamic therapy of cancer. *Photodiagnosis Photodyn. Ther.* **2019**, *25*, 480–491, doi:10.1016/j.pdpdt.2019.02.014.

13.   Abdel Fadeel, D.; Al-Toukhy, G.M.; Elsharif, A.M.; Al-Jameel, S.S.; Mohamed, H.H.; Youssef, T.E. Improved photodynamic efficacy of thiophenyl sulfonated zinc phthalocyanine loaded in lipid nano-carriers for hepatocellular carcinoma cancer cells. *Photodiagnosis Photodyn. Ther.* **2018**, *23*, 25–31, doi:10.1016/j.pdpdt.2018.06.003.

14.   Mehraban, N.; Musich, P.; Freeman, H. Synthesis and Encapsulation of a New Zinc Phthalocyanine Photosensitizer into Polymeric Nanoparticles to Enhance Cell Uptake and Phototoxicity. *Appl. Sci.* **2019**, *9*, 401, doi:10.3390/app9030401.

15.   Foresto, E.; Gilardi, P.; Ibarra, L.E.; Cogno, I.S. Light-activated green drugs: How we can use them in photodynamic therapy and mass-produce them with biotechnological tools.

Phytomedicine Plus **2021**, *1*, 100044, doi:10.1016/j.phyplu.2021.100044.

16. Siewert, B.; Stuppner, H. The photoactivity of natural products – An overlooked potential of phytomedicines? *Phytomedicine* **2019**, *60*, 152985, doi:10.1016/j.phymed.2019.152985.

17. Machado, F.C.; Adum de Matos, R.P.; Primo, F.L.; Tedesco, A.C.; Rahal, P.; Calmon, M.F. Effect of curcumin-nanoemulsion associated with photodynamic therapy in breast adenocarcinoma cell line. *Bioorg. Med. Chem.* **2019**, *27*, 1882–1890, doi:10.1016/j.bmc.2019.03.044.

18. Duse, L.; Pinnapireddy, S.R.; Strehlow, B.; Jedelská, J.; Bakowsky, U. Low level LED photodynamic therapy using curcumin loaded tetraether liposomes. *Eur. J. Pharm. Biopharm.* **2018**, *126*, 233–241, doi:10.1016/j.ejpb.2017.10.005.

19. Jamali, Z.; Khoobi, M.; Hejazi, S.M.; Eivazi, N.; Abdolahpour, S.; Imanparast, F.; Moradi-Sardareh, H.; Paknejad, M. Evaluation of targeted curcumin (CUR) loaded PLGA nanoparticles for *in vitro* photodynamic therapy on human glioblastoma cell line. *Photodiagnosis Photodyn. Ther.* **2018**, *23*, 190–201, doi:10.1016/j.pdpdt.2018.06.026.

20. de Matos, R.P.A.; Calmon, M.F.; Amantino, C.F.; Villa, L.L.; Primo, F.L.; Tedesco, A.C.; Rahal, P. Effect of Curcumin-Nanoemulsion Associated with Photodynamic Therapy in Cervical Carcinoma Cell Lines. *Biomed Res. Int.* **2018**, *2018*, 4057959, doi:10.1155/2018/4057959.

21. de Paula Rodrigues, R.; Tini, I.R.P.; Soares, C.P.; da Silva, N.S. Effect of photodynamic therapy supplemented with quercetin in HEp-2 cells. *Cell Biol. Int.* **2014**, *38*, 716–722, doi:10.1002/cbin.10251.

22. Thakur, N.S.; Mandal, N.; Patel, G.; Kirar, S.; Reddy, Y.N.; Kushwah, V.; Jain, S.; Kalia, Y.N.; Bhaumik, J.; Banerjee, U.C. Co-administration of zinc phthalocyanine and quercetin via hybrid nanoparticles for augmented photodynamic therapy. *Nanomedicine Nanotechnology, Biol. Med.* **2021**, *33*, 102368, doi:10.1016/j.nano.2021.102368.

23. Yang, J.; Xu, Y.; Jiang, M.; Zou, D.; Yang, G.; Shen, L.; Zou, J. Photochemical property of two Ru(II) compounds based on 5-(2-pyrazinyl)tetrazole for cancer phototherapy by changing auxiliary ligand. *J. Inorg. Biochem.* **2019**, *193*, 124–129, doi:10.1016/j.jinorgbio.2019.01.015.

24. González-Larraza, P.G.; López-Goerne, T.M.; Padilla-Godínez, F.J.; González-López, M.A.; Hamdan-Partida, A.; Gómez, E. IC 50 Evaluation of Platinum Nanocatalysts for Cancer Treatment in Fibroblast, HeLa, and DU-145 Cell Lines. *ACS Omega* **2020**, *5*, 25381–25389, doi:10.1021/acsomega.0c03759.

25. Badisa, R.B.; Ayuk-Takem, L.T.; Ikediobi, C.O.; Walker, E.H. Selective Anticancer Activity of Pure Licamichauxiioic-B Acid in Cultured Cell Lines. *Pharm. Biol.* **2006**, *44*, 141–145, doi:10.1080/13880200600592301.

26. Aung, T.; Qu, Z.; Kortschak, R.; Adelson, D. Understanding the Effectiveness of Natural Compound Mixtures in Cancer through Their Molecular Mode of Action. *Int. J. Mol. Sci.* **2017**, *18*, 656, doi:10.3390/ijms18030656.

27. Skvortsov, D.A.; Kalinina, M.A.; Zhirkina, I.V.; Vasilyeva, L.A.; Ivanenkov, Y.A.; Sergiev, P.V.; Dontsova, O.A. From Toxicity to Selectivity: Coculture of the Fluorescent Tumor and Non-Tumor Lung Cells and High-Throughput Screening of Anticancer Compounds. *Front. Pharmacol.* **2021**, *12*, 713103, doi:10.3389/fphar.2021.713103.

28. Baldi, A.; De Luca, A.; Maiorano, P.; D'Angelo, C.; Giordano, A. Curcumin as an Anticancer Agent in Malignant Mesothelioma: A Review. *Int. J. Mol. Sci.* **2020**, *21*, 1839, doi:10.3390/ijms21051839.

29. Tomeh, M.A.; Hadianamrei, R.; Zhao, X. A review of curcumin and its derivatives as anticancer agents. *Int. J. Mol. Sci.* **2019**, *20*, 1033, doi:10.3390/ijms20051033.

30. Rauf, A.; Imran, M.; Khan, I.A.; Ur-Rehman, M.-; Gilani, S.A.; Mehmood, Z.; Mubarak, M.S. Anticancer potential of quercetin: A comprehensive review. *Phyther. Res.* **2018**, *32*, 2109–2130, doi:10.1002/ptr.6155.

31. Hashemzaei, M.; Far, A.D.; Yari, A.; Heravi, R.E.; Tabrizian, K.; Taghdisi, S.M.; Sadegh, S.E.; Tsarouhas, K.; Kouretas, D.; Tzanakakis, G.; et al. Anticancer and apoptosis-inducing effects of quercetin *in vitro* and *in vivo*. *Oncol. Rep.* **2017**, *38*, 819–828, doi:10.3892/or.2017.5766.

32. Du, G.-J.; Zhang, Z.; Wen, X.-D.; Yu, C.; Calway, T.; Yuan, C.-S.; Wang, C.-Z. Epigallocatechin Gallate (EGCG) Is the Most Effective Cancer Chemopreventive Polyphenol in Green Tea. *Nutrients* **2012**, *4*, 1679–1691, doi:10.3390/nu4111679.

33. Hayakawa, S.; Ohishi, T.; Miyoshi, N.; Oishi, Y.; Nakamura, Y.; Isemura, M. Anti-Cancer Effects of Green Tea Epigallocatchin-3-Gallate and Coffee Chlorogenic Acid. *Molecules* **2020**, *25*, 4553, doi:10.3390/molecules25194553.

34. Melgoza, D.; Hernández-Ramírez, A.; Peralta-Hernández, J.M. Comparative efficiencies of the decolourisation of Methylene Blue using Fenton's and photo-Fenton's reactions. *Photochem. Photobiol. Sci.* **2009**, *8*, 596–599, doi:10.1039/b817287k.

35. Kofler, B.; Romani, A.; Pritz, C.; Steinbichler, T.; Schartinger, V.; Riechelmann, H.; Dudas, J. Photodynamic Effect of Methylene Blue and Low Level Laser Radiation in Head and Neck Squamous Cell Carcinoma Cell Lines. *Int. J. Mol. Sci.* **2018**, *19*, 1107, doi:10.3390/ijms19041107.

36. dos Santos, A.F.; Terra, L.F.; Wailemann, R.A.M.; Oliveira, T.C.; Gomes, V. de M.; Mineiro, M.F.; Meotti, F.C.; Bruni-Cardoso, A.; Baptista, M.S.; Labriola, L. Methylene blue photodynamic therapy induces selective and massive cell death in human breast cancer cells. *BMC Cancer* **2017**, *17*, 194, doi:10.1186/s12885-017-3179-7.

37. Romio, K.B.; dos Santos, K.F.; da Silva, R.J.; Pedro, M.F.C.; Kalck, A.S.; da Silva Sousa, M.; Possamai, L.M.; Souto, P.C.S.; Silva, J.R.; de Souza, N.C. Incorporation of triclosan and acridine orange into liposomes for evaluating the susceptibility of Candida albicans. *J. Photochem. Photobiol. B Biol.* **2017**, *173*, 514–521, doi:10.1016/j.jphotobiol.2017.06.034.

38. Shenderovich, I. The Partner Does Matter: The Structure of Heteroaggregates of Acridine

Orange in Water. *Molecules* **2019**, *24*, 2816, doi:10.3390/molecules24152816.

39.   Osman, H.; Elsahy, D.; Saadatzadeh, M.R.; Pollok, K.E.; Yocom, S.; Hattab, E.M.; Georges, J.; Cohen-Gadol, A.A. Acridine Orange as a Novel Photosensitizer for Photodynamic Therapy in Glioblastoma. *World Neurosurg.* **2018**, *114*, e1310–e1315, doi:10.1016/j.wneu.2018.03.207.

40.   Lin, Y.-C.; Lin, J.-F.; Tsai, T.-F.; Chen, H.-E.; Chou, K.-Y.; Yang, S.-C.; Tang, Y.-M.; Hwang, T.I.S. Acridine orange exhibits photodamage in human bladder cancer cells under blue light exposure. *Sci. Rep.* **2017**, *7*, 14103, doi:10.1038/s41598-017-13904-0.

41.   Ouyang, J.; Zhu, K.; Liu, Z.; Huang, J. Prooxidant Effects of Epigallocatechin-3-Gallate in Health Benefits and Potential Adverse Effect. *Oxid. Med. Cell. Longev.* **2020**, *2020*, 9723686, doi:10.1155/2020/9723686.

42.   Pires, F.; Santos, J.F.; Bitoque, D.; Silva, G.A.; Marletta, A.; Nunes, V.A.; Ribeiro, P.A.; Silva, J.C.; Raposo, M. Polycaprolactone/Gelatin Nanofiber Membranes Containing EGCG-Loaded Liposomes and Their Potential Use for Skin Regeneration. *ACS Appl. Bio Mater.* **2019**, *2*, 4790–4800, doi:10.1021/acsabm.9b00524.

43.   Mun, S.T.; Bae, D.H.; Ahn, W.S. Epigallocatechin gallate with photodynamic therapy enhances anti-tumor effects *in vivo* and *in vitro*. *Photodiagnosis Photodyn. Ther.* **2014**, *11*, 141–147, doi:10.1016/j.pdpdt.2014.03.003.

44.   Ferrario, A.; Luna, M.; Rucker, N.; Wong, S.; Gomer, C.J. Pro-apoptotic and anti-inflammatory properties of the green tea constituent epigallocatechin gallate increase photodynamic therapy responsiveness. *Lasers Surg. Med.* **2011**, *43*, 644–650, doi:10.1002/lsm.21081.

45.   Mondal, S.; Ghosh, S.; Moulik, S.P. Stability of curcumin in different solvent and solution media: UV–visible and steady-state fluorescence spectral study. *J. Photochem. Photobiol. B Biol.* **2016**, *158*, 212–218, doi:10.1016/j.jphotobiol.2016.03.004.

46.   Abdel Fadeel, D.A.; Kamel, R.; Fadel, M. PEGylated lipid nanocarrier for enhancing photodynamic therapy of skin carcinoma using curcumin: in-vitro/in-vivo studies and histopathological examination. *Sci. Rep.* **2020**, *10*, 10435, doi:10.1038/s41598-020-67349-z.

47.   Al Hageh, C.; Al Assaad, M.; El Masri, Z.; Samaan, N.; El-Sibai, M.; Khalil, C.; Khnayzer, R.S. A long-lived cuprous bis-phenanthroline complex for the photodynamic therapy of cancer. *Dalt. Trans.* **2018**, *47*, 4959–4967, doi:10.1039/C8DT00140E.

48.   Mari, C.; Pierroz, V.; Rubbiani, R.; Patra, M.; Hess, J.; Spingler, B.; Oehninger, L.; Schur, J.; Ott, I.; Salassa, L.; et al. DNA Intercalating Ru II Polypyridyl Complexes as Effective Photosensitizers in Photodynamic Therapy. *Chem. - A Eur. J.* **2014**, *20*, 14421–14436, doi:10.1002/chem.201402796.

49.   Karges, J.; Blacque, O.; Goldner, P.; Chao, H.; Gasser, G. Towards Long Wavelength Absorbing Photodynamic Therapy Photosensitizers via the Extension of a [Ru(bipy) 3] 2+ Core. *Eur. J. Inorg. Chem.* **2019**, *2019*, 3704–3712, doi:10.1002/ejic.201900569.

50.   Griendling, K.K.; Touyz, R.M.; Zweier, J.L.; Dikalov, S.; Chilian, W.; Chen, Y.-R.; Harrison,

D.G.; Bhatnagar, A. Measurement of Reactive Oxygen Species, Reactive Nitrogen Species, and Redox-Dependent Signaling in the Cardiovascular System. *Circ. Res.* **2016**, *119*, e39–e75, doi:10.1161/RES.0000000000000110.

51.   Klimaszewska-Wisniewska, A.; Halas-Wisniewska, M.; Tadrowski, T.; Gagat, M.; Grzanka, D.; Grzanka, A. Paclitaxel and the dietary flavonoid fisetin: a synergistic combination that induces mitotic catastrophe and autophagic cell death in A549 non-small cell lung cancer cells. *Cancer Cell Int.* **2016**, *16*, 10, doi:10.1186/s12935-016-0288-3.

52.   Kozar, I.; Margue, C.; Rothengatter, S.; Haan, C.; Kreis, S. Many ways to resistance: How melanoma cells evade targeted therapies. *Biochim. Biophys. Acta - Rev. Cancer* **2019**, *1871*, 313–322, doi:10.1016/j.bbcan.2019.02.002.

OPTIMIZATION OF NANOLIPOSOMES FOR THE TOPICAL DELIVERY OF PHOTOSENSITIZERS [1]

Abstract: Photodynamic therapy uses photosensitizer molecules for the photo-mediated treatment of several diseases such as cancer and skin disorders. However, most of the photosensitizer molecules present problems such as aggregation and low solubility in physiological environments which hinders the treatment efficacy. To overcome these problems, the development of stable liposomes as drug delivery systems of the photosensitizing molecules can be explored. Therefore, these systems turned into promising alternatives to enhance cellular uptake and the therapy's efficacy. In this work, liposomes composed by different lipids with or without surfactants were characterized for the encapsulation of photosensitizer molecules such as methylene blue (MB) and acridine orange (AO). Liposomes were produced by the thin-film hydration method followed by extrusion to reduce particles size and were characterized by Dynamic Light Scattering. Encapsulation efficiency was evaluated as well as the release profile of these molecules from the liposomes systems. To investigate the cytotoxicity and phototoxicity, studies on non-cancer keratinocytes and cancer keratinocytes were performed. Results showed that liposomes' stability depends on the composition of lipids in presence or not of surfactants. Most stable liposomes were mainly those with cholesterol plus the surfactants Span® 80 or sodium cholate that were able to provide higher stability for the liposomes considering the encapsulation of the MB and AO photosensitizers. Encapsulation efficiency (EE) studies revealed that AO had greater affinity for the vesicles presenting high EE (≥97%) while for MB the encapsulation was, in general, moderate (>60%). Greater phototoxicity was observed for MET1 SCC cells treated with AO-liposomes, achieving similar half-maximal inhibition concentration (IC_{50}) as for the free drug. Finally, two different possible approaches were found, namely, MB-liposomes with the potential as a cytotoxic agent for cancer cells; and AO-liposomes with a great phototoxicity potential at very low concentrations.

6.1 Introduction

Candidate drugs for photosensitizing application have been broadly explored essentially because of the interest that photodynamic therapy (PDT) has gained in the past few decades [1–3]. In PDT, three components are required for its effective action: a source of light, presence of oxygen and a photosensitizer (PS). Therefore, photosensitizing molecules have an important role for the efficacy of the treatment [4,5]. Photosensitizers are molecules that, under irradiation by specific wavelengths, can be excited and generate photochemical reactions that lead to cell death [1,6]. The photosensitizers should have limited dark cytotoxicity and capacity to result in cytotoxicity when submitted to light presenting a high quantum yield of $^1O_2$ [7,8].

The first class of photosensitizers were the hematoporphyrin derivatives such as Photofrin® which were the first to be approved for clinical use [9,10]. Second generation of photosensitizers such as phthalocyanine and benzoporphyrin have been developed to overcome problems provoked by the first generation such as the prolonged sensitization of the skin. The photosensitizers of the second generation can absorb light at longer wavelengths which influences in a deeper skin penetration and also cause less sensitization compared to the first class [10]. The third class of photosensitizers are currently being developed together with nanotechnology to achieve a better efficacy of PDT [10,11]. Other non-porphyrin like photosensitizers are also under investigation for the application in PDT including dyes such as rose bengal, phenothiazinium dyes (methylene blue, toluidine blue) and acridines [9,10]. An important strategy to enhance the efficacy of PDT is to ensure an adequate distribution of PS to the target tissue and, consequently, also to reduce side effects [1]. In this context, nanotechnology has emerged to overcome problems of traditional medicine [11].

Liposomes are self-assembled vesicles created from the spontaneous organization of phospholipids into a bilayer that tends to fold on itself resulting into a vesicle [12]. Due to the lipidic nature, liposomes present some advantages such as low toxicity, biodegradability and biocompatibility, thus can be used as drug carriers [13]. The composition of liposomes can be widely varied as there are a miscellaneous of options: positively charged, negatively charged or neutral lipids; natural and synthetic lipids; lipids with different degrees of saturation and many other features that must be taken into account for liposomes preparation [14]. Liposomes systems offer several advantages such as the encapsulation of hydrophilic and hydrophobic molecules as well as their release in a sustained way [15,16].

New derivatives of liposomes such as the transfersomes and ethosomes were developed in order to give more flexibility to the vesicles towards an enhanced permeation [17]. The transfersomes' composition consists of a phospholipid composition with addition of an edge activator like a surfactant while ethosomes present a high concentration of ethanol in their composition. Both systems are more flexible when compared to the conventional liposomes and due to the penetration enhancer, the vesicles can penetrate into deeper layers of the skin [15,18]. In the literature it is usually found the use of polysorbates (e.g., Tween® 20, Tween® 80), sorbitan esters (e.g., Span® 20, Span® 80), sodium cholate and sodium

deoxycholate as edge-active surfactants [19–21]. These single chain surfactants, at the certain concentrations, are able to provide a higher fluidity of the bilayer by the decrease of the interfacial tension [20,22]. It can also provide stability to the formulation and influence the size of the particle. Furthermore, these formulations can enhance the encapsulation of drugs [23].

Recent studies showed that the encapsulation of PS into liposomes was effective in suppressing tumor growth in several types of cancer such as for breast cancer, biliary tract cancer and gastric cancer [24–26]. Furthermore, encapsulation of PS reduced the dark cytotoxicity of the drug and improved the cellular uptake [27,28]. Under this compliance, there are many reasons to believe that liposomes are good carriers for phototherapy application, along with the advancement in the search and development of new photosensitizers.

The dyes methylene blue (MB) and acridine orange (AO) have been tested with nanoparticles for PDT applications. Jesus et al. [29], for example, studied the combination of gold nanoparticles and silver nanoparticles with MB in breast adenocarcinoma and MB encapsulated in polymeric nanoparticles were tested with dental plaque bacteria [30]. This shows a great opportunity of assembling MB with nanoparticles, which can be done with liposomes as some works demonstrated that MB in liposomes could be used as antibacterial and PDT of cancer cells [31,32]. AO is not as popular as MB, however, encapsulation of AO has been gaining attention in the last years such as the study of Liu et al. [33] that reported the encapsulation AO in mesoporous manganese dioxide nanoparticles for radiotherapy while Romio et al. [34] studied the incorporation of AO in liposomes with triclosan for antibacterial purpose.

In this study the optimization of liposomes prepared with the lipids 1,2-dipalmitoyl-sn-glycero-3-phosphocholine (DPPC), 1,2-dipalmitoyl-sn-glycero-3-phospho-(1'-rac-glycerol) sodium salt (DPPG), 1,2-Dioleoyl-sn-glycero-3-phospho-rac-(1-glycerol) sodium salt (DOPG) and cholesterol (CHOL) was tested without or with the surfactants Tween® 80, Span® 80 and sodium cholate in order to accomplish the most stable formulations for the encapsulation of the photosensitizers methylene blue and acridine orange. Liposomes were characterized regarding their size, the encapsulation efficiency and the release profile. *In vitro* studies showed that liposomes were, in general, tolerated by non-cancer cells likely to what was observed for the cancer cell line.

6.2 Materials and Methods

6.2.1 Materials

1,2-Dipalmitoyl-sn-glycero-3-phosphocholine (DPPC) was purchased from Tokyo Chemical Industry, 1,2-dipalmitoyl-sn-glycero-3-phospho-(1'-rac-glycerol) sodium salt (DPPG) was obtained from Avanti, 1,2-Dioleoyl-sn-glycero-3-phospho-rac-(1-glycerol) sodium salt (DOPG), cholesterol (CHOL), polysorbate 80 (Tween® 80), sorbitan monooleate (Span® 80), sodium cholate, methylene blue

and acridine orange hemi(zinc chloride) salt were obtained from Sigma-Aldrich. Dulbecco's Modified Eagle Medium (DMEM) and fetal bovine serum (FBS) were purchased from Biowest. Penicillin-Streptomycin and TrypLE™ Express Enzyme 1 X were purchased from Gibco.

6.2.2 Preparation of Liposomes

The lipids were prepared in a mixture of chloroform and methanol (8:2), dried gently using nitrogen air blast and submitted to vacuum overnight to remove solvent residues achieving a lipid film on the test tube walls. Mixture of lipids were tested and prepared according to Table 6.1, with a final concentration of 2 mg/mL. The liposomes were prepared by the thin-film hydration method [35] where, after dried, lipids were hydrated with phosphate-buffered saline (PBS) 10 mM, pH 7.4, and submitted to five cycles of heating and cooling with vortex agitation between cycles. Then, lipid suspensions were extruded 21 times through a 0.2 µm polycarbonate membranes (Avanti). The surfactants Tween® 80, Span® 80 and sodium cholate were also tested with the previously described lipid combinations achieving 5% (w/v) of surfactant in each liposomal preparation. For the encapsulation of the photosensitizers, MB and AO solutions in PBS were prepared at 0.1 mM and 0.05 mM, respectively, added during the hydration step and then the thin-film hydration procedure was equally performed. After the preparation, samples were stored at 4 ℃.

Table 6.1: Combination of lipids for liposomes preparation.

Liposomes	Proportion (weight ratio)			
	DPPC	DPPG	CHOL	DOPG
L1	7	3	-	-
L2	7	2	1	-
L3	7	2	-	1

The combinations described in Table 6.1 were based on the desire to obtain liposomes formulations with a high phase-transition temperature, which would be appropriate for topical delivery and would be more stable regarding temperature changes.

6.2.3 Characterization of Liposomes

Liposomes were evaluated by Dynamic Light Scattering (DLS) technique to obtain Z-average size and Polydispersity Index (PdI) of each formulation. Samples were prepared by the dilution of liposomes suspension in PBS (1:200) and analyzed by a Zetasizer Nano S (Malvern).

Encapsulation efficiency (EE) was evaluated through an indirect method using centrifugation. For the quantification of EE, liposomes were centrifuged at 5,000 x g in Amicon® Ultra Centrifugal filter [36] with a 10 kDa cut-off. The filtrate was evaluated by Ultraviolet-visible technique using a spectrophotometer (UV-2101PC, Shimadzu) and the unencapsulated amount was quantified using a calibration curve based on the absorbance at 664 nm and 486 nm for MB and AO, respectively. EE was calculated indirectly using Equation 6.1 where C_t is total concentration of MB or AO and C_f is the concentration of non-encapsulated drug found in the filtrate.

$$\text{Equation 6.1} \qquad EE(\%) = \frac{C_t - C_f}{C_t} \cdot 100$$

6.2.4 Release studies

For the study of the release profile of MB and AO from the liposomes suspensions MB_L2sp, MB_L2sc, AO_L2sp and AO_L2sc, where L2sp is related to L2 composition with Span® 80 and L2sc is related to the L2 composition with sodium cholate, were placed in a regenerated cellulose membrane (MWCO 12,000-14,000). The membrane was kept under stirring in release media (PBS 10 mM, pH 7.4). At selected times, an aliquot was removed and analysed by Ultraviolet-visible technique using a spectrophotometer (UV-2101PC, Shimadzu). An equal volume to the aliquot was replaced to maintain the sink condition. Quantification of MB and AO were based on the absorbance at 664 nm and 486 nm, respectively, and calculated according to Equation 6.2, where Q is the amount released, C_n is the concentration at the selected time, V_t is the total volume of PBS, V_a is the volume of aliquot withdrawn from the experiment and Q_t is the total amount of drug.

$$\text{Equation 6.2} \qquad Q(\%) = \frac{C_n \cdot V_t + \sum_{i=1}^{n} C_{n_i-1} \cdot V_a}{Q_t} \cdot 100$$

6.2.5 *In vitro* cytotoxicity and phototoxicity

6.2.5.1 Cell culture

MET1 SCC cells (squamous cells carcinoma) obtained from Ximbio and HaCaT cells obtained from AddexBio were cultured in DMEM, low glucose and high glucose, respectively, supplemented with 10% FBS and antibiotics (penicillin 100 U/mL and streptomycin 100 µg/mL. Cells were cultivated in an incubator (Sanyo MCO-19AIC-UV) at 37 °C in a 5% CO_2 humidified atmosphere. To release the

cells from the flasks was used TrypLE™ Express Enzyme 1X. For the assays, cells were counted and seeded in 96-well plates at a cell density of 20,000 cells/cm² and incubated overnight.

6.2.5.2   Cytotoxicity

Cells seeded on 96-well plates were treated with different samples of liposomes (L2, L2sp [with Span® 80] and L2sc [with sodium cholate]) with and without MB or AO. For that, the medium was aspirated from the 96-well plate and replaced by the samples diluted in the medium using the concentration range from 1.25 µM to 40 µM for MB and for AO from 0.31 µM to 10 µM. Cells without treatment and cells with 10% of DMSO were used as negative (NC) and positive control (PC), respectively. After 24 hours or 48 hours samples were removed, and cells were washed with PBS. Resazurin diluted in medium at a concentration of 0.02 mg/mL was added, and plates were incubated for 3 hours. The absorbance was measured in a microplate reader (ELX800UV, Biotek Instruments) using the wavelengths of 570 nm and 600 nm. The corrected absorbance is proportional to cell viability and propagation of uncertainties was used to calculate the combined standard uncertainty.

6.2.5.3   Phototoxicity

96-well plates already seeded with MET1 SCC cells were submitted to the treatment with liposomes by removing the medium and replacing with MB_L2, MB_L2sp or MB_L2sc diluted in medium using the range of 1.25 µM to 40 µM. The same was performed for AO_L2, AO_L2sp and AO_L2sc but with range of concentrations of 0.31 µM to 10 µM. Cells without treatment and cells treated with 10% DMSO were considered as NC and PC, respectively. After 24 hours the medium was removed, wells were washed with PBS and replaced by medium without phenol red. Plates used as dark control were kept in the dark while the others were irradiated at 640 nm or 457 nm for MB and AO-liposomes, respectively, with a dose of 2.5 J/cm². Plates were incubated for more 24 hours and lastly resazurin assay was performed as previously described in section 6.2.5.2.

6.3 Results and Discussions

6.3.1 Liposomes Characterization

A set of liposomes formulations was tested to evaluate different lipid compositions and their effect on Z-average size and PdI over time. The main lipidic compositions were based on the mass ratio proportion with 70% of DPPC while other lipids such as DPPG, DOPG and CHOL were included at lower percentages. DPPC is a zwitterionic phospholipid with a large polar portion and studies showed

that this the large polar "head" gives better stability against hydrolysis. The length of the acyl chain is directly connected to the gel-liquid crystal transition temperature, therefore larger lipids such as DPPC present better stability [37]. DPPG is an anionic lipid and is associated to a better encapsulation efficiency however, DPPG liposomes are usually unstable and tend to agglomerate, therefore, mixtures of DPPC and DPPG are often used as a model for cell membrane studies. Furthermore, the concentration of cholesterol is important to guarantee stability and modulation of the release [38].

Relying on these information, three main lipid compositions were prepared namely L1 (DPPC + DPPG), L2 (DPPC + DPPG + CHOL) and L3 (DPPC + DPPG + DOPG) with different proportions, as described in Table 6.1. Aiming the improvement of the formulation and to enhance stability, the following surfactant molecules were tested on these compositions: Tween® 80, Span® 80 or sodium cholate.

The stability was carried out during approximately one month using the parameters Z-average size and PdI as shown on Figure 6.1. L1 and derivatives compositions are represented by Figure 6.1 – A, where is possible to observe that L1 without surfactant present consistent size around 130 nm along time with low PdI that is maintained stable during the time analyzed. The addition of Tween® 80 shows great deviation on size measurements and increase of PdI from the second day of measurement which was also observed later, on the third measurement. On the other side, incorporation of Span® 80 to L1 showed slightly higher size than L1, also with an increase on the PdI until the last day of measurement. Differently from the other surfactants, sodium cholate addition apparently did not have effect on the size during the stability evaluation but exhibit a PdI increase.

L2 and derivative formulations with surfactants (Figure 6.1 – B) were the most stable group of liposomes during the stability studies. The presence of cholesterol had a great impact on the size of liposomes and the maintenance of the size and PdI over time [39,40]. On the first and last measurement, L2 present a size around 140 nm showing that this system is stable. Differently from L1, composition that do not contain cholesterol, the addition of the surfactants shows no significant difference between the formulations, with exception for Tween® 80 which present a slightly higher size.

The L3 composition contains DOPG, an unsaturated phospholipid that is known to be susceptible to a destabilization over time [41,42] as can be observed in Figure 6.1 – C, where liposomes prepared with this lipid showed initial PdI of 0.136 ± 0.060 and at the end of the stability study PdI was 0.288 ± 0.059. Liposomes L3 with the addition of Tween® 80 exhibited an increase of size and its deviation along time as well as the PdI with values higher than 0.200 at the first measurement. It was observed a continued increase of these parameters, which means the ease destabilization of this formulation. Differently from composition with Tween® 80, L3 prepared with Span® 80 and sodium cholate presented a slight increase of size and PdI, following a similar pattern as L3.
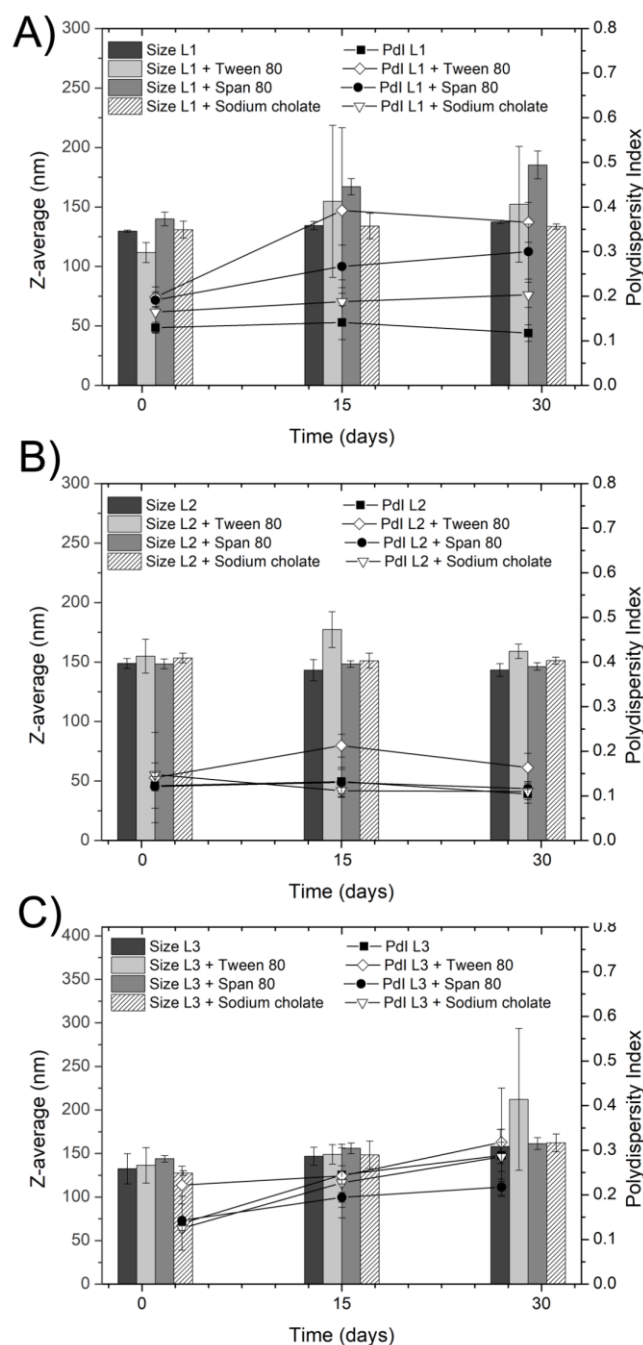
Figure 6.1: Comparison of Z-average size and PdI of different lipid compositions submitted to stability studies over time. A) Lipid composition L1 based on DPPC + DPPG without and with surfactants Tween® 80, Span® 80 and sodium cholate; B) Composition L2 based on DPPC + DPPG + CHOL without and with surfactants Tween® 80, Span 80® and sodium cholate; C) Lipid composition L3 based on DPPC + DPPG + DOPG without and with surfactants Tween® 80, Span® 80 and sodium cholate. Mean ± SD (n=3).

From the data shown in Figure 6.1, one can conclude that formulations L1 and L2 are more stable when compared with L3 liposomes which contain the unsaturated lipid DOPG. Despite the addition of surfactants, DOPG has unsaturation in its acyl chain that makes it more susceptible to destabilization. Regarding the addition of surfactants, Tween® 80 generally results on higher PdI and greater

deviation of particle size after a few days of preparation. Span® 80 based liposomes (L1sp, L2sp and L3sp) present different characteristics depending on the lipid composition. Liposomes with Span® 80 exhibited similar size around 144 nm on the first day of measurement and the PdI is higher for L1sp compared to L2sp and L3sp. However, after two and four weeks the particles increased their sizes for L1sp and L3sp as well as their PdI and L2 with Span® 80 remained with similar size and PdI. Similar pattern was observed for liposomes with sodium cholate (L1sc, L2sc and L3sc) that displayed L2sc as the most stable along time.

Two of the surfactants employed (Tween® 80 and Span® 80) are non-ionic surfactants while sodium cholate is an anionic bile salt, also used as surfactant. Tween® 80 has the lowest critical micelle concentration among the surfactants employed, which can indicate the formation of micelles and destabilization of the system over time [43,44].

For the continuation of the studies regarding the encapsulation of the MB and AO molecules, the liposomes systems L1, L2, L2sp and L2sc were selected. The concentration of photosensitizers used was 0.1 mM and 0.05 mM for MB and AO, respectively, and was determined according to the method of preparation and also considering the half-maximal inhibitory concentration (IC_{50}) of the molecules in the skin cancer cell line MET1 SCC. The size distribution of these four compositions of liposomes are exhibited in the Appendix for the empty liposomes (Appendix Figure B.1), liposomes with MB (Appendix Figure B.2) and with AO (Appendix Figure B.3).
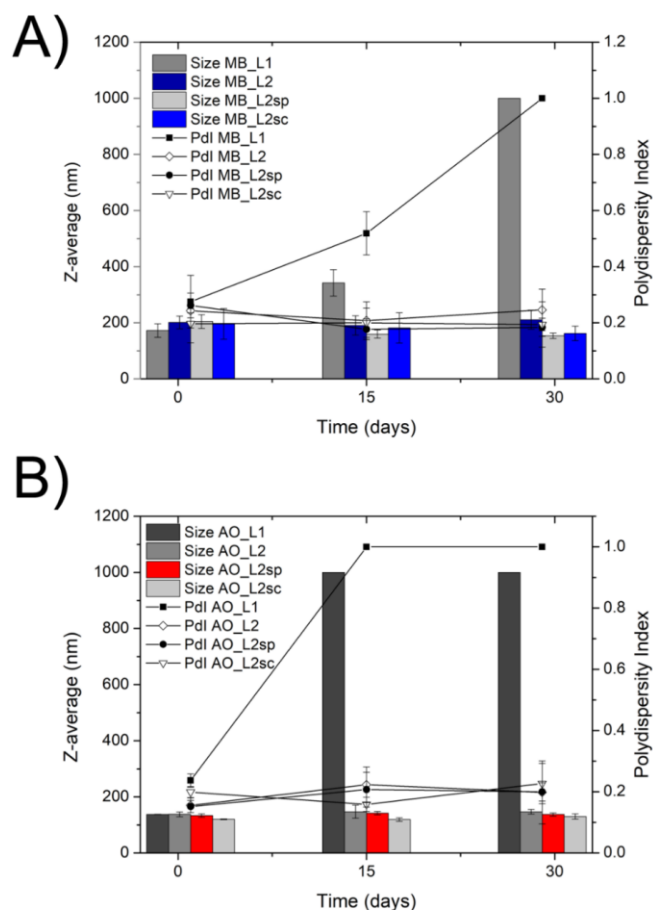
Figure 6.2: Z-average size and polydispersity index of liposomes with A) MB or B) AO. Values are displayed as mean and SD (n=3) and the measurements that showed micrometric particles (>1 μM) with high PdI are plotted as 1000 nm of Z-average and PdI of 1.0. MB: methylene blue, AO: acridine orange.

As displayed in Figure 6.2 – A, liposomes with MB, in general, have an increased size compared to empty liposomes, presenting sizes around 200 nm on the first day of measurement. The PdI of MB_L1, MB_L2 and MB_L2sp take values around 0.250 while MB_L2sc presents lower PdI value of 0.197. There is a clear difference in the stability between the samples mainly for liposomes MB_L1 that exhibit an increase in size along time while the others show a slight decrease. MB_L2 present a stable size around 200 nm and PdI around 0.240 during all the time studied as occur for the other formulations MB_L2sp and MB_L2sc with sizes around 170 nm and 180 nm, respectively, and PdI around 0.200 for both formulations. Therefore, one can conclude that MB_L2, MB_L2sp and MB_L2sc were stable along the time studied.

Table 6.2 shows the encapsulation efficiency of MB-liposomes, with EE values above 60%, which is a good encapsulation despite the hydrophilic characteristic of methylene blue. The formulations MB_L2 and MB_L2sp showed a higher EE (above 80%) while MB_L2sc formulation presents a lower EE. The higher encapsulation values for the liposomes containing cholesterol is an indication that the amount of cholesterol is adequate to the system, as the literature says that the concentration of

cholesterol has influence in the encapsulation and drug release [38]. The lower encapsulation of MB_L2sc liposomes is possibly connected to an existence of interaction between the surfactant sodium cholate, which is an anionic surfactant with a carboxyl group, and methylene blue that is a cationic dye. Furthermore, liposomes have in their composition DPPG that is a negatively charged phospholipid, indicating that part of the methylene blue is not encapsulated and is possibly attached to the liposomes' surface, interacting with sodium cholate and DPPG.

Table 6.2: Encapsulation efficiency (EE), cumulative release (CR) and time constant (τ) of liposomes with methylene blue (MB) and acridine orange (AO). Values are displayed as mean $\pm$ SD.

Liposomes	MB			AO		
	EE (%)	CR (%)	τ (h)	EE (%)	CR (%)	τ (h)
L1	74.5 ± 0.9	-	-	98.6 ± 1.3	-	-
L2	81.7 ± 2.6	-	-	99.6 ± 0.5	-	-
L2sp	85.9 ± 8.4	59.3 ± 2.2	0.33 ± 0.02	97.0 ± 2.5	32.9 ± 7.6	0.84 ± 0.13
L2sc	63.1 ± 4.6	70.0 ± 4.0	0.41 ± 0.04	98.8 ± 1.6	36.4 ± 5.6	2.00 ± 0.44

In contrast to the MB encapsulation, the dye AO shows different results in the size and PdI of the liposomes vesicles during the stability studies (Figure 6.2 – B). AO_L1 formulation presents destabilization with increase of size and PdI while the others kept size slightly lower than empty liposomes, showing values of 138.1 nm, 133.3 nm and 119.9 nm for AO_L2, AO_L2sp and AO_L2sc, respectively. These liposomes, differently from L1, do not show a significant difference in the size and PdI along time. The encapsulation of AO in liposomes is very different from MB with EE above 97%. AO is a slightly cationic dye, usually associated as a cell-permeable dye [45], showing that AO is hydrophobic enough to cross lipid membrane, which can indicate the affinity to the liposome bilayer or even its entrapment into the aqueous core.

6.3.2 Release studies

As we know that interaction between liposomes occurred differently for the dyes MB and AO, the release studies were performed to evaluate the profile of drug's liberation at physiological pH in PBS buffer. As shown in Figure 6.3 – A, the methylene blue is quickly released during the first two hours, with a more contained continuation of liberation resulting in a sustained release from the second to the fourth hour and achieving a plateau around 60% of MB release. The same profile is observed for both samples MB_L2sp and MB_L2sc, with a more prominent release from the liposomes containing sodium cholate in the composition. As previously discussed, in MB_L2sc there is the anionic surfactant sodium cholate, which possibly create an extra interaction that causes the attachment of MB in the

liposomes surface and explain the higher rate of MB release in the first two hours. This is corroborated by previous studies with MB in liposomes, which shows that indeed there is a fast release of MB [32]. The characteristic time constant (τ) values for the curves were obtained from the exponential fitting and are listed in Table 6.2.

For the liposomes containing AO (Figure 6.3 – B), the release profile is very different from MB, with a maximum release around of 35% in four hours, with a final plateau suggesting a sustained release from that point. This is in accordance with EE results, which show a much better encapsulation of AO in the liposomes, which also impact on a different rate of release when compared to MB. Romio et al. [34] studied the release profile of AO from DPPC liposomes in LBL films and showed release in question of a few hours and was enhanced by irradiation.
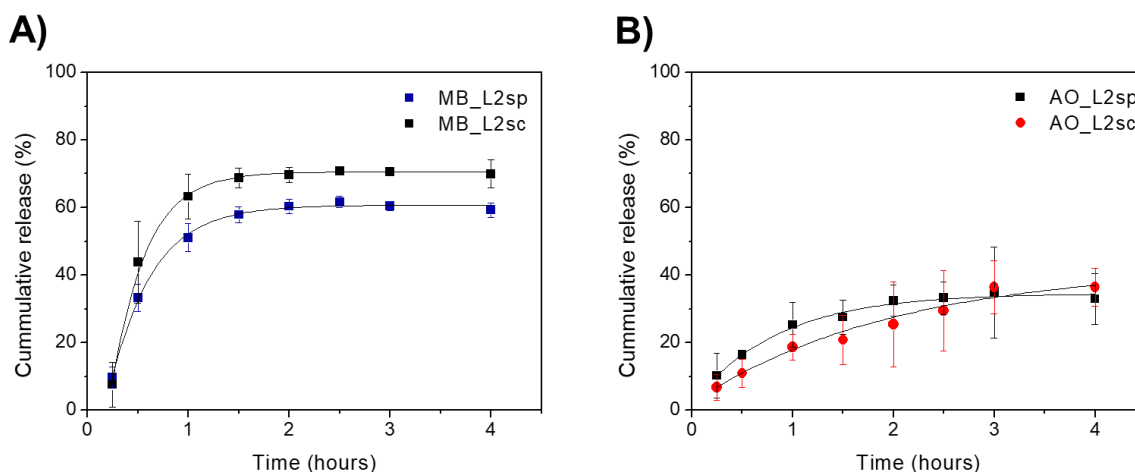
Figure 6.3: Release of MB (A) and AO (B) from liposomes composed by DPPC + DPPG + CHOL and Span® 80 (L2sp) or sodium cholate (L2sc). Values are displayed as mean ± SD (n=3). MB: methylene blue, AO: acridine orange.

6.3.3 Cytotoxicity in HaCaT and MET1 SCC cells

Cytotoxicity studies were performed in non-cancer and cancer keratinocytes cells. The encapsulation of drug in nanoparticles can affect the biological activity, therefore, it is important to evaluate the behaviour of MB and AO encapsulated in liposomes with different compositions.

Previous studies from our group showed that the PDT action of MB can be observed in a range of low concentrations mainly between 1.25 µM and 10 µM [46]. Therefore, the experiments with liposomes containing MB were executed in the range of 1.25 to 40 µM. The same volume of MB-liposomes used in the dilutions were used to study empty liposomes.

Cytotoxicity of empty liposomes in HaCaT cells and MET1 SCC cells are shown in Figure 6.4 – A and Figure 6.5 – A, respectively. It is possible to observe that, according to the ISO 10993-5 [47], all the empty liposomes were not cytotoxic in the 24 and 48 hours studies exhibiting cell viability above

90% at all the conditions. These results are important to show that the effect discovered for liposomes with the dyes are not inherent to the nanoparticles alone but to their combination with the molecules.

Cytotoxic studies in HaCaT cell line show the toxic potential of MB-liposomes (Figure 6.4 – B) and the IC_{50} obtained was below 11 µM (Table 6.3). Comparing the IC_{50} values of MET1 SCC and HaCaT in the 24 hours experiment, one observes that for MB-liposomes there is a decrease of these values for both cell lines when compared to MB non-encapsulated (MET1 SCC IC_{50} 14.2 µM and 4.2 µM; HaCaT IC_{50} 11.6 µM and 7.1 µM, for the 24 and 48 hours experiments, respectively [46]) . Despite 24 hours experiments values are very similar for both cell lines, one can observe slightly higher IC_{50} values in HaCaT cells for the longer periods of treatment. This indicates that liposomes with methylene blue can be more selective for the cancer cell line at longer periods of treatment. The same situation can be noticed for the AO-liposomes that showed, in HaCaT cells, slightly higher values of cell viability at the highest concentrations (Figure 6.4 – C) compared to MET1 SCC cells.

Figure 6.4: Cell viability of HaCaT cell line treated for 24 or 48 hours with liposomes: A) without dye, B) containing the dye methylene blue (MB), and C) containing acridine orange (AO). L2 is the liposome composition containing the lipids DPPC + DPPG + CHOL; L2sp is related to the liposomes with Span® 80 and L2sc to the
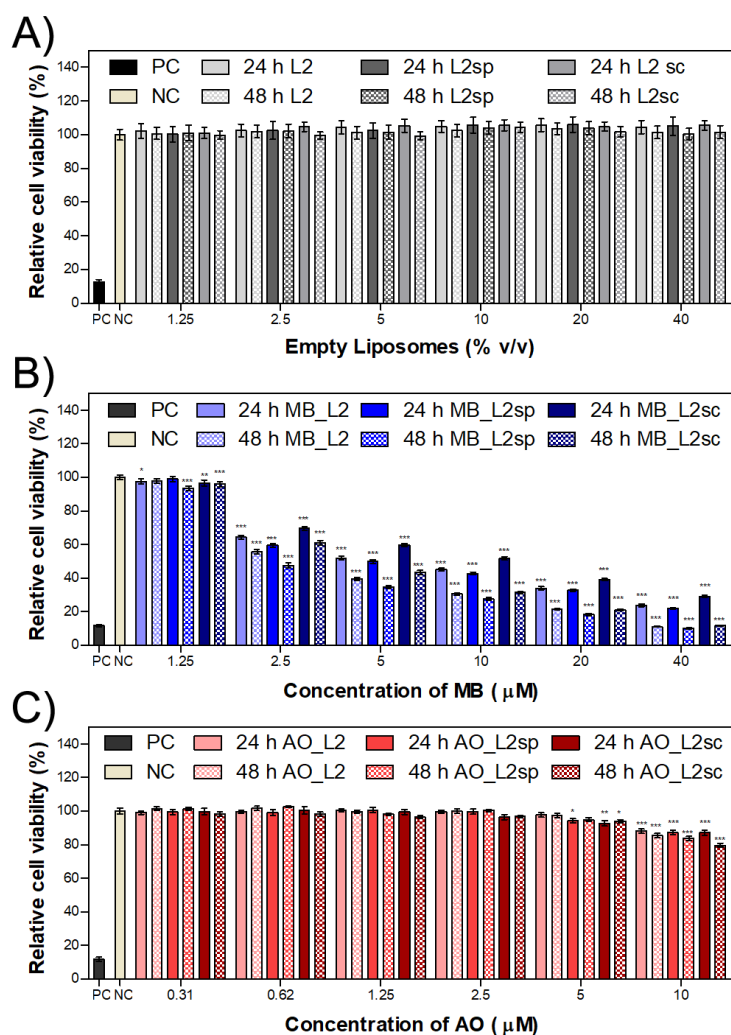
liposomes with sodium cholate. Values are presented by the mean $\pm$ combined standard uncertainty (n=3) and statistical analysis comparing the results to the cell viability of the negative control was performed by a two-way ANOVA with Bonferroni post-test where * p <0.05, ** p <0.01 and *** p <0.001.

In our results with MET1 SCC cells, one found that the IC_{50} of liposomes containing MB were lower than 11 µM (Table 6.3). The cell viability shows a pattern of severe cytotoxicity from the 2.5 µM mainly for the longer times of treatment (Figure 6.5 – B). For the IC_{50} values we can notice some differences between conventional liposome containing DPPC + DPPG + CHOL (MB_L2) and the others containing the surfactants Span® 80 and sodium cholate (MB_L2sp and MB_L2sc, respectively). For the 24 hours cytotoxicity there is a decrease in the IC_{50} for MB_L2sp and MB_L2sc, however, all the MB-encapsulated samples show a significant reduction of IC_{50} when compared to our previous studies with free MB (IC_{50} of 14.2 and 4.2 for 24 hours and 48 hours, respectively [46]). The encapsulation of MB into the liposomes increases the cytotoxicity by the cell viability reduction, which was previously reported by Wu et al. [32]. For the liposomes containing AO (Figure 6.5 – C) we studied a smaller range 0.31 µM to 10 µM and the MET1 SCC cell viability of these liposomes remained above 90%, indicating not be cytotoxic with exception of the concentration 10 µM AO in L2 and L2sc that showed moderate cytotoxicity in the 48 hours experiment [47].

Here, one can find two different possible approaches: liposomes containing MB with an enhanced cytotoxicity, and liposomes containing AO with no cytotoxicity at the range studied. It is interesting to observe both different systems, with different effects, can result in distinct applications. Considering the search for more effective anticancer drugs, with the potential administration of lower dose, which can suggest a reduced side effective, liposomes containing MB seems like a promising system for the treatment of skin cancer. In the meanwhile, liposomes containing AO do not suit as an anticancer system by itself, at least at the conditions studied, however, the application of AO-liposome in PDT is investigated further ahead.

Table 6.3: Calculated IC_{50} of 24 and 48 hours cytotoxicity experiments using MET1 SCC cells treated with liposomes containing the dye methylene blue (MB). L2 is the liposome composition containing the lipids DPPC + DPPG + CHOL; L2sp is related to the liposomes with Span® 80 and L2sc to the liposomes with sodium cholate.

Liposome	IC_{50} (µM)			
	MET1 SCC		HaCaT	
	24 h	48 h	24 h	48 h
MB_L2	10.3	3.4	7.8	4.4
MB_L2sp	7.8	3.2	7.0	3.6
MB_L2sc	8.4	3.3	10.9	4.9
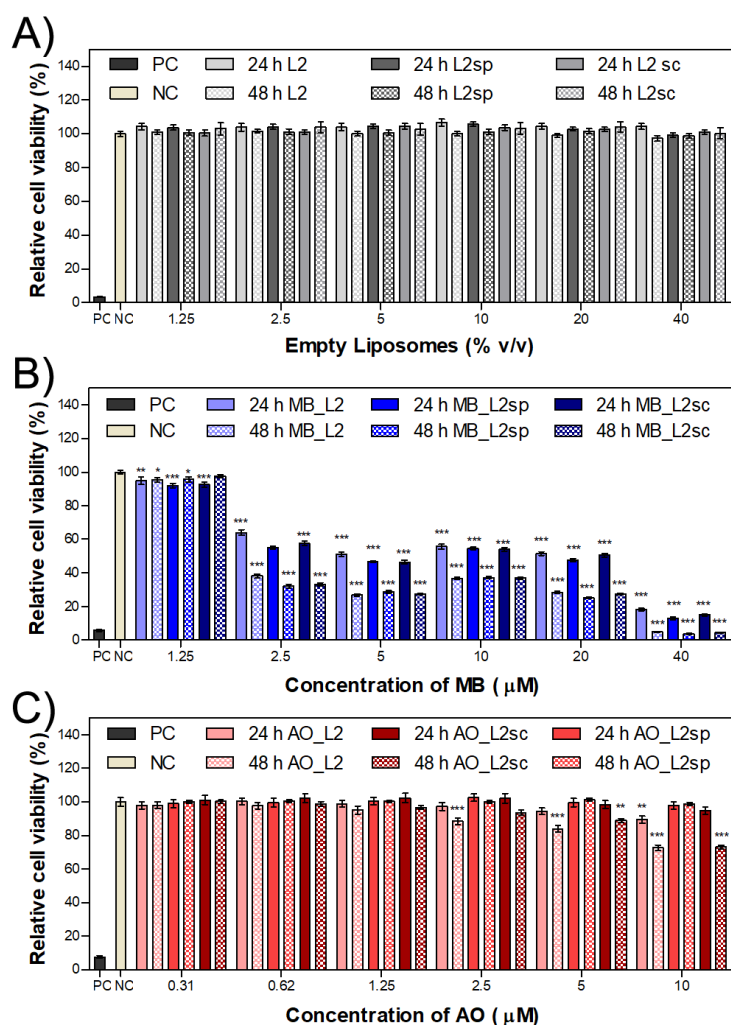
Figure 6.5: Cytotoxicity studies in MET1 SCC cell line treated for 24 or 48 hours with liposomes: A) without any dye, B) containing the dye methylene blue (MB), and C) containing Acridine Orange (AO). L2 is the liposome composition containing the lipids DPPC + DPPG + CHOL; L2sp is related to the liposomes with Span® 80 and L2sc to the liposomes with sodium cholate. Values are presented by the mean ± combined standard uncertainty (n=3) and statistical analysis comparing the results to the cell viability of the negative control was performed by a two-way ANOVA with Bonferroni post-test where * p <0.05, ** p <0.01 and *** p <0.001.

6.3.4 Phototoxicity in MET1 SCC cells

Phototoxicity assays were done to evaluate the proper delivery of drugs and photosensitizing effect in cells treated with liposomes containing the selected PS.

It is possible to visualize a significant difference between the controls of cells treated with MB-liposomes kept in dark and those irradiated by a 640 nm LED light (Figure 6.6 – A). The most significant effect can be observed for the concentrations of 2.5 µM, 5 µM and 10 µM due to a high viability of the controls in the dark (above 70% of cell viability) while the irradiated cells present lower cell viability. Here, one cannot notice a big difference between the three liposomal compositions, however we can see

that, in fact, MB-liposomes are able to generate phototoxicity. As we can see in Table 6.4, the phototoxic IC_{50} values of MB-liposomes are around 5 µM, slightly higher than free MB ($IC_{50} = 3.8$ µM).

AO-liposomes are not toxic at dark conditions (Figure 6.6 – B), however, for the cells treated with AO-liposomes and irradiated by a 457 nm LED light, one can see a significant decrease in cell viability with the increase of AO concentration. From the concentration 0.62 µM AO-liposomes are already phototoxic, with exception of AO_L2sc containing sodium cholate, that show viability around 80%. This can be attributed to the dual action of some bile salts such as sodium cholate and sodium deoxycholate that are able to increase cancer cells viability at low concentrations while there is a decrease at high concentrations of these surfactants [48]. The greater phototoxicity was observed for AO_L2 and AO_L2sp with IC_{50} of 0.6 µM and 0.5 µM, respectively (Table 6.4). Comparing these results to phototoxicity studies of free AO ($IC_{50} = 0.4$ µM), as previously studied [46], show that except for AO_L2sc, liposomes were able to conduct to a very similar phototoxicity as the one obtained for the free photosensitizer.

Indeed, MB-liposomes and AO-liposomes present different situation regarding their phototoxicity as one can see that the IC_{50} values of AO-liposomes are much lower than the ones of MB-liposomes. It is a result that can be directly related to the light source due to the higher frequency of blue light that carries more energy than red light. Therefore, it is important to take in consideration the dose of light and its energy to obtain a more efficient PDT.

Table 6.4: Values of IC_{50} from the phototoxicity studies in MET1 SCC cells treated with the liposomes containing methylene blue (MB) or acridine orange (AO). L2 is the liposome composition containing the lipids DPPC + DPPG + CHOL; L2sp is related to the liposomes with Span® 80 and L2sc to the liposomes with sodium cholate.

	IC_{50} (µM)		
Sample	**L2**	**L2sp**	**L2sc**
MB	5.6	5.6	5.3
AO	0.6	0.5	1.0
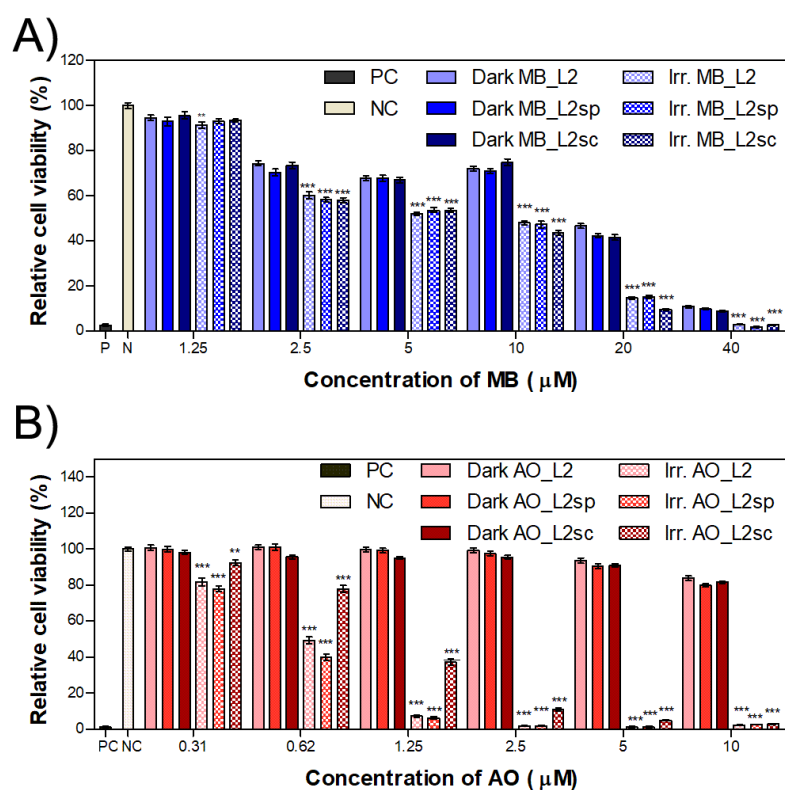
Figure 6.6: Cell viability from the phototoxicity studies in MET1 SCC cells treated with the liposomes containing: A) methylene blue (MB), and B) containing acridine orange (AO). L2 is the liposome composition containing the lipids DPPC + DPPG + CHOL; L2sp is related to the liposomes with Span® 80 and L2sc to the liposomes with sodium cholate. Values are presented by the mean ± combined standard uncertainty (n=3) and statistical analysis comparing the results to the cell viability of the respective dark control was performed by a Two-way ANOVA with Bonferroni post-test where ** p <0.01 and *** p <0.001.

6.4 Conclusions

Liposomes were prepared with different lipid compositions and were also tested with the surfactants Tween® 80, Span® 80, sodium cholate and, apart from vesicles containing only DPPC + DPPG, liposomes with cholesterol in the composition were the most stable even when considered the addition with the surfactants Span® 80 and sodium cholate. These are also able to provide higher stability for the liposomes regarding the encapsulation of the photosensitizers MB and AO, while the same is not observed for DPPC+ DPPG only. Encapsulation efficiency shows that AO had greater affinity for the vesicles presenting high EE (≥97%) while for MB the encapsulation was, in general, moderated (>60%), resulting in a slower and a faster release, respectively. Analysis of the cytotoxicity and phototoxicity studies on keratinocytes with and without carcinoma show that empty liposomes are not cytotoxic while at the concentrations tested MB-liposomes present cytotoxicity in skin cancer cell line. Liposomes with acridine orange can be more selective for the cancer cell line since was demonstrated that in HaCaT

cells were obtained slightly higher values of cell viability at the highest concentrations. Greater photo-toxicity is observed for MET1 SCC cells treated with AO-liposomes, achieving similar IC_{50} as occurs for free drug. Two different possible approaches can summarize the biological results found in this work: MB-liposomes with the potential as a cytotoxic agent for cancer cells; and AO-liposomes with a great potential phototoxicity at very low concentrations.

Acknowledgments

References

1. Zhang, J.; Jiang, C.; Figueiró Longo, J.P.; Azevedo, R.B.; Zhang, H.; Muehlmann, L.A. An updated overview on the development of new photosensitizers for anticancer photodynamic therapy. *Acta Pharm. Sin. B* **2018**, *8*, 137–146, doi:10.1016/j.apsb.2017.09.003.

2. Kim, J.; Jo, Y.; Na, K. Photodynamic therapy with smart nanomedicine. *Arch. Pharm. Res.* **2020**, *43*, 22–31, doi:10.1007/s12272-020-01214-5.

3. Pivetta, T.P.; Botteon, C.E.A.; Ribeiro, P.A.; Marcato, P.D.; Raposo, M. Nanoparticle Systems for Cancer Phototherapy: An Overview. *Nanomaterials* **2021**, *11*, 3132, doi:10.3390/nano11113132.

4. Gunaydin, G.; Gedik, M.E.; Ayan, S. Photodynamic Therapy for the Treatment and Diagnosis of Cancer–A Review of the Current Clinical Status. *Front. Chem.* **2021**, *9*, 686303, doi:10.3389/fchem.2021.686303.

5. Vallejo, M.C.S.; Moura, N.M.M.; Gomes, A.T.P.C.; Joaquinito, A.S.M.; Faustino, M.A.F.; Almeida, A.; Gonçalves, I.; Serra, V.V.; Neves, M.G.P.M.S. The Role of Porphyrinoid Photosensitizers for Skin Wound Healing. *Int. J. Mol. Sci.* **2021**, *22*, 234, doi:10.3390/ijms22084121.

6. Mfouo-Tynga, I.S.; Dias, L.D.; Inada, N.M.; Kurachi, C. Features of third generation photosensitizers used in anticancer photodynamic therapy: Review. *Photodiagnosis Photodyn.*

Ther. **2021**, *34*, 102091, doi:10.1016/j.pdpdt.2020.102091.

7. Kou, J.; Dou, D.; Yang, L. Porphyrin photosensitizers in photodynamic therapy and its applications. *Oncotarget* **2017**, *8*, 81591–81603, doi:10.18632/oncotarget.20189.

8. Juarranz, Á.; Jaén, P.; Sanz-Rodríguez, F.; Cuevas, J.; González, S. Photodynamic therapy of cancer. Basic principles and applications. *Clin. Transl. Oncol.* **2008**, *10*, 148–154, doi:10.1007/s12094-008-0172-2.

9. Abrahamse, H.; Hamblin, M.R. New photosensitizers for photodynamic therapy. *Biochem. J.* **2016**, *473*, 347–364, doi:10.1042/BJ20150942.

10. O'Connor, A.E.; Gallagher, W.M.; Byrne, A.T. Porphyrin and Nonporphyrin Photosensitizers in Oncology: Preclinical and Clinical Advances in Photodynamic Therapy. *Photochem. Photobiol.* **2009**, *85*, 1053–1074, doi:10.1111/j.1751-1097.2009.00585.x.

11. Liu, R.; Gao, Y.; Liu, N.; Suo, Y. Nanoparticles loading porphyrin sensitizers in improvement of photodynamic therapy for ovarian cancer. *Photodiagnosis Photodyn. Ther.* **2021**, *33*, 102156, doi:10.1016/j.pdpdt.2020.102156.

12. Balazs, D.A.; Godbey, W. Liposomes for Use in Gene Delivery. *J. Drug Deliv.* **2011**, *2011*, 326497, doi:10.1155/2011/326497.

13. Nakhaei, P.; Margiana, R.; Bokov, D.O.; Abdelbasset, W.K.; Jadidi Kouhbanani, M.A.; Varma, R.S.; Marofi, F.; Jarahian, M.; Beheshtkhoo, N. Liposomes: Structure, Biomedical Applications, and Stability Parameters With Emphasis on Cholesterol. *Front. Bioeng. Biotechnol.* **2021**, *9*, 705886, doi:10.3389/fbioe.2021.705886.

14. Large, D.E.; Abdelmessih, R.G.; Fink, E.A.; Auguste, D.T. Liposome composition in drug delivery design, synthesis, characterization, and clinical application. *Adv. Drug Deliv. Rev.* **2021**, *176*, 113851, doi:10.1016/j.addr.2021.113851.

15. Hua, S. Lipid-based nano-delivery systems for skin delivery of drugs and bioactives. *Front. Pharmacol.* **2015**, *6*, 2019, doi:10.3389/fphar.2015.00219.

16. Akbarzadeh, A.; Rezaei-sadabady, R.; Davaran, S.; Joo, S.W.; Zarghami, N. Liposome : classification , preparation , and applications. *Nanoscale Res. Lett.* **2013**, *8*, 102, doi:10.1186/1556-276X-8-102.

17. Sudhakar, K.; Fuloria, S.; Subramaniyan, V.; Sathasivam, K. V.; Azad, A.K.; Swain, S.S.; Sekar, M.; Karupiah, S.; Porwal, O.; Sahoo, A.; et al. Ultraflexible Liposome Nanocargo as a Dermal and Transdermal Drug Delivery System. *Nanomaterials* **2021**, *11*, 2557, doi:10.3390/nano11102557.

18. Ascenso, A.; Raposo, S.; Batista, C.; Cardoso, P.; Mendes, T.; Praça, F.G.; Bentley, M.V.L.B.; Simões, S. Development , characterization , and skin delivery studies of related ultradeformable vesicles: transfersomes , ethosomes , and transethosomes. *Int. J. Nanomedicine* **2015**, *10*, 5837–5851.

19. Khan, I.; Needham, R.; Yousaf, S.; Houacine, C.; Islam, Y.; Bnyan, R.; Sadozai, S.K.; Elrayess,

M.A.; Elhissi, A. Impact of phospholipids, surfactants and cholesterol selection on the performance of transfersomes vesicles using medical nebulizers for pulmonary drug delivery. *J. Drug Deliv. Sci. Technol.* **2021**, *66*, 102822, doi:10.1016/j.jddst.2021.102822.

20. Zhang, J.; Froelich, A.; Michniak-Kohn, B. Topical Delivery of Meloxicam using Liposome and Microemulsion Formulation Approaches. *Pharmaceutics* **2020**, *12*, 282, doi:10.3390/pharmaceutics12030282.

21. Sguizzato, M.; Esposito, E.; Cortesi, R. Lipid-Based Nanosystems as a Tool to Overcome Skin Barrier. *Int. J. Mol. Sci.* **2021**, *22*, 8319, doi:10.3390/ijms22158319.

22. Singh, S.; Vardhan, H.; Kotla, N.G.; Maddiboyina, B.; Sharma, D.; Webster, T.J. The role of surfactants in the formulation of elastic liposomal gels containing a synthetic opioid analgesic. *Int. J. Nanomedicine* **2016**, *11*, 1475–1482, doi:10.2147/IJN.S100253.

23. Gaynanova, G.; Vasileva, L.; Kashapov, R.; Kuznetsova, D.; Kushnazarova, R.; Tyryshkina, A.; Vasilieva, E.; Petrov, K.; Zakharova, L.; Sinyashin, O. Self-Assembling Drug Formulations with Tunable Permeability and Biodegradability. *Molecules* **2021**, *26*, 6786, doi:10.3390/molecules26226786.

24. Yang, Y.; Yang, X.; Li, H.; Li, C.; Ding, H.; Zhang, M.; Guo, Y.; Sun, M. Near-infrared light triggered liposomes combining photodynamic and chemotherapy for synergistic breast tumor therapy. *Colloids Surfaces B Biointerfaces* **2019**, *173*, 564–570, doi:10.1016/j.colsurfb.2018.10.019.

25. Kim, D.H.; Im, B.N.; Hwang, H.S.; Na, K. Gemcitabine-loaded DSPE-PEG-PheoA liposome as a photomediated immune modulator for cholangiocarcinoma treatment. *Biomaterials* **2018**, *183*, 139–150, doi:10.1016/j.biomaterials.2018.08.052.

26. Igarashi, A.; Konno, H.; Tanaka, T.; Nakamura, S.; Sadzuka, Y.; Hirano, T.; Fujise, Y. Liposomal photofrin enhances therapeutic efficacy of photodynamic therapy against the human gastric cancer. *Toxicol. Lett.* **2003**, *145*, 133–141, doi:10.1016/S0378-4274(03)00241-8.

27. Duse, L.; Pinnapireddy, S.R.; Strehlow, B.; Jedelská, J.; Bakowsky, U. Low level LED photodynamic therapy using curcumin loaded tetraether liposomes. *Eur. J. Pharm. Biopharm.* **2018**, *126*, 233–241, doi:10.1016/j.ejpb.2017.10.005.

28. Gaio, E.; Scheglmann, D.; Reddi, E.; Moret, F. Uptake and photo-toxicity of Foscan®, Foslip® and Fospeg® in multicellular tumor spheroids. *J. Photochem. Photobiol. B Biol.* **2016**, *161*, 244–252, doi:10.1016/j.jphotobiol.2016.05.011.

29. Jesus, V.P.S.; Raniero, L.; Lemes, G.M.; Bhattacharjee, T.T.; Caetano Júnior, P.C.; Castilho, M.L. Nanoparticles of methylene blue enhance photodynamic therapy. *Photodiagnosis Photodyn. Ther.* **2018**, *23*, 212–217, doi:10.1016/j.pdpdt.2018.06.011.

30. Klepac-Ceraj, V.; Patel, N.; Song, X.; Holewa, C.; Patel, C.; Kent, R.; Amiji, M.M.; Soukos, N.S. Photodynamic effects of methylene blue-loaded polymeric nanoparticles on dental plaque bacteria. *Lasers Surg. Med.* **2011**, *43*, 600–606, doi:10.1002/lsm.21069.

31.   Boccalini, G.; Conti, L.; Montis, C.; Bani, D.; Bencini, A.; Berti, D.; Giorgi, C.; Mengoni, A.; Valtancoli, B. Methylene blue-containing liposomes as new photodynamic anti-bacterial agents. *J. Mater. Chem. B* **2017**, *5*, 2788–2797, doi:10.1039/C6TB03367A.

32.   Wu, P.-T.; Lin, C.-L.; Lin, C.-W.; Chang, N.-C.; Tsai, W.-B.; Yu, J. Methylene-Blue-Encapsulated Liposomes as Photodynamic Therapy Nano Agents for Breast Cancer Cells. *Nanomaterials* **2019**, *9*, 14, doi:10.3390/nano9010014.

33.   Liu, J.; Zhang, W.; Kumar, A.; Rong, X.; Yang, W.; Chen, H.; Xie, J.; Wang, Y. Acridine Orange Encapsulated Mesoporous Manganese Dioxide Nanoparticles to Enhance Radiotherapy. *Bioconjug. Chem.* **2020**, *31*, 82–92, doi:10.1021/acs.bioconjchem.9b00751.

34.   Romio, K.B.; dos Santos, K.F.; da Silva, R.J.; Pedro, M.F.C.; Kalck, A.S.; da Silva Sousa, M.; Possamai, L.M.; Souto, P.C.S.; Silva, J.R.; de Souza, N.C. Incorporation of triclosan and acridine orange into liposomes for evaluating the susceptibility of Candida albicans. *J. Photochem. Photobiol. B Biol.* **2017**, *173*, 514–521, doi:10.1016/j.jphotobiol.2017.06.034.

35.   Duarte, A.A.; Botelho do Rego, A.M.; Salerno, M.; Ribeiro, P.A.; El Bari, N.; Bouchikhi, B.; Raposo, M. DPPG Liposomes Adsorbed on Polymer Cushions: Effect of Roughness on Amount, Surface Composition and Topography. *J. Phys. Chem. B* **2015**, *119*, 8544–8552, doi:10.1021/acs.jpcb.5b02384.

36.   Panikar, S.S.; Ramírez-García, G.; Banu, N.; Vallejo-Cardona, A.A.; Lugo-Fabres, P.; Camacho-Villegas, T.A.; Salas, P.; De la Rosa, E. Ligand-targeted Theranostic Liposomes combining methylene blue attached upconversion nanoparticles for NIR activated bioimaging and photodynamic therapy against HER-2 positive breast cancer. *J. Lumin.* **2021**, *237*, 118143, doi:10.1016/j.jlumin.2021.118143.

37.   Anderson, M.; Omri, A. The Effect of Different Lipid Components on the *In Vitro* Stability and Release Kinetics of Liposome Formulations. *Drug Deliv.* **2004**, *11*, 33–39, doi:10.1080/10717540490265243.

38.   Roy, B.; Guha, P.; Bhattarai, R.; Nahak, P.; Karmakar, G.; Chettri, P.; Panda, A.K. Influence of Lipid Composition, pH, and Temperature on Physicochemical Properties of Liposomes with Curcumin as Model Drug. *J. Oleo Sci.* **2016**, *65*, 399–411, doi:10.5650/jos.ess15229.

39.   Shaker, S.; Gardouh, A.; Ghorab, M. Factors affecting liposomes particle size prepared by ethanol injection method. *Res. Pharm. Sci.* **2017**, *12*, 346–352, doi:10.4103/1735-5362.213979.

40.   Khvedelidze, M.; Mdzinarashvili, T.; Shekiladze, E.; Schneider, M.; Moersdorf, D.; Bernhardt, I. Structure of drug delivery DPPA and DPPC liposomes with ligands and their permeability through cells. *J. Liposome Res.* **2015**, *25*, 20–31, doi:10.3109/08982104.2014.911316.

41.   Shahidi, F.; Zhong, Y. Lipid oxidation and improving the oxidative stability. *Chem. Soc. Rev.* **2010**, *39*, 4067–4079, doi:10.1039/b922183m.

42.   Qiao, L.; Ge, A.; Osawa, M.; Ye, S. Structure and stability studies of mixed monolayers of saturated and unsaturated phospholipids under low-level ozone. *Phys. Chem. Chem. Phys.* **2013**,

15, 17775–17785, doi:10.1039/c3cp52484a.

43. Badran, M.; Shalaby, K.; Al-Omrani, A. Influence of the Flexible Liposomes on the Skin Deposition of a Hydrophilic Model Drug, Carboxyfluorescein: Dependency on Their Composition. *Sci. World J.* **2012**, *2012*, 134876, doi:10.1100/2012/134876.

44. Owusu Apenten, R.K.; Zhu, Q.-H. Interfacial parameters for selected Spans and Tweens at the hydrocarbon—water interface. *Food Hydrocoll.* **1996**, *10*, 27–30, doi:10.1016/S0268-005X(96)80050-6.

45. Lin, Y.-C.; Lin, J.-F.; Tsai, T.-F.; Chen, H.-E.; Chou, K.-Y.; Yang, S.-C.; Tang, Y.-M.; Hwang, T.I.S. Acridine orange exhibits photodamage in human bladder cancer cells under blue light exposure. *Sci. Rep.* **2017**, *7*, 14103, doi:10.1038/s41598-017-13904-0.

46. Pivetta, T.P.; Vieira, T.; Silva, J.C.; Ribeiro, P.A.; Raposo, M. Screening on cells of the phototoxic potential of different DNA-intercalators to be applied on skin cancer therapy. *Submitted manuscript*.

47. ISO 10993-5:2009 Biological evaluation of medical devices — Part 5: Tests for *in vitro* cytotoxicity. *International Organisation for Standardization*.

48. Gándola, Y.B.; Fontana, C.; Bojorge, M.A.; Luschnat, T.T.; Moretton, M.A.; Chiapetta, D.A.; Verstraeten, S. V.; González, L. Concentration-dependent effects of sodium cholate and deoxycholate bile salts on breast cancer cells proliferation and survival. *Mol. Biol. Rep.* **2020**, *47*, 3521–3539, doi:10.1007/s11033-020-05442-2.

Exploiting the use of Acridine Orange and Methylene Blue in biological systems I:
an Analysis of the Dyes effects on the DNA [1]

Abstract: As a vital biomolecule, DNA is a known target of antineoplastic drugs for the cancer therapy. These drugs can show different modes of interaction with the DNA, being the intercalation and groove binding the most common types. The intercalation of anticancer drugs with the DNA can lead to the disruption of its normal function, influencing on the cell proliferation. Methylene blue (MB) and acridine orange (AO) are examples of DNA-intercalating agents that have been studied for the application against some types of cancer, mainly for the photodynamic therapy. In this work, the impact of the irradiation on these compounds in the absence and presence of the DNA was analyzed by UV-vis spectroscopy. Bathochromic and hypochromic shifts were observed in the absorbance spectra revealing the intercalation of the dyes with the DNA base pairs. Dyes with and without DNA present different profile of photodegradation, where the dyes alone are more susceptible to degradation. This is justified by the intercalation of the dyes on the DNA bases pairs allowing that DNA molecule partially hinders the molecules exposition and, therefore, reducing their degradation.

7.1 Introduction

In living cells, the deoxyribonucleic acid (DNA) play an important role as the macromolecule responsible for the genetic information carriage and proper development and division of cells and it is involved in several processes such as the synthesis of proteins, enzymes, mutagenesis and carcinogenesis [1]. DNA is often pointed as a target for drugs used in cancer therapy [2]. These drugs can interact

---

[1] This chapter is based on the manuscript submitted for publication:

Pivetta, T.P., Ribeiro, P.A., Raposo, M. Analyzing the effect of irradiation plus the dyes Methylene Blue and Acridine Orange on the DNA.

with the DNA mainly by intercalation or by groove binding. DNA-intercalating molecules can interact by the insertion of these molecules between the DNA base pairs leading to a disrupt in the normal function and can consequently affect cell proliferation, resulting in an anticancer activity [3–5].

Methylene blue (MB) is a photosensitizing agent that has been employed in many studies based on photodynamic therapy (PDT) for different types of cancer such as breast cancer, melanoma, cervical cancer [6–9]. Due to the cationic nature of MB, it can interact with the DNA phosphate backbone through electrostatic interaction while a second possible interaction is attributed to the stacking with the DNA base pair, therefore, in the intercalation mode [10–13].

Acridine orange (AO) is a weak base and a known intercalating agent that is widely used in fluorescence. AO molecules can interact with acidic molecules such as the double-strand DNA resulting in green fluorescence or with single-strand DNA or RNA resulting in red fluorescence and can also interact with acidic structures such as the lysosomes [10,14–17]. AO already demonstrated promising application with PDT in bladder cancer and glioblastoma [18,19]. Furthermore, AO can be more selective to cancer cells. This selectivity is due to cancer cells that present an acidic environment while normal cells are not acidic and, therefore, can eliminate AO quickly [20]. The dimeric form of AO presents electrostatic interactions predominantly to the DNA external part while the monomeric form acts mostly as intercalator of the DNA base pairs [1]. As studied previously by Amado et al. [21], the interaction of DNA with AO present two stages related to changes in the spectra with the increase of DNA. At low DNA concentrations it presents a decrease in the ratio of absorbance at 490/470 and at a second stage there is an increase in the ratio, indicating an aggregation of AO. Therefore, there is a certain proportion between AO and DNA that determines the mode of interaction.

For the application of drugs that interact with the DNA, it is important to comprehend the involved interactions [1] as well as the effect of radiation on both DNA and molecules during PDT. Results obtained in previous studies in cell culture showed the potential of MB and AO molecules acting as photosensitizers [22]. As known DNA-intercalating agents, these compounds can play an important role in the photo-mediated damage of cancer cells. In this work, the interaction and the effect of radiation at different wavelengths was investigated for the MB and AO molecules in the absence and presence of DNA. Results demonstrated that the effect of radiation is stronger on the MB and AO molecules, while in the presence of DNA molecules were not as susceptible to degradation as for molecules only.

7.2 Materials and Methods

7.2.1 Materials

Calf thymus DNA (ct-DNA), tris-HCl, methylene blue and acridine orange were obtained from Sigma-Aldrich.

7.2.2 Preparation of samples

Stock solution of ct-DNA was prepared by dissolving 50 mg of ct-DNA in tris-HCl buffer 10 mM pH 7.4. To completely dissolve DNA, it was stirred for 48 hours and after complete dissolution of DNA fibers, it was transferred to a volumetric flask and the volume was adjusted with the buffer.

The compounds solutions were prepared from stock solutions of MB and AO to achieve a final concentration of 25 µM. The ct-DNA was added or not the samples at the concentration of 50 µg/mL. The solutions were prepared in tris-HCl 10 mM pH 7.4 and transferred to a quartz cuvette. These were sealed to proceed with the irradiation studies.

7.2.3 Irradiation studies

For the irradiation studies, the solutions were placed in the closed quartz cuvettes to be irradiated. MB and DNA solutions, AO and DNA solutions were exposed to a red LED light source at 640 nm and a blue LED light at 457 nm, respectively. All the solutions were submitted to UVC light with peak at 254 nm (PHILIPS TUV PL-S 5W/2P Hg). The closed quartz cuvettes filled with the solution were placed 12 cm under the source of light with an average irradiance of 9.5 W/m² for the UVC light, 38.9 W/m² for blue light and 24.3 W/m² for red light. The irradiance was measured in Delta OHM photo/Radiometer (HD 2102.2). The solutions were submitted to different times of irradiation (cumulative time), with temperature and humidity maintained around 22 ºC and 60%, respectively. Analysis was performed by ultraviolet visible in a Shimadzu spectrophotometer (UV-2101PC) with scanning from 900 nm to 190 nm, using appropriate solutions as reference.

As the changes induced by irradiation observed in the UV–vis spectra of mixtures of molecules are not straightforward to analyse a mathematical technique, 2D-correlation spectroscopy, was applied. This technique was applied to analyse minimal changes in the spectra [23] caused by the effect of the wavelength irradiation on the dyes molecules with and without DNA. For the two-dimensional correlation spectroscopy was used the software 2D Shige, free software developed by Shigeaki Morita (Osaka Electro-Communication University, Japan) [24,25].

7.3 Results and discussion

The analysis of the dyes interaction with the DNA and the effect of irradiation on the molecules was carried out by UV-vis spectroscopy. The UV-vis spectra of the DNA, MB and AO molecules are presented in Figure 7.1. Three main regions in these spectra were analysed namely region I where the DNA absorbance peak at 260 nm appears, region II related to the AO absorbance characteristic peak and region III related to the MB absorbance peaks.

The DNA absorbance characteristic band at 260 nm is associated to the DNA bases [26,27]. The MB spectrum displayed in Figure 7.1 is also in accordance with literature, presenting the band at 664 nm associated to n–π* electronic transitions related to the $C=S^+$ chromophore group present in the dye [28], the band at 614 nm associated to vibronic 0-1 transition [29], and the band at 292 nm to π–π* benzene electronics transition [28]. In the case of AO spectra there are two main peaks one around 488 nm and another at 266 nm, both corresponding to π–π* transitions [30].
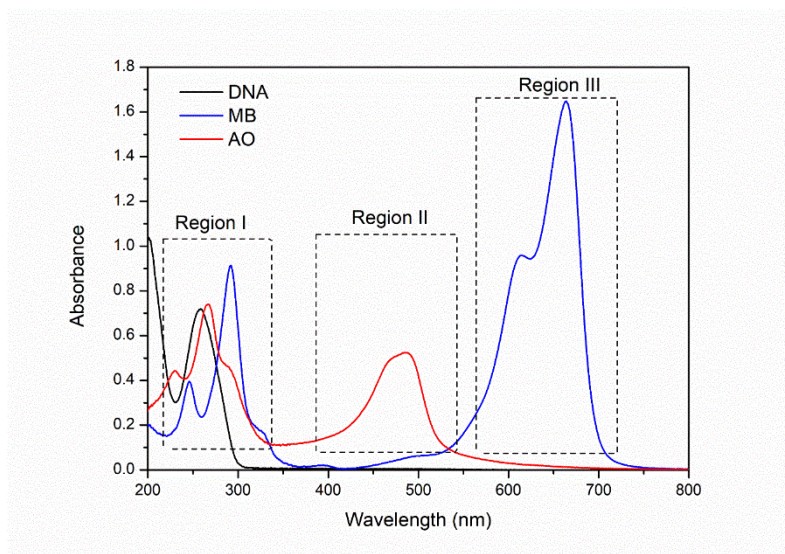
Figure 7.1: Spectra of DNA, MB and AO where is exhibited three main regions of interest namely region I, II and III, related to DNA band, AO characteristic band and MB characteristic band, respectively. MB: methylene blue, AO: acridine orange.

Figure 7.2 shows the comparison of the spectra of the solutions of the dyes prepared with and without the DNA. These spectra reveal the bathochromic effect that occurs in the MB band caused by the DNA shifting from 664 nm to 667 nm and with a decrease about 1.5 times in the absorbance when in presence of DNA which is expected from a DNA intercalator [31]. For AO, on the other side, there

is a slight hypochromic effect with a significant shift in the band from 488 nm to 497 nm in presence of DNA.

Figure 7.2: Comparison of the molecules spectra with and without DNA. A) MB (black line) and DNA + MB (blue line), B) AO (black line) and DNA + AO (red line). MB: methylene blue.

To understand the effect of irradiation on the DNA molecule in presence of the dyes, irradiation kinetic studies were performed on MB and AO solutions in the presence and absence of DNA. UV-vis spectra of control solutions without irradiation (Appendix Figure C.1, Figure C.2 and Figure C.3), kept in the dark for 24 hours, did not reveal significant changes in the spectra.
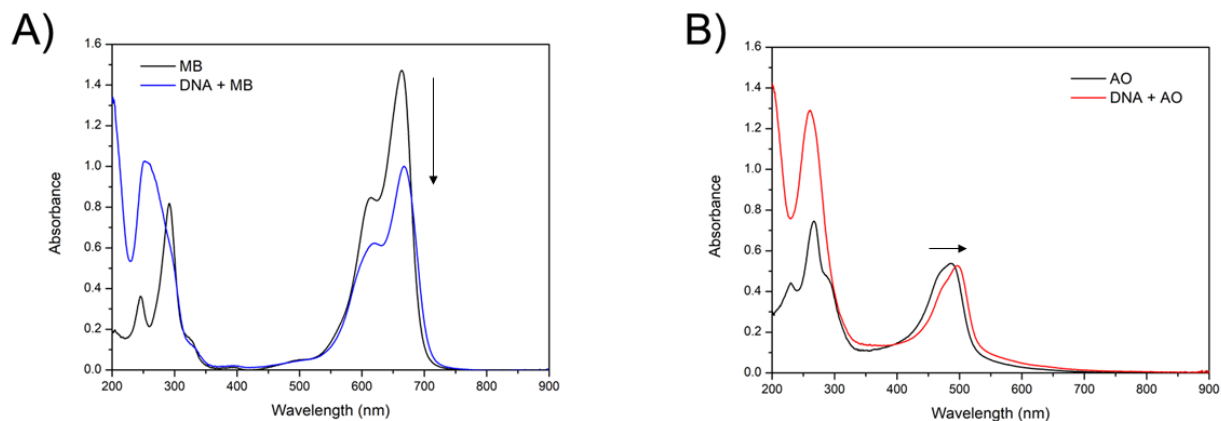
Spectra of MB, DNA + MB, and DNA solutions irradiated with 640 nm wavelength light during several periods of time are shown in Figure 7.3 – A, B and C, respectively. From the evolution of MB and DNA+MB spectra with irradiation time, one can observe a decrease of absorbance revealing the damage of MB molecules in both cases. The damage is stronger when the MB is alone meaning that DNA is avoiding the MB degradation. Furthermore, a bathochromic shift, with deviation of the MB band when in presence of DNA, changing from 664 nm to 667 nm is observed and a hypochromic shift that is related to the intercalation between the DNA base pairs [31]. However, the irradiation of DNA solutions does not lead to DNA damage at the same irradiation conditions. The values of normalized absorbance at the 260 nm and 664 nm or 667 nm peaks as a function of irradiation time for the different solutions are shown in Figure 7.3 – D. The absorbance at 260 nm is time independent for the DNA solutions and decreases slightly for the case of DNA and DNA+MB solutions. As the decay is similar for these last two solutions reveals that DNA is not being damaged by light of 640 nm. Furthermore, the MB peak around 664 nm shows different results from normalized absorbance, indicating that MB alone was more susceptible to the damage by irradiation than MB in presence of the DNA.

The AO, DNA + AO, and DNA solutions were irradiated with 457 nm wavelength light. The UV-vis spectra achieved for the different periods of irradiation time are presented in Figure 7.4 – A, B and C, respectively. The evolution of the AO absorbance (Figure 7.4 – A) shows an accentuated decrease

in the AO characteristic band and, comparing to Figure 7.4 – B, the presence of the DNA lead to a shift from 488 nm to 497 nm AO band. The plot of the normalized absorbance (Figure 7.4 – D) shows a slight decrease of the normalized absorbance at 260 nm for the DNA and DNA + AO, that is more significant for AO only. For the absorbance region around 488 nm, there is a significant difference of samples without and with DNA, which show a higher damage of AO in the absence of the DNA molecule.

Therefore, the spectra of AO in presence of DNA also show the same pattern as observed for MB, with minimal hypochromic shift and a significant bathochromic shift in the UV-vis spectra which are characteristic of intercalator agents [31]. However, by the normalized absorbance it is possible to observe that the presence of DNA resulted in a lower degradation of these molecules, which can possibly be attributed to insertion of the MB and AO in the DNA, partially hindering the effect of irradiation on these molecules.
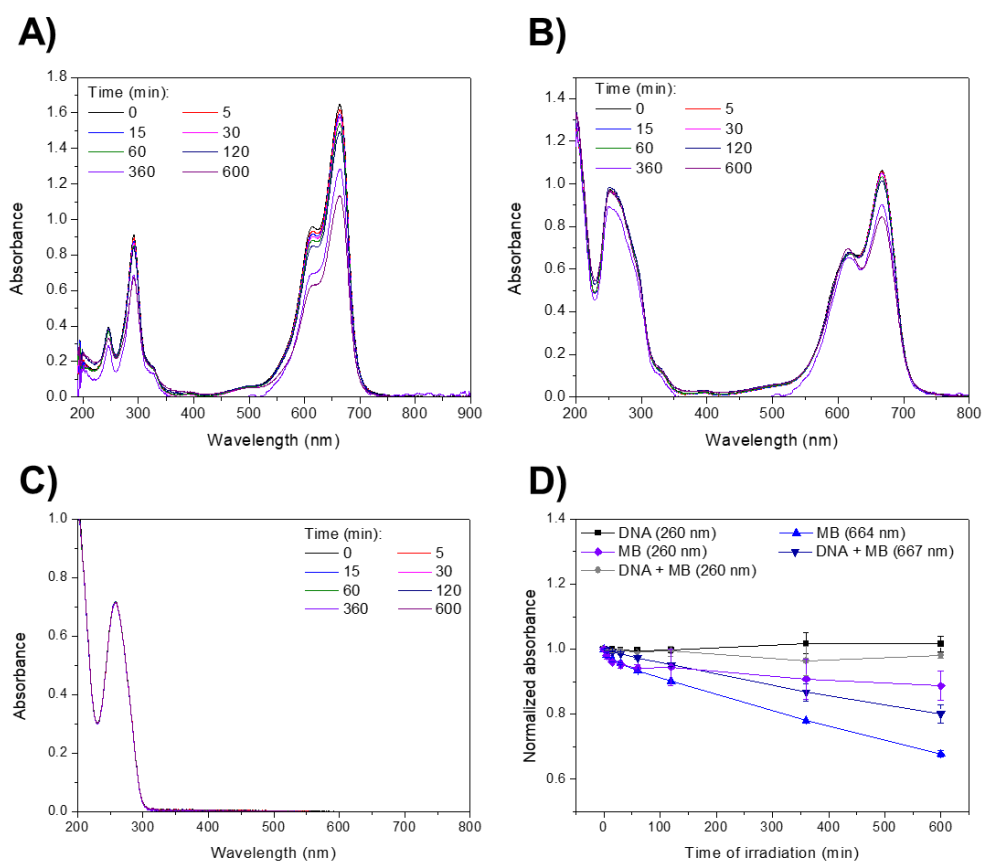

Figure 7.3: Kinetics of samples submitted to irradiation at 640 nm. A), B) and C) Spectra of the irradiated samples: MB, DNA + MB and DNA, respectively. D) Kinetics of the two main characteristic absorbance regions found for these samples: region of the DNA (260 nm) and region of MB (approximately 664 nm). MB: methylene blue.
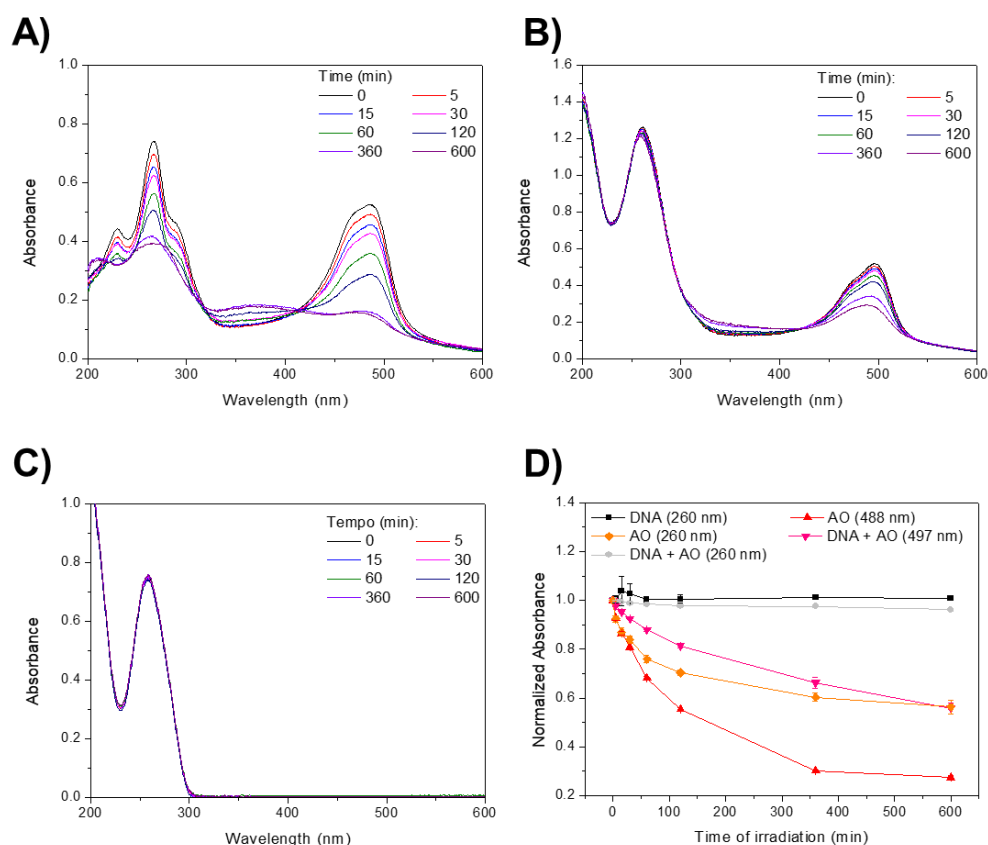
Figure 7.4: Kinetics of samples submitted to irradiation at 457 nm. A), B) and C) Spectra of the irradiated samples: AO, DNA + AO and DNA, respectively. D) Kinetics of the two main characteristic absorbance regions found for these samples: region of the DNA (260 nm) and region of AO (approximately 488 nm). AO: acridine orange.

Since the dyes and the DNA present bands in region from 200 nm – 300 nm, the UVC light can affect leading to the degradation of these molecules and, therefore, irradiation studies using UVC lamp are shown in Figure 7.5, where both intercalators were irradiated with UVC lamp in presence and absence of DNA. It is possible to observe some degradation of the MB in the absence and presence of the DNA, as well as for AO. DNA only (Figure 7.5 – E) show a minimal decrease of absorbance at 260 nm. This indicates some damage of the biomolecule which was not observed for the case of DNA irradiated with other wavelengths. In the Figure 7.5 – F, the plot of the normalized absorbance in function of the irradiation time shows that for samples containing DNA the peak at 260 nm has not a significant decay effect when compared to the absorbance decay related to the MB and AO characteristic bands. Comparing the absorbance of the peaks of MB with AO, is possible to see a higher degradation affecting the AO band, mainly for AO alone.

117
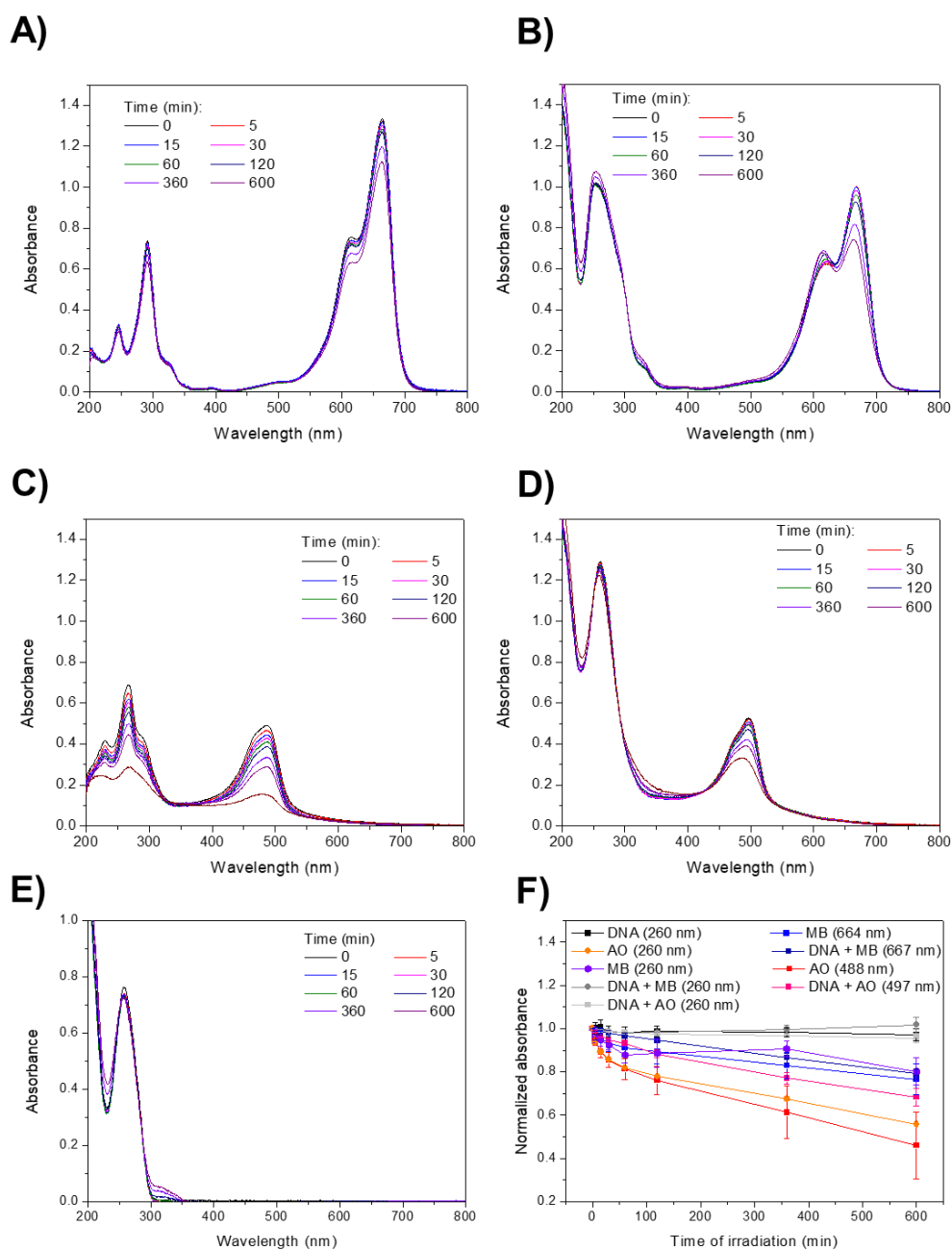
Figure 7.5: Kinetics of samples submitted to irradiation at 254 nm. A), B), C), D), E) Spectra of the irradiated samples: MB, DNA + MB, AO, DNA + AO and DNA, respectively. F) Kinetics of the three main characteristic absorbance regions found for these samples: region of the DNA (260 nm), region of AO (approximately 488 nm), region of MB (approximately 664 nm). MB: methylene blue, AO: acridine orange.

The fitting with an exponential function of the normalized absorbance exhibited different characteristics time constants (τ) as shown in Table 7.1. The results showed that for the region of MB characteristic band, is clear that for both irradiation sources (red light and UVC) the degradation was faster for the MB alone when compared to MB with DNA, with an increase in the time constant value, approximately the double of the time constant obtained for MB only. The same behaviour was observed

for AO, which shows time constant around 130 minutes for the AO alone, while for the system containing AO with the DNA increased almost twice the time constant. This observed behaviour demonstrate that the addition of the DNA affected the degradation of the molecules by increasing the time constant of the compounds' degradation. This is possibly connected to the mode of interaction of the molecules that, by the intercalation between the DNA base pairs, are less susceptible for the irradiation when compared to solution without DNA. On the other side, as the interaction of the DNA with these molecules hinder their degradation, DNA can be or not more susceptible to the radiation.

Although the light sources did not present the same irradiance values, there is not much difference of the time constant obtained from the normalized absorbance of the AO peak, in the absence of the DNA. For the DNA + AO, the time constant of the AO peak of sample irradiated with the blue light presents a slightly reduced value when compared to the one achieved for the irradiation with UVC. This may be attributed to the high sensitivity of AO to the blue light [32]. MB, on the other side, was more affected by UVC light when compared to the system irradiated with red light showing that despite the different irradiance, the red light is less energetic [33] leading to smaller degradation when compared to UVC.

Table 7.1: Comparison of the time constant (τ) obtained from the exponential fitting of the regions of interest for the samples irradiated at 640 nm, 457 nm and 254 nm.

Sample	Peak (nm)	τ (minutes)		
		Red light (640 nm)	Blue light (457 nm)	UVC (254 nm)
MB	664	639.4 ± 191.3	-	181.1 ± 87.3
AO	488	-	129.4 ± 14.8	179.2 ± 60.2
DNA + MB	667	1167.3 ± 258.3	-	-
DNA + AO	497	-	279.5 ± 43.9	328.9 ± 71.5

The UV-vis spectra were analysed over irradiation time using 2D spectroscopy. Synchronous 2D correlation maps of AO, DNA + AO and DNA samples submitted to irradiation with blue light (457 nm) and UVC (254 nm) light sources are shown in Figure 7.6 – A and B, respectively. The synchronous maps resulted from spectra related to AO solutions irradiated at 457 nm are show in Figure 7.6 – A(i), where is possible to observe two autopeaks, one around 266 nm and another at 488 nm which indicate a change in the intensity of the absorbance bands associated to π–π* transitions. A cross peak at 266 nm, 488 nm indicates the spectral variation of the 266 nm peak is related to the changes in the 488 nm peak. It also shows a negative correlation from the 300 nm to 400 nm. From the synchronous correlation map achieved from the DNA + AO solutions spectra as shown in Figure 7.6 – A(ii) it is possible to see

a significantly less intensive autopeak near the 488 nm, meaning that the change along time was minimal compared to AO alone. Figure 7.6 – A(iii) show the synchronous map of the DNA submitted to the same wavelength of irradiation. This map only presents a very low intensity autopeak around the 200 nm. For the case of samples irradiated with 254 nm wavelength light, on the synchronous map of AO solutions spectra shows the two autopeaks at 266 nm and 488 nm associated to AO degradation (Figure 7.6 – B) and also the cross peak at 266 nm, 488nm. In the presence of the DNA, only the autopeaks at 488 nm is observed being less intensive that the observed in the case of AO only. The synchronous map of DNA submitted to irradiation at 254 nm shows a minor signal near the 200 nm, indicating some minimal changes in the DNA molecules.

Figure 7.6: Synchronous 2D correlation maps in the wavelength range of 190 nm to 600 nm of AO solutions in presence or not of DNA. A) Samples submitted to irradiation at 457 nm, B) Samples submitted to irradiation at 254 nm. AO: acridine orange.

The 2D-correlation maps from the spectra of MB in presence and absence of DNA are presented in Figure 7.7 – A, and B for the 640 nm and 254 nm irradiation, respectively. For the map of MB spectra submitted to irradiation of 640 nm, it is possible to observe a region of red colour around the 600 nm – 700 nm, with two autopeaks which are related to the decrease of the MB absorbance bands associated to both n–π* electronic and vibronic 0-1 transitions. The intensity of these autopeaks is higher than the one observed for the spectra of MB with DNA submitted to the same irradiation conditions as shown in Figure 7.7 – A(ii), that also show a small autopeak around the 664 nm band. For the sample of DNA only (Figure 7.7 – A(iii)) is possible to observe a small signal around the 200 nm while for the DNA submitted to the 254 nm irradiation (Figure 7.7 – B(iii)) it shows a slightly more intense signal, meaning

some changes in the DNA band. For the case of MB and DNA + MB solutions irradiated with 254 nm, the synchronous correlation maps are shown in Figure 7.7 – B(i) and Figure 7.7 – B(ii), respectively, and show similar patterns regarding the autopeaks, as those irradiated with 640 nm, mainly at the region between 600 nm – 700 nm.
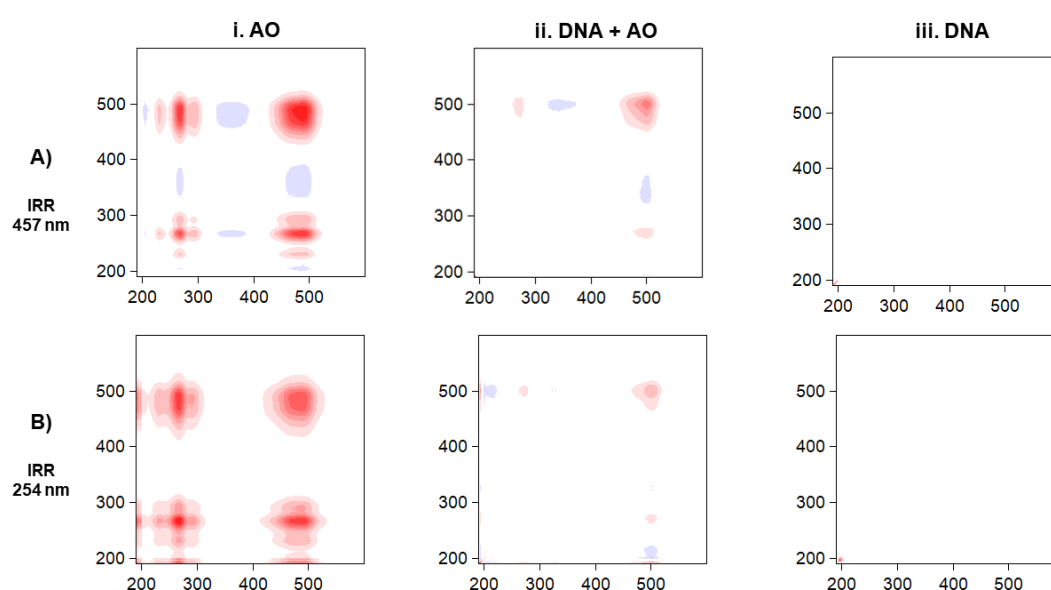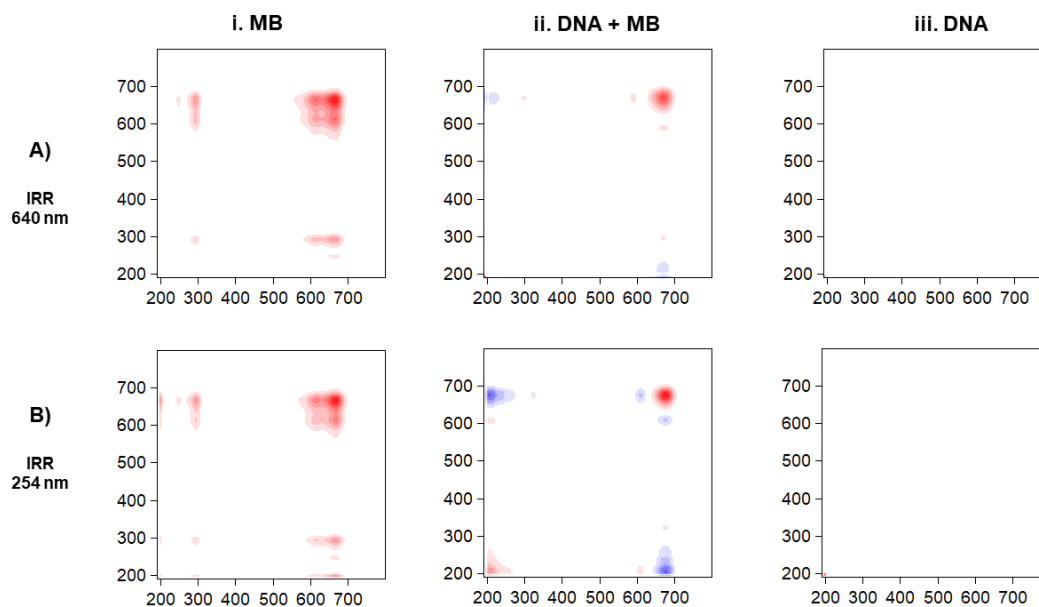

Figure 7.7: Synchronous 2D correlation maps in the wavelength range of 190 to 600 nm of MB solutions in presence of not of DNA. A) Samples submitted to irradiation at 640 nm, B) Samples submitted to irradiation at 254 nm. MB: methylene blue.

7.4 Conclusions

The interaction of ct-DNA with the MB and AO molecules was confirmed by the bathochromic and hypochromic shifts observed in the UV-vis spectra of DNA in presence of photosensitizer molecules. These shifts are explained by the intercalation of photosensitizer molecules between the DNA base pairs. From the point of view of the analysis of the effect of radiation on the DNA in presence of the dyes molecules, distinct profiles of degradation with different characteristics times were observed for dyes in presence and in absence of DNA. These results demonstrated that the dyes in the absence of DNA are more susceptible to photodegradation. This is justified by the intercalation of the dyes on the DNA bases pairs allowing that DNA molecule partially hinders the molecules exposition and, therefore, reducing their degradation. However, further studies should focus on the effects the intercalants cause on the DNA molecules, as it was not observed a significant difference in the absorbance at 260 nm, the characteristic peak of the DNA.

Acknowledgments

References

1. Sayed, M.; Krishnamurthy, B.; Pal, H. Unraveling multiple binding modes of acridine orange to DNA using a multispectroscopic approach. *Phys. Chem. Chem. Phys.* **2016**, *18*, 24642–24653, doi:10.1039/C6CP03716J.

2. Zhang, F.; Sheng, H.; Wang, S.; Ma, Y.; Cai, C. Screening DNA-targeted anticancer drug *in vitro* based on cancer cells DNA-templated silver nanoclusters. *Sci. Rep.* **2019**, *9*, 8911, doi:10.1038/s41598-019-45523-2.

3. Gill, M.R.; Harun, S.N.; Halder, S.; Boghozian, R.A.; Ramadan, K.; Ahmad, H.; Vallis, K.A. A ruthenium polypyridyl intercalator stalls DNA replication forks, radiosensitizes human cancer cells and is enhanced by Chk1 inhibition. *Sci. Rep.* **2016**, *6*, 31973, doi:10.1038/srep31973.

4. Palchaudhuri, R.; Hergenrother, P.J. DNA as a target for anticancer compounds: methods to determine the mode of binding and the mechanism of action. *Curr. Opin. Biotechnol.* **2007**, *18*, 497–503, doi:10.1016/j.copbio.2007.09.006.

5. Baguley, B.C.; Drummond, C.J.; Chen, Y.Y.; Finlay, G.J. DNA-Binding Anticancer Drugs: One Target, Two Actions. *Molecules* **2021**, *26*, 552, doi:10.3390/molecules26030552.

6. Panikar, S.S.; Ramírez-García, G.; Banu, N.; Vallejo-Cardona, A.A.; Lugo-Fabres, P.; Camacho-Villegas, T.A.; Salas, P.; De la Rosa, E. Ligand-targeted Theranostic Liposomes combining methylene blue attached upconversion nanoparticles for NIR activated bioimaging and photodynamic therapy against HER-2 positive breast cancer. *J. Lumin.* **2021**, *237*, 118143, doi:10.1016/j.jlumin.2021.118143.

7. Wu, P.-T.; Lin, C.-L.; Lin, C.-W.; Chang, N.-C.; Tsai, W.-B.; Yu, J. Methylene-Blue-Encapsulated Liposomes as Photodynamic Therapy Nano Agents for Breast Cancer Cells. *Nanomaterials* **2018**, *9*, 14, doi:10.3390/nano9010014.

8. Santos, G.M.P.; Oliveira, S.C.P.S.; Monteiro, J.C.S.; Fagnani, S.R.; Sampaio, F.P.; Correia, N.A.; Crugeira, P.J.L.; Pinheiro, A.L.B. ROS-induced autophagy reduces B16F10 melanoma cell proliferative activity. *Lasers Med. Sci.* **2018**, *33*, 1335–1340, doi:10.1007/s10103-018-2489-

6.

9.   Yu, J.; Hsu, C.-H.; Huang, C.-C.; Chang, P.-Y. Development of Therapeutic Au–Methylene Blue Nanoparticles for Targeted Photodynamic Therapy of Cervical Cancer Cells. *ACS Appl. Mater. Interfaces* **2015**, *7*, 432–441, doi:10.1021/am5064298.

10. Nafisi, S.; Saboury, A.A.; Keramat, N.; Neault, J.-F.; Tajmir-Riahi, H.-A. Stability and structural features of DNA intercalation with ethidium bromide, acridine orange and methylene blue. *J. Mol. Struct.* **2007**, *827*, 35–43, doi:10.1016/j.molstruc.2006.05.004.

11. Zhang, L.Z.; Tang, G.-Q. The binding properties of photosensitizer methylene blue to herring sperm DNA: a spectroscopic study. *J. Photochem. Photobiol. B Biol.* **2004**, *74*, 119–125, doi:10.1016/j.jphotobiol.2004.03.005.

12. Vardevanyan, P.O.; Antonyan, A.P.; Parsadanyan, M.A.; Shahinyan, M.A.; Petrosyan, N.H. Study of interaction of methylene blue with DNA and albumin. *J. Biomol. Struct. Dyn.* **2021**, *0*, 1–7, doi:10.1080/07391102.2021.1902397.

13. Pires, F.; Coelho, M.; Ribeiro, P.A.; Raposo, M. Methylene blue: A trendy photosensitizer in medicine and in solar-energy conversion systems. In Proceedings of the 2016 4th International Conference on Photonics, Optics and Laser Technology (PHOTOPTICS); 2016; pp. 1–5.

14. Pitchaimani, A.; Renganathan, A.; Cinthaikinian, S.; Premkumar, K. Photochemotherapeutic effects of UV-C on acridine orange in human breast cancer cells: potential application in anticancer therapy. *RSC Adv.* **2014**, *4*, 22123–22128, doi:10.1039/c4ra01647e.

15. Pierzyńska-Mach, A.; Janowski, P.A.; Dobrucki, J.W. Evaluation of acridine orange, LysoTracker Red, and quinacrine as fluorescent probes for long-term tracking of acidic vesicles. *Cytom. Part A* **2014**, *85*, 729–737, doi:10.1002/cyto.a.22495.

16. Damas-Souza, D.M.; Nunes, R.; Carvalho, H.F. An improved acridine orange staining of DNA/RNA. *Acta Histochem.* **2019**, *121*, 450–454, doi:10.1016/j.acthis.2019.03.010.

17. Thomé, M.P.; Filippi-Chiela, E.C.; Villodre, E.S.; Migliavaca, C.B.; Onzi, G.R.; Felipe, K.B.; Lenz, G. Ratiometric analysis of acridine orange staining in the study of acidic organelles and autophagy. *J. Cell Sci.* **2016**, *129*, 4622–4632, doi:10.1242/jcs.195057.

18. Lin, Y.-C.; Lin, J.-F.; Tsai, T.-F.; Chen, H.-E.; Chou, K.-Y.; Yang, S.-C.; Tang, Y.-M.; Hwang, T.I.S. Acridine orange exhibits photodamage in human bladder cancer cells under blue light exposure. *Sci. Rep.* **2017**, *7*, 14103, doi:10.1038/s41598-017-13904-0.

19. Osman, H.; Elsahy, D.; Saadatzadeh, M.R.; Pollok, K.E.; Yocom, S.; Hattab, E.M.; Georges, J.; Cohen-Gadol, A.A. Acridine Orange as a Novel Photosensitizer for Photodynamic Therapy in Glioblastoma. *World Neurosurg.* **2018**, *114*, e1310–e1315, doi:10.1016/j.wneu.2018.03.207.

20. Kusuzaki, K.; Murata, H.; Matsubara, T.; Satonaka, H.; Wakabayashi, T.; Matsumine, A.; Uchida, A. Acridine orange could be an innovative anticancer agent under photon energy. *In Vivo (Brooklyn).* **2007**, *21*, 205–214.

21.   Amado, A.M.; Pazin, W.M.; Ito, A.S.; Kuzmin, V.A.; Borissevitch, I.E. Acridine orange interaction with DNA: Effect of ionic strength. *Biochim. Biophys. Acta - Gen. Subj.* **2017**, *1861*, 900–909, doi:10.1016/j.bbagen.2017.01.023.

22.   Pivetta, T.P.; Vieira, T.; Silva, J.C.; Ribeiro, P.A.; Raposo, M. Screening on cells of the phototoxic potential of different DNA-intercalators to be applied on skin cancer therapy. *Submitted manuscript*.

23.   Pires, F.; Geraldo, V.P.N.; Antunes, A.; Marletta, A.; Oliveira, O.N.; Raposo, M. On the role of epigallocatechin-3-gallate in protecting phospholipid molecules against UV irradiation. *Colloids Surfaces B Biointerfaces* **2019**, *173*, 312–319, doi:10.1016/j.colsurfb.2018.09.065.

24.   Noda, I. Advances in two-dimensional correlation spectroscopy. *Vib. Spectrosc.* **2004**, *36*, 143–165, doi:10.1016/j.vibspec.2003.12.016.

25.   Raposo, M.; Coelho, M.; Gomes, P.J.; Vieira, P.; Ribeiro, P.A.; Mason, N.J.; Hunniford, C.A.; McCullough, R.W. DNA damage induced by carbon ions (C 3+) beam accessed by independent component analysis of infrared spectra. *Int. J. Radiat. Biol.* **2014**, *90*, 344–350, doi:10.3109/09553002.2014.892650.

26.   Isaacson, M. Interaction of 25 keV Electrons with the Nucleic Acid Bases, Adenine, Thymine, and Uracil. I. Outer Shell Excitation. *J. Chem. Phys.* **1972**, *56*, 1803–1812, doi:10.1063/1.1677456.

27.   Gomes, P.J.; Ribeiro, P.A.; Shaw, D.; Mason, N.J.; Raposo, M. UV degradation of deoxyribonucleic acid. *Polym. Degrad. Stab.* **2009**, *94*, 2134–2141, doi:10.1016/j.polymdegradstab.2009.09.013.

28.   Párkányi, C.; Boniface, C.; Aaron, J..; Maafi, M. A quantitative study of the effect of solvent on the electronic absorption and fluorescence spectra of substituted phenothiazines: evaluation of their ground and excited singlet-state dipole moments. *Spectrochim. Acta Part A Mol. Spectrosc.* **1993**, *49*, 1715–1725, doi:10.1016/0584-8539(93)80239-7.

29.   Heger, D.; Jirkovský, J.; Klán, P. Aggregation of Methylene Blue in Frozen Aqueous Solutions Studied by Absorption Spectroscopy. *J. Phys. Chem. A* **2005**, *109*, 6702–6709, doi:10.1021/jp050439j.

30.   Le Bahers, T.; Di Tommaso, S.; Peltier, C.; Fayet, G.; Giacovazzi, R.; Tognetti, V.; Prestianni, A.; Labat, F. Acridine orange in a pumpkin-shaped macrocycle: Beyond solvent effects in the UV–visible spectra simulation of dyes. *J. Mol. Struct. THEOCHEM* **2010**, *954*, 45–51, doi:10.1016/j.theochem.2010.01.031.

31.   Hajian, R.; Shams, N.; Mohagheghian, M. Study on the interaction between doxorubicin and Deoxyribonucleic acid with the use of methylene blue as a probe. *J. Braz. Chem. Soc.* **2009**, *20*, 1399–1405, doi:10.1590/S0103-50532009000800003.

32.   Byvaltsev, V.A.; Bardonova, L.A.; Onaka, N.R.; Polkin, R.A.; Ochkal, S. V.; Shepelev, V. V.;

Aliyev, M.A.; Potapov, A.A. Acridine Orange: A Review of Novel Applications for Surgical Cancer Imaging and Therapy. *Front. Oncol.* **2019**, *9*, 925, doi:10.3389/fonc.2019.00925.

33. Espinoza, J.H.; Mercado-Uribe, H. Visible light neutralizes the effect produced by ultraviolet radiation in proteins. *J. Photochem. Photobiol. B Biol.* **2017**, *167*, 15–19, doi:10.1016/j.jphotobiol.2016.11.023.

Exploiting the use of Acridine Orange and Methylene Blue in biological systems II: an Investigation of the Dyes effects on Lipids [1]

Abstract: Recent studies demonstrated that methylene blue (MB) and acridine orange (AO) seem to be interesting photosensitizer molecules to be used in photodynamic therapy. However, the effect of these molecules can be enhanced by their encapsulation being liposomes adequate to work as photosensitizer nanocarriers. In this context, we analysed the effect of MB and AO on mixed lipid Langmuir monolayers with and without surfactants to obtain more information regarding their interaction with different monolayers composition. The lipids 1,2-dipalmitoyl-sn-glycero-3-phosphocholine (DPPC), 1,2-dipalmitoyl-sn-glycero-3-phospho-(1'-rac-glycerol) (DPPG) and cholesterol were mixed at a proportion of 7:2:1 (weight ratio) and was determined as the main lipid mixture (LM) while the mixtures with the surfactants Span® 80 and sodium cholate were named as LM-SP and LM-SC, respectively. LM monolayers on aqueous surface showed lower area at 30 mN.m^{-1} when compared to a predicted average area per molecule, indicating that there were attractive forces in the lipids of the mixture. The monolayers in contact with AO molecules presented an interaction that has a significant effect on the increase of membrane flexibility. The same event was observed for the higher concentration of MB. These results are corroborated by the PM-IRRAS analysis where the orientational order of CH_2 shows that the order decreases for all samples containing AO. Furthermore, through the calculation of the hydration of carbonyl and phosphate it was possible to hypothesize that due to sodium cholate, the LM-SC monolayers presented lower hydration and therefore, molecules probably interact more at the external polar regions of the monolayer resulting in a non-significative change of extrapolated area, while for the other molecules an increased hydration was observed as well as there was an increase of the extrapolated area when the

---

compounds MB and AO are in contact with the monolayer. Finally, this study indicates that both MB and AO are retained near the lipids polar head in the monolayers.

8.1 Introduction

Currently the interest on therapies that allow a minimally invasive and more selective effect has increased and, among the new strategies, photodynamic therapy has been widely explored [1,2]. PDT is highly dependent on the components light, oxygen, and a photosensitizer, therefore, the selection of the photosensitizer is important to achieve an efficient treatment [3]. Most recently, non-porphyrin photo-sensitizers have gained some attention such as methylene blue (MB) and acridine orange (AO) (Figure 8.1) [4].

Methylene blue is a cationic dye that was very used in the industry but also in research for the staining in histology [5,6]. MB is also a promising photosensitizer and has been investigated for anti-bacterial, antiparasitic, antifungal and anticancer application [7–11]. The incorporation of methylene blue to nanoparticles has been explored in the past few years to increase the treatments efficacy [12]. Boccalini and collaborators [8] investigated the MB effect in a bacteria culture and showed that, com-pared to MB in solution, there was an increase in the antibacterial activity when it was incorporated in liposomes.

Acridine orange is a basophilic dye that present affinity to nucleic acids and, therefore, is com-monly used for the nucleic acid staining [13]. A green and red fluorescence are obtained when bound to DNA and RNA, respectively. However, AO molecules can also accumulate in acidic organelles, result-ing in an orange or red fluorescence, serving also for the identification of acidic vesicular organelles (AVOs) [14–16]. As photosensitizer, AO has recently gained more attention for the cancer therapy [14,17,18]. In the studies from Lin et al. [18], the photodamage potential of AO was investigated in bladder cancer cells and showed a successful cytotoxicity with blue light irradiation that was very se-lective for the cancer cells and practically did not show phototoxicity in the human immortalized uroep-ithelial cell line.
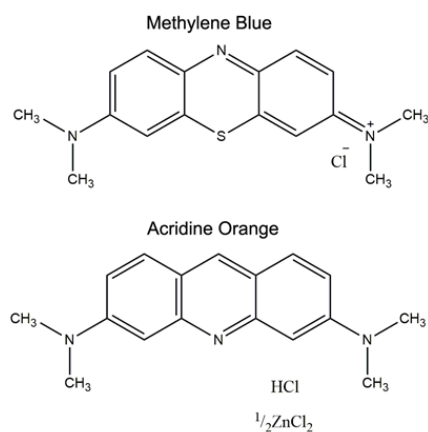
Figure 8.1: Chemical structures of methylene blue and acridine orange.

The increasing interest in nanotechnology approaches and association with PDT led to the incorporation of photosensitizer (PS) molecules into nanoparticles such as liposomes [2]. However, the successful encapsulation/incorporation of these molecules is highly dependent on the interactions with the liposomes' material. Langmuir monolayers are often employed to study intermolecular interactions between lipids and molecules of biological interest [19]. It has been already used to study different drugs such as antifungal, antibacterial, anti-inflammatory, antioxidant, antitumor, wound healing, and many others [20–27]. As it can represent half of a cell membrane, it is very useful to study interactions occurring at the membrane surface [28]. Langmuir films can also serve as a model to studies of drugs incorporation in the membrane and even for delivery systems [27]. It is a versatile technique that can give useful information to study the lipid systems.

In this work three different mixed monolayers were investigated regarding the interaction with the dyes MB and AO to understand the effect on the lipid monolayers. Mixtures containing 1,2-dipalmitoyl-sn-glycero-3-phosphocholine (DPPC), 1,2-dipalmitoyl-sn-glycero-3-phospho-(1'-rac-glycerol) (DPPG), and cholesterol (CHOL) (Figure 8.2) were prepared and the addition of the surfactants Span® 80 or sodium cholate was also investigated.
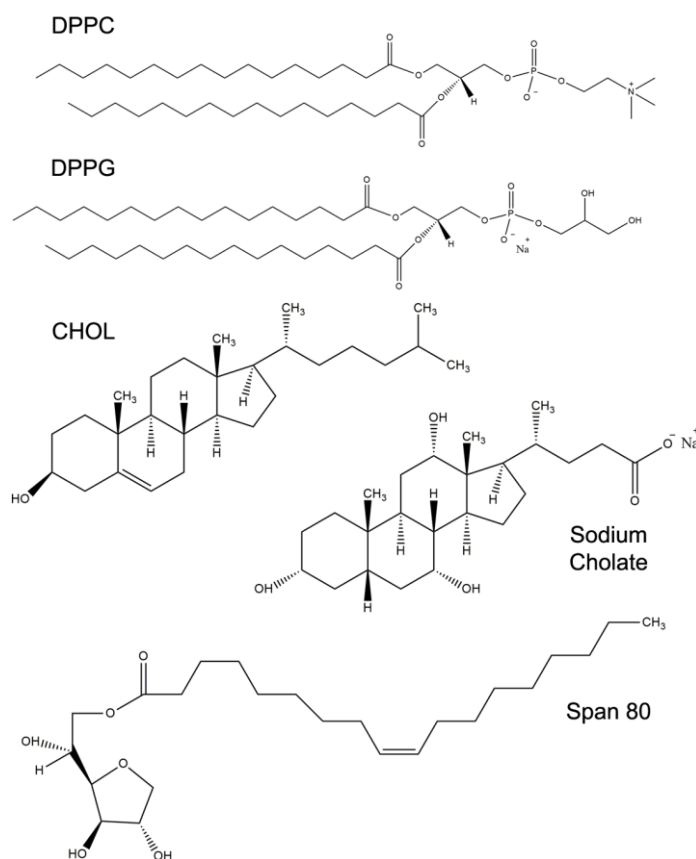
Figure 8.2: Chemical structures of 1,2-dipalmitoyl-sn-glycero-3-phosphocholine (DPPC), 1,2-dipalmitoyl-sn-glycero-3-phospho-(1'-rac-glycerol) (DPPG), cholesterol (CHOL), sodium cholate and Span® 80.

8.2 Materials and Methods

8.2.1 Materials

1,2-Dipalmitoyl-sn-glycero-3-phosphocholine (DPPC), 1,2-dipalmitoyl-sn-glycero-3-phospho-(1'-rac-glycerol) (DPPG), and cholesterol (CHOL) were obtained from Avanti, sorbitan monooleate (Span® 80), sodium cholate, methylene blue and acridine orange were obtained from Sigma-Aldrich. DPPC, DPPG and CHOL solutions were prepared at 1.0 mg/mL in a mixture of chloroform/methanol (8:2). The same solvent mixture was used to prepare solutions of Span® 80 and sodium cholate at a concentration of 0.5 mg/mL. Experiments were carried out only with lipids, as reference, and with the preparation of lipid mixtures containing DPPC, DPPG and CHOL (7:2:1 weight ratio) with or without 5% (w/v) of the surfactants Span® 80 and sodium cholate. Phosphate buffered saline (PBS) 10 mM pH 7.4 was used as subphase and for the experiments with MB and AO, solutions of these chemicals were prepared in the buffer.

8.2.2 Langmuir monolayers

Surface pressure experiments were performed in a Langmuir trough with an area of 243 cm² coupled to a KSV NIMA device equipped with a Wilhelmy plate made of filter paper. Experiments were carried out in a class 10,000 clean room with temperature of 22 ± 1 °C. Langmuir monolayers were prepared by spreading the lipid solution on the aqueous surface of the PBS solution subphase placed in the trough. The system was equilibrated during 15 minutes for the solvent evaporation and then the experiment was initiated. Two symmetric barriers started to compress the monolayer at a constant rate of 10 mm.min^{-1} and the isotherms correlating surface pressure per area were obtained. At least three measurements for each sample were obtained to ensure results reproducibility. From the isotherms the compressibility modulus (Cs^{-1}) was calculated according to Equation 8.1, where A_m is the mean molecular area, π is the surface pressure and T is the temperature. The compressional modulus is usually employed for the analysis of monolayer´s phase transition and elasticity. Higher Cs^{-1} indicate a less compressible monolayer while a low Cs^{-1} indicate a better compressibility [29].

$$\text{Equation 8.1:} \quad Cs^{-1} = -A.\left(\frac{\partial \pi}{\partial A_m}\right)_T$$

8.2.3 Polarization-modulation infrared reflection absorption spectroscopy (PM-IRRAS)

Experiments were performed in a KSV PMI 550 (KSV Instruments, Finland) with an incidence angle of 80° and spectra were obtained at 30 mN.m^{-1} and kept stable during the measurement time (10 minutes, 3000 scans). Spectra were obtained using the subphase spectrum as background. The spectral ranges of 1000 cm^{-1} to 1800 cm^{-1} and 2800 cm^{-1} to 3000 cm^{-1} were investigated.

8.3 Results and discussion

8.3.1 Surface pressure – area isotherms

Isotherms of neat lipids and lipid mixtures were obtained to characterize the effect of the MB and AO dyes on the lipids' monolayers. As shown in Figure 8.3 – A, one can observe the surface pressure – area isotherms for the different lipids used for the preparation of the mixtures. As previously

demonstrated in the literature [30], in PBS buffer of pH 7.4 the lipids DPPC and DPPG present a phase transition at $\pi = 7$ mN.m^{-1} and $\pi = 10$ mN.m^{-1}, respectively. As the main component of the lipid mixture is DPPC, the lipid mixture presents a brief first-order transition around 5 mN.m^{-1} from the liquid expanded to the liquid condensed (LE/LC). A significant decrease of area for the mixture (44.1 ± 0.7 Å²) was observed when compared to neat DPPC (49.1 ± 0.9 Å²) and neat DPPG (51.9 ± 0.8 Å²) areas. This is probably due to the amount of cholesterol in the mixture, as cholesterol present a smaller area (38.4 ± 0.7 Å²), whose values of extrapolated area for pure lipids are close to those found in the literature [31,32]. For mixtures it is possible to calculate a predicted average area per molecule (A^0_{123}) that is calculated according to Equation 8.2 [29], where x_1, x_2 and x_3 are the lipids proportion (from the higher to the lower proportion DPPC > DPPG > CHOL) and A_{m1}, A_{m2} and A_{m3} are the areas of the respective lipids at a determined pressure, in this case, was selected the surface pressure of 30 mN.m^{-1}.

$$\text{Equation 8.2:} \quad A^0{}_{123} = x_1.A_{m1} + x_2.A_{m2} + x_3.A_{m3}$$

The calculated value of A^0_{123} was of 40.4 Å² while the experimental area was 37.5 Å² . The small value achieved experimentally indicates the possible existence of attractive forces between DPPC, DPPG and CHOL molecules which is in accordance with literature [29,33]. Himeno et al. [34] studied the mixture of the lipids DPPC and DPPG with cholesterol and found that the phospholipids head groups interaction has an impact on the localization of cholesterol and the structure stability. Also, they observed a phase separation for mixtures containing above 30% of DPPG. Therefore, we can conclude that the mixture obtained containing 7:2:1 (weight ratio) of DPPC, DPPG and CHOL resulted in a one-phase monolayer, with attractive interactions of the lipids.

The surface pressure – area isotherms achieved for the lipid mixtures containing the surfactants Span® 80 and sodium cholate (Figure 8.3 – B) reveal an area expansion. The values of the area at condensed phase were extrapolated to zero pressure (A_0) and exhibited in Table 8.1. These mixtures present the same profile as the lipid mixture without surfactant, with a brief transition around 5 mN.m^{-1}, which is a direct result from the mixture with cholesterol, showing a decrease of the known surface pressure at the LE/LC transition of DPPC and DPPG.
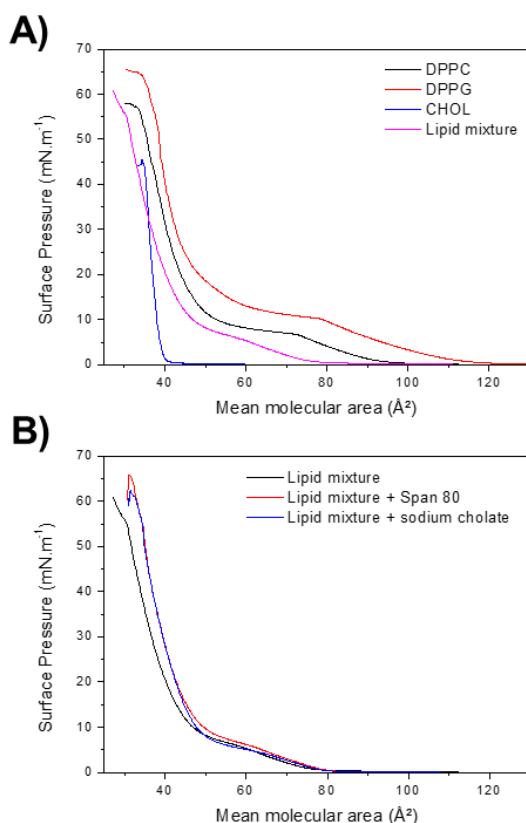
Figure 8.3: Surface pressure – area isotherms of A) lipids DPPC, DPPG, CHOL and the lipid mixture containing DPPC, DPPG and CHOL (7:2:1 weight ratio); B) lipid mixture with Span® 80 or sodium cholate, or in the absence of the surfactants.

The dyes solutions were placed in the trough as subphase, and lipids solutions were spread over the dye/PBS subphase for the characterization of the influence of MB and AO in the mixed monolayers. Figure 8.4 shows the surface pressure – area isotherms for the mixtures with MB and the respective compressional modulus plots. One can observe in Figure 8.4 – A that with the increase of MB concentration there is an expansion in the area, with a significant increase in A_0 with values of 44.1 Å², 47.4 Å² and 49.8 Å² for samples without MB and with 1 µM and 10 µM of MB, respectively. The inverse occurred for the collapse pressure (π_c), obtaining a collapse at 56.1 mN.m^{-1}, 61.6 mN.m^{-1} and 67.4 mN.m^{-1} for 0 µM, 1 µM and 10 µM of MB, respectively.

Lipid mixtures containing the surfactant Span® 80 and in contact or not with MB exhibited a small expansion of area, with a slight increase in A_0 for LM-SP. However, in comparison with lipid mixture without surfactant, $A_0 = 44.1$ Å², there is a visible increase on the area. There was a small area expansion due to the effect of MB in the lipid mixtures containing Span® 80 and no expansion for the monolayers containing sodium cholate. Regardless of the surfactant, it is seen that MB does not significantly influence the isotherms as much as happens for the case of the lipid mixture without surfactants.

Different collapse pressures were observed for lipid mixtures with the surfactants, exhibiting a decrease for lipid mixtures with Span® 80 + MB. For LM-SC there is an increase in the collapse pressure for the higher concentration of MB with $\pi_c = 68.2$ mN.m^{-1}. The compressional modulus values were calculated and plotted in Figure 8.4 – B. In this figure, one can observe an increase in Cs^{-1} mainly for 1 µM of MB. The values of Cs^{-1} at $\pi = 30$ mN.m^{-1} are displayed in Table 8.1, where is also possible to see a higher Cs^{-1} for 1 µM of MB compared to the other samples with the same conditions. When the monolayer is prepared on the surface of MB buffer solution at high concentration presents the lowest Cs^{-1}, demonstrating that, in this case, monolayers are less rigid. The most reduced Cs^{-1} values of 120.6 mN.m^{-1} and 117.3 mN.m^{-1} were obtained for LM-SP while for LM-SC the achieved Cs^{-1} values are of 139.7 mN.m^{-1} and 126.2 mN.m^{-1}. These results demonstrate that MB interaction with LM-SP resulted in a more flexible monolayer.

MB has pKa around 3.8 and it is positively charged at physiological conditions [35,36] therefore, from the obtained results, one could assume that there is MB adsorption on the monolayer specially because of the electrostatic interaction to the lipids as the monolayer contain the zwitterionic lipid DPPC and the negatively charged DPPG. This is in accordance with studies from Schmidt et al. [33], where it was suggested that the cationic portion of MB had the tendency to be near the phosphate group.

Surface pressure – area isotherms obtained for monolayers on the AO subphases for the different lipid mixtures are displayed Figure 8.5 – A. For the different lipid mixtures, it is possible to observe a significant area expansion, demonstrated by the extrapolated area values 44.1 Å², 49.4 Å² and 54.3 Å² for 0 µM, 1 µM and 10 µM, respectively. For the monolayers containing lipid mixture with surfactants, AO influences in a greater expansion for LM-SP compared to LM-SC. These observations are in accordance with extrapolated values of mean molecular area obtained as exhibited in Table 8.1. A maximum A_0 was obtained for the monolayers LM and LM-SP with AO 10 µM.

Considering the subphase containing AO, great expansion is observed for LM that contain DPPC, DPPG and CHOL when comparing to LM-SP that despite the same lipid composition has also an addition of a non-ionic surfactant Span® 80, showing an interaction. On the other hand, LM-SC that have in addition the negatively charged surfactant sodium cholate, there is a small area expansion. The presence of sodium cholate influences on a different manner of AO interaction with the monolayer.

The compressional modulus plots (Figure 8.5 – B) show that AO has an evident influence in the decrease of Cs^{-1} of monolayers containing the surfactants Span® 80 and sodium cholate. The values of Cs^{-1} obtained values for $\pi = 30$ mN.m^{-1} are exhibited in Table 8.1. Looking at these values, it is possible to see a decrease of compressibility for all the lipid mixtures in contact with 1 µM or 10 µM of AO, but mainly for LM-SC that exhibits Cs^{-1} of 113.2 mN.m^{-1} and 112.0 mN.m^{-1}, which means that for all the monolayers studies AO interaction influences the rigidity of the monolayers, which became more flexible.

Alike the MB compound, AO is a weak base with pKa around 9.8 and [37] that is protonated under physiological conditions. Therefore, it can also interact with the polar groups of the lipids, mainly due to ion-dipole interactions.

Table 8.1: Summary of data obtained from the lipid mixtures isotherms, represented by the surface pressure at the collapse (π_c), the extrapolated area at zero surface pressure (A_0) and the compressional modulus (Cs^{-1}). Values are displayed as mean $\pm$ SD (n = 3). LM: lipid mixture, LM-SP: lipid mixture + Span$^®$ 80, LM-SC: lipid mixture + sodium cholate.

| Samples		π_c (mN.m^{-1})	A_0 (Å^2)	Cs^{-1} (mN.m^{-1})
LM	0 µM	56.1 $\pm$ 0.2	44.1 $\pm$ 0.7	137.2 $\pm$ 16.8
	1 µM MB	61.6 $\pm$ 2.0	47.4 $\pm$ 1.4	142.7 $\pm$ 9.4
	10 µM MB	67.4 $\pm$ 1.7	49.8 $\pm$ 0.3	132.7 $\pm$ 6.0
	1 µM AO	55.2 $\pm$ 0.7	49.4 $\pm$ 0.6	134.9 $\pm$ 8.5
	10 µM AO	62.7 $\pm$ 1.4	54.3 $\pm$ 1.3	122.5 $\pm$ 5.1
LM-SP	0 µM	66.3 $\pm$ 0.8	47.9 $\pm$ 0.7	136.4 $\pm$ 4.1
	1 µM MB	59.3 $\pm$ 1.0	50.6 $\pm$ 0.4	120.6 $\pm$ 5.9
	10 µM MB	59.6 $\pm$ 0.8	51.1 $\pm$ 0.7	117.3 $\pm$ 18.3
	1 µM AO	56.7 $\pm$ 0.4	52.4 $\pm$ 1.2	125.4 $\pm$ 5.7
	10 µM AO	64.3 $\pm$ 3.2	54.3 $\pm$ 1.1	130.3 $\pm$ 8.9
LM-SC	0 µM	64.5 $\pm$ 1.9	47.7 $\pm$ 1.0	137.3 $\pm$ 7.6
	1 µM MB	60.8 $\pm$ 4.3	48.7 $\pm$ 0.4	139.7 $\pm$ 9.0
	10 µM MB	68.2 $\pm$ 2.5	48.7 $\pm$ 0.9	126.2 $\pm$ 6.8
	1 µM AO	58.8 $\pm$ 0.9	48.6 $\pm$ 0.8	113.2 $\pm$ 15.4
	10 µM AO	55.8 $\pm$ 0.9	48.3 $\pm$ 0.7	112.0 $\pm$ 8.2
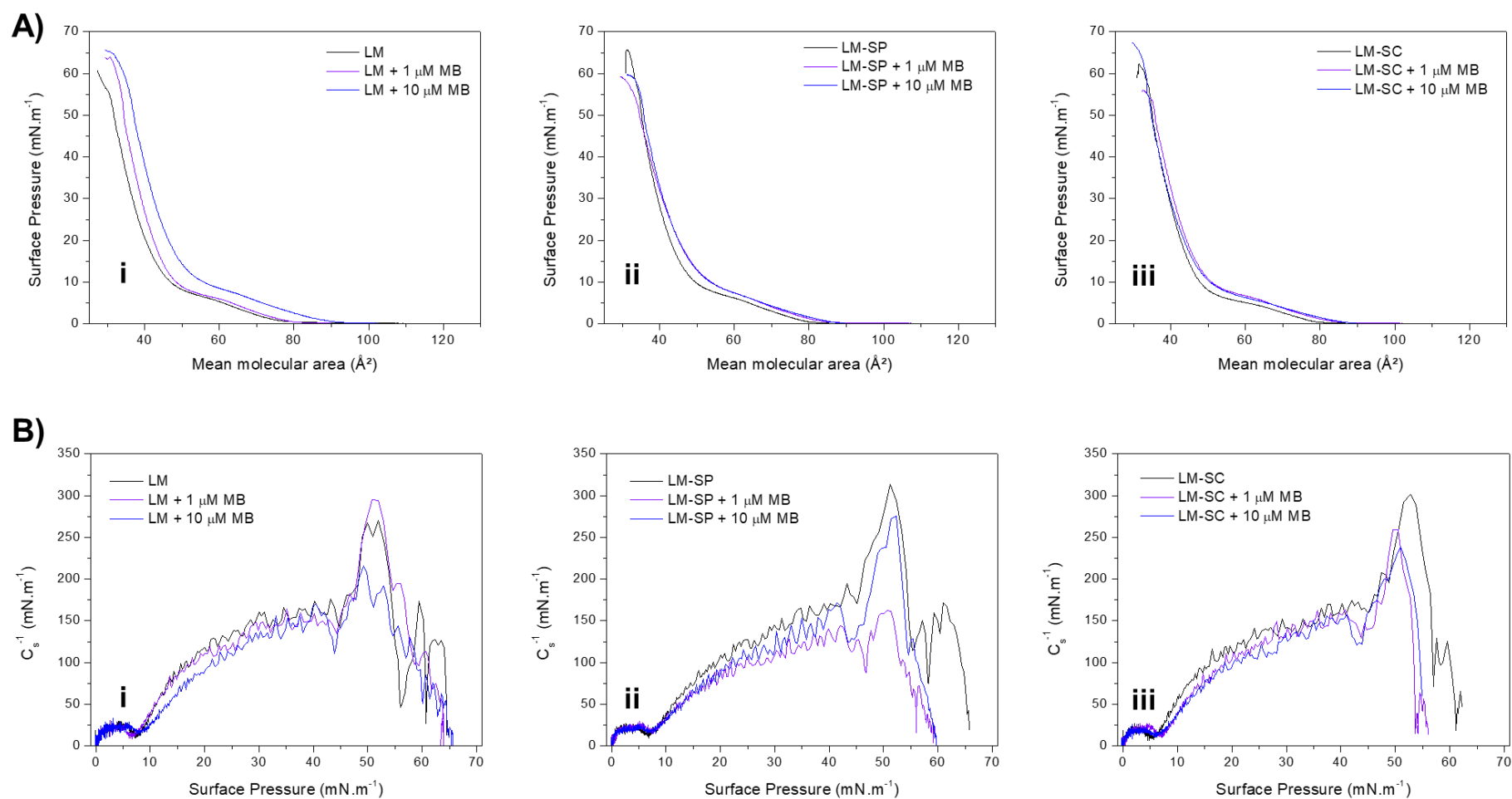
Figure 8.4: Langmuir monolayers containing or not methylene blue (MB). A) Surface pressure – area isotherms with and without MB; B) compressional modulus of the surface pressure – area isotherms. (i) Lipid mixture (ii) lipid mixture + Span® 80, (iii) lipid mixture + sodium cholate. LM: lipid mixture, LM-SP: Lipid mixture with Span® 80, LM-SC: lipid mixture with sodium cholate.
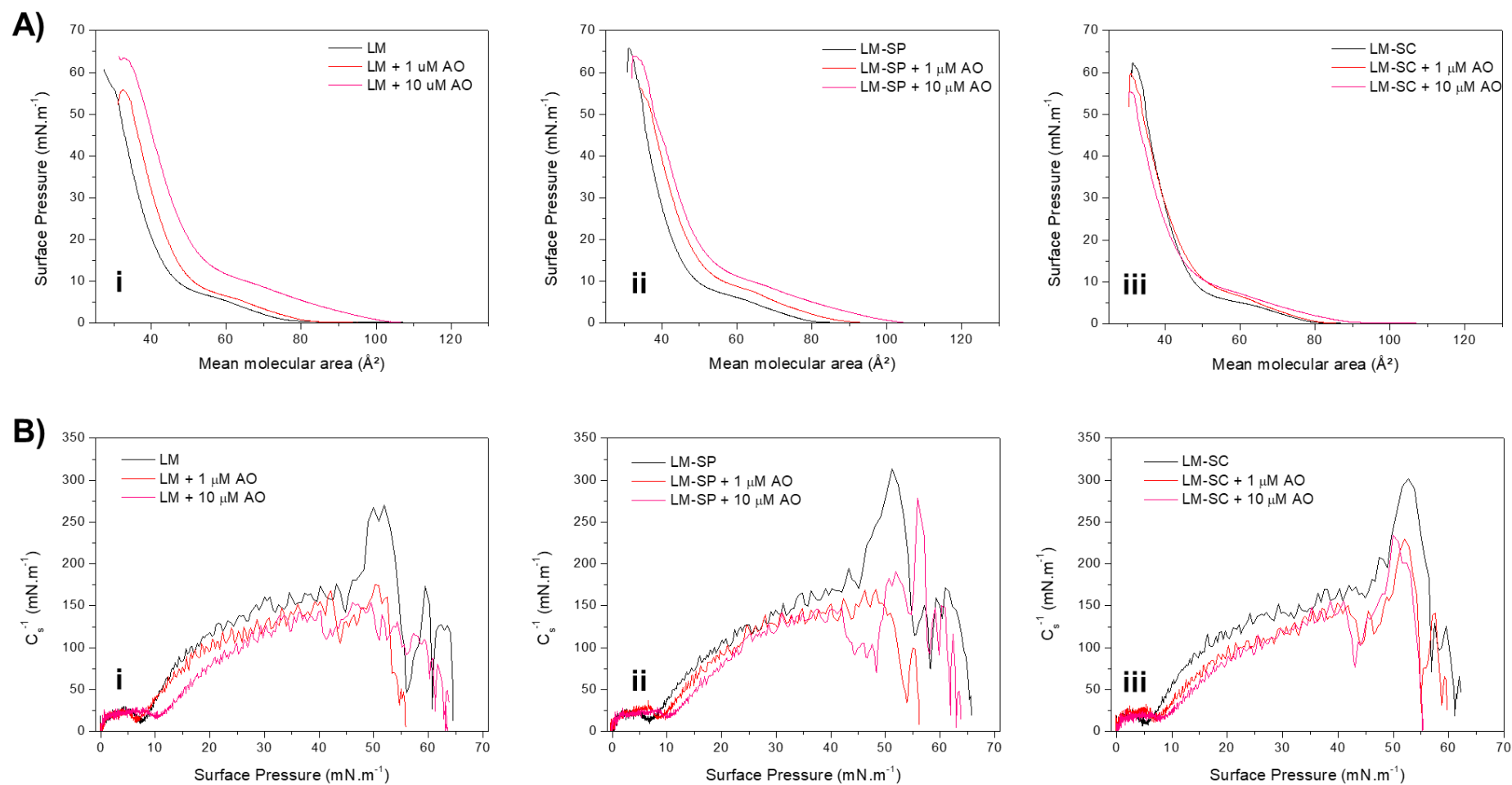
Figure 8.5: Langmuir monolayers containing or not acridine orange (AO). A) Surface pressure – area isotherms with and without AO; B) compressional modulus of the surface pressure – area isotherms. (i) Lipid mixture (ii) lipid mixture + Span® 80, (iii) lipid mixture + sodium cholate. LM: lipid mixture, LM-SP: Lipid mixture with Span® 80, LM-SC: lipid mixture with sodium cholate.

8.3.2 PM-IRRAS

PM-IRRAS spectra for the different monolayers of lipid mixtures, in absence or presence of 10 μM of MB or AO were obtained in the 2800 cm^{-1} - 3000 cm^{-1} and in the 1000 cm^{-1} - 1800 cm^{-1} wavenumber ranges and are presented in Figure 8.6. In these figures, the first wavenumber range (i) is related to C-H stretches and the second (ii) is related with other chemical groups of the lipids. Figure 8.6 – A(i) shows the PM-IRRAS spectra of LM in absence or presence of MB or AO, and it is possible to observe the bands attributed to C-H stretches in CH_2 and CH_3 mainly associated to DPPC and DPPG acyl chains. Table 8.2 present the peak positions obtained from the spectra in Figure 8.6 for the different monolayers. Two prominent peaks should be emphasized namely near 2847 cm^{-1} and 2917 cm^{-1} which are attributed to the symmetric and to asymmetric stretches of CH_2 group, respectively, while the symmetric and asymmetric stretches of CH_3 group are near 2874 cm^{-1} and 2967 cm^{-1}, respectively [38–40]. Comparing the LM to the other samples the stretch related to the asymmetric CH_3 is shifted to a lower position while an opposite pattern is observed for the symmetric CH_3 stretches. These shifts values can vary up to 20 cm^{-1} for the different monolayers. Minor shifts can be observed for the bands corresponding to asymmetric and symmetric CH_2. In fact, some changes in peak position are observed as well as considerable changes in the width and appearance of bands in the wavenumber region attributed to CH_2 stretches. These changes indicate the increase of the all-trans/gauche conformers ratio [29], indicating structural disorder. As the bands assigned C-H stretches are related to the orientation of the acyl chain, the bands of the symmetric CH_2, symmetric CH_3 and asymmetric CH_2 show several changes when comparing the different compositions and, therefore, were deconvoluted (Annex Table D.1) to calculate the orientational order parameter of CH_2 chain. According to Pires et al. [24], the order is calculated by the ratio of the peak area assigned to asymmetric CH_2 and the symmetric CH_2. The results showed values of 3.77, 2.15 and 1.44 for LM without molecules and with MB and AO, respectively. For LM-SP the order results were lower compared to LM, as shown in Figure 8.7. Lastly, LM-SC show increased values of order for LM- with and without MB. LM-SC with AO presented order of 1.67, which is lower compared to the monolayers with the same composition. These results indicate that sodium cholate can lead to a more organized CH_2 chain while the other lipids mixtures, mainly with the addition of the molecules, present decrease of order of CH_2 chain.
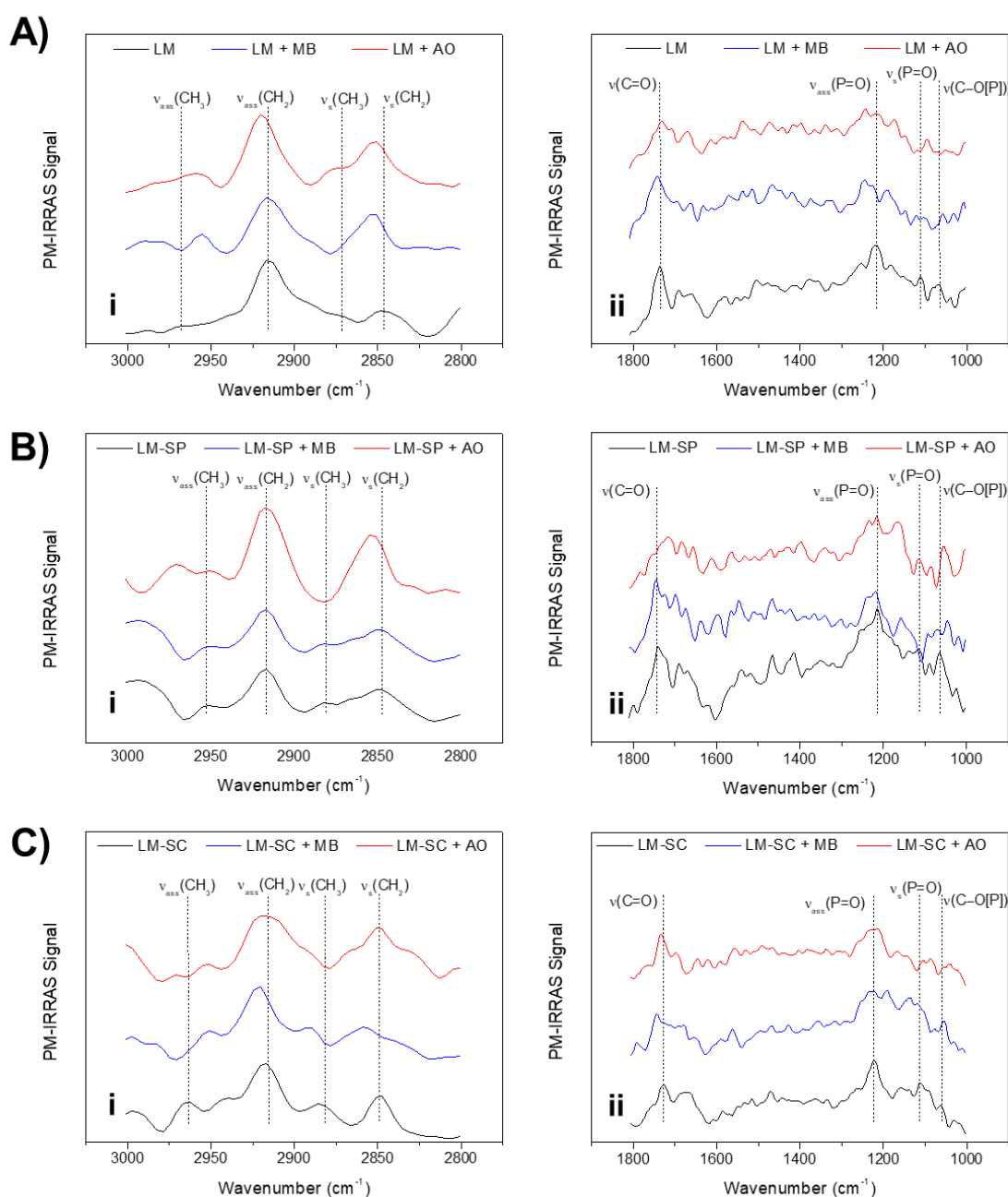
Figure 8.6: PM-IRRAS spectra for monolayers of lipid mixture containing DPPC, DPPG and CHOL (7:2:1 weight ratio) with Span® 80 or sodium cholate, or without the surfactants. Spectra were obtained at 30 mN.m^{-1} with 10 µM of MB or AO or without the dyes. LM: Lipid mixture, LM-SP: lipid mixture with Span® 80, LM-SC: lipid mixture with sodium cholate. Spectra are displayed at i) 2800-3000 cm^{-1} and ii) 1000-1800 cm^{-1} wavenumber range.

The PM-IRRAS 1000 cm^{-1} - 1800 cm^{-1} wavenumber region for the different monolayers are demonstrated in Figure 8.6. In these graphs, the dashed marks show the bands for the polar groups of the lipids which includes the phosphate, the carbonyl, and the C-O stretch. As the relative amount of these chemical groups is not as high as from CH$_2$, the bands present lower intensity as this magnitude is

also dependent on the additive contributions of ordered chemical groups. In general, the bands between 1000 cm^{-1} and 1300 cm^{-1} are attributed to P=O stretches and minor C-H and C-O vibrations [24,33,38–41]. The degree of hydration influences not only the phosphate bands but also the bands between 1700 cm^{-1} - 1800 cm^{-1} attributed to C=O stretches [24,33,39,40]. Some differences are noted upon the incorporation of MB and AO which agrees with our first hypothesis that due to the cationic nature of MB and AO occurs a re-accommodation at high surface pressure to interact attractively with the terminal "head" groups of DPPC and DPPG, such as the phosphate, driven by ion-dipole interactions.

The bands corresponding to the carbonyls were deconvoluted with Gaussian curves and the percentage of hydration of the carbonyls was calculated by the ratio of the area of the hydrated carbonyl peak (~ 1710 cm^{-1} – 1720 cm^{-1}) and the total area of the C=O group wavenumber region [24]. As shown in Table 8.3, it is possible to observe that for LM the C=O hydration was 43.52% and it was increased with the addition of MB (53.46%) and AO (45.14%). The same pattern was observed for LM-SP while the opposite effect was observed for LM-SC, where the hydration of carbonyl decreased. Four contributions were obtained from the deconvolution of the phosphate groups, and it was already reported by previous studies that these bands can present several components possibly related to different degrees of hydration (di-hydrated, mono-hydrated and non-hydrated) [39]. Following the same standard from C=O stretches, the assigned bands to hydrated P=O (~ 1210 cm^{-1} – 1220 cm^{-1}) were used for the calculation of the hydration percentage by the ratio between the hydrated phosphate peak area and the total area of the band [24]. The results exhibit a similar pattern to the hydration of the C=O, showing that the LM and LM-SP present an increase in the hydration with the addition of the photosensitizers while for LM-SC there was a decrease of hydration. These achievements indicates that LM-SC has a significant interaction with the polar parts of the lipids, probably due to electrostatic interaction since sodium cholate is an anionic surfactant present in LM-SC composition. Differently from LM-SC, the other compositions probably present more access to interior sites for interactions which leads to a higher entry of water and consequently an increased hydration.

Table 8.2: Summary of the data obtained from the PM-IRRAS spectra regarding some groups of interest in the ranges of 2800-3000 cm^{-1} and in the1000-1800 cm^{-1}. LM: Lipid mixture, LM-SP: Lipid mixture with Span® 80, LM-SC: lipid mixture with sodium cholate, MB: methylene blue, AO: acridine orange.

| Type of vibration (cm^{-1})		LM	LM + MB	LM + AO	LM-SP	LM-SP + MB	LM-SP + AO	LM-SC	LM-SC + MB	LM-SC + AO
C–H stretching	Asymmetric CH$_3$	2967	2955	2959	2951	2951	2951	2963	2951	2951
	Asymmetric CH$_2$	2917	2917	2921	2917	2917	2917	2916	2920	2920
	Symmetric CH$_3$	2874	-	2874	2882	2882	-	2882	2890	2893
	Symmetric CH$_2$	2847	2851	2851	2847	2847	2851	2847	2859	2851
C=O stretching		1736	1743	1732	1740	1744	1736	1728	1744	1744
P=O stretching	Asymmetric P=O	1215	1231	1215	1215	1219	1223	1215	1215	1215
	Symmetric P=O	1111	1122	1119	1115	-	1115	1107	1107	1107
–C–O–[P] stretching		1065	1057	1049	1065	1069	1057	1065	1057	1057
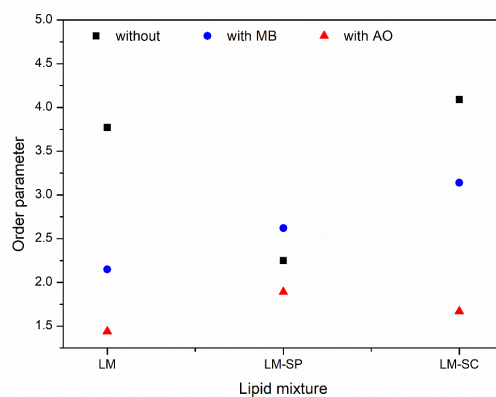
Figure 8.7: Orientational order parameter of CH_2 chain for the different lipid mixtures with and without the molecules. MB: methylene blue, AO: acridine orange.

Table 8.3: Calculated hydration percentage of the carbonyl (C=O) and phosphate (P=O) groups.

Samples		Hydration (%)	
		C=O	**P=O**
LM	-	43.52	53.29
	MB	53.46	56.74
	AO	45.14	64.31
LM-SP	-	54.97	47.45
	MB	56.21	55.34
	AO	78.85	48.66
LM-SC	-	61.67	54.40
	MB	48.71	45.76
	AO	58.26	40.98

As a summary of the results found through the Langmuir monolayers and PM-IRRAS spectra a scheme for each monolayer was prepared. An illustrative organization of DPPC, DPPG and CHOL for LM is shown in Figure 8.8 – A as well as the mode of interaction of the photosensitizers mainly associated to interactions to the phosphate groups. The expected Span® 80 interaction the LM-SP monolayer is displayed in Figure 8.8 – B, where a similar interaction is observed for the cationic molecules with the phosphate groups. Lastly, Figure 8.8 – C shows the possible interaction of sodium cholate to the monolayer, with the polar groups interacting with the subphase and, hence, hindering the hydration of phosphate and carbonyl groups and, additionally, with possible interactions with the cationic dyes MB and AO.
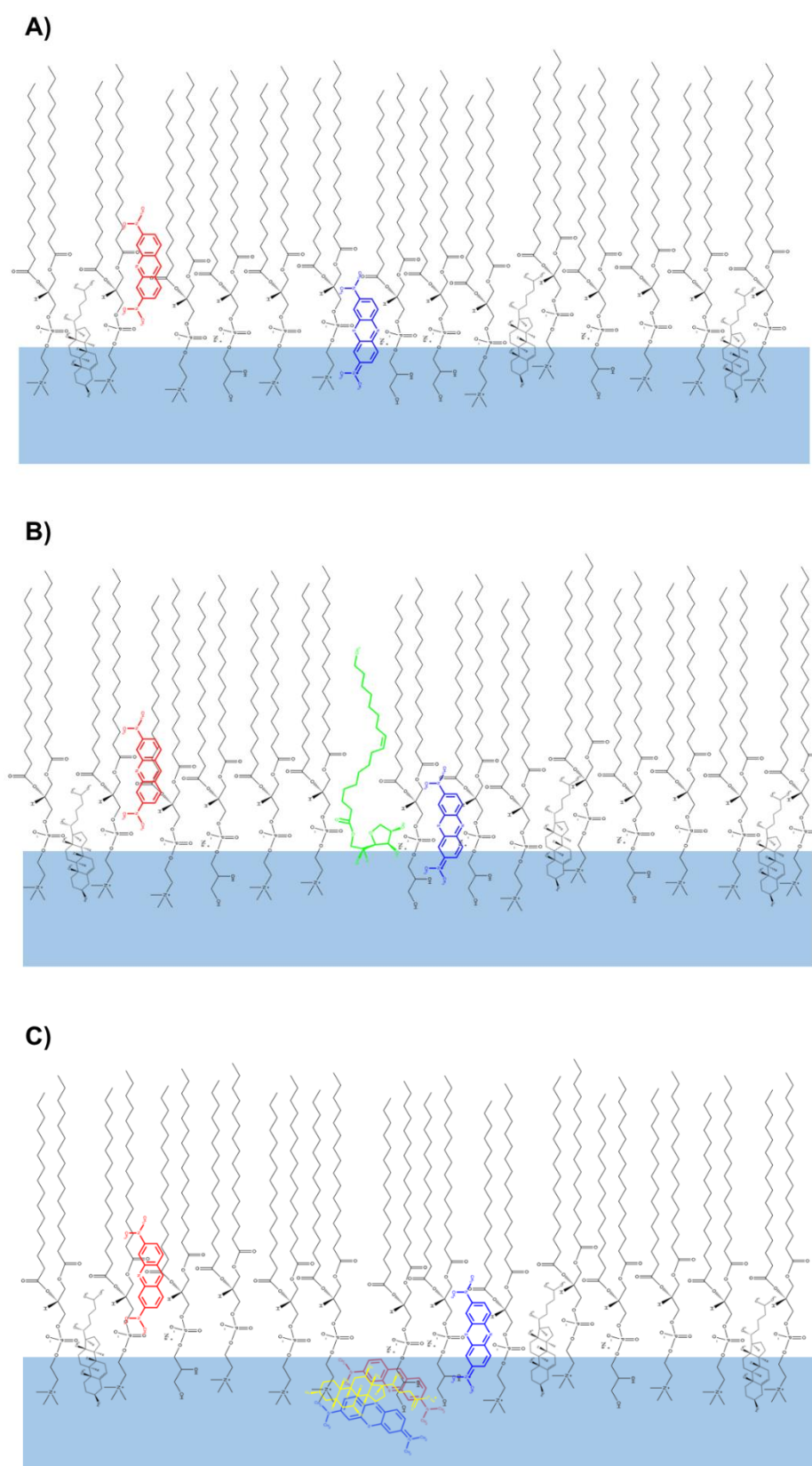
Figure 8.8: Scheme of Langmuir monolayers considering interactions that can occurs with the dyes MB (blue molecule) and AO (red molecule). A) Mixed monolayers containing DPPC, DPPG and CHOL B) mixed

monolayer with the addition of Span® 80 (molecule coloured green) and C) mixed monolayers with the surfactant sodium cholate (molecule coloured yellow).

8.4 Conclusions

Monolayer's study of the different lipid mixtures and with MB or AO in buffer solution allowed to understand better the interaction of the MB and AO photosensitizer molecules with the mixed monolayers. The AO has a greater effect on the expansion of the molecular area while MB has lower effect in this parameter. Furthermore, the decrease of the compressional modulus of monolayers with the addition of the molecules, indicates more flexibility for the monolayer. By the PM-IRRAS analysis, an increase of the hydration of the carbonyl and phosphate groups of LM and LM-SP monolayers when compared to LM-SC monolayer was identified. This means that the LM-SC monolayer is the less hydrated. This result could be attributed to different sites of interaction of Span® 80 and sodium cholate, whereas the sodium cholate interacts more superficially to the polar groups, hindering the entry of water in the interior of the monolayer and, therefore, reducing the hydration when compared to the other samples. These results are also corroborated by the higher orientational order of CH_2 chain for LM-SC monolayer. Analysing this parameter, it was clear that the addition of molecules caused a decrease in the monolayer order and, consequently, increased elasticity, especially in the case of monolayers prepared on the surface with AO buffer solution that present very low order values. Therefore, one can conclude that the addition of both molecules turns the monolayer more disorganized, giving a higher flexibility to the monolayer.

Acknowledgments

References

1. Kwiatkowski, S.; Knap, B.; Przystupski, D.; Saczko, J.; Kędzierska, E.; Knap-Czop, K.; Kotlińska, J.; Michel, O.; Kotowski, K.; Kulbacka, J. Photodynamic therapy – mechanisms, photosensitizers and combinations. *Biomed. Pharmacother.* **2018**, *106*, 1098–1107, doi:10.1016/j.biopha.2018.07.049.

2. Pivetta, T.P.; Botteon, C.E.A.; Ribeiro, P.A.; Marcato, P.D.; Raposo, M. Nanoparticle Systems for Cancer Phototherapy: An Overview. *Nanomaterials* **2021**, *11*, 3132, doi:10.3390/nano11113132.

3. Oniszczuk, A.; Wojtunik-Kulesza, K.A.; Oniszczuk, T.; Kasprzak, K. The potential of photodynamic therapy (PDT)—Experimental investigations and clinical use. *Biomed. Pharmacother.* **2016**, *83*, 912–929, doi:10.1016/j.biopha.2016.07.058.

4. Pivetta, T.P.; Vieira, T.; Silva, J.C.; Ribeiro, P.A.; Raposo, M. Screening on cells of the phototoxic potential of different DNA-intercalators to be applied on skin cancer therapy. *Submitted manuscript*.

5. Lackovičová, M.; Baranyaiová, T.; Bujdák, J. The chemical stabilization of methylene blue in colloidal dispersions of smectites. *Appl. Clay Sci.* **2019**, *181*, 105222, doi:10.1016/j.clay.2019.105222.

6. Felgenträger, A.; Maisch, T.; Dobler, D.; Späth, A. Hydrogen Bond Acceptors and Additional Cationic Charges in Methylene Blue Derivatives: Photophysics and Antimicrobial Efficiency. *Biomed Res. Int.* **2013**, *2013*, 482167, doi:10.1155/2013/482167.

7. Klosowski, E.M.; de Souza, B.T.L.; Mito, M.S.; Constantin, R.P.; Mantovanelli, G.C.; Mewes, J.M.; Bizerra, P.F.V.; Menezes, P.V.M. da C.; Gilglioni, E.H.; Utsunomiya, K.S.; et al. The photodynamic and direct actions of methylene blue on mitochondrial energy metabolism: A balance of the useful and harmful effects of this photosensitizer. *Free Radic. Biol. Med.* **2020**, *153*, 34–53, doi:10.1016/j.freeradbiomed.2020.04.015.

8. Boccalini, G.; Conti, L.; Montis, C.; Bani, D.; Bencini, A.; Berti, D.; Giorgi, C.; Mengoni, A.; Valtancoli, B. Methylene blue-containing liposomes as new photodynamic anti-bacterial agents. *J. Mater. Chem. B* **2017**, *5*, 2788–2797, doi:10.1039/C6TB03367A.

9. Pinto, J.G.; Martins, J.F. de S.; Pereira, A.H.C.; Mittmann, J.; Raniero, L.J.; Ferreira-Strixino, J. Evaluation of methylene blue as photosensitizer in promastigotes of Leishmania major and Leishmania braziliensis. *Photodiagnosis Photodyn. Ther.* **2017**, *18*, 325–330, doi:10.1016/j.pdpdt.2017.04.009.

10. Sousa, J.N.L. de; Queiroga, B.H. de; Kocerginsky, P. de O.; Marinho, P.H.C.; Araki, Â.T. Photoinactivation of Candida albicans using methylene blue as photosensitizer. *RGO - Rev. Gaúcha Odontol.* **2015**, *63*, 411–417, doi:10.1590/1981-863720150003000063028.

11. Kofler, B.; Romani, A.; Pritz, C.; Steinbichler, T.; Schartinger, V.; Riechelmann, H.; Dudas, J. Photodynamic Effect of Methylene Blue and Low Level Laser Radiation in Head and Neck Squamous Cell Carcinoma Cell Lines. *Int. J. Mol. Sci.* **2018**, *19*, 1107, doi:10.3390/ijms19041107.

12. Lim, D.-J. Methylene Blue-Based Nano and Microparticles: Fabrication and Applications in Photodynamic Therapy. *Polymers (Basel).* **2021**, *13*, 3955, doi:10.3390/polym13223955.

13. Damas-Souza, D.M.; Nunes, R.; Carvalho, H.F. An improved acridine orange staining of DNA/RNA. *Acta Histochem.* **2019**, *121*, 450–454, doi:10.1016/j.acthis.2019.03.010.

14. Byvaltsev, V.A.; Bardonova, L.A.; Onaka, N.R.; Polkin, R.A.; Ochkal, S. V.; Shepelev, V. V.; Aliyev, M.A.; Potapov, A.A. Acridine Orange: A Review of Novel Applications for Surgical Cancer Imaging and Therapy. *Front. Oncol.* **2019**, *9*, 925, doi:10.3389/fonc.2019.00925.

15. Pierzyńska-Mach, A.; Janowski, P.A.; Dobrucki, J.W. Evaluation of acridine orange, LysoTracker Red, and quinacrine as fluorescent probes for long-term tracking of acidic vesicles. *Cytom. Part A* **2014**, *85*, 729–737, doi:10.1002/cyto.a.22495.

16. Thomé, M.P.; Filippi-Chiela, E.C.; Villodre, E.S.; Migliavaca, C.B.; Onzi, G.R.; Felipe, K.B.; Lenz, G. Ratiometric analysis of acridine orange staining in the study of acidic organelles and autophagy. *J. Cell Sci.* **2016**, *129*, 4622–4632, doi:10.1242/jcs.195057.

17. Osman, H.; Elsahy, D.; Saadatzadeh, M.R.; Pollok, K.E.; Yocom, S.; Hattab, E.M.; Georges, J.; Cohen-Gadol, A.A. Acridine Orange as a Novel Photosensitizer for Photodynamic Therapy in Glioblastoma. *World Neurosurg.* **2018**, *114*, e1310–e1315, doi:10.1016/j.wneu.2018.03.207.

18. Lin, Y.-C.; Lin, J.-F.; Tsai, T.-F.; Chen, H.-E.; Chou, K.-Y.; Yang, S.-C.; Tang, Y.-M.; Hwang, T.I.S. Acridine orange exhibits photodamage in human bladder cancer cells under blue light exposure. *Sci. Rep.* **2017**, *7*, 14103, doi:10.1038/s41598-017-13904-0.

19. Pavinatto, F.J.; Caseli, L.; Oliveira, O.N. Chitosan in Nanostructured Thin Films. *Biomacromolecules* **2010**, *11*, 1897–1908, doi:10.1021/bm1004838.

20. Hąc-Wydro, K.; Kapusta, J.; Jagoda, A.; Wydro, P.; Dynarowicz-Łątka, P. The influence of phospholipid structure on the interactions with nystatin, a polyene antifungal antibiotic. *Chem. Phys. Lipids* **2007**, *150*, 125–135, doi:10.1016/j.chemphyslip.2007.06.222.

21. Barbosa, S.C.; Nobre, T.M.; Volpati, D.; Ciancaglini, P.; Cilli, E.M.; Lorenzón, E.N.; Oliveira, O.N. The importance of cyclic structure for Labaditin on its antimicrobial activity against Staphylococcus aureus. *Colloids Surfaces B Biointerfaces* **2016**, *148*, 453–459, doi:10.1016/j.colsurfb.2016.09.017.

22. Geraldo, V.P.N.; Pavinatto, F.J.; Nobre, T.M.; Caseli, L.; Oliveira, O.N. Langmuir films containing ibuprofen and phospholipids. *Chem. Phys. Lett.* **2013**, *559*, 99–106, doi:10.1016/j.cplett.2012.12.064.

23. Jurak, M.; Szafran, K.; Cea, P.; Martín, S. Analysis of Molecular Interactions between

Components in Phospholipid-Immunosuppressant-Antioxidant Mixed Langmuir Films. *Langmuir* **2021**, *37*, 5601–5616, doi:10.1021/acs.langmuir.1c00434.

24. Pires, F.; Geraldo, V.P.N.; Rodrigues, B.; Granada-Flor, A. De; de Almeida, R.F.M.; Oliveira, O.N.; Victor, B.L.; Machuqueiro, M.; Raposo, M. Evaluation of EGCG Loading Capacity in DMPC Membranes. *Langmuir* **2019**, *35*, 6771–6781, doi:10.1021/acs.langmuir.9b00372.

25. Węder, K.; Mach, M.; Hąc-Wydro, K.; Wydro, P. Studies on the interactions of anticancer drug - Minerval - with membrane lipids in binary and ternary Langmuir monolayers. *Biochim. Biophys. Acta - Biomembr.* **2018**, *1860*, 2329–2336, doi:10.1016/j.bbamem.2018.05.019.

26. Wnętrzak, A.; Łątka, K.; Marzec, M.; Dynarowicz-Łątka, P. Langmuir Monolayer Characteristics of Erucylphosphocholine - A Novel Anti-Tumor Drug. *Acta Phys. Pol. A* **2012**, *121*, 468–473, doi:10.12693/APhysPolA.121.468.

27. Fernández, L.; Reviglio, A.L.; Heredia, D.A.; Morales, G.M.; Santo, M.; Otero, L.; Alustiza, F.; Liaudat, A.C.; Bosch, P.; Larghi, E.L.; et al. Langmuir-Blodgett monolayers holding a wound healing active compound and its effect in cell culture. A model for the study of surface mediated drug delivery systems. *Heliyon* **2021**, *7*, e06436, doi:10.1016/j.heliyon.2021.e06436.

28. Rojewska, M.; Smułek, W.; Kaczorek, E.; Prochaska, K. Langmuir Monolayer Techniques for the Investigation of Model Bacterial Membranes and Antibiotic Biodegradation Mechanisms. *Membranes (Basel).* **2021**, *11*, 707, doi:10.3390/membranes11090707.

29. Oliveira, O.N.; Caseli, L.; Ariga, K. The Past and the Future of Langmuir and Langmuir–Blodgett Films. *Chem. Rev.* **2022**, 122, 6459-6513, doi:10.1021/acs.chemrev.1c00754.

30. de Oliveira Pedro, R.; Ribeiro Pereira, A.; Oliveira, O.N.; Barbeitas Miranda, P. Interaction of chitosan derivatives with cell membrane models in a biologically relevant medium. *Colloids Surfaces B Biointerfaces* **2020**, *192*, 111048, doi:10.1016/j.colsurfb.2020.111048.

31. Pereira, M.S.; Maximino, M.D.; Martin, C.S.; Aoki, P.H.B.; Oliveira Jr, O.N.; Alessio, P. Lipid-matrix effects on tyrosinase immobilization in Langmuir and Langmuir-Blodgett films. *An. Acad. Bras. Cienc.* **2021**, *93*, 1–13, doi:10.1590/0001-3765202120200019.

32. Rudolphi-Skórska, E.; Filek, M.; Zembala, M. The Effects of the Structure and Composition of the Hydrophobic Parts of Phosphatidylcholine-Containing Systems on Phosphatidylcholine Oxidation by Ozone. *J. Membr. Biol.* **2017**, *250*, 493–505, doi:10.1007/s00232-017-9976-8.

33. Schmidt, T.F.; Caseli, L.; Oliveira, O.N.; Itri, R. Binding of Methylene Blue onto Langmuir Monolayers Representing Cell Membranes May Explain Its Efficiency as Photosensitizer in Photodynamic Therapy. *Langmuir* **2015**, *31*, 4205–4212, doi:10.1021/acs.langmuir.5b00166.

34. Himeno, H.; Shimokawa, N.; Komura, S.; Andelman, D.; Hamada, T.; Takagi, M. Charge-induced phase separation in lipid membranes. *Soft Matter* **2014**, *10*, 7959–7967, doi:10.1039/C4SM01089B.

35. Chen, F.; Zhao, E.; Kim, T.; Wang, J.; Hableel, G.; Reardon, P.J.T.; Ananthakrishna, S.J.; Wang,

T.; Arconada-Alvarez, S.; Knowles, J.C.; et al. Organosilica Nanoparticles with an Intrinsic Secondary Amine: An Efficient and Reusable Adsorbent for Dyes. *ACS Appl. Mater. Interfaces* **2017**, *9*, 15566–15576, doi:10.1021/acsami.7b04181.

36. Sousa, H.R.; Silva, L.S.; Sousa, P.A.A.; Sousa, R.R.M.; Fonseca, M.G.; Osajima, J.A.; Silva-Filho, E.C. Evaluation of methylene blue removal by plasma activated palygorskites. *J. Mater. Res. Technol.* **2019**, *8*, 5432–5442, doi:10.1016/j.jmrt.2019.09.011.

37. Shaikh, M.; Mohanty, J.; Singh, P.K.; Nau, W.M.; Pal, H. Complexation of acridine orange by cucurbit[7]uril and β-cyclodextrin: photophysical effects and pK a shifts. *Photochem. Photobiol. Sci.* **2008**, *7*, 408–414, doi:10.1039/B715815G.

38. Wrobel, E.C.; de Lara, L.S.; do Carmo, T.A.S.; Castellen, P.; Lazzarotto, M.; de Lázaro, S.R.; Camilo, A.; Caseli, L.; Schmidt, R.; DeWolf, C.E.; et al. The antibacterial activity of p-tert -butylcalix[6]arene and its effect on a membrane model: molecular dynamics and Langmuir film studies. *Phys. Chem. Chem. Phys.* **2020**, *22*, 6154–6166, doi:10.1039/D0CP00432D.

39. Mendelsohn, R.; Mao, G.; Flach, C.R. Infrared reflection–absorption spectroscopy: Principles and applications to lipid–protein interaction in Langmuir films. *Biochim. Biophys. Acta - Biomembr.* **2010**, *1798*, 788–800, doi:10.1016/j.bbamem.2009.11.024.

40. Pires, F.; Magalhães-Mota, G.; Geraldo, V.P.N.; Ribeiro, P.A.; Oliveira, O.N.; Raposo, M. The impact of blue light in monolayers representing tumorigenic and nontumorigenic cell membranes containing epigallocatechin-3-gallate. *Colloids Surfaces B Biointerfaces* **2020**, *193*, 111129, doi:10.1016/j.colsurfb.2020.111129.

41. Madrid, E.; Horswell, S.L. Effect of Electric Field on Structure and Dynamics of Bilayers Formed From Anionic Phospholipids. *Electrochim. Acta* **2014**, *146*, 850–860, doi:10.1016/j.electacta.2014.01.035.

$$\bigg| \; 9$$

CONCLUSIONS

In this chapter the main conclusions of this thesis work are presented according to the sequence of the chapters related to the results obtained, namely the chapters 5, 6, 7 and 8. Therefore the main conclusions follow the sequence of the screening of the DNA-intercalating drugs regarding their photosensitizing potential in skin cancer cells. Then the results showed the liposomes optimization process to obtain the most stable formulations for the encapsulation of the methylene blue (MB) and acridine orange (AO) molecules. Finally, the interactions of these molecules with the DNA and lipids were evaluated.

The first batch of experiment focused on the selection of some DNA-intercalating agents with photosensitizing potential. Several molecules from different classes such as dyes (methylene blue, acridine orange and gentian violet), natural products (quercetin, epigallocatechin gallate and curcumin) and chelating agents (neocuproine, 1,10-phenanthroline and 2,2'-bipyridyl) were investigated in cytotoxicity studies of 24 and 48 hours and phototoxicity studies in cancer cells submitting the treated cells to different wavelength light irradiation. From these results mainly two compounds presented significant phototoxicity activity in cancer keratinocytes, with an elevated IC_{50} of the cells kept in the dark in comparison with cells irradiated at specific wavelength light sources, showing that for MB and AO there was a very significant difference with the irradiation of the treated cells leading to a reduced cell viability. For the continuation of the studies, these promising molecules were tested for the detection of ROS production by fluorescence microscopy, where acridine orange showed a significant production of ROS species with the probe used in the study, while methylene blue did not exhibit as efficient as AO. Lastly, to evaluate the potential application in other types of cancer, the compounds were test in melanoma cell line and exhibited again photodamage compared to the controls kept in the dark, however the IC_{50} of the phototoxicity studies in melanoma cells was higher compared to keratinocytes cancer cell line, showing that these cells are indeed more resistant for the treatment.

Based on the selected DNA-intercalating agents as photosensitizers in keratinocytes cancer cells, an optimization of liposomes was performed to encapsulate these molecules aiming the skin delivery. For that, several combinations of the lipids DPPC, DPPG, DOPG and cholesterol were tested in

presence or not of the surfactant molecules Tween® 80, Span® 80 and sodium cholate. The results show that among the three lipid compositions, the DOPG led to a destabilization of the liposomes along time. The same was observed for formulations containing the surfactant Tween® 80. Finally, analysing the different compositions we observed that formulations containing cholesterol showed great stability as well as the dual lipid formulation of DPPC + DPPG. However, when the photosensitizers were added to the liposomes, the simplest formulation containing only DPPC and DPPG was not able to encapsulate the molecules and maintain the formulation stable along the time studied. The formulations containing cholesterol and with Span® 80 or sodium cholate showed good stability however the size of the particles was very different when considered the encapsulation of MB and AO, indicating that these molecules interacted in different ways with the lipid bilayer. The encapsulation efficiency showed good encapsulation of MB but even better encapsulation of the AO molecules. The studies in the cancer keratinocytes cells showed two different possible approaches: MB-liposomes with the potential as a cytotoxic agent for cancer cells; and AO-liposomes with a great potential phototoxicity at very low concentrations.

The effect of the irradiation on the MB and AO molecules with and without the DNA was investigated. The intercalation with the DNA resulted in a significant difference of normalized absorbance kinetic pattern of degradation, compared to solutions with the compounds only. These results suggest that the molecules had significant insertion in the DNA in a way that delays the effect of the radiation in comparison with the compounds alone.

Based on the three main lipid compositions of DPPC, DPPG and CHOL in the absence and in the presence of Span® 80 and sodium cholate it was studied the interaction of the molecules with mixed monolayers containing the cited lipids. It was possible to observe that the surfactants caused an increase in the area expansion in the lipid mixture monolayer and, analysing the effect of the molecules, AO had a greater effect on the expansion of the molecular area while MB showed lower effect in this parameter. However, analysing the compressional modulus values, it possible to predict that the addition of the molecules leads to a higher flexibility of the monolayers. These results were corroborated by the PM-IRRAS spectra analysis where the addition of MB and AO resulted in several shifts of the peaks related to the C-H stretches and also from the peaks related to the polar group of the lipids such as the carbonyl and the phosphates, which indicated structural disorder. The interaction of MB and AO also influence the hydration of the carbonyl and the phosphates which was enhanced in the lipid mixture of DPPC, DPPG and CHOL without and with Span® 80, however different results were obtained for the lipid mixture containing sodium cholate, showing that the mode of interaction of this anionic surfactant had an effect on the mode of the molecules interaction as well as the hydration of the monolayer.

In summary, this thesis enabled the screening of several DNA-intercalating molecules and the selection of the most promising molecules as well as the development of a nanocarrier system for the encapsulation of the photosensitizers aiming the topical application for the photodynamic therapy of skin cancer. Lastly, some studies of interactions were important to understand the interaction of the

molecules and the lipids as well as with the DNA, launching for new ideas and better comprehension of the application of the systems developed for the clinical application.

Future directions

To go beyond the conclusions discussed in this work, some additional experiments should be considered and performed to obtain more data concerning the application of the liposomes for PDT as well as confirm the interactions occurring between the lipids of the nanoparticles and the molecules. Therefore, some possibilities are described ahead:

Concerning the studies *in vitro* in cell culture:

- Continuation of the ROS studies using other types of probes for the specific identification of the reactive species.
- The investigation of the pathway leading to the cell death after the irradiation should also be addressed.
- The study of DNA degradation by the Comet assay should be performed, as a very important study to understand whether the photosensitizing effect had an impact on the DNA.

Additional studies with the nanoparticles for PDT:

- Characterization of the liposomes by Atomic Force Microscopy (AFM).
- To understand the effect that the different lipid compositions can impair on the liberation of the molecules MB and AO, permeation and retention studies should be performed to evaluate the extension of the delivery of these molecules in the different layers of the skin.
- Regarding the *in vitro* studies in cell culture with the liposomes, the cellular uptake should be studied to understand in detail the delivery of the photosensitizers from the nanocarriers, evaluating different times of cell uptake.
- The development of a suitable formulation for the incorporation of the liposomes aiming the topical application as well as the characterization of the formulation.
- *In vivo* experiments in skin cancer models.

Future studies for the unveiling of the interaction of the photosensitizers with the lipids and the DNA:

- For the study of the intercalating agents and the DNA, further characterization of the systems submitted to irradiation should also be performed by fluorescence spectroscopy and Fourier-transform infrared spectroscopy (FTIR).
- Brewster angle microscopy (BAM) should be considered for the morphologic characterization of the mixed monolayers.

- Furthermore, molecular dynamics simulations should be performed to confirm from the computational perspective the hypothesis of the interactions occurring between the photosensitizers and the lipids used in the monolayer, as well as the mode of interaction of the surfactants with the lipids.

APPENDIX

DNA-INTERCALATING AGENTS: A STUDY OF THE PHOTOSENSITIZING EFFECT

To calculate the IC_{50} of AO irradiated by blue light it was necessary to use a range of low concentrations (0.31 μM to 10 μM) and for the calculation of the IC_{50} of the compounds quercetin (QT), epigallocatechin gallate (EGCG) and 2,2'-bipyridyl the experiment was repeated with an increased range up to 320 μM, results that are showed below.
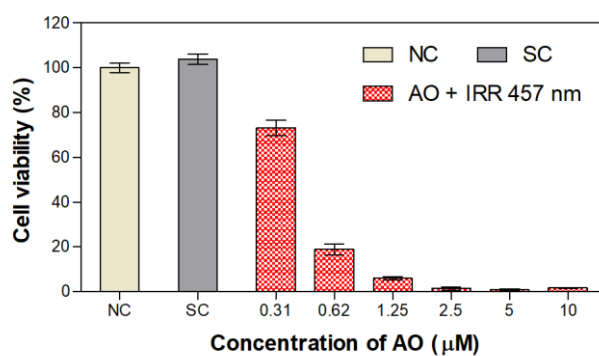
Figure A.1: Cell viability of MET1 SCC cell line treated with AO and irradiated with blue light (457 nm). Values are mean ± combined standard uncertainty (n=6). AO: acridine orange.
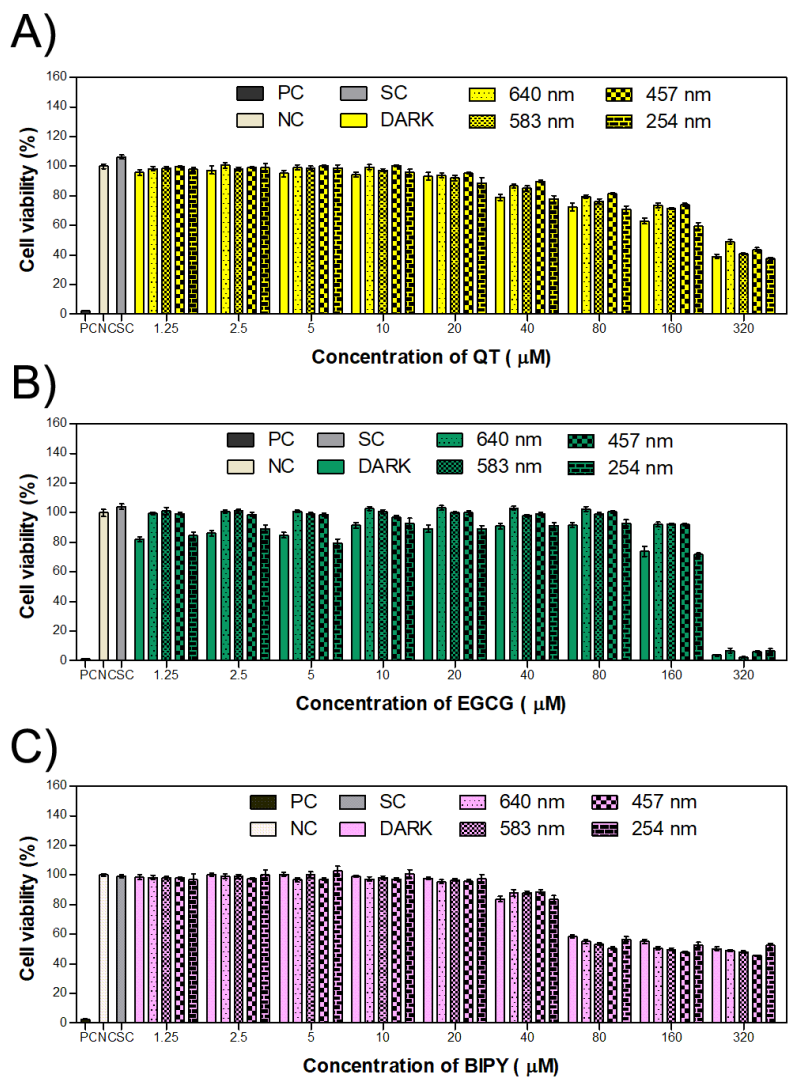
Figure A.2: Cell viability of MET1 SCC cell line treated with QT, EGCG and BIPY. Samples kept in the dark were used as control compared to those submitted to different wavelengths irradiation. Values are mean ± combined standard uncertainty (n=6). QT: quercetin, EGCG: epigallocatechin gallate, BIPY: 2,2'-bipyridyl.

OPTIMIZATION OF NANOLIPOSOMES FOR THE TOPICAL DELIVERY OF PHOTOSENSITIZERS

The evaluation for the obtention of the most promising liposomes formulations considered the stability of the nanoparticle along the time by size measurements. Therefore, the distribution profile was also important to verify if there were particles in the region of the micrometer. Below it is exhibited the size distribution on day 1 of the empty liposomes and with MB or AO, for the four different lipid compositions that showed better results in a first stage.
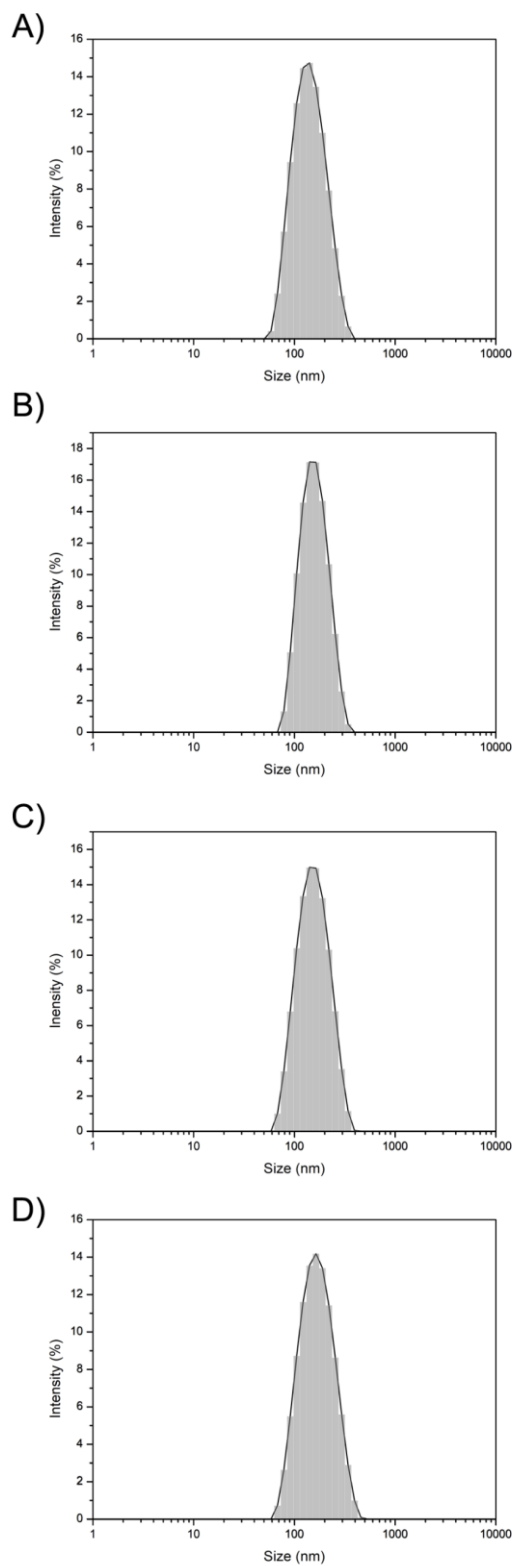
Figure B.1: Size distribution of different empty liposomes. A) L1 composition, B) L2 composition, C) L2 composition with the addition of Span® 80 and D) the L2 composition with the addition of sodium cholate.
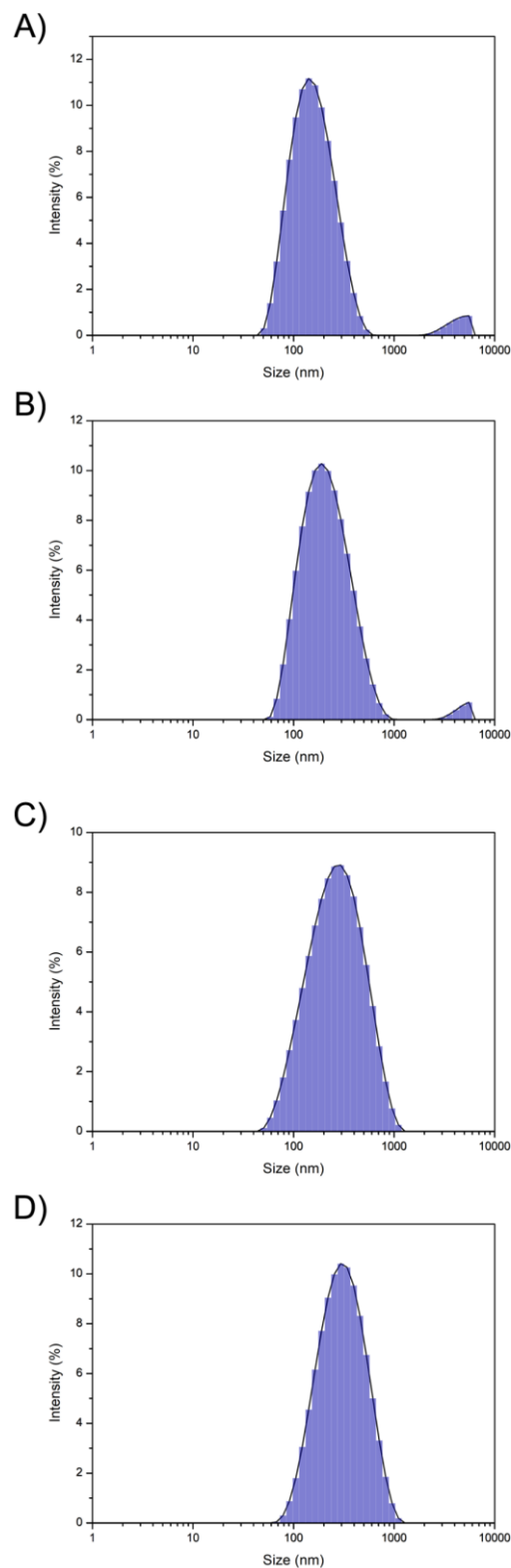
Figure B.2: Size distribution of different composition of liposomes containing MB. A) L1 composition, B) L2 composition, C) L2 composition with the addition of Span® 80 and D) the L2 composition with the addition of sodium cholate. MB: methylene blue.
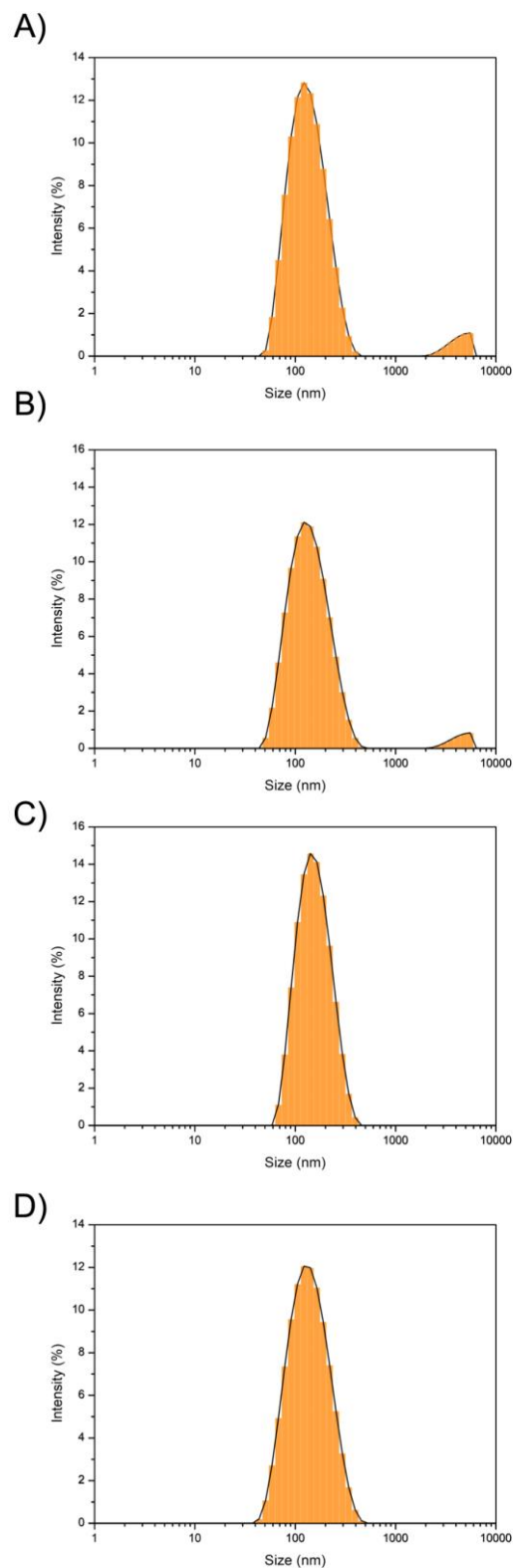
Figure B.3: Size distribution of different liposomes compositions containing AO. A) L1 composition, B) L2 composition, C) L2 composition with the addition of Span® 80 and D) the L2 composition with the addition of sodium cholate. AO: Acridine orange.

Exploiting the use of Acridine Orange and Methylene Blue in biological systems I:
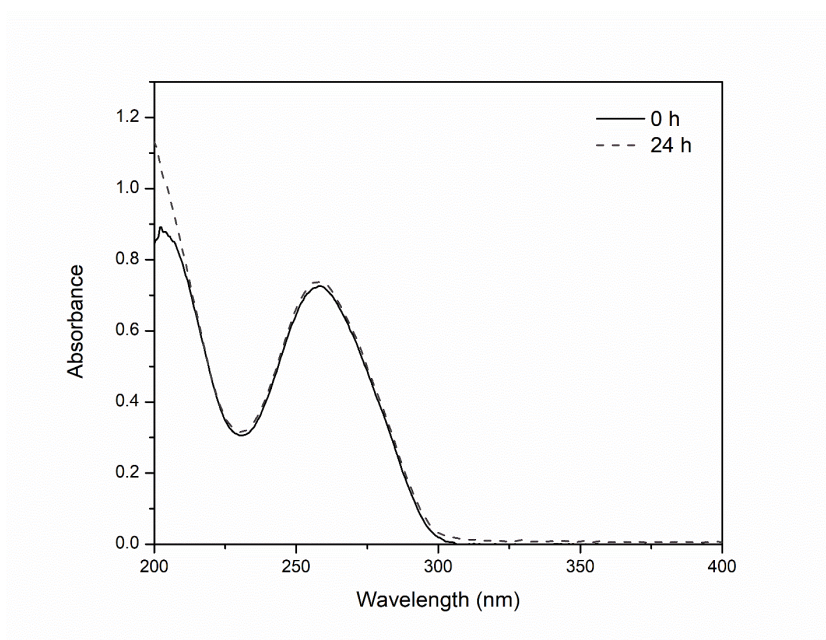## an Analysis of the Dyes effects on the DNA

Figure C.1: Spectra of ct-DNA kept in the dark with measurements after the preparation (0 hours) and 24 hours after the first measurement.
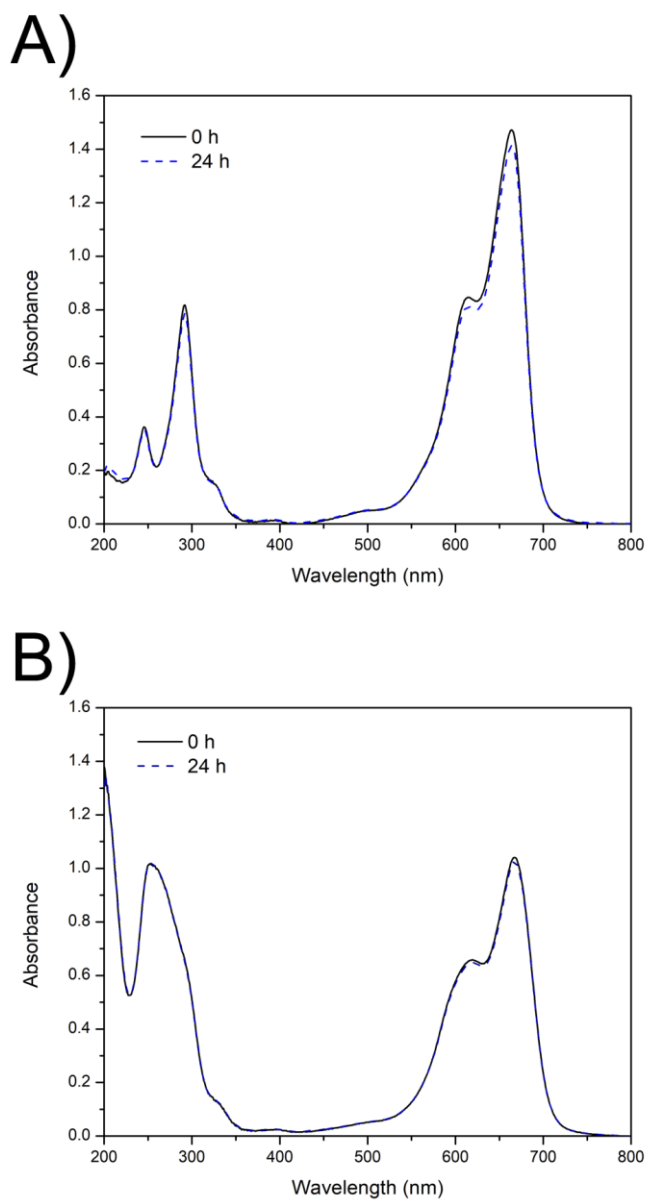
Figure C.2: Spectra of methylene blue without (A) and with DNA (B) kept in the dark with measurements after the preparation (0 hours) and 24 hours later.
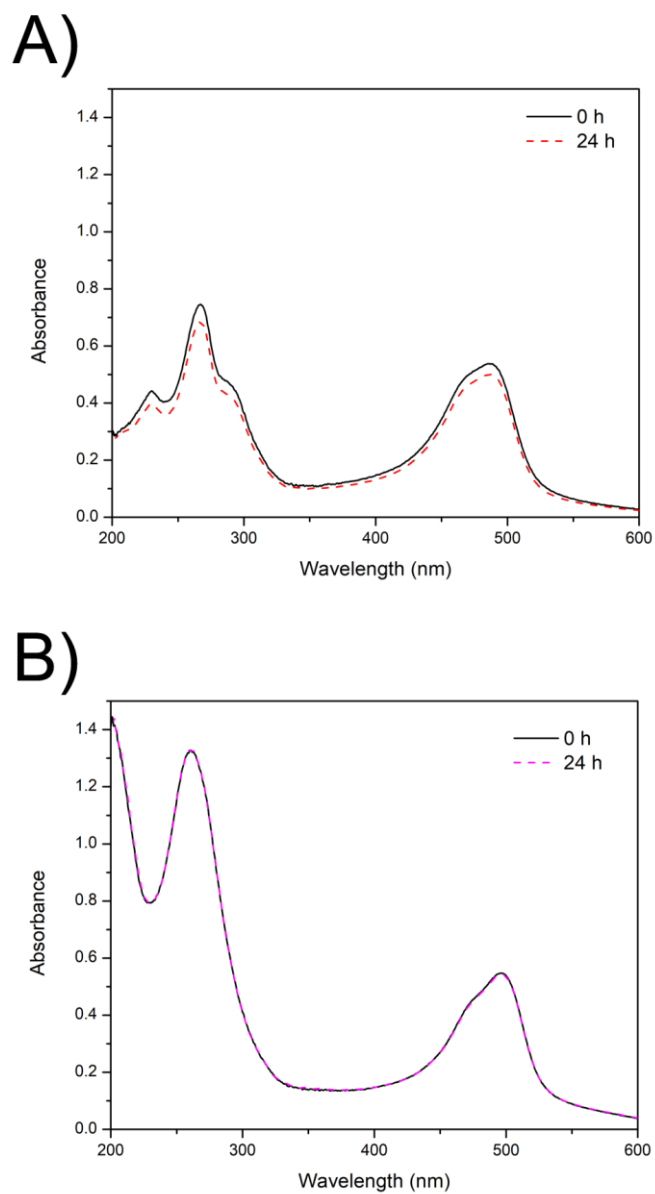
Figure C.3: Spectra of acridine orange without (A) and with DNA (B) kept in the dark with measurements after the preparation (0 hours) and 24 hours later.

D

Exploiting the use of Acridine Orange and Methylene Blue in biological systems II: an Investigation of the Dyes effects on Lipids

Table D.1: Data of the peak and the normalized area obtained from the deconvolution of the PM-IRRAS spectra, regarding to the peaks of the C-H stretches, the carbonyl group (C=O) and the phosphate group (P=O). LM: lipid mixture, LM-SP: lipid mixture + Span® 80, LM-SC: lipid mixture + sodium cholate. MB: methylene blue, AO: acridine orange.

Sample	C-H		C=O		P=O	
	Peak	Normalized area	Peak	Normalized area	Peak	Normalized area
LM	2846.03	0.19	1717.33	0.44	1214.33	0.53
	2872.34	0.08	1735.57	0.38	1229.51	0.10
	2888.17	0.11	1751.24	0.11	1254.43	0.30
	2915.16	0.62	1757.10	0.03	1278.74	0.06
			1774.40	0.05		
LM + MB	2853.03	0.30	1720.18	0.53	1228.67	0.57
	2866.73	0.05	1744.86	0.40	1247.97	0.17
	2895.62	0.11	1761.63	0.04	1258.97	0.16
	2916.05	0.54	1771.53	0.01	1283.80	0.10
			1779.83	0.01		
LM + AO	2852.16	0.38	1709.71	0.45	1216.93	0.64
	2877.43	0.07	1723.70	0.03	1243.86	0.13
	2903.04	0.05	1733.43	0.29	1262.75	0.20
	2920.03	0.50	1750.96	0.23	1281.13	0.03
			1766.67	0.01		

Table D.1: Continued.

LM-SP	2847.27	0.26	1724.16	0.55	1213.08	0.47
	2866.23	0.15	1741.41	0.11	1234.96	0.15
	2883.09	0.05	1759.71	0.28	1254.16	0.30
	2918.15	0.54	1781.01	0.02	1281.97	0.08
			1799.71	0.04		
LM-SP + MB	2851.35	0.27	1723.67	0.56	1217.61	0.55
	2889.56	0.03	1744.69	0.16	1240.45	0.29
	2901.90	0.12	1753.77	0.16	1244.95	0.13
	2917.41	0.58	1768.28	0.10	1278.05	0.03
			1784.27	0.02		
LM-SP + AO	2852.33	0.33	1716.48	0.79	1214.73	0.49
	2866.03	0.06	1736.58	0.02	1236.01	0.13
	2910.22	0.03	1758.21	0.12	1253.78	0.34
	2916.83	0.59	1783.53	0.06	1290.02	0.04
			1796.84	0.01		
LM-SC	2847.40	0.13	1706.08	0.62	1220.59	0.54
	2854.55	0.05	1728.00	0.15	1226.36	0.30
	2879.67	0.09	1733.08	0.07	1263.66	0.12
	2888.77	0.07	1756.92	0.13	1279.07	0.04
	2918.72	0.66	1763.11	0.03		
LM-SC + MB	2839.51	0.04	1709.33	0.49	1191.25	0.46
	2859.11	0.20	1724.54	0.03	1222.35	0.23
	2872.47	0.003	1744.53	0.33	1239.75	0.20
	2891.91	0.14	1759.89	0.08	1257.09	0.11
	2921.86	0.62	1789.98	0.07		
LM-SC + AO	2829.88	0.09	1723.42	0.58	1210.81	0.41
	2849.78	0.26	1733.50	0.25	1237.00	0.46
	2867.76	0.06	1741.38	0.05	1260.87	0.10
	2899.17	0.20	1763.10	0.07	1269.94	0.03
	2919.48	0.39	1775.16	0.04		

LIPOSOMES ENCAPSULATING DNA-INTERCALATING MOLECULES: AN APPROACH FOR PHOTODYNAMIC THERAPY APPLICATION

THAIS PRISCILLA PIVETTA

2022